

SUPRAMOLECULAR SELF-ASSOCIATING AMPHIPHILES

Thesis for the degree of Doctor of Philosophy



By Lisa Jane White

UNIVERSITY OF KENT
SCHOOL OF PHYSICAL SCIENCES
September 2020

UNIVERSITY OF KENT
SCHOOL OF PHYSICAL SCIENCES
Doctor of Philosophy
Supramolecular Self-Associated Amphiphiles (SSAs)
By Lisa Jane White

Abstract

This thesis reports the synthesis of 30 structurally related compounds, related by stepwise variation of a hydrogen bond donor-acceptor amphiphilic salt. The self-associative and corresponding global properties of these compounds were investigated in the solid state, solution state and gas phase to enable elucidation of any structure-activity relationships. In the solution state, it was established that the molecular self-association of these compounds could be controlled through modification of the solvent environment. In organic DMSO these compounds principally form dimeric species and in an aqueous environment, spherical aggregates were preferentially formed. The addition of salt to the aqueous solution resulted in the generation of a hydrogel. The physicochemical properties and antimicrobial properties of these gelled materials were then investigated, where it was shown that these hydrogels exhibit antimicrobial properties against both Gram-negative and Gram-positive bacteria. Finally, a tool-kit of novel high-throughput microplate reader technology was developed to assess the presence of dimers, spherical aggregates or fibres in the solution state.

Publications generated as a result of the PhD studies presented herein

1. **High-throughput characterisation of supramolecular gelation processes using a combination of optical density, fluorescence and UV-Vis absorption measurements** L. J. White, C. Wark, L. Croucher, E. R. Draper and J. R. Hiscock, *Chem. Commun.*, 2020, **56** (66), 9557-9560.¹
2. **Controllable hydrogen bonded self-association for the formation of multifunctional antimicrobial materials** L. J. White, J. E. Boles, N. Allen, L. S. Alesbrook, J. M. Sutton, C. K. Hind, K. L. F. Hilton, L. R. Blackholly, R. J. Ellaby, G. T. Williams, D. P. Mulvihill and J. R. Hiscock, *J. Mater. Chem. B*, 2020, **8**, 4694–4700.²
3. **Towards the Prediction of Global Solution State Properties for Hydrogen Bonded, Self-Associating Amphiphiles** L. J. White, S. N. Tyuleva, B. Wilson, H. J. Shepherd, K. K. L. Ng, S. J. Holder, E. R. Clark and J. R. Hiscock, *Chem. - Eur. J.*, 2018, **24**, 7761–7773.³

Acknowledgements

In the first instance, I would like to express my utmost gratitude to my supervisor Dr Jennifer R. Hiscock for all of her help, support and endless guidance over the past three years, you truly have turned me from an 'I don't know what I am doing kind of woman' into a 'scientist',
thank you.

I would like to thank all the members of the Hiscock group past (Stella, Milan, Kendrick, Gina, Faith, Liam, Oni and Nova), and present (Lorenzo, George, Kira, Nyasha and Jack).

A special thank you goes to Jess and Rebecca, the other two legs of my tripod. You truly have made the last three years amazing, with your assistance and input but most of all your
friendship.

Last but not least I would like to thank my wonderful family who have been by my side, supporting me throughout this entire journey. My husband Paul who encouraged me to continue through the low times and celebrated the achievements through the high times, you were my rock and I could not have done it without you.

Table of Contents

Abstract.....	2
Publications generated as a result of the PhD studies presented herein.....	3
Acknowledgements.....	4
Declaration of authorship.....	7
Abbreviations.....	8
Chapter 1.....	10
1.1 The history of supramolecular chemistry.....	10
1.2 Non-covalent interactions.....	13
1.3 Non-covalent interactions in nature.....	17
1.4 Self-assembly.....	20
1.5 Anion directed self-assembled systems.....	21
1.6 Amphiphiles and supra-amphiphiles.....	23
1.6.1 Amphiphiles.....	23
1.6.2 Supra-amphiphiles.....	26
1.7 PhD aims and objectives.....	28
1.7.1 Aim of PhD thesis:.....	28
1.7.2 Objectives.....	28
Chapter 2.....	30
2.1 Introduction.....	30
2.2 Synthesis.....	40
2.3 Solid state: single-crystal X-ray diffraction.....	42
2.4 Gas phase: mass spectrometry.....	52
2.5 Solution state self-association studies.....	56
2.5.1 Dynamic light scattering.....	56
2.5.2 Surface tension and critical micelle concentration studies.....	61
2.5.3 ¹ H NMR self-association studies.....	69
2.6 Low level <i>in silico</i> modelling.....	85
2.7 Next-generation prediction models.....	90
2.8 Chapter 2: Summary.....	93
2.9 Chapter 2: Conclusion.....	97
2.10 Future work.....	97
Chapter 3.....	99
3.1 Introduction.....	99
3.2 Hydrogel determination.....	107
3.2.1 Inversion test and minimum gelation concentration (MGC) studies.....	107

3.3 Characterisation of supramolecular hydrogels.....	110
3.3.1 Minimum gelation concentration (MGC).....	110
3.3.2 Rheology	113
3.3.3 Microscopy studies	117
3.4 Antimicrobial efficacy determination	125
3.4.1 Solution state antimicrobial properties	125
3.4.2 Antimicrobial hydrogel properties.....	128
3.4.3 Co-formulated hydrogel properties	131
3.5 Chapter 3: Summary	137
3.6 Chapter 3: Conclusion	138
3.7 Future work.....	139
Chapter 4.....	140
4.1 Introduction	140
4.2 UV-Vis absorbance measurements.....	145
4.3 Optical density measurements	154
4.3.1 OD ₄₅₀ ratio	166
4.4 Fluorescence spectroscopy.....	171
4.5 Chapter 4: Summary	174
4.6 Chapter 4: Conclusion	174
4.7 Future work.....	174
Chapter 5.....	176
5.1 Final conclusion.....	176
Chapter 6.....	177
6.1 General information.....	177
6.1.1 General information: Chapter 2.....	177
6.1.2 General information: Chapter 3.....	179
6.1.3 General information: Chapter 4.....	181
6.2 Synthetic procedures	185
6.3 References	197

Declaration of authorship

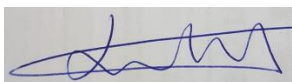
I, Lisa Jane White, declare that the thesis entitled

Supramolecular self-associating amphiphiles (SSAs) and the work presented in this thesis are both my own and have been generated by me as the result of my original research.

I confirm that:

- this work was done wholly or mainly while in candidature for a research degree at this university;
- where any part of this thesis has previously been submitted for a degree or any other qualification at this university or any other institution, this has been clearly stated;
- where I have consulted the published work of others, this is always clearly attributed;
- where I have quoted from the work of others, the source is always given. With the exception of such quotations, this thesis is entirely my own work;
- I have acknowledged all main sources of help;
- where the thesis is based on work done by myself jointly with others, I have made clear exactly what was done by others and what I have contributed myself;
- parts of this work have been published as:
 - **Towards the Prediction of Global Solution State Properties for Hydrogen Bonded, Self-Associating Amphiphiles** L. J. White, S. N. Tyuleva, B. Wilson, H. J. Shepherd, K. K. L. Ng, S. J. Holder, E. R. Clark and J. R. Hiscock, *Chem. - Eur. J.*, 2018, 24, 7761–7773.³ (Chapter 2)
 - **Controllable hydrogen bonded self-association for the formation of multifunctional antimicrobial materials** L. J. White, J. E. Boles, N. Allen, L. S. Alesbrook, J. M. Sutton, C. K. Hind, K. L. F. Hilton, L. R. Blackholly, R. J. Ellaby, G. T. Williams, D. P. Mulvihill and J. R. Hiscock, *J. Mater. Chem. B*, 2020, 8, 4694–4700.² (Chapter 3)
 - **High-throughput characterisation of supramolecular gelation processes using a combination of optical density, fluorescence and UV-Vis absorption measurements** L. J. White, C. Wark, L. Croucher, E. R. Draper and J. R. Hiscock, *Chem. Commun.*, 2020, 56 (66), 9557-9560.¹ (Chapter 4)

Signed:



Abbreviations

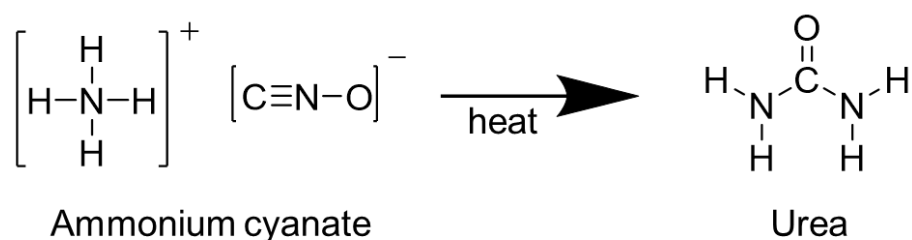
Å	Ångström
AMS	Aminomethane sulfonic acid
CDI	1,1'-Carbonyldiimidazole
CMC	Critical Micelle Concentration
d	Doublet (NMR)
DLS	Dynamic Light Scattering
DMSO	Dimethylsulfoxide
DNA	Deoxyribonucleic acid
FTIR	Fourier transform infrared spectroscopy
HBA	Hydrogen bond acceptor
HBD	Hydrogen bond donator
ESI-MS	Electron spray ionisation- Mass Spectrometry
J	Coupling constant (NMR)
K_a	Association constant
LMWG	Low molecular weight gelator
LMWM	Low molecular weight monomers
m	Multiplet (NMR)
mN/m	Millinewtons per meter
m/z	Mass to charge ratio (Mass Spectroscopy)
NaOH	Sodium hydroxide
NMR	Nuclear magnetic resonance spectroscopy
PK_a	Acid dissociation constant
ppm	Parts per Million
q	Quartet (NMR)
SSA	Supramolecular Self-associating Amphiphile
t	Triplet (NMR)

TBA	Tetrabutylammonium
TBAOH	Tetrabutylammonium hydroxide
TEA	Tetraethylammonium
TEAOH	Tetraethylammonium hydroxide
THA	Tetrahexylammonium
TMA	Tetramethylammonium
TPA	Tetrapropylammonium
TPAOH	Tetrapropylammonium hydroxide
TPeA	Tetrapentylammonium
TPeAOH	Tetrapentylammonium hydroxide
UV-Vis	Ultraviolet-visible spectroscopy
vdW	Van der Waals
XRD	X-ray diffraction
μL	Microlitre

Chapter 1

1.1 The history of supramolecular chemistry

Supramolecular chemistry has become a fast-growing interdisciplinary research area, heavily influenced by three of its pioneers, Charles Pedersen,⁴ Donald Cram,⁵ and Jean-Marie Lehn⁶ who were awarded the Nobel Prize in 1987 for their investigation and development of molecules which exhibit structure-specific interactions of high selectivity. Supramolecular chemistry – defined as chemistry ‘beyond the molecule’ by Jean-Marie Lehn, is the study of highly complex chemical systems that result from the association of two or more chemical components that interact and are organised by non-covalent intermolecular forces.⁷ Examples of these forces are hydrogen bonds, van der Waals forces (vdW), electrostatic interactions, and π -donor- π -acceptor interactions. These reversible forces facilitate the production of self-assembling systems,⁸ biological processes,⁹ as well as the construction of complex materials and molecular machinery.¹⁰ Supramolecular chemistry is still in its infancy when compared to molecular chemistry.¹¹ Areas of study relating to molecular chemistry have been the principal focus of chemistry investigation for over a hundred years, undergoing substantial development since initiation in 1828 by Friedrich Wöhler, who contributed to the foundation of modern chemistry through the successful synthesis of urea, displacing vital force theory (Scheme 1).¹²



Scheme 1 - Friedrich Wöhler's displacement of vital force theory with the synthesis of ammonium cyanate (inorganic compound) into urea crystals (organic compound).¹³

In 1913 American chemist Gilbert Newton Lewis first formulated the basic principle of valence theory, ‘the chemical bond consists of a pair of electrons held jointly by two atoms’ (Figure 1)^{14,15} - later coined the covalent bond by Irving Langmuir.¹⁶

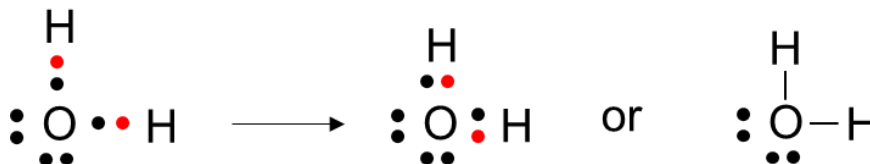


Figure 1 – Example of valence theory using a singular water molecule.¹⁶

It was in 1873 (almost five decades after Wöhlers discovery) that the then-unnamed field of supramolecular chemistry was borne, where whilst developing a theory to account for the properties of real gases, Johannes Diderik van der Waals first proposed the existence of ‘intermolecular forces’.¹⁷ Closely followed by the ‘lock and key’ principle hypothesised by German chemist Emil Fisher, concerning the presence of non-covalent interactions between enzymes and their substrates,¹⁸ now referred to as host-guest chemistry.¹⁹ His hypothesis subsequently led to a greater understanding of the essential design of pharmaceuticals.²⁰

The early twentieth century brought Worth Rodebush and Wendell Latimer into this field, who continued development on Tom Moore and Thomas Winmills research,²¹ increasing the understanding of the non-covalent bond, with emphasis on the study of the hydrogen bond.²² Charles Pederson went on to apply this type of non-covalent interaction towards synthetic systems, such as the development of crown ethers in 1960.²³ This same decade Jean-Marie Lehn⁷ and Donald Cram²⁴ continued to build upon Pederson's fundamental discovery with the development of novel macrocyclic molecules that exhibited more advanced selectivity when forming host:guest complexes, these are illustrated in Figure 2. Although, Lehn and Crams research focussed on alkali metal cation coordination, Jean-Marie Lehn, whilst giving his Nobel Prize lecture, highlighted the importance of the then unestablished area of anion coordination chemistry. This emphasised the relevance for its development from both biological and chemical perspectives.

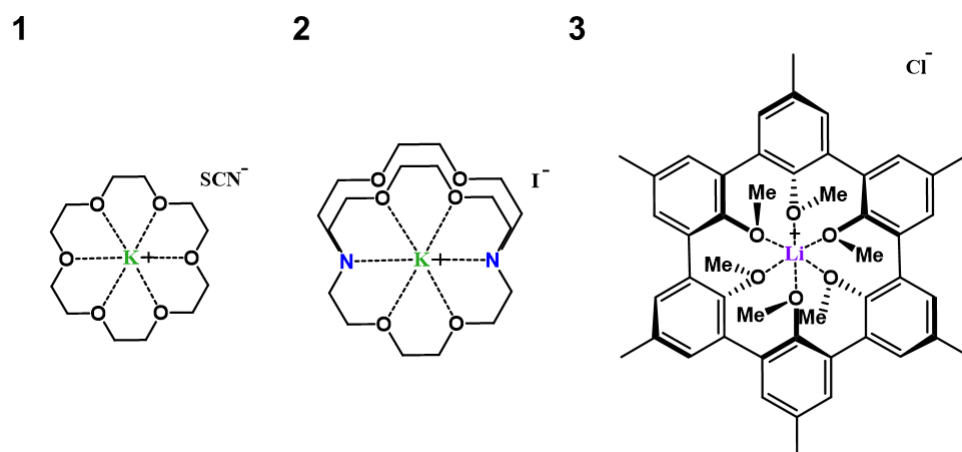


Figure 2 – Host:guest complexes produced by **1**) Charles Pederson (crown ether), **2**) Jean-Marie Lehn (cryptate) and **3**) Donald Cram (spherand)^{4,7,24}

The year 2016 was another astounding year for the evolution of supramolecular chemistry when a further Nobel Prize in chemistry was awarded. The three men jointly awarded this honour were Sir J. Fraser Stoddart, Jean-Pierre Sauvage and Bernard L. Feringa for their trail-blazing work in the design and synthesis of molecular-sized machinery, which has the potential to be used in the development of new materials, energy storage systems and as molecular sensors.²⁵ The synthesis of these molecular-sized machineries comprised of a catenane, first developed by Jean-Pierre Sauvage in 1983, which is a mechanically-interlocked chain consisting of two linked molecular rings (Figure 3a).²⁶ In 1991 Stoddart and co-workers advanced on this concept with the development of a rotaxane in which the molecular ring was able to move along an axle upon initiation from an external stimulus (Figure 3b).²⁷ In addition, Feringa and co-workers became the first group to develop a molecular motor resulting in the construction of the 'Nano-car' in 1999 (Figure 3c).²⁸

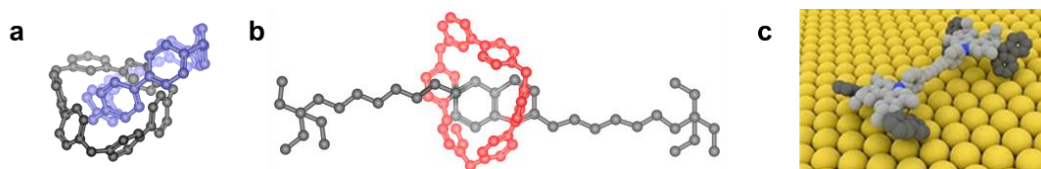


Figure 3 – Examples of molecular-sized machinery: a) [2]catenane; b) [2]rotaxane; c) Nano-car.²⁸ Image reproduced with permission from the University of Groningen.

Finally, more than two decades after this type of molecular investigation was initiated, Stoddart and Bruns developed mechanically mobile rings into systems which are reminiscent of biocompatible molecular muscles,²⁷ to amplify and harness molecular mechanical motions, as demonstrated in Figure 4.²⁹

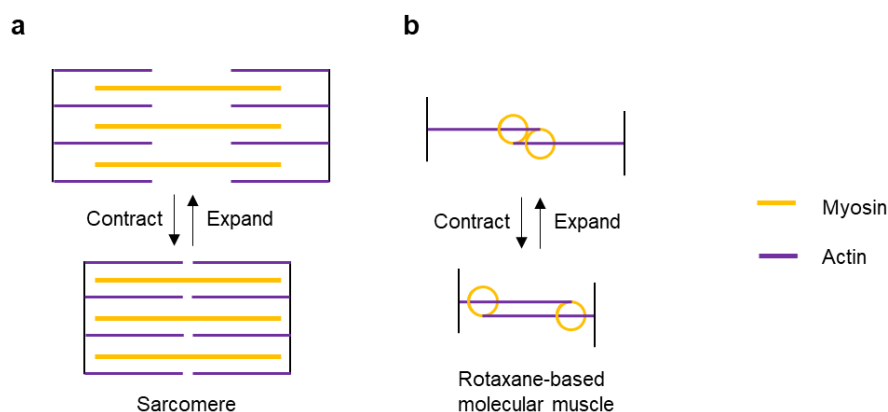


Figure 4 - Examples of contracting and expanding the molecular motions of a) human muscle (sarcomere) and b) mechanical rotaxane-based molecular muscle system.²⁹

1.2 Non-covalent interactions

Non-covalent interactions can occur between single molecules in a system and are formed as a result of the electron distribution between two or more molecules. Intermolecular interactions promote the process of self-association which results in extended structure formation such as dimers, trimers or polymers etc. Intramolecular interactions are interactions between different functional groups within a singular molecule. When compared to the covalent bond, which has bond strengths ranging from 150 to 1000 kJ mol⁻¹, these non-covalent interactions are generally a few orders of magnitude weaker this weakness however, does not imply that they are of less importance.³⁰ There are several different types of non-covalent interactions, which include: vdW forces; dipole-dipole interactions; ion-dipole interactions and ion-ion interactions. Electrostatic interactions such as vdW forces are induced in the presence of random fluctuations in electron cloud density.

Individually these are some of the weakest non-covalent interactions with bond energies $< 5 \text{ kJ mol}^{-1}$,³¹ however, the net effect of multiple interactions can lead to greater structural stability,³² dipole-dipole interactions are formed when there is a complementary alignment of one dipole with another. This type of interaction exhibits an energy range of 5 to 50 kJ mol^{-1} (Figure 5a);³² ion-dipole interactions have an energy range of 50 to 200 kJ mol^{-1} , where ions such as Na^+ bind with polar molecules like H_2O (Figure 5b);³³ The strongest of the electrostatic interactions are ion-ion interactions, these are similar in strength to that of the weakest covalent bond, with energies between 100 to 350 kJ mol^{-1} (Figure 5c).³⁴

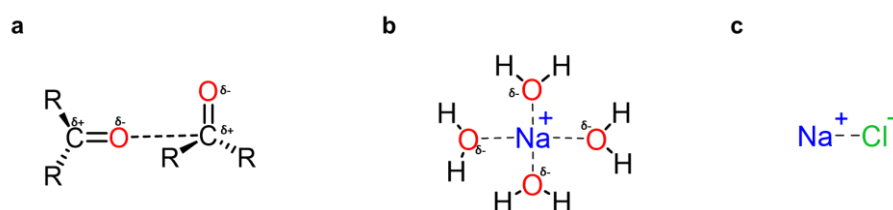


Figure 5 – Representation of three forms of electrostatic interactions: a) dipole-dipole; b) ion-dipole, and c) ion-ion.

Additional classes of non-covalent interactions are π -interactions which comprise of electron-rich aromatic units that interact with either an anion, a cation or another π -arrangement. Described as basic electrostatic interactions by Hunter and Sanders in 1990,³⁵ with energies of 5-40 kJ mol^{-1} , stacking π - π -interactions are generated due to the intermolecular overlapping of p-orbitals in π -conjugated systems. This allows for functional supramolecular assemblies to be achieved both in solution and in the solid state. The alignment of these aromatic rings is relative to the π electron density creating a quadrupole moment, with partial positive charges around the periphery, and partial negative charges above both aromatic faces.³⁶ These stack systems have the potential to exhibit three different confirmations as illustrated in Figure 6: face centred stacking (6a),³⁷ this confirmation is considered the least energetically favourable as two quadrupole moments in close vicinity will cause the stack to askew in favour of offset (6b)³⁸ or edge to face (T-shaped) (6c).³⁹

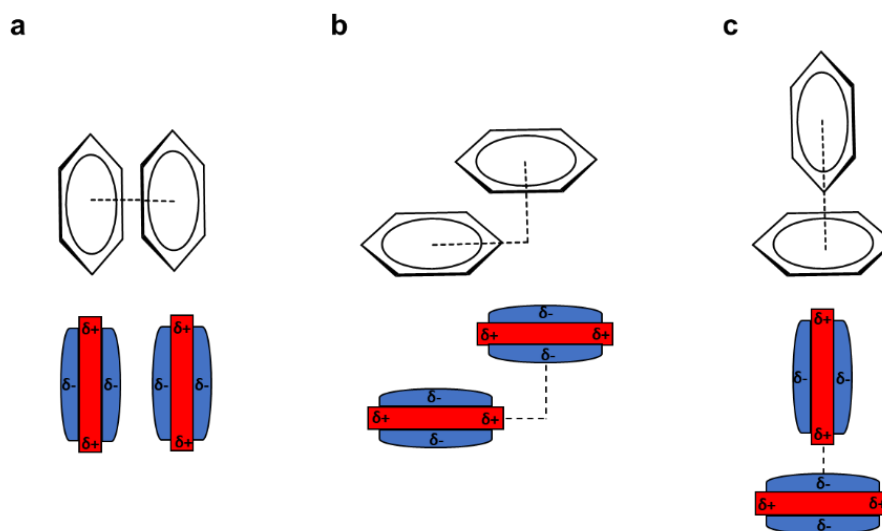


Figure 6 - Representation of π - π interactions: a) face centred stacking (unfavourable); b) offset (favourable), and c) edge to face (T-shaped) (favourable).

Hydrogen bonding interactions have bond lengths ranging from 1.2-4.0 Å (strong to weak)³² and a broad energy range of between 4-165 kJ mol⁻¹. Weak electrostatic interactions exhibit energy < 12 kJ mol⁻¹, mid-strength electrostatic interactions are 16-20 kJ mol⁻¹ and those > 60 kJ mol⁻¹ which are predominantly covalent in character,⁴⁰ an example of this is the bifluoride ion (HF₂⁻) which has self-associative intermolecular bond energy > 155 kJ mol⁻¹.⁴¹ In the early 1900s, those stronger bonds observed were originally believed to be limited to crystalline states, however, as research progressed into the latter half of this century it was discovered that they were also present in aprotic solution states.⁴² Due to their labile and dynamic features, the structural properties of these hydrogen bonds are influenced by a well-defined range of factors, which include: i) the electron-withdrawing/donating properties of any functional groups associated with the binding mode; ii) temperature;⁴³ iii) chemical environment;⁴⁴ iv) reactant concentrations;⁴⁵ v) pressure;⁴⁶ vi) bond angle.⁴⁷ Complexes which form predominantly as a result of intermolecular hydrogen bonds contain a complementary array of hydrogen bond donor and acceptor groups. The hydrogen bond donating unit is primarily a strongly electronegative element such as nitrogen, oxygen or fluorine with a hydrogen atom attached.

Due to an equivalent partial negative charge on the atom bound to the hydrogen, this atom can, therefore act as an HBA, accepting hydrogen bonds from a different molecule (intermolecular hydrogen bond) or even belonging to the same molecule (intramolecular hydrogen bond). Hydrogen bonds can be either primary and/or secondary interactions, where ‘primary’ refers to a direct interaction between hydrogen bond donor (D) and hydrogen bond acceptor (A) groups. There are six primary geometries that can be adopted in a hydrogen bonded complex,⁴⁷ these are summarised in Figure 7.

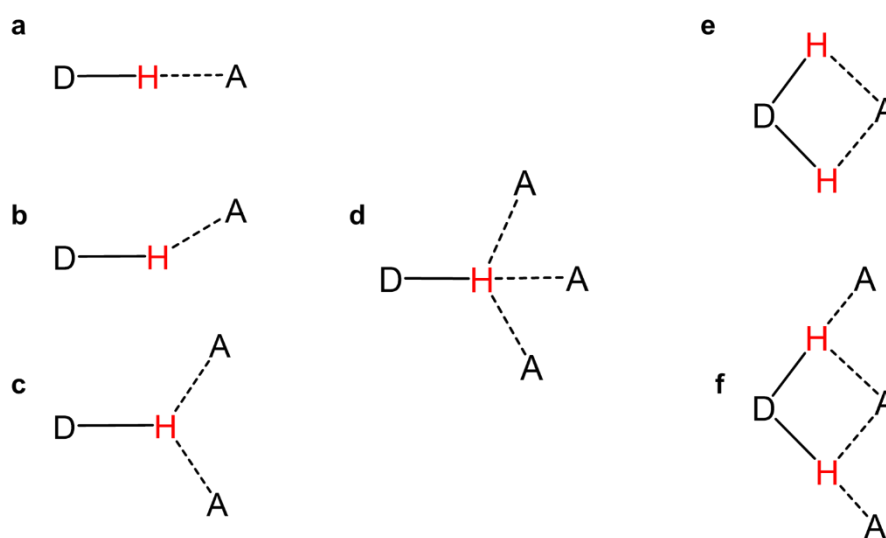


Figure 7 - Illustration of the six geometries adopted via primary interactions: a) linear; b) bent; c) donating bifurcated; d) trifurcated; e) accepting bifurcated; f) three-centred bifurcated.⁴⁷

In single donor systems, the hydrogen bond has a preference for linearity (Figure 7a)⁴⁸ with colinear bonds such as N-H---O exhibiting the strongest hydrogen bonding. Pimentel and McClellan suggest that in these systems a deviation of 20 ° from linearity leads to a decrease in the binding energy of approximately 10 %.⁴⁹ Whereas in double acceptor systems, non-linear bifurcated angles are of preference⁵⁰ (Figure 7c), this is due to being energetically more stable.⁵¹ However, the more molecular species involved in the self-assembly process the more variables there are to consider, for example, the preference for the more thermodynamically stable six-membered ring cyclisation.⁵²

When investigating hydrogen bond strength, consideration should also be taken for the partial charges between two neighbouring groups, these are classed as secondary interactions and either decrease the binding strength due to repulsions from partial charges of the same sign (Figure 8a) or increase by virtue of attraction between opposite charges, as shown in Figure 8b.⁴⁷

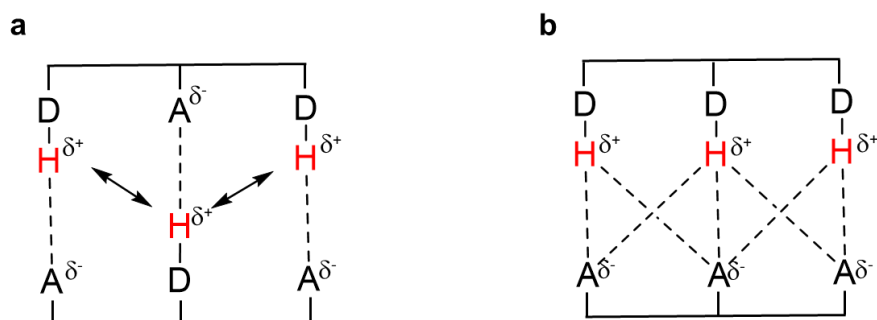


Figure 8 – Examples of secondary hydrogen bond interactions between two neighbouring groups a) repulsions (\longleftrightarrow) from mixed donor/acceptor arrangements and b) attractive interactions (-----) between DDD and AAA arrangements.⁴⁷

1.3 Non-covalent interactions in nature

Historically, supramolecular architectures found inspiration from nature where non-covalent interactions are critical for stabilising the three-dimensional structure of large molecules such as proteins⁵³ and nucleic acids.⁵⁴ Due to the nature of intermolecular hydrogen bonds, large complexes can dissolve in water at high concentrations.⁵⁵ It is because of this assisted solubility of large complexes and the strength of these hydrogen bonding interactions being much stronger than stacking interactions (< 165 compared to < 40 kJ mol^{-1}), that hydrogen bonds were hypothesised to be the key influence in determining bio-molecular structure stability.⁵⁶ However, Pavel Hobza when investigating this theory, concluded that both motifs are in fact comparable in aiding in the stabilisation of large molecular complexes.⁵⁷

The primary structures of proteins are constructed from general units of amino acids held together by peptide bonds. The property of each amino acid is determined by the presence of different R-groups which can be either hydrophobic or hydrophilic in character.⁵⁸

Whilst the hydrophobic effect provides the primary thermodynamic drive for the overall structure of proteins in water, the hydrogen bonds role is to provide the majority of the directional interactions, which underpin rigidity to the structure, specificity in molecular recognition and protein folding. Proteins contain many sites capable of forming a hydrogen bond such as the carbonyl and amide groups on the peptide backbone,⁵⁹ in addition to the polar functional groups (hydroxyls, acids, amides, and amines) on several of the amino acid side chains.⁶⁰ The central core of most proteins is comprised of secondary structures (Figure 9), formed from the self-assembly of the primary structures. Examples of these structures include: parallel/anti-parallel β -sheets (Figure 9ai/a ii); β -turns/coils (Figure 9bi/bii) and α -helices (Figure 9c) which are stabilised by hydrogen bonds between the peptide backbone carbonyl oxygen and the amide nitrogen contained in the hydrophobic core.⁶¹

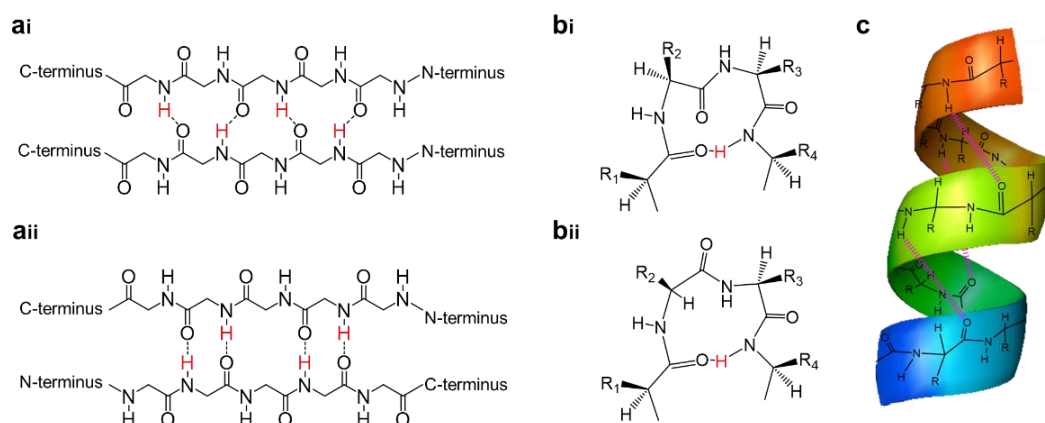


Figure 9 – Hydrogen bonds in protein secondary structures: ai) parallel β -sheet; a ii) anti-parallel β -sheet; bi) β -turn (type 1); bii) β -turn (type 2); c) α -helix.

The tertiary structure of a protein is the general three-dimensional organisation of its polypeptide chain in space, stabilised by the internal hydrophobic interactions between the non-polar amino acid side chains and external hydrogen bond and ionic bond interactions.⁶² Finally, the protein quaternary structure is assembled via either multiple folded protein subunits or co-factors, this structure is predominantly driven by the hydrophobic effect, and further stabilised by a range of non-covalent and covalent interactions.⁶³

Another prominent biological molecule that is reliant on non-covalent interactions for stability is deoxyribonucleic acid (DNA). The structure of DNA was first discovered in 1953 by Francis Crick, James Watson and Rosalind Franklin.⁶⁴ DNA relies on stabilisation through multiple non-covalent interaction events occurring simultaneously. These range from stacking interactions such as vdW forces between the nitrogenous bases, hydrophobic effects of the nucleobases and hydrophilic effect of the negatively charged phosphate backbone. As commonly known the solvent environment can modify the relative importance of the different non-covalent interactions involved in the assembly process. As a cellular environment is aqueous and polar, the hydrophobic nitrogenous bases located in the interior of the DNA helix are sequestered away from the surrounding aqueous environment, whilst the exposed hydrophilic phosphate heads interact with the water. Essentially, it is this property that increases the solubility of DNA in polar aqueous conditions. Additionally, ionic interactions of the external negatively charged phosphates with positively charged ions such as Mg^{2+} and cationic proteins aid in structural stability. Hydrogen bonding is fundamental in the formation of the three-dimensional helix structure, observed between complementary base pair nucleotides (adenine/thymine and guanine/cytosine) universally known as Watson-Crick base pairing (Figure 10).⁶⁵

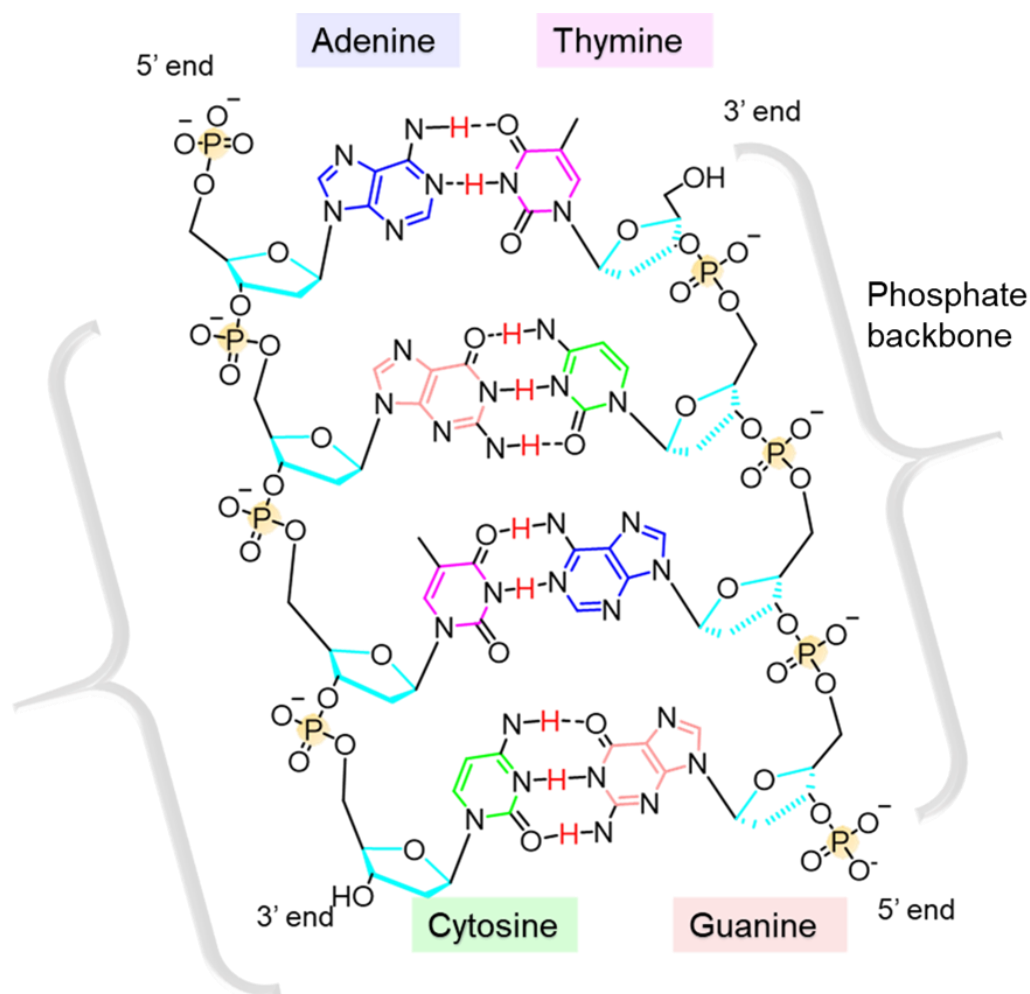


Figure 10 – Cartoon illustrating the DNA double helix and base pairing of cytosine and guanine assembled through three hydrogen bonds and thymine and adenine assembled through two hydrogen bonds.⁶⁵

1.4 Self-assembly

Self-assembly is scientifically interesting as well as technologically important, having facilitated the generation of complex matter.⁶⁶ Self-assembly involves the process in which components of a system, either separate or linked, spontaneously assemble to form well-defined, functional lower or higher-ordered structures by design.⁶⁷ These can be done through the pre-organisation of a covalent framework or by the method of self-organisation of intermolecular interactions as shown in Figure 11.⁶⁸ Ordered structures can only be generated through self-assembly if one of two events can occur: i) the association process is reversible, or ii) the components can adjust their positions within the aggregate once it has formed.⁶⁹

As non-covalent interactions are naturally weaker than covalent bonds, the self-assembly process is characteristically controlled by thermodynamics and formed under equilibria controlled conditions.⁴⁵ These self-assembled aggregates primarily occur at smooth interfaces or in solution as these environments allow for mobility of the different components involved within self-association processes.

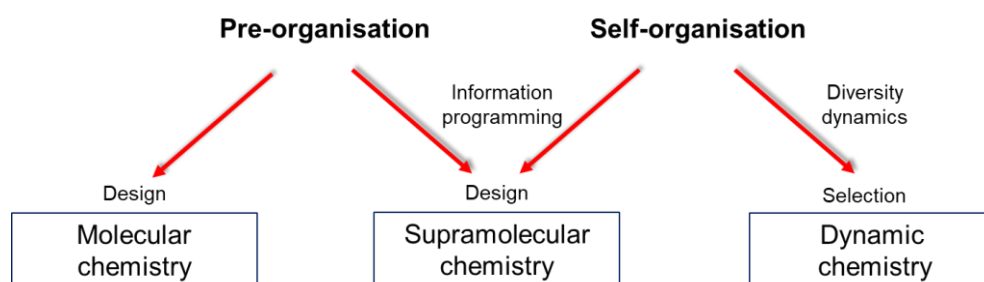


Figure 11 – Principles for molecular, supramolecular and dynamic chemistry self-assembly.⁶⁸

Powerful synthetic strategies involving multiple hydrogen bonding interactions have been continually utilised to enhance complex stability through increased strength and/or directionality. These strategies, which are integral to the formation of a desired self-assembled complex can be designed by increasing association selectivity. This is achieved by increasing the number of sites which are capable of hydrogen bonding, and/or by incorporating a linker which will aid in the control of the type of self-assembled motif observed.

1.5 Anion directed self-assembled systems

The origins of the field of anion supramolecular chemistry can be traced back to 1968 when Park and Simmons recognised the ability for synthetic ammonium cage assemblies to complex halide anions.⁷⁰ However, in the years following this discovery, relatively few anion recognition systems emerged. Anion recognition sites were traditionally positioned within covalent macro(poly)cyclic structures, taking advantage of molecular pre-organisation, to achieve selective and strong anion bound complexes.^{71,72}

Nowadays, anion supramolecular chemistry is a dynamic field of research which has stretched far beyond the preparation of receptors, with anions now functioning as templates to assist primary bonding for the synthesis of complex architectures. Examples of these primary bonds include but are not limited to, coordinate bonds in metal complexes and covalent bonds in macrocyclisation.⁷³ As supramolecular chemistry has evolved, so has the discovery of supermolecules formed through the self-assembly of anionic interactions, Figure 12. This superstructure was formed from [5]pseudorotaxanes which provided concentric spheres of cationic and neutral ligands for the total encapsulation of the anion PF_6^- .^{74,75}

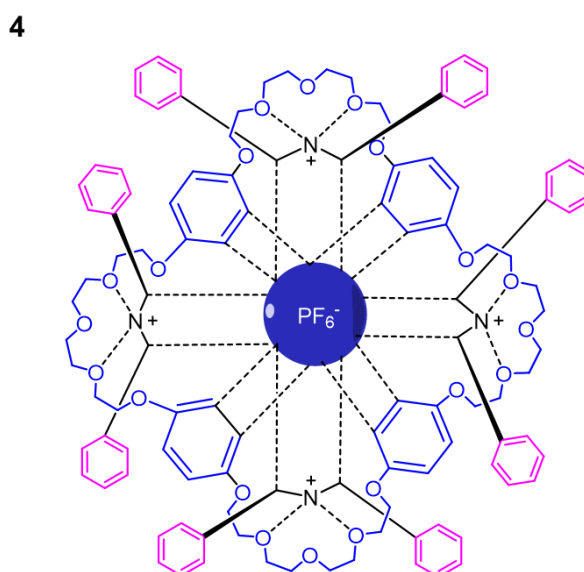
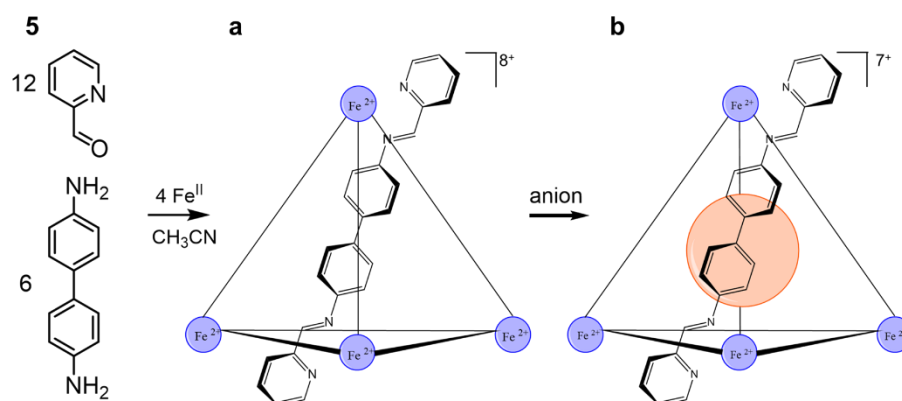


Figure 12 – Cartoon representation of a superstructure formed from [5]pseudorotaxanes.⁷²

The selective binding of anionic species is relevant to a variety of scientific areas which include: biology; pharmaceuticals; catalysis, and has significant environmental importance. As previously mentioned anions are commonly utilised as templating agents in macrocycle synthesis,⁷⁶ this is as well as supramolecular architectures such as molecular knots, polygons, gels, polymers and cages. An example of self-assembled cages incorporating anions was explored by Clegg and co-workers (Scheme 2) who looked at adapting systems with the addition of anionic guest molecules. These systems expressed a novel combination of diastereomers that synergistically bound the guest molecule.⁷⁷

For this process to occur, the cage diastereomers underwent two major structural changes, first, they were interconverted, then the internal volume of the individual cages physically adapted through bond rotation. This process provided a tailor-made binding space which encapsulated the anionic species.⁷⁷



Scheme 2 – Synthesis of the self-assembled tetrahedral $[Fe_4L_6]^{8+}$ cage complex (a) and with the addition of an anionic guest (b).⁷⁷ Ligands (2-6) omitted for clarity.

1.6 Amphiphiles and supra-amphiphiles

1.6.1 Amphiphiles

An amphiphile is a universal term that describes any compound that comprises of two distinctly covalently bound components which exhibit differing affinities for the solvent within the same system. It is this combination that makes this class of molecule ambivalent. For phospholipid type amphiphiles, one component will have a head group which displays a high affinity for polar solvents such as water (hydrophilic). A second component is a tail group, generally composed of a hydrocarbon chain, although fluorinated groups⁷⁸ and aromatic rings are sufficiently hydrophobic to act as a barrier against water-soluble substances.^{79,80} These amphiphiles display a high affinity for non-polar solvents such as ethers, esters or hydrocarbons (hydrophobic).

There are four different classes of an amphiphilic molecule: i) zwitterion (carrying opposing charges on the same molecule bridged through alkyl chains or other spacers, Figure 13, **6**); ii) cationic (carry a positive charge, Figure 13, **7**); iii) anionic (carry a negative charge, Figure 13, **8**), and iv) non-ionic (with no net charge, Figure 13, **9**).

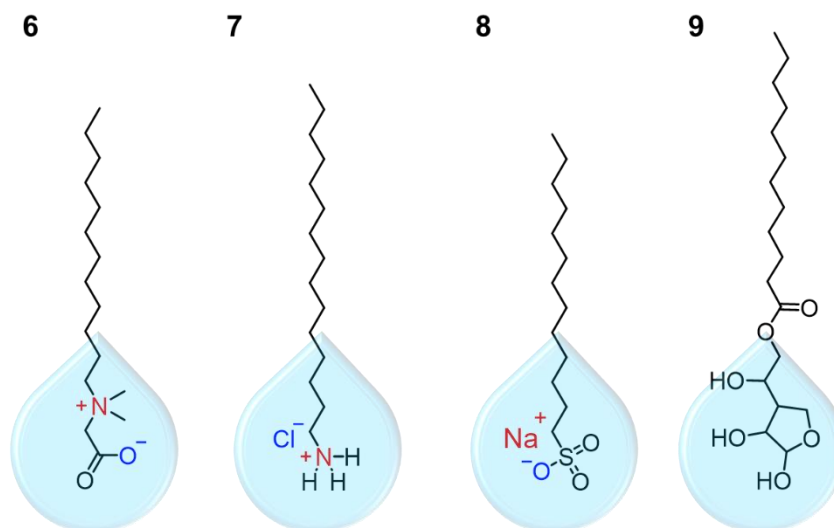


Figure 13 - Examples of amphiphilic molecules: **6**) zwitterionic ((carboxylatomethyl)dodecyldimethylammonium); **7**) cationic (pentadecan-1-aminium); **8**) anionic (sodium lauryl sulfate, SLS); **9**) non-ionic (sorbitan laurate).

Surfactants and some lipid molecules are common, everyday examples of amphiphiles.

Surfactants are substances that adhere to a surface interface inducing a noticeable decrease in interfacial tension by adsorption. An anionic surfactant usually contains polar head groups of either: carboxylate, sulfonate or phosphate, coordinated with a positively charged counter cation such as sodium, potassium or ammonium. An example of an anionic surfactant is sodium lauryl sulfate (SLS) (Figure 13, **8**). This surfactant is water-soluble at room temperature and commonly used pharmaceutically in medicated shampoos as well as a preoperative skin cleaner, as this compound exhibits antimicrobial activity against Gram-positive bacteria.⁸¹ Cationic surfactants frequently contain a nitrogen-based hydrophilic head which also plays a vital role pharmaceutically due to their bactericidal activity against a wide range of both Gram-negative and Gram-positive organisms.⁸² Relatively non-toxic, nonionic surfactants have multiple functions some of which include wetting agents, emulsifiers, and solubilisers.⁸³

Additionally, these non-ionic surfactants are strong P-glycoprotein inhibitors, a property useful for enhancing drug absorption and specific tissue targeting.⁸⁴ Zwitterionic amphiphiles exhibit electrical neutral properties which endow extremely high polarity.⁸⁵ Due to the zwitterionic amphiphiles non-toxicity, they are frequently studied and widely used in cosmetic products and personal care.⁸⁶

At comparatively low concentrations, surfactants occur predominantly as monomers at the interface and in the bulk aqueous solution, the distribution of which are in equilibrium. As the concentration is increased these monomers start to interact and self-assemble. Amphiphilic molecules can associate into a variety of assemblies in bulk aqueous conditions. When the solution environment (temperature,⁸⁷ pressure⁸⁸ or pH⁸⁹) is altered these assemblies are able to transform from one type of aggregated structure to another as shown in Figure 14. However, the type of assembly present can be restricted by the forces which act to keep the polar/non-polar components in favourable environments.⁹⁰

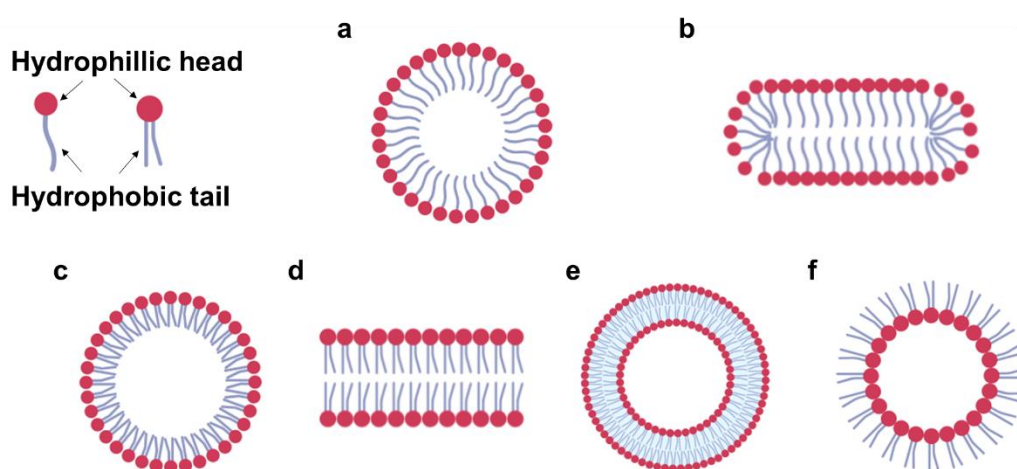


Figure 14 – Cartoon representation of possible amphiphilic morphologies of monolayer and bilayer systems formed in solution: a) spherical micelle (single hydrocarbon chain); b) cylindrical c) spherical micelle (multiple hydrocarbon chain); d) bilayer; e) vesicle (liposome); f) inverse micelle.⁹⁰

As mentioned previously, the solvent environment plays an integral role in the self-assembly of amphiphilic molecules which can then result in the formation of macromolecular structures. In aqueous conditions micelles or lipid bilayers are commonly formed.

Examples of these structures can be observed in Figure 14 where the hydrophilic head group preferentially interacts with an aqueous solution and the hydrophobic tail orientates towards the hydrophobic central core. Micelles are widely used in biological and industrial applications due to their ability to dissolve and transport non-polar materials through an aqueous medium.⁹¹

Where amphiphiles such as phospholipids exhibit multiple hydrocarbon chains, they preferentially form either a bilayer such as that found in a cell membrane⁹² (< 5 nm in size), or significantly larger vesicles (Figure 14d and 14e respectively).⁹³ The preference for these structures to form is due to the hydrophobic chains being too large to fit in the internal cavity of the micelle, as micelles are typically much smaller structures.⁹⁴ In a solvent environment where the exposure of the hydrophilic head group is energetically unfavourable, inverse micelles are formed instead, where the hydrophobic head is exposed and the hydrophilic tail is sequestered internally (Figure 14f).⁹⁵

1.6.2 Supra-amphiphiles

Inspired by nature and termed supra-amphiphiles, as they are formed from a combination of supramolecules and amphiphiles. In contrast with conventional amphiphiles, supra-amphiphiles refer to amphiphiles fabricated on the basis of various non-covalent interactions and/or dynamic covalent bonds connecting the hydrophobic and hydrophilic components.^{96,97} The reversible non-covalent driving force interactions that aid complex formation includes: hydrogen bonds,⁹⁸ electrostatic interactions;⁹⁹ charge-transfer interactions;¹⁰⁰ imine bonds;¹⁰¹ boronic ester bonds¹⁰² and host-guest recognition.¹⁰³ Modification of these interactions changes the amphiphilicity which award supra-amphiphiles with unique properties such as stimuli responsiveness and controllability of the self-assembly and disassembly processes.¹⁰⁴ Examples of these supra-amphiphiles incorporating non-covalent interactions can be observed in Figure 15. This Figure illustrates Zhang and co-workers spherical aggregates (**10**), these were constructed using wedge-shaped amphiphiles assembled through π - π stacking interactions.¹⁰⁵

Kabanov and co-workers developed structures resembling micelles which were fabricated through electrostatic interactions of conventional single-chain head-to-tail supra-amphiphiles (Figure 15, **11**).¹⁰⁶ Shown in Figure 15, **12** are complimentary interacting groups, melamine and isocyanuric acid investigated by Wang and co-workers. This double and single chain supra-amphiphile is fashioned through extended hydrogen bond arrays.⁹⁶

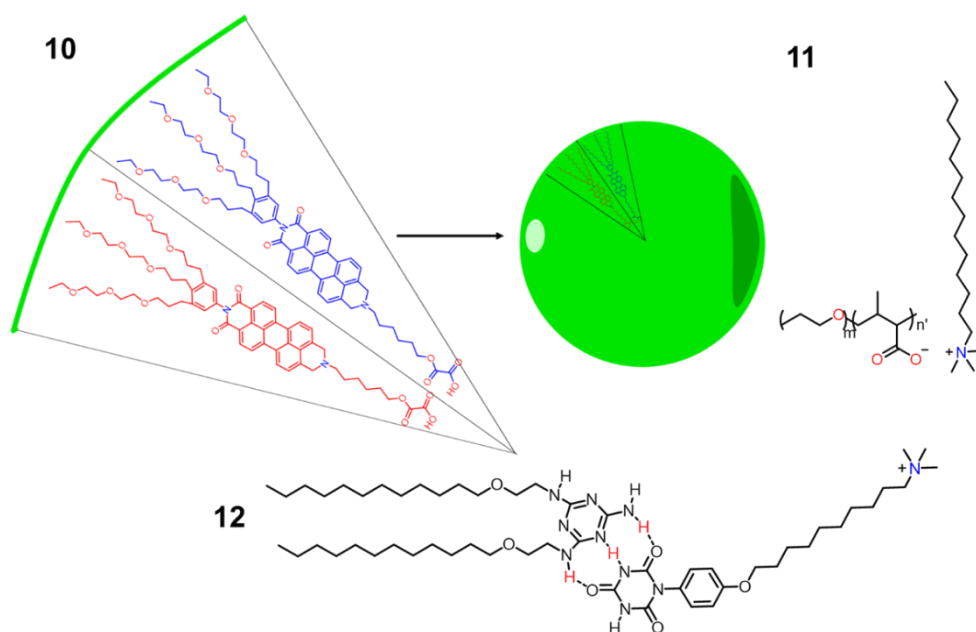


Figure 15 - Examples of supra-amphiphiles assembled through non-covalent interactions: 10) π - π stacking;¹⁰⁵ 11) electrostatic,¹⁰⁶ and 12) hydrogen bonding.⁹⁶

Additionally, supra-amphiphiles can also be formed through dynamic covalent bonds such as imine and disulphide, which, under certain conditions can reversibly form and break,¹⁰⁷ similar to non-covalent interactions.⁹⁷ The physicochemical properties and the applications of a supra-amphiphile are dictated by the topology. Aside from the conventional single-chain head-to-tail supra-amphiphile, there are other forms: i) multi-chain head-to-tail, of which there are several types, here multiple tails are present on just the hydrophilic, just hydrophobic or both components;⁸⁰ ii) bola-forms, these contain two hydrophilic water-soluble groups positioned at both ends of a hydrophobic skeleton,⁹⁶ commonly utilised in solubilisation and drug or gene delivery vehicles;⁸⁸ and finally iii) polymeric supra-amphiphiles, which are fabricated from either non-covalent or dynamically covalent bound polymeric segments of two or more,¹⁰⁸ frequently used in cancer therapies and the formation of surfactants and nanocarriers.¹⁰⁹

1.7 PhD aims and objectives

1.7.1 Aim of PhD thesis:

To be able to understand and tailor, the self-association and antimicrobial properties of a novel class of supramolecular self-associating amphiphile (SSA).

1.7.2 Objectives

- To synthesise a library of compounds which will enable elucidation of molecular structure and physicochemical property relationships, across the solid state, solution state and gas phase. (Chapter 2)
- To control the self-association of the aggregate structure of an SSA through modification of the solvent environment, from dimer to spherical aggregate to hydrogel. (Chapter 3)
- To enable high-throughput characterisation of those molecules that form multiple different materials. (Chapter 4)

Chapter 2

2.1 Introduction

As previously discussed in Chapter 1, supramolecular self-assembly relies on the formation of non-covalent interactions. The formation of those bonds associated with this self-assembly process, in addition to the hydrophilic/hydrophobic solvent interaction is known to drive molecular self-association and aid structure stabilisation of any resultant aggregate.¹⁰³ This, in turn, dictates the aggregate properties in either the solution or solid state.¹¹⁰ In recent years the design of non-covalent self-associated materials, particularly those that incorporate the use of hydrogen bonds, have become a focus of interest due to their capacity for application in many fields. Specific examples of these applications include the construction of novel molecular semi-conductors formed through multiple hydrogen bonds by Yagai and co-workers.¹¹¹ Additionally, Ikkala and co-workers used non-covalent complex formation to drive the self-assembly of cobalt nanostructures for capsid production.¹¹² Finally, Zhou and co-workers have developed nanotubes as novel gene/drug delivery systems which were constructed by the self-assembly of amphiphilic macrocycles via non-covalent interactions. Here the nanopores formed by the insertion of these nanotubes into the hydrophobic core of lipid bilayers were shown to mediate highly selective transmembrane ion transport, in addition to aiding efficient transmembrane water permeability. Compounds **13-15** (Figure 16) show the designs of the macrocycles which assembled to form hydrogen-bonded nanotubes. The methyl groups present in the cavity of **15** were shown to hinder proton influx when compared to those of **13** and **14** where an enhanced rate of proton influx was mediated.¹¹³

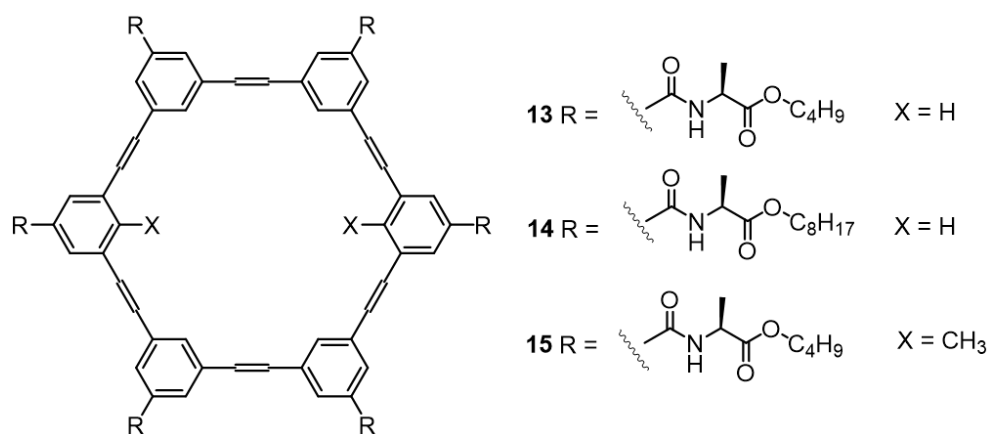


Figure 16 – Macrocycles which assemble into hydrogen-bonded nanotubes.¹¹³

The field of low molecular weight (< 500 g/mol) anion receptor chemistry has expanded greatly over the last few decades,^{114,115} with (thio)urea moieties being extensively explored in the development for anion binding frameworks.¹¹⁶ This is a practical choice due to the ease of their synthesis as well as their binding selectivity through two-directional hydrogen bonds with other anionic molecules, as shown in Figure 17.¹¹⁷

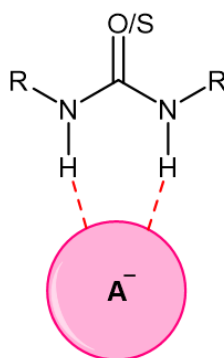


Figure 17 – Example of (thio)urea selectively binding through two hydrogen bonds.

In 1990, the simple diphenyl urea was one of the first urea receptors reported in literature. This planar molecule contains an aromatic substituent directly bound to each side of the urea moiety (Figure 18). It was initially anticipated that the size of the aromatic groups would induce steric hindrance, consequently affecting the hydrogen bonding process, when compared to those molecules with aliphatic chains present in the molecular structure.

16

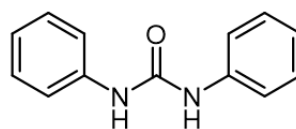


Figure 18 – One of the first urea receptors reported in literature.¹¹⁸

However, Etter and co-workers showed this hypothesis to be untrue, and with the addition of electron-withdrawing nitro substituents situated in different positions on the aromatic ring systems (ortho/meta/para), found that this increased the acidity of the urea moiety and as a consequence, the hydrogen bond donating properties (Figure 19, **17-19**).¹¹⁸

17 - ortho
18 - meta
19 - para

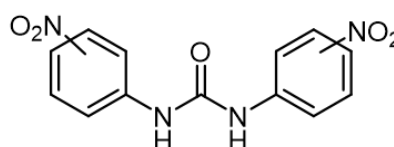


Figure 19 – Dinitro phenyl structures synthesised to investigate the effect increased acidity has on the binding properties of simple urea receptors.¹¹⁸

Inspired by Etters findings, Wilcox and co-workers investigated the binding affinities (when fitted to a 1:1 binding isotherm) of various oxoanions with (thio)urea derivatives in chloroform. It was found that although the mono-(*m*-nitroaryl)thiourea receptor was a better host, it was realised that **18** was more susceptible to nucleophilic and electrophilic attack, therefore more likely to partake in undesirable side reactions.¹¹⁹ Consequently, they focussed their initial investigations on the host. Wilcox and co-workers reported that the mono-(*m*-nitroaryl)urea receptor exhibited strong hydrogen binding with the counter anion of TBA salts of sulfonate (6.1×10^3), carboxylate (2.7×10^4) and phosphate (9.0×10^3) (Figure 20, **20**).¹¹⁹ Upon comparison of the calculated binding constants, the bis(*m*-nitrophenyl)urea (Figure 19, **18**) exhibited higher values than the mono-(*m*-nitroaryl)urea (Figure 20, **20**). However, the option for functionalisation of the mono-(*m*-nitroaryl)urea receptor makes this molecule much more attractive¹²⁰ and reinforces their importance in applications such as membrane transport,¹²¹ sensing¹²² and material science.¹²³ As a result, the roles that (thio)urea functionalities play in anion binding events have continued to be extensively researched and compared.^{124,125}

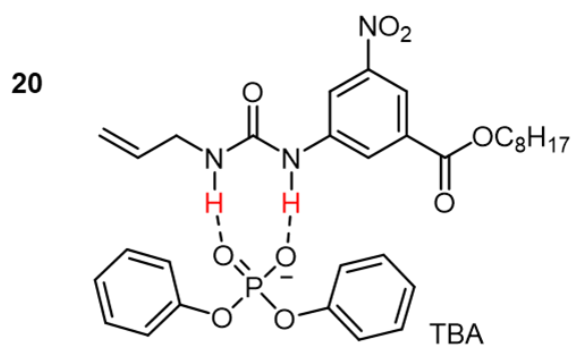


Figure 20 – Mono-(*m*-nitroaryl)urea receptor hydrogen bonding to a diphenyl phosphate TBA salt.¹¹⁹

In the early 21st century these supramolecular principles were successfully applied by Supuran and co-workers for the design of novel antimycobacterials, some of which exhibited effective activity against standard strains of *M. tuberculosis* (H37Rv).¹²⁶ These substituted urea derivatives as illustrated in Figure 21, **21-30** produced a growth inhibition of ≥ 78 % at a concentration of 6.25 μ M. Compounds **24** and **25** both exhibited growth inhibition values of 89 % against *M. tuberculosis* (H37Rv), these values are comparable with isoniazid (85 %) and rifampin (93 %), two current clinically relevant treatments for mycobacterium tuberculosis. Presently, no new drugs to treat TB have been developed for many years, this breakthrough could be considered interesting for the potential development of new antimycobacterial drugs.¹²⁶

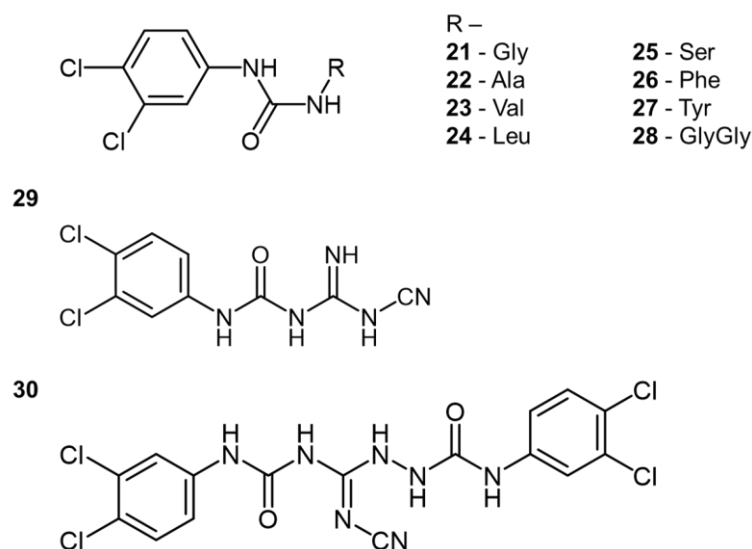


Figure 21 – Urea antimycobacterial derivatives.¹²⁶

More recently (thio)urea moieties were incorporated into structures designed and synthesised by Gale and co-workers to encourage selective hydrogen bonded coordination of neutral species over anionic phosphate centred species.¹²⁷ Additionally, Steed and co-workers utilised a urea motif (**31**) which demonstrated that covalent bonds can be substituted for hydrogen bonds, for the fabrication of novel supramolecular gels as shown in Figure 22.¹²⁸

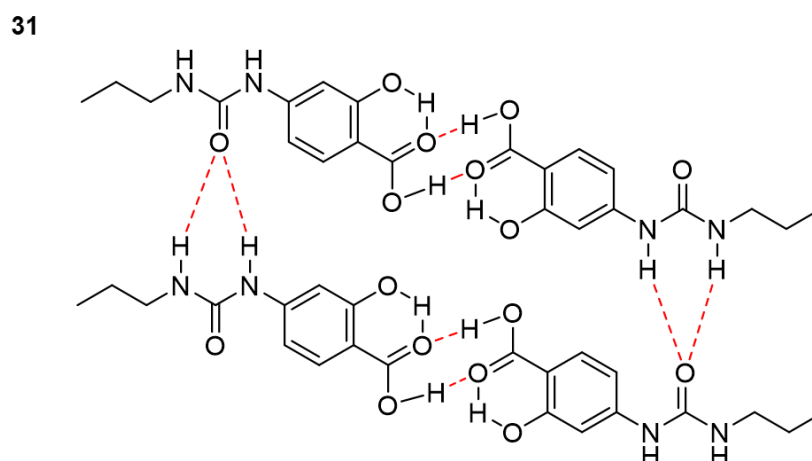


Figure 22 – Hypothesised parallel packing arrangement of urea derivatives, used in the formulation of supramolecular gels.¹²⁸

The surfactant properties of a series of hydrogen bond donating anions containing a urea-spacer-carboxylate/sulfonate motif have been investigated by Faustino and co-workers as illustrated in Figure 23. The results from their studies established a correlation between critical micelle concentration (CMC) and amino acid residues of **32-36**, where the CMC decreased with decreasing number of carbons on the side chain of the amino acid. Furthermore, the substitution of the carboxylate group (**33**) for sulfonate (**37**), sulfate (**38**), or phosphate (**39**) groups, showed a CMC decrease, in the order of $\text{CO}_2^- > \text{OPO}_3^{2-} > \text{SO}_3^- > \text{OSO}_3^-$. This is hypothesised to be due to the higher polarisability values of those surfactants with sulfur or phosphorous atoms in their polar head groups. Compounds with increased (**40**) or branching (**41**) alkyl chains gave the lowest calculated values of $\text{CMC} \leq 3.04 \times 10^{-2} \text{ mol dm}^{-3}$. Faustino and co-workers attributed this to the steric hindrance caused by the closely connected hydrocarbon chains preventing micellisation.¹²⁹

The calculated CMC values for **32-41** were shown to be similar to that of the well-documented surfactants sodium decanoate ($1.09 \times 10^{-1} \text{ mol dm}^{-3}$) and trimethyldecylammonium bromide ($6.7 \times 10^{-2} \text{ mol dm}^{-3}$).¹²⁹⁻¹³³

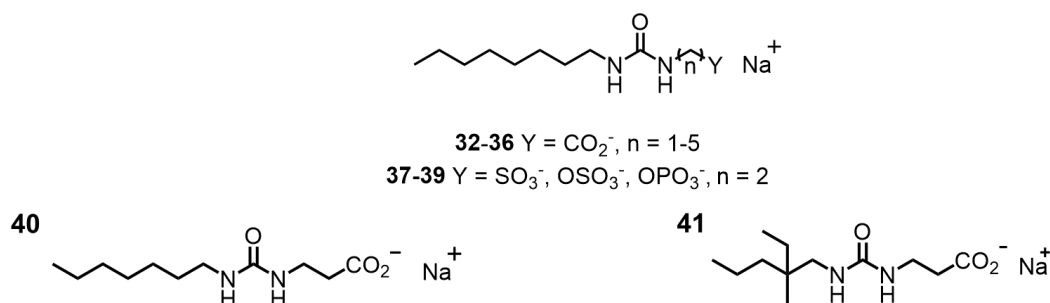


Figure 23 – Examples of urea-spacer-carboxylate/sulfonate/phosphate motifs synthesised by Faustino et al. to enable exploration into their surfactant properties.

Drawing inspiration from Faustino's work, Hiscock and co-workers developed a series of “*Supramolecular Self-associating Amphiphiles*” (SSAs) which incorporated the (thio)urea-spacer-sulfonate motif. This general structure designed by Hiscock and co-workers, shown in Figure 24 comprises of an anionic hydrogen bond accepting (HBA) group; a (thio)urea hydrogen bond accepting/donating moiety (HBA/HBD) and a hydrophobic region. The acidity of the amine groups was altered through stepwise modification of the R-groups within the hydrophobic region.^{134,135}

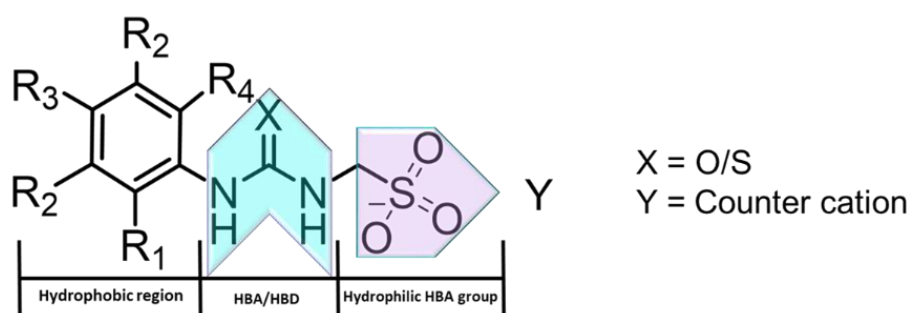
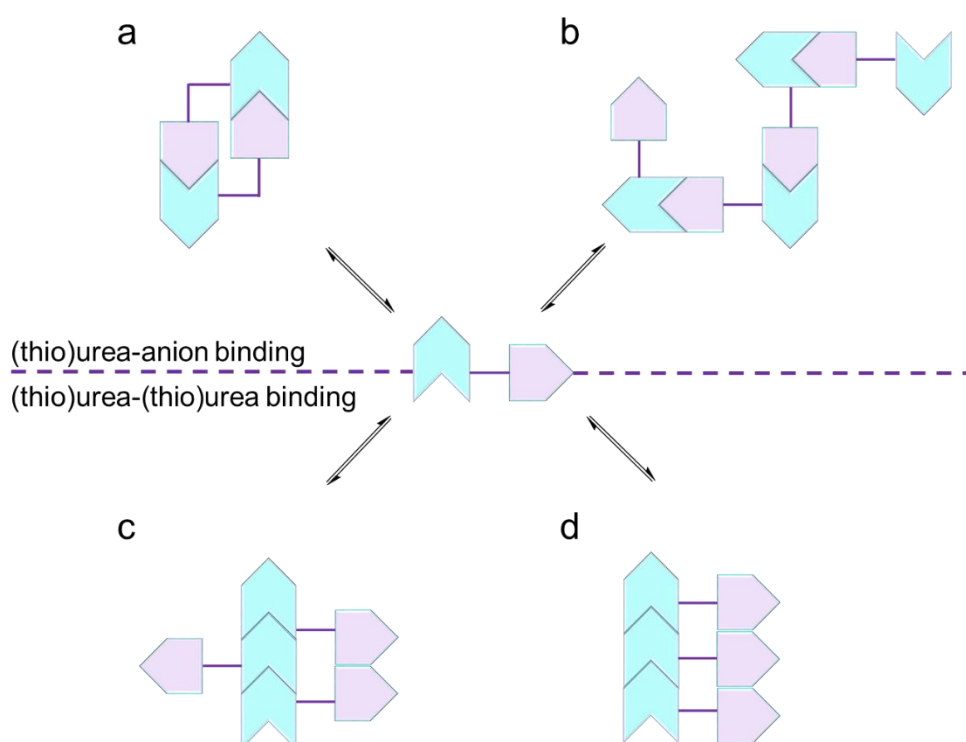


Figure 24 – General structure of the sulfonate-(thio)urea amphiphilic salts synthesised by Hiscock *et al.*^{134,135}

The SSAs illustrated in Figure 24 contain two possible HBA sites (the (thio)urea and sulfonate functionalities), and only one HBD site (the NHs in the (thio)urea functionality), the competitive nature of these two substituents gives rise to a ‘*frustrated*’ system.

As a result, these SSAs discussed can adopt at least four different self-associated hydrogen bonding modes as shown in Scheme 3: (thio)urea-anion dimer (3a); (thio)urea-anion stacking (3b); *anti*-(thio)urea-(thio)urea stacking (3c) and *syn*-(thio)urea)-(thio)urea-stacking (3d). These binding modes could be manipulated through alteration of the physical state, chemical composition, solvent environment and/or through modification of the cationic units. Through modulation of the HBD acidity with the substitution of the R and X groups, the length and angle of the hydrogen bonds formed within the complex were found to differ, which in turn altered the angle of dimerisation. Furthermore, increased acidity of the HBD groups resulted in the more optimal formation of the urea-anion hydrogen bond. It was also shown that the presence of a weakly sulfonate coordinating counter cation such as TBA resulted primarily in the formation of urea-anion dimers. However when TBA was replaced with strong sulfonate coordinating cations such as sodium or potassium, the formation of the urea-anion binding mode was prevented, giving rise to the urea-urea binding mode instead.¹³⁵



Scheme 3 - Possible self-associated hydrogen bonded modes for this class of amphiphilic salt: a) dimer; b) tape; c) (thio)urea-(thio)urea *anti*-stacking; d) (thio)urea-(thio)urea *syn*-stacking.^{134,135}

More recently Hiscock and co-workers focused on the synthesis and self-associated properties of a series of intrinsically fluorescent SSAs. Here they discovered that the solvent environment played an integral role in the size of aggregate formed, with smaller predominantly dimeric species (< 10 nm) observed in 100 % DMSO. However, when Hiscock and co-workers increased the percentage of water, a greater percentage of larger aggregates > 100 nm in diameter were observed to be present. These larger structures were studied through a combination of dynamic light scattering (DLS), ¹H NMR, tensiometry to derive the CMC and directly visualised through a combination of transmission and fluorescence microscopy. In addition to dimeric species (< 10 nm) being present in the solution state (100 % DMSO) they were also shown to exist in the gas phase and the solid state. These were identified through high-resolution electrospray ionisation mass spectrometry (ESI-MS) and single-crystal X-ray diffraction techniques (XRD) respectively.

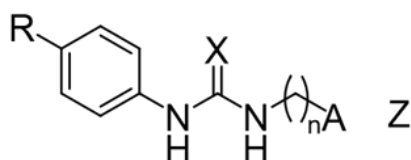
Computationally derived electrostatic potential maps were employed to calculate comparative surface energy maximum (E_{\max}) and minimum (E_{\min}) values using low-level semi-empirical PM6 modelling methods. These predicted values were found to correlate well with both the dimerisation constants derived from the ¹H NMR studies and the CMC values. Hiscock and co-workers concluded that it may be possible to predict the surfactant properties of this class of SSA (Figure 24) by measuring the dimerisation constant and/or simple computational techniques.¹³⁶

Gaining an understanding of the supramolecular interactions involved within the self-assembly process at the molecular level will allow for the informed construction of monomeric units. This will ultimately enable the fabrication of pre-designed supramolecular functional materials, exhibiting global properties of choice. By having predictable control of these self-associated interactions at a fundamental level, will not only influence scientific fields associated with nanostructure formation,¹³⁷ specifically two-component self-associated systems.¹³⁸ This will also enable stepwise-changes in the fields of supramolecular materials such as low molecular weight gelators.¹³⁹

This chapter builds on these initial findings and explores the molecular self-associated properties of 30 structurally related compounds (Figure 25, **42-58** and **60-72**), by a combination of complementary techniques in the gas phase, solid state and solution state. Compound **59** could not be stabilised so has been excluded from this study. The techniques employed to investigate the structure-activity relationship properties include single-crystal XRD; ESI-MS; DLS; ^1H NMR; and Diffusion Ordered Spectroscopy (DOSY) ^1H NMR. The global properties of these SSAs will be further explored using tensiometry to derive the CMC and low-level computational studies to derive electrostatic potential maps which will enable calculation of E_{max} and E_{min} values. Compounds **73-80** (Figure 25) were synthesised to allow exploration of ion-pair effects within our systems'. It is hypothesised that this study will not only verify Hiscock and co-workers previous hypothesis, but it will also allow for improved predictive models and more defined associated limitations to be developed.

The work detailed in this chapter has been published within the following peer-reviewed journal article:

3. Towards the Prediction of Global Solution State Properties for Hydrogen Bonded, Self-Associating Amphiphiles L. J. White, S. N. Tyuleva, B. Wilson, H. J. Shepherd, K. K. L. Ng, S. J. Holder, E. R. Clark and J. R. Hiscock, *Chem. - Eur. J.*, 2018, **24**, 7761–7773.³



- | | |
|---|---|
| 42 - R = CF ₃ ; X = O; n = 1; A = SO ₃ ⁻ ; Z = TBA | 55 - R = NH ₂ ; X = O; n = 1; A = SO ₃ ⁻ ; Z = TBA |
| 43 - R = CF ₃ ; X = O; n = 2; A = SO ₃ ⁻ ; Z = TBA | 56 - R = OMe; X = O; n = 1; A = SO ₃ ⁻ ; Z = TBA |
| 44 - R = CF ₃ ; X = O; n = 3; A = SO ₃ ⁻ ; Z = TBA | 57 - R = H; X = O; n = 1; A = SO ₃ ⁻ ; Z = TBA |
| 45 - R = CF ₃ ; X = S; n = 1; A = SO ₃ ⁻ ; Z = TBA | 58 - R = NO ₂ ; X = O; n = 1; A = SO ₃ ⁻ ; Z = TBA |
| 46 - R = CF ₃ ; X = S; n = 2; A = SO ₃ ⁻ ; Z = TBA | 59 - R = NH ₂ ; X = S; n = 1; A = SO ₃ ⁻ ; Z = TBA |
| 47 - R = CF ₃ ; X = S; n = 3; A = SO ₃ ⁻ ; Z = TBA | 60 - R = OMe; X = S; n = 1; A = SO ₃ ⁻ ; Z = TBA |
| 48 - R = CF ₃ ; X = O; n = 1; A = SO ₃ ⁻ ; Z = Na ⁺ | 61 - R = H; X = S; n = 1; A = SO ₃ ⁻ ; Z = TBA |
| 49 - R = CF ₃ ; X = O; n = 1; A = SO ₃ ⁻ ; Z = PyrH ⁺ | 62 - R = NO ₂ ; X = S; n = 1; A = SO ₃ ⁻ ; Z = TBA |
| 50 - R = CF ₃ ; X = O; n = 1; A = SO ₃ ⁻ ; Z = TMA | 63 - R = CF ₃ ; X = O; n = 1; A = COO ^t Bu; Z = n/a |
| 51 - R = CF ₃ ; X = O; n = 1; A = SO ₃ ⁻ ; Z = TEA | 64 - R = CF ₃ ; X = O; n = 1; A = COOH; Z = n/a |
| 52 - R = CF ₃ ; X = O; n = 1; A = SO ₃ ⁻ ; Z = TPA | 65 - R = CF ₃ ; X = O; n = 1; A = COO ^t Bu; Z = TBA |
| 53 - R = CF ₃ ; X = O; n = 1; A = SO ₃ ⁻ ; Z = TPeA | 66 - R = CF ₃ ; X = S; n = 1; A = COO ^t Bu; Z = n/a |
| 54 - R = CF ₃ ; X = O; n = 1; A = SO ₃ ⁻ ; Z = THA | 67 - R = CF ₃ ; X = S; n = 1; A = COOH; Z = n/a |
| | 68 - R = CF ₃ ; X = S; n = 1; A = COO ⁻ ; Z = TBA |

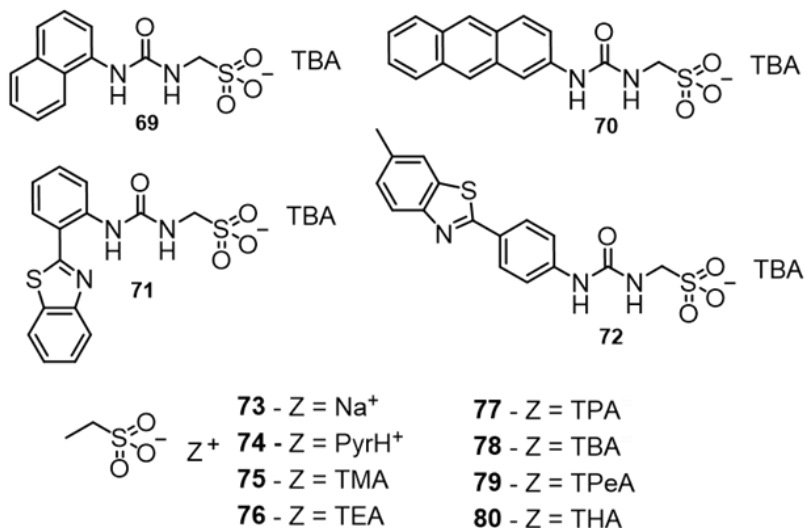
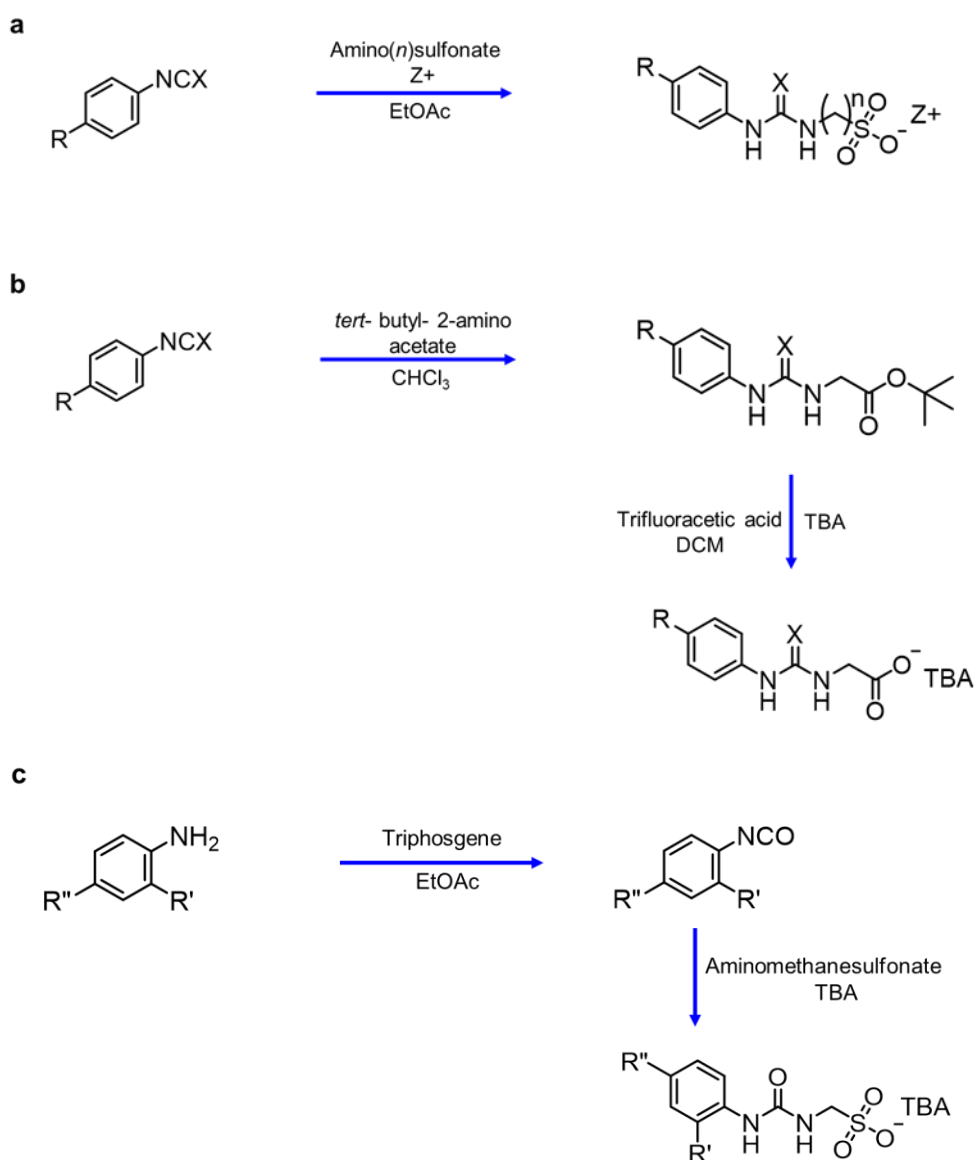


Figure 25 – Chemical structures of the 39 compounds discussed in this chapter.

Scheme 4 – Synthesis of compounds discussed in this thesis. Compounds: a) **42-62**; b) **63-68**; c) **69-72**.

2.2 Synthesis

The compounds (**42-72**) discussed within this chapter were designed through stepwise modification of **42**. Compounds **42-47**, **56-58** and **60-62** were synthesised by the reaction of the appropriate amino sulfonic acid with either isocyanate or isothiocyanate and TBAOH in methanol. After further purification, the pure products were obtained as either white solids in yields of 52 %, 60 %, 56 %, 63 %, 60 % and 76 % (**42-47**), as cream solids in yields 78 % and 81 % (**56-57**), as a yellow solid in a yield of 78 % (**58**) as white solids in yields 50 % and 61 % (**60-61**) or as a yellow solid in a yield of 89 % (**62**) respectively.

Compound **48** was synthesised by the reaction of AMS with the appropriate isocyanate in pyridine and isolated as a white solid in a yield of 89 %. Compounds **49-54** were synthesised by the reaction of AMS with the appropriate isocyanate in pyridine, followed by the addition of either NaOH in water or one equivalent of the appropriate quaternary ammonium hydroxide and isolated as white solids in yields of 94 %, 97 %, 97 %, 97 %, 98 %, and 98 % respectively. The reduction of **57** using hydrazine hydrate and palladium on carbon resulted in the formation of crude **55**. After further purification **55** was obtained as a brown solid in a yield of 96 %. The reduction of **62** using tin shavings and concentrated hydrochloric acid resulted in the formation of crude **59**. This compound (**59**) could not be further purified (Scheme 4a).

Compounds **63** and **66** were synthesised by the reaction of *tert*-butyl 2-amino acetate with either isocyanate or isothiocyanate to give the products as white solids in yields of 45 % and 75 % respectively. Compounds **64** and **67** were formed through the deprotection of **63** and **66** using concentrated trifluoroacetic acid, after further purification the products (**64** and **67**) were obtained as white and brown solids in yields of 65 % and 83 % respectively. The addition of TBAOH to **64** and **67** resulted in the formation of compounds **65** and **68**, in yields of 100 % (Scheme 4b).

Compound **69** was obtained through the reaction of TBA AMS with 1-naphthyl isocyanate in pyridine. The pure product was obtained as a pale brown solid with a yield of 31 %. Compounds **70** and **72** were synthesised by reaction of 2-aminoanthracene or 4-(6-methylbenzothiazole)aniline as appropriate, with triphosgene in ethyl acetate to give the corresponding isocyanate. This was followed by the addition of TBA AMS. After further purification, **70** and **72** were obtained as yellow solids in yields of 43 % and 65 % respectively. Compound **71** was synthesised through the activation of 2-(2-aminophenyl)benzothiazole with 1,1'-carbonyldiimidazole in chloroform followed by the addition of TBA AMS. The pure product was obtained as a pale-yellow solid with a yield of 42 % (Scheme 4c).

2.3 Solid state: single-crystal X-ray diffraction

Single-crystal XRD is a routinely used non-destructive analytical technique in the field of supramolecular chemistry for the identification of crystalline materials. Using this technique, the self-associated binding modes of **42-58** and **60-72** were first explored within the solid state. Crystal structures have been previously obtained for **42, 45, 48, 49, 56-58, 69, 71** and **72**.^{135,136} With (thio)urea-anion **42, 45, 56, 58, 69, 71** and **72** shown to dimerise through (thio)urea-anion hydrogen bond formation. Contrastingly, the structures of **49** and **57** exhibit hydrogen bonded self-association through the formation of urea-anion tapes over the optimal urea-anion dimer. This was hypothesised to be due to the replacement of the TBA as demonstrated in **42** with a more competitive HBD pyridinium cation as shown in **49**.¹³⁵ Finally, the structure obtained for **48** which contains a Na⁺ within its molecular structure, exhibited self-association through the formation of urea-urea hydrogen bonded tapes. This was hypothesised to be due to anion pair effects.^{135,136}

The crystallography data discussed in this chapter was obtained and refined by Dr Jennifer Ruth Hiscock. Novel single-crystal X-ray structures of **43, 44, 46, 47, 50, 55** and **62, 63** and **65** were obtained from a two-week crystallisation process through slow evaporation of EtOH:H₂O solutions containing the relevant compound. The crystal structures obtained for **43, 44, 47, 55** and **62** were all shown to form self-associated (thio)urea-sulfonate dimers through four intermolecular hydrogen bonds. The structure for **43** not only exhibits an intermolecular hydrogen bonded dimer forming through the urea-sulfonate portion of the amphiphilic salt, but there is also an intramolecular hydrogen bond between the alkyl N-H and the sulfonate group observed. This six-membered energetically favourable formation is made possible due to the extended length of the alkyl chain with the addition of a CH₂ ($n=2$). Evidence of the bond formation for **43** is illustrated in Figure 26. The interior bond angle of **43**, calculated from the intersecting planes of the urea substituents was calculated to be 180.0 °, a graphical example of how this value is determined is shown in Figure 27.

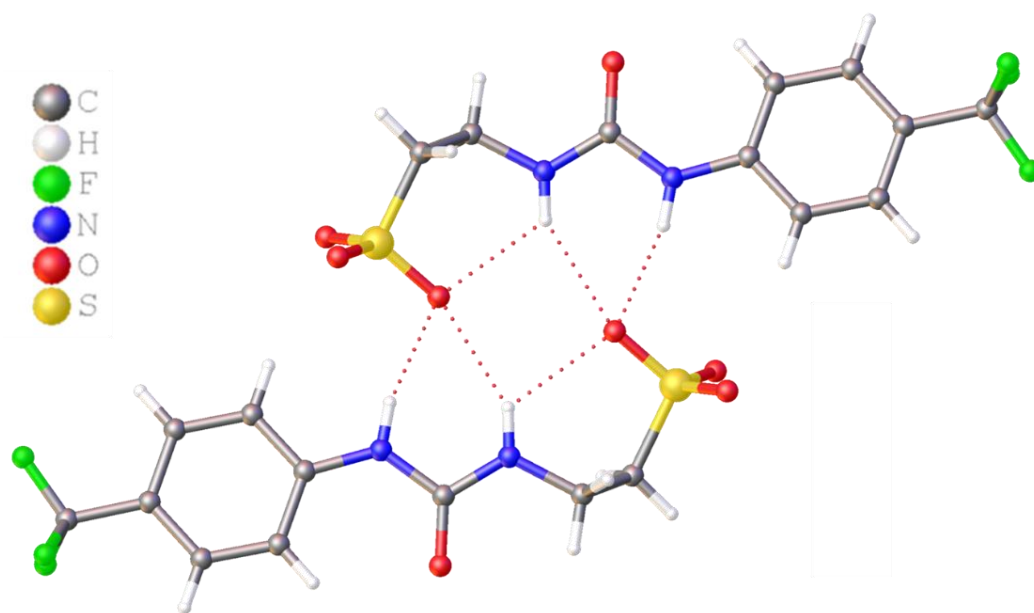


Figure 26 – Single-crystal X-ray structure of **43**, illustrating intramolecular bonding and intermolecular dimerisation through urea-anion complexation. TBA counter cation has been omitted for clarity.

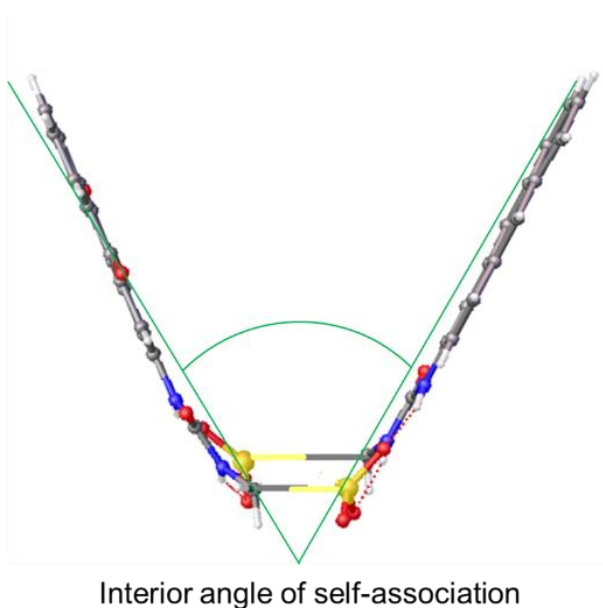


Figure 27 - Ball and stick representation of the interior angle of self-associated dimerisation calculated from the intersecting planes of the (thio)urea substituents.

With SSA urea-anion **44**, further extension of the alkyl chain length from $n=2$ to $n=3$, shows the intramolecular hydrogen bond ring system was found to be no longer favourable. However, stabilisation through two different binding modes was observed. Figure 28a demonstrates the N-H HBD groups shown to bind with one HBA sulfonate oxygen, whereas in Figure 28b a single N-H HBD group binding with two HBA sulfonate oxygens is observed.

The interior dimerisation angles of these complexes were calculated to be 170.9 ° and 175.7 ° respectively.

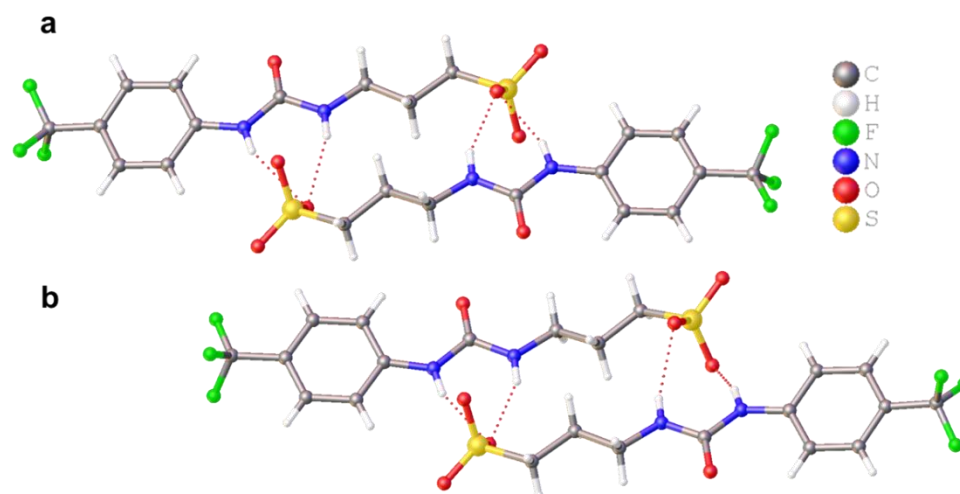


Figure 28 - Single-crystal X-ray structure of **44**, illustrating intermolecular dimerisation through urea-anion complexation a) N-H HBD with one HBA sulfonate oxygen and b) N-H HBD with two HBA sulfonate oxygens. TBA counter cation has been omitted for clarity.

Compound **47** (CF₃ substituted thiourea-sulfonate) again self-associates through intermolecular interactions of the urea N-H to the sulfonate anionic moiety, unlike CF₃ substituted urea-sulfonate **44**, with this compound the HBD N-H groups are self-associating through four hydrogen bonds with different HBA sulfonate oxygens as illustrated in Figure 29. Exchanging the urea functionality (**44**) for thiourea group (**47**) resulted in a comparatively twisted binding mode with an interior dimerisation angle of 180.0 °, slightly larger than those calculated for **44** (170.9 ° and 175.7 °).

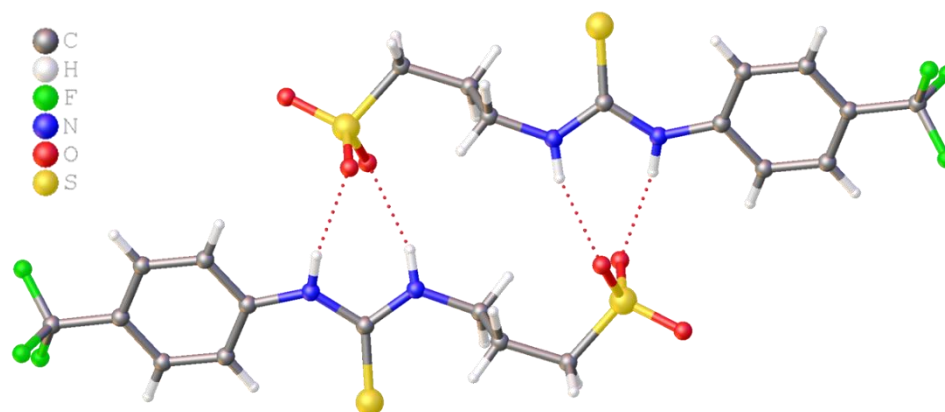


Figure 29 – Single-crystal X-ray structure of **47**, illustrating intermolecular dimerisation through thiourea-anion complexation. TBA counter cation has been omitted for clarity.

Modification to the R-group on the aromatic substituent from a CF_3 to an additional HBA/HBD primary amino group within **55**, results in a structure, which not only exhibits the common (thio)urea-anion dimer but also a hydrogen bonded amino-sulfonate tetramer with an interior dimerisation angle of 180.0° (Figure 30).

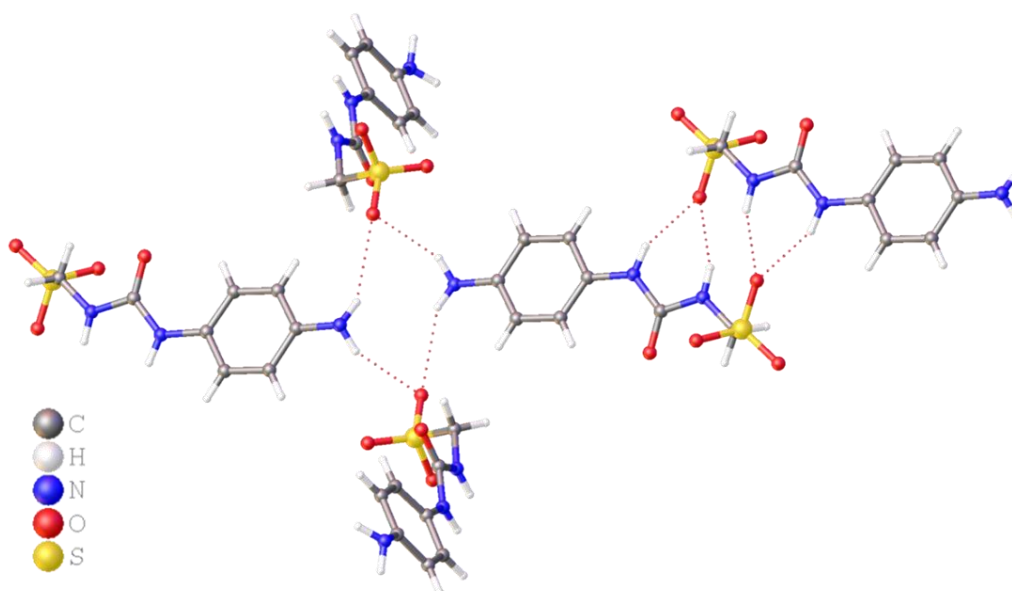


Figure 30 - Single-crystal X-ray structure of **55**, illustrating intermolecular dimerisation through urea-anion complexation and tetramer formation through amine-anion complexation. TBA counter cation has been omitted for clarity.

The self-associated complex formation events discussed so far (Figures 26 and 28-30) have shown that the structures of **43**, **44**, **47** and **55** are planar in nature, with an interior angle of dimerisation $\approx 180.0^\circ$. When the compound is modified with the addition of a nitro group in the *para*-position as shown for compound **62** (Figure 31) a decrease in the interior angle of dimerisation is observed. This dimer instead exhibits an interior angle of dimerisation of 24.6° , comparable to the value obtained for **58**, the analogous urea, which exhibited an interior angle of dimerisation of 19.9° .

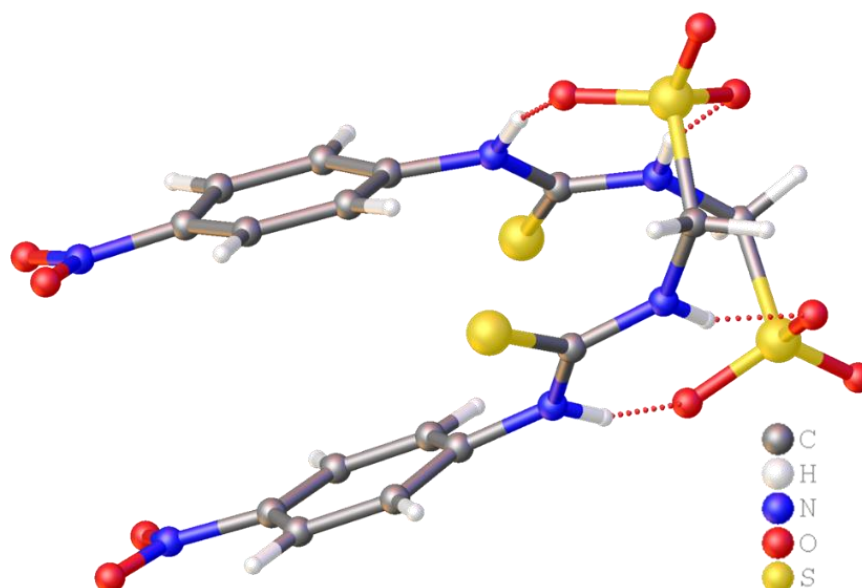


Figure 31 - Single-crystal X-ray structure of **62**, illustrating intermolecular dimerisation through thiourea-anion complexation. TBA counter cation has been omitted for clarity.

Compounds **46**, **50** and **65** all show (thio)urea-sulfonate tapes stabilised through two intermolecular sulfonate-(thio)urea bonds. This is particularly interesting with regards to CF_3 substituted thiourea-sulfonate **46** (Figure 32), as previously discussed the analogous urea (**43**), forms a self-associated urea-sulfonate dimer. This difference in hydrogen bonding mode was attributed to either the instability of the dimer due to the formation of an intramolecular hydrogen bond or crystal packing forces.

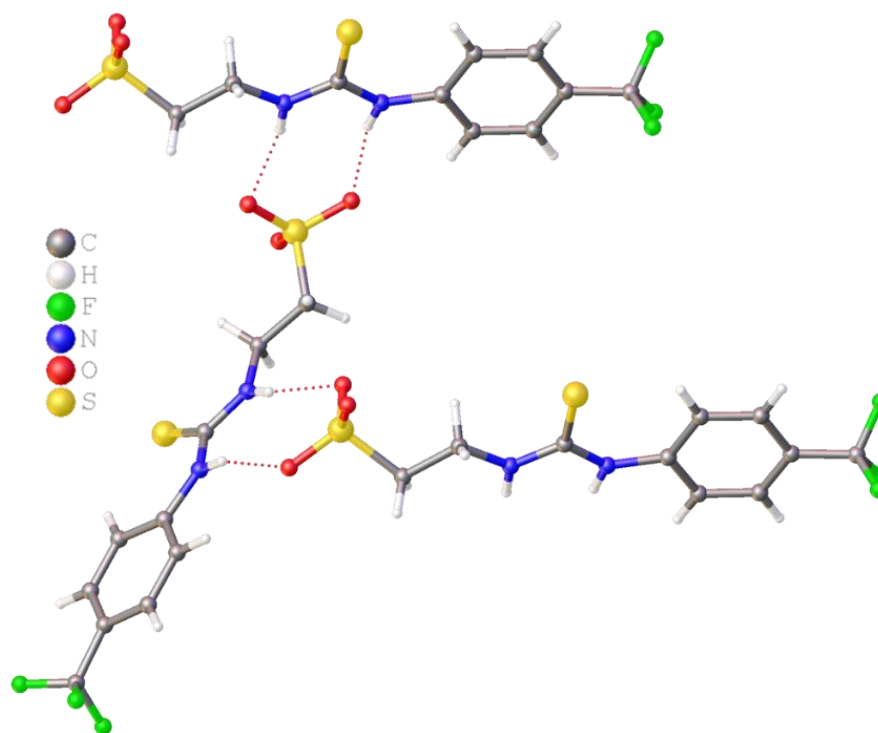


Figure 32 - Single-crystal X-ray structure of **46**, illustrating intermolecular polymerisation through thiourea-anion complexation. TBA counter cation has been omitted for clarity.

Replacing the TBA counter cation of **42** with TMA produces compound **50**. Previously published **42** was shown to exhibit hydrogen bonded dimerisation through a urea-anion binding mode.¹³⁵ However, compound **50** forms a urea-sulfonate tape as illustrated in Figure 33. This switch of binding modes is attributed to the electrostatic interactions between the anionic functionality and the TMA counter cation.

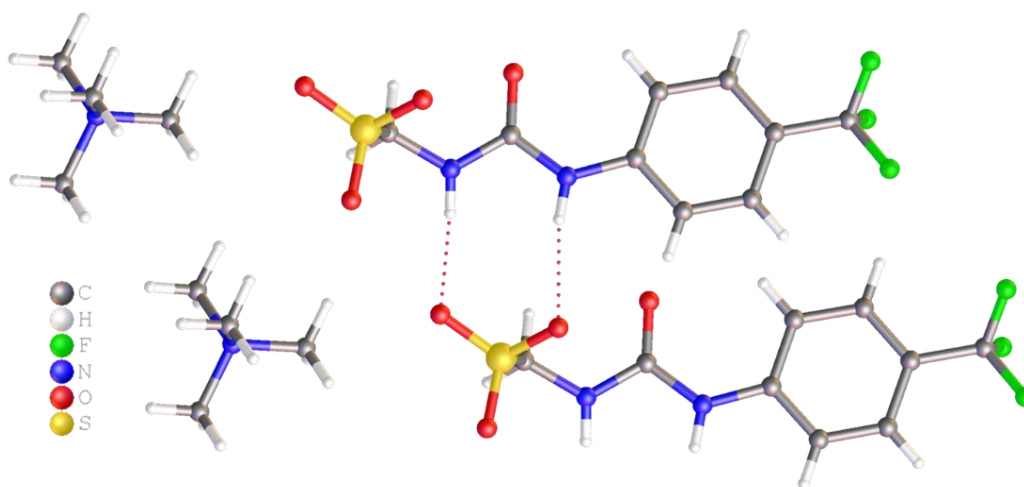


Figure 33 - Single-crystal X-ray structure of **50**, illustrating intermolecular polymerisation through urea-anion complexation.

Compound **63** does not contain an anionic functionality. In this comparative example, the anionic group is instead protected by a *tert*-butyl ester. This compound exhibits no hydrogen bonded self-association but instead forms a hydrogen bonded complex with a water molecule acting as a principle HBA/HBD group, as shown in Figure 34.

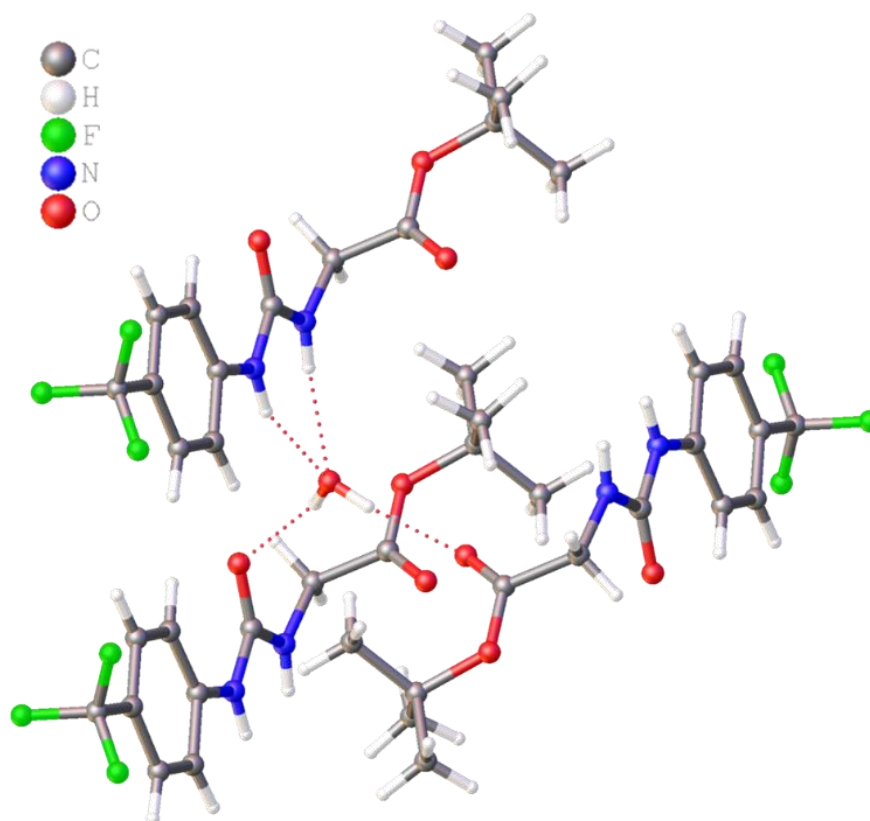


Figure 34 - Single-crystal X-ray structure of **63**, illustrating intermolecular polymerisation through thiourea-anion complexation.

The removal of the *tert*-butyl ester from **63** and the addition of TBA produced the corresponding carboxylate (**65**). However, during the two-week crystallisation process, the CF_3 group was converted to a carboxylic acid functionality as shown in Figure 35, **65a** and **65b**. Investigations into what influences caused this conversion is still ongoing.

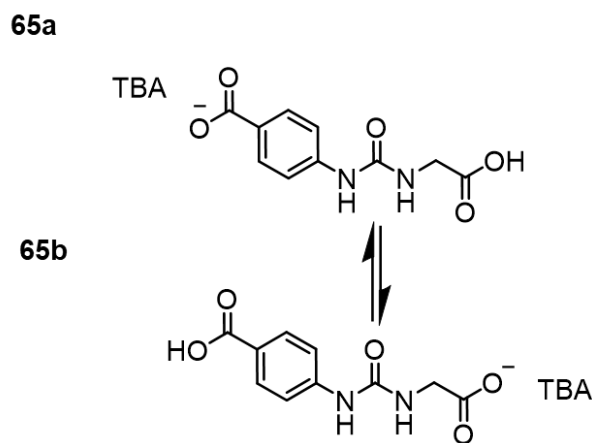


Figure 35 – Compounds **65a** and **65b** crystallised from a solution containing **65** over a two-week period.

The structure for **65a/b** shows self-association occurring through two intermolecular carboxylate-urea bonds (Figure 36). It was observed that tape formation is preferred over dimer formation, this was hypothesised to be due to anion geometry, where the trigonal planar carboxylate moiety favours end-on urea–anion interactions (Figure 37a). While the analogous tetrahedral sulfonate group favours dimer formation through the creation of four urea-anion hydrogen bonds as illustrated in Figure 37b. Investigations into these preferred binding modes are still ongoing.

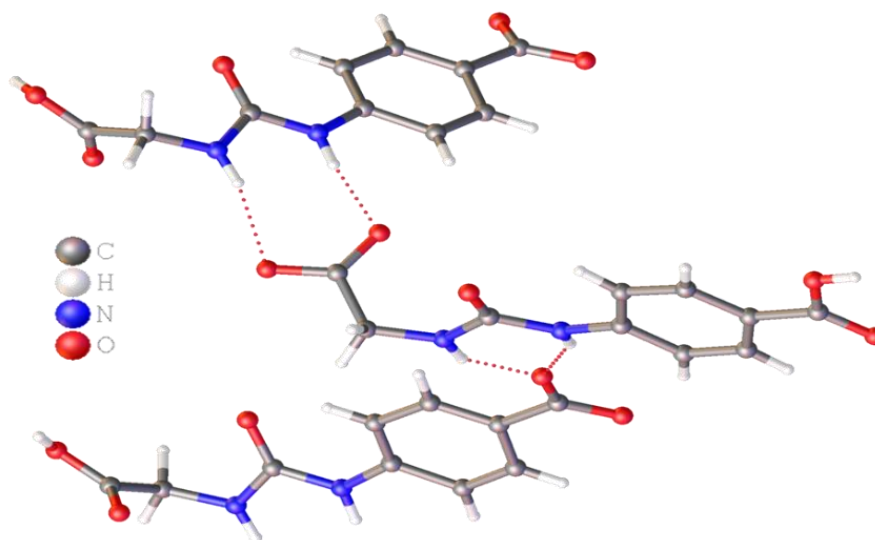


Figure 36 – Single-crystal X-ray structure of **65a/b**, illustrating intermolecular polymerisation through urea-anion complexation.

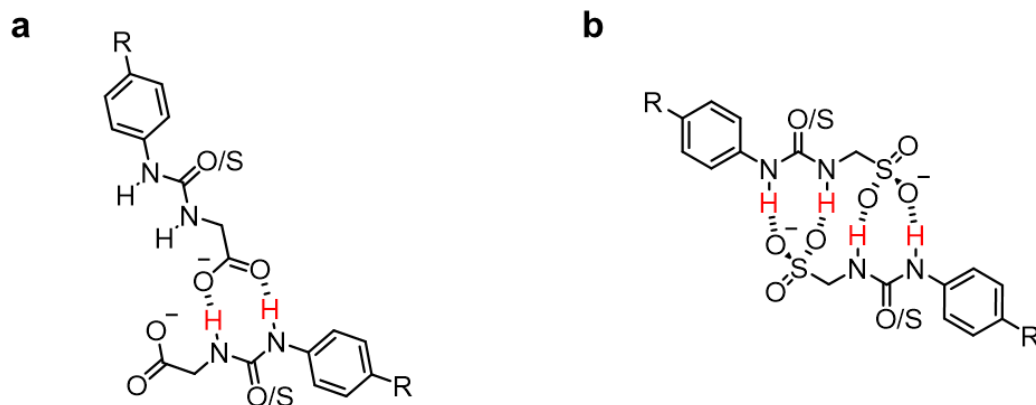


Figure 37 – A possible effect of anion geometry on hydrogen bonding mode, a) trigonal planer carboxylate and b) tetrahedral sulfonate.

The hydrogen bond distances and angles for **43**, **44**, **46**, **47**, **50**, **55**, **62** and **65**, calculated from single-crystal X-ray structures are shown in Table 1. These calculated results demonstrate the hydrogen bond length from donor to acceptor (D-A) range from 2.81-3.42 Å with hydrogen bond angles between D-H—A ranging from 122.3-174.1 °.

Table 1 - Hydrogen bond distances and angles involved in N-H-anion hydrogen bonded self-association, calculated from single-crystal X-ray structures.

Compound no.	HBD	Hydrogen atom	HBA	Hydrogen bond length (D...A) (Å)	Hydrogen bond angle (D-H...A) (°)
43	N1	H1	O2	2.8954 (18)	163.42 (10)
43	N2	H2	O2	3.0960 (17)	149.23 (10)
43	N2	H2	O2	2.9813 (18)	122.31 (16)
44	N1	H1	O7	2.889 (13)	156.9 (7)
44	N2	H2	O7	2.917 (16)	154.0 (7)
44	N3	H3	O1	3.105 (15)	150.4 (7)
44	N4	H4	O1	2.967 (16)	151.7 (7)
44	N5	H5	O15	3.096 (15)	158.1 (7)
44	N6	H6	O14	2.980 (16)	148.1 (7)
44	N7	H7A	O9	2.909 (13)	157.5 (7)
44	N8	H8A	O9	2.916 (15)	152.4 (7)
46	N1	H1	O2	2.829 (4)	159.1 (2)
46	N2	H2	O1	2.918 (4)	159.9 (3)
47	N1	H1	O1	3.149 (5)	169.4 (3)
47	N2	H2	O3	3.013 (4)	141.7 (3)
50	N1	H1	O2	2.987 (3)	169.32 (18)
50	N2	H2	O3	2.862 (3)	172.3 (2)
55	N1	H1A	O3	3.094 (3)	154.41 (16)
55	N1	H1B	O3	3.423 (3)	153.24 (17)
55	N2	H2	O4	2.927 (2)	155.24 (15)
55	N3	H3	O4	2.903 (3)	152.77 (15)
62	N1	H1	O3	2.860 (3)	161.71 (16)
62	N2	H2	O1	2.897 (3)	154.17 (17)
65	N1	H1	O10	2.831 (13)	174.1 (10)
65	N2	H2	O9	2.828 (12)	159.9 (9)
65	N3	H3A	O1	2.884 (15)	155.2 (9)
65	N4	H4B	O1	2.812 (16)	152.2 (9)

In summary, it has been shown that the anionic moiety and the hydrogen bond donating (thio)urea groups are key substituents in self-association, aiding in the formation of stable intermolecular bonded dimer and tape species. It was shown that when weakly coordinating TBA is substituted with a stronger coordinating counter cation such as TMA the self-associated hydrogen bonded tape formation is favoured over the dimer.

Finally, it is hypothesised that anion geometry plays a significant role in the binding mode, with compounds containing the carboxylate moiety (**65**) favouring end-on urea-anion interactions, while the analogous tetrahedral sulfonate group favours dimer formation through the creation of four urea-anion hydrogen bonds (Chapter 2.3, Figure 37).

2.4 Gas phase: mass spectrometry

ESI-MS was initially utilised for measurement of molecular mass and structural characterisation of biologically important macromolecules such as proteins¹⁴⁰ and nucleic acids.¹⁴¹ More recently this application has been extended to a broad range of analytes which include: inorganic compounds, examples of which are boron compounds, where conventional ionisation methods had previously proven to be problematic. However, ESI-MS is useful for the analysis of these (sometimes air-sensitive) compounds;¹⁴² polar organic compounds, where work was undertaken by Wilson and Wu for the detection of common reagent hexamethyl phosphoric triamide (**81**) using ESI-MS. The Na⁺ adducts, [M + Na]⁺ (**81a**) and [2M + Na]⁺ (**81b**) were observed to be present in the gas phase (Figure 38).¹⁴³ and finally metal-organic complexes where Keith-Roach discovered ESI-MS a straightforward method for obtaining complex formation and species distribution information.¹⁴⁴

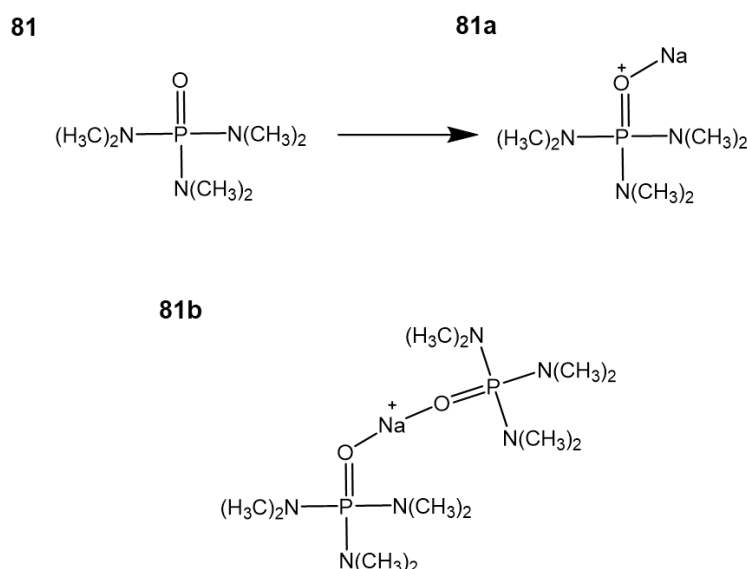


Figure 38 - Utilising ESI-MS the Na⁺ adducts of hexamethylphosphoric triamide (**81**), were shown to be present in the gas phase, [M + Na]⁺ (**81a**) and [2M + Na]⁺ (**81b**).¹⁴³

ESI is termed as a soft ionisation technique as very little residual energy is retained by the analyte and in general, no fragmentation occurs upon ionisation.¹⁴⁵ Furthermore, as this is a 'soft' technique, non-covalent interactions such as the hydrogen bond are preserved in the gas phase.¹⁴⁶ ESI-MS is an innovative approach to studying intermolecular interactions; this technique was utilised within this study to determine if dimerisation or self-association is limited to the solid and solution states for compounds **42-58** and **60-72**, or whether these compounds exhibit dimeric species in the gas phase.

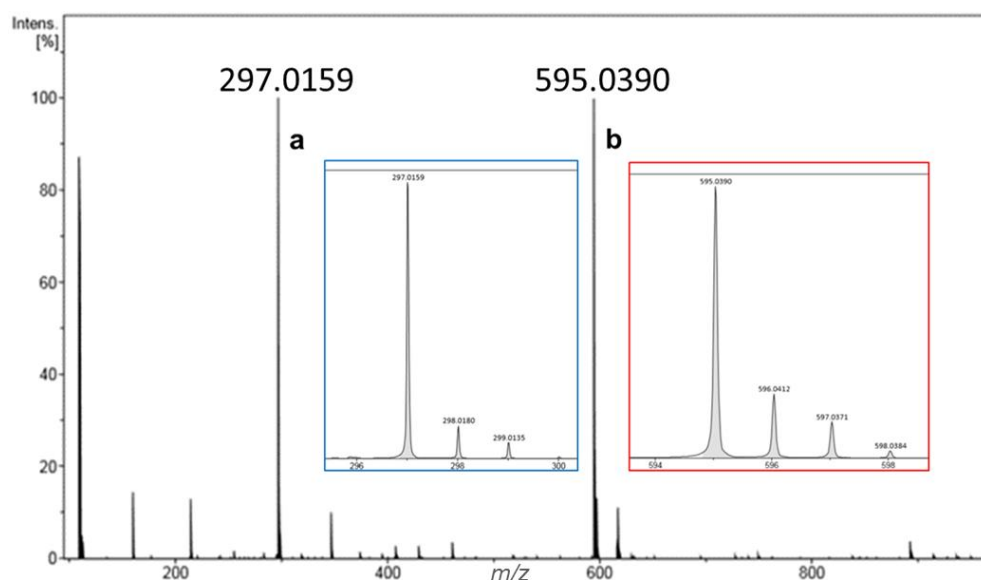
As expected, data obtained from high-resolution ESI-MS studies show **42-58** and **60-72** to exist in the monomeric state $[M]^-$, where $[M]^-$ represents the anionic component of the corresponding amphiphilic salt. As **63**, **64**, **66** and **67** are neutral compounds, $[M-H]^+$, therefore, represents the conjugate base of these molecules. It is not possible to distinguish the difference between the anionic monomer $[M]^-$ and a dimeric species $[M+M]^{2-}$ due to the mass to charge ratio. However, it was possible to identify self-associated dimers $[M+M+H]^-$ of **42-58**, **64**, **65**, **67-70** and **72** and the Na^+ adducts of **60-62** $[M+M+Na]^-$ to be present in the gas phase, with correspondence between the theoretical and actual m/z peaks, which exhibit a relative abundance range from 2 % to 98 %, as overviewed in Table 2.

Table 2 - High-resolution ESI⁻ mass spectrometry theoretical and experimentally derived values. (RA. = relative abundance)

Compound no.	m/z [M+M+H] ⁻			Compound no.	m/z [M+M+H] ⁻		
	Theoretical	Actual	RA (%)		Theoretical	Actual	RA (%)
42	595.0397	595.0390	98	57 ^[a]	459.0578	459.0649	52
43	623.0710	623.0689	17	58	549.0351	549.0525	3
44	651.1023	651.0996	9	60 ^[b]	573.0224	573.0431	28
45	626.9941	626.9936	81	61 ^[b]	513.0012	512.9840	2
46	655.0254	655.0236	7	62 ^[b]	602.9714	602.9997	2
47	683.0567	683.0529	4	63	Not observed		
48	595.0397	595.0418	69	64	523.1058	523.1025	27
49	595.0397	595.0408	88	65b	545.0877	545.1039	11
50	595.0397	595.0423	60	66	Not observed		
51	595.0397	595.0385	31	67	555.0601	555.0577	12
52	595.0397	595.0423	59	68	555.0601	555.0591	5
53	595.0397	595.0377	14	69 ^[a]	559.0890	558.9373	24
54	595.0397	595.0347	14	70 ^[a]	659.1204	659.1210	28
55	489.0868	489.0853	4	71 ^[a]	Not observed		
56	519.0861	519.0867	4	72 ^[a]	752.0862	753.0864	50

[a] Previously published results.¹³⁶[b] Obtained as the [M+M+Na]⁻ ion.

Using CF₃ substituted urea-sulfonate **42** as an example, the ESI-MS spectrum presented in Figure 39 shows the presence of an anionic monomer [M]⁻ with an m/z of 297.0159 (39a) and the mono-protonated sulfonate-urea dimeric species [M+M+H]⁻ with an m/z of 595.0390 (297.0159 + 297.0159 + 1.007) (39b).

Figure 39 - ESI spectrum of **42**, showing both the monomeric and protonated dimeric species, monomeric species (insert, a) and protonated dimeric species insert (b).

Within the molecular structures of *tert*-butyl protected **63** (urea) and **66** (thiourea), there are no anionic substituents or ionisable carboxylic acid residues, therefore, the presence of a dimeric species was not observed. The protonated dimeric species for previously published *ortho*-substituted benzothiazole **71** was also not shown to be present, this was hypothesised to be due to the formation of the intramolecular hydrogen bond between the urea N-H and the nitrogen on the benzothiazole substituent (Figure 40), limiting the number of potential HBD groups available to stabilise the formation of the dimer.¹³⁶

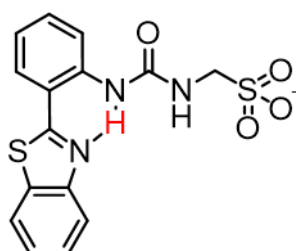
71

Figure 40 – The proposed structure of monomer of **71**, demonstrating intramolecular bond formation, as observed in the gas phase.¹³⁶

All ESI-MS spectra that display the abundance percentage of different isotopes for **42-58** and **60-68** are presented in Appendix 1.3, Figures S70-S95.

In summary, it has been shown that for mono-protonated sulfonate-(thio)urea or mono-protonated carboxylate-(thio)urea dimeric species to be present in the gas phase, it was established that compounds were required to contain an anionic substituent or an ionisable carboxylic acid residue. Since compounds **42-58**, **60-62**, **64**, **65**, **67-70** and **72** all fulfil this requirement, they were all shown to form self-associated dimers either as $[M+M+H]^-$ or as the Na⁺ adduct $[M+M+Na]^-$. Furthermore, limiting the number of HBD groups involved in the self-association process, from two to one as shown for **71** results in dimeric destabilisation in the gas phase. The stability of those dimer formations identified in the gas phase cannot be determined, therefore the compounds discussed will be further explored in the solution state using a combination of complementary techniques.

2.5 Solution state self-association studies

Unlike the solid state, in which the molecular interactions observed are influenced by crystal packing forces or the gas phase where the same interactions can be subject to experimental conditions, the solution state introduces solvent-solute interactions. These solvent-solute interactions exert influence on molecular self-association events and resultant aggregate, micelle¹⁴⁷ or inverse micelle formation processes.¹⁴⁸ This is commonly observed in solvents with HBA or HBD groups, such as DMSO or water.¹⁴⁹

Intermolecular forces between the solute and solvents compete with those of between the solute molecules. Thus creating solvent-solute hydrogen bonded self-associated complexes, which must be disrupted to allow for the formation of hydrogen bonded self-associated complexes. The conformation of extended aggregates formed will also be dependent on the type of solvent within a system.¹³⁶ Maximising the hydrophilic or hydrophobic interactions with the surrounding environment will result in more robust self-association complex formation.

2.5.1 Dynamic light scattering

Dynamic light scattering analyses are routinely used in chemical and biological laboratories for the detection of aggregates in solutions of macromolecules.¹⁵⁰ This well-established, non-invasive standardised technique is based on the Brownian motion of dispersed particles, on the principle that particles are constantly colliding with solvent molecules. Such collisions produce a constant amount of transferable energy, which in turn induces particle movement. As expected this energy transfer has a greater effect on smaller particles than those that are larger in size.¹⁵¹ When these particles are irradiated with visible monochromatic light, the intensities of the then scattered light fluctuates in a time-dependent manner due to the continuously changing distances between the particles, analyses of these intensities allows for the determination of the diffusion coefficient (D). Using this parameter and others outlined in the Stokes-Einstein equation, the hydrodynamic diameter (d_H) can be calculated (Equation 1).¹⁵²

Equation 1 - The Stokes-Einstein equation that enables calculation of the diffusion coefficient measured by DLS.¹⁵²

$$d_H = \frac{k_B T}{3\pi\eta D}$$

d_H = Hydrodynamic diameter
 D = Translational diffusion constant
 k_B = Boltzmann's constant
 T = Thermodynamic temperature
 η = Dynamic viscosity

Limitations of this technique for acquiring particle measurements include i) an upper size limit of 1000 nm where particles larger than this can be attributed to the onset of sedimentation or amalgamation of smaller aggregates: ii) a lower size limit of 1 nm, this value is defined by the signal-to-noise ratio as small particles do not scatter a sufficient amount of light, resulting in a poor measurement signal; iii) the d_H is the calculated diameter of the 'hypothetical' particle on the assumption that particles are spherical in shape.¹⁵³ However, in reality, the dispersed particles can be non-spherical, dynamic and solvated/hydrated (Figure 41), therefore DLS provides only an indicative size of a particle, colloid or aggregated species.¹⁵⁴ Finally, the graphs produced within this study are intensity distributions, weighted by size. As the compounds discussed within this thesis are novel, refractive index calculations have yet to be investigated, therefore, number or volume distribution information could not be attained.

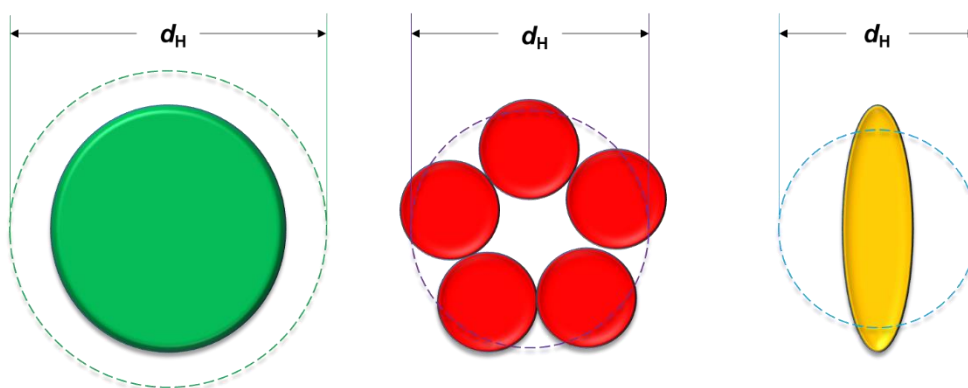


Figure 41 - Cartoon representation of the hydrodynamic radius (d_H) measurements of different shaped self-associated aggregates using DLS.

In this study the average intensity particle size distribution for compounds **42-56**, **58**, and **60-68** was investigated in a solution of EtOH:H₂O (1:19) and DMSO using DLS and compared with previously published results for **57** and **69-72**.¹³⁶

These solvent systems were chosen as the monomeric units of **57** and **69-72** have previously shown to self-associate to form either spherical aggregates or dimeric species under these conditions¹³⁶ (the addition of the EtOH in the aqueous system was required to aid compound solubility and allow effective measurement comparison for the entire SSA library to date).

Extended self-associated aggregates (peak maxima > 50 nm) were all shown to form with compounds **42-52**, **55-58**, **60-62**, **64**, **65**, and **67-72** at a concentration of 5.56 mM in an aqueous solution of EtOH:H₂O (1:19). At concentrations of 0.56 mM and 5.56 mM, a broad range of aggregate sizes with a peak maxima from 21 nm – 5560 nm were observed, as overviewed in Table 3, with a PDI (%) range of 13.02 – 42.01 % as shown in Appendix 1.4.1, Table S3.

Table 3 - Peak maxima obtained from an average intensity particle size distribution of **42-52**, **55-58**, **60-62**, **64**, **65**, and **67-72** obtained at 0.56 mM and 5.56 mM in an EtOH:H₂O (1:19) system by DLS. Hydrodynamic aggregate diameter is given in nm. An annealing process was applied in which the samples were heated to approximately 40 °C before being allowed to cool to a measurement temperature of 25 °C. (No. = compound number, conc. = concentration).

No.	Conc. (mM)	Peak maxima (nm)	No.	Conc. (mM)	Peak maxima (nm)	No.	Conc. (mM)	Peak maxima (nm)
42	5.56	164, 4	52	5.56	190	63	5.56	[b]
	0.56	142, 14		0.56	220		0.56	[b]
43	5.56	459, 59	53	5.56	[b]	64	5.56	396
	0.56	190, 28		0.56	[b]		0.56	330, 33
44	5.56	122	54	5.56	[b]	65	5.56	220
	0.56	295		0.56	[b]		0.56	190,33
45	5.56	342, 295	55	5.56	342	66	5.56	[b]
	0.56	142, 24		0.56	459, 28		0.56	[b]
46	5.56	142	56	5.56	190	67	5.56	459
	0.56	68-4145		0.56	220		0.56	255
47	5.56	122	57 ^[a]	5.56	220	68	5.56	164
	0.56	4145, 44		0.56	396		0.56	106
48	5.56	531	58	5.56	91	69 ^[a]	5.56	164
	0.56	295, 21		0.56	79		0.56	255
49	5.56	220	60	5.56	220	70 ^[a]	5.56	220
	0.56	91		0.56	190, 18		0.56	164
50	5.56	164	61	5.56	190	71 ^[a]	5.56	295
	0.56	190		0.56	190		0.56	220
51	5.56	190	62	5.56	106, 1	72 ^[a]	5.56	59, 300
	0.56	220		0.56	122-5560		0.56	120

[a] Previously published results.¹³⁶ [b] not calculated due to sample solubility.

Prior to these DLS studies being undertaken, the samples underwent an annealing process (heating to 40 °C and cooling back to 25 °C) to ensure any self-associated aggregates present had achieved a thermodynamic minimum. Due to compound insolubility in an aqueous environment at comparable concentrations, compounds containing TPEA (**53**), THA (**54**) or a *tert-butyl* ester within their molecular structure (**63** (urea) and **66** (thiourea)), could not be included within these studies.

It was observed that those self-associated aggregates present in the DLS studies split into one of three different classes. The first class are those with a d_h from 1-10 nm and only observed with solutions containing CF₃ substituted urea-sulfonate **42** and *nitro*-substituted thiourea-sulfonate **62**, at 5.56 mM these values are indicative of lower-order structures such as monomers, dimers and trimers. However, with **42** and **62** there are also larger structures present (164 and 106 nm respectively).

The second class contains 5.56 mM solutions of CF₃ substituted urea-sulfonate **43**, *nitro*-substituted urea-sulfonate **58** and *para*-benzothiazole substituted **72**, where structures have a d_H of between 10-100 nm. Finally, the third class is for those structures with a d_H between 100-550 nm. This size of structure (100-550 nm) was observed for every compound studied at 5.56 mM except *nitro*-substituted urea-sulfonate **58**, which has a d_H of 91 nm. The existence of this size of the self-associated structure, reported by these DLS studies, has already been confirmed through a combination of complementary fluorescence and transmission microscopy studies at comparative concentrations, using intrinsically fluorescent *ortho*-benzothiazole substituted **71** and *para*-benzothiazole substituted **72**.¹³⁶ Solutions containing **42**, **43**, **45** and **72** indicate two distinct aggregate size distributions coexisting in the same 5.56 mM solution.

In a 0.56 mM solution the majority of the compounds (**42-45**, **48**, **50-52**, **55-57**, **60**, **61**, **64**, **65**, **67-69** and **70-72**) all exhibit structures with a d_H representative of class three (100-550 nm). As observed these larger structures still persist at lower concentrations, therefore, the size of the self-associated hydrogen bonded aggregates are not (for these compounds) disrupted by the competitive binding of solvent molecules. Solutions containing CF₃ substituted thiourea-sulfonate **46** or **47** and *nitro*-substituted thiourea-sulfonate **62** at 0.56 mM exhibit structures that exceed the limitations of the experiment $d_H > 1000$ nm. These structures are attributed to amalgamations of smaller structures.

Finally, in a solution of DMSO at comparable concentrations of 5.56 mM and 0.56 mM, **42-52**, **55-58**, **60-62**, **64**, **65**, and **67-72** show evidence of aggregates > 100 nm in diameter (Appendix 1.4, Figures S96-S181). It is hypothesised that these structures are amalgamations of smaller self-associated species, as this DLS information was obtained from an intensity distribution, the presence of a few large structures can potentially mask the presence of smaller ones. Further studies discussed in section 2.5.3.2 suggest that the proportion of compound in these associated materials is within the error measurement of NMR, therefore it is a very low proportion of material that ends up in those aggregates > 100 nm in diameter.

In summary, DLS studies conducted at concentrations of 0.56 mM and 5.56 mM show a broad range of aggregate sizes from 21 nm – 5560 nm were observed in an aqueous solution of EtOH:H₂O (1:19). With extended self-associated aggregates (> 50 nm) shown to be present for compounds **42-52**, **55-58**, **60-62**, **64**, **65**, and **67-72** at a concentration of 5.56 mM. Small lower-order structures (d_H 1-10 nm) are proposed to be monomers, dimers or trimers and were observed with solutions containing **42** and **62**, at 5.56 mM, these were in addition to the presence of structures with a d_H of 164 and 106 nm respectively. Solutions containing compounds **43**, **58** and **72** (5.56 mM) were shown to exhibit structures with a d_H of between 10-100 nm.

Finally, in an aqueous environment at 5.56 mM, all compounds (except **58**) have a prevalence to form higher-order self-associated hydrogen bonded aggregates with a d_H between 100-550 nm.

2.5.2 Surface tension and critical micelle concentration studies

The amphiphilic nature of surfactant molecules (such as SSAs) is responsible for their self-associated properties, with the balance of hydrophobic and hydrophilic effects driving the monomers to self-assemble, forming energy favourable structures. A common example of these aggregate formations are micelles, where the polar head group seeks to interact with an aqueous medium, and the hydrophobic tail is sequestered internal to the structure.¹⁵⁵

Here CMC is elucidated by determining the surface tension of a serially diluted series of compound solutions. At a low concentration, the presence of molecules at the surface disrupts the cohesive energy of the solvent and therefore lowers surface tension (Figure 42a). As molecular concentration increases, the surface interface becomes saturated by these surface-active molecules (Figure 42b), the surface tension is found to no longer decrease with increasing molecular concentration.¹⁵⁶ This point is defined as the CMC, where the number of micelles, vesicles or aggregated species present increase, in the volume phase above this transition point (Figure 42c) and the surface tension becomes independent of concentration.

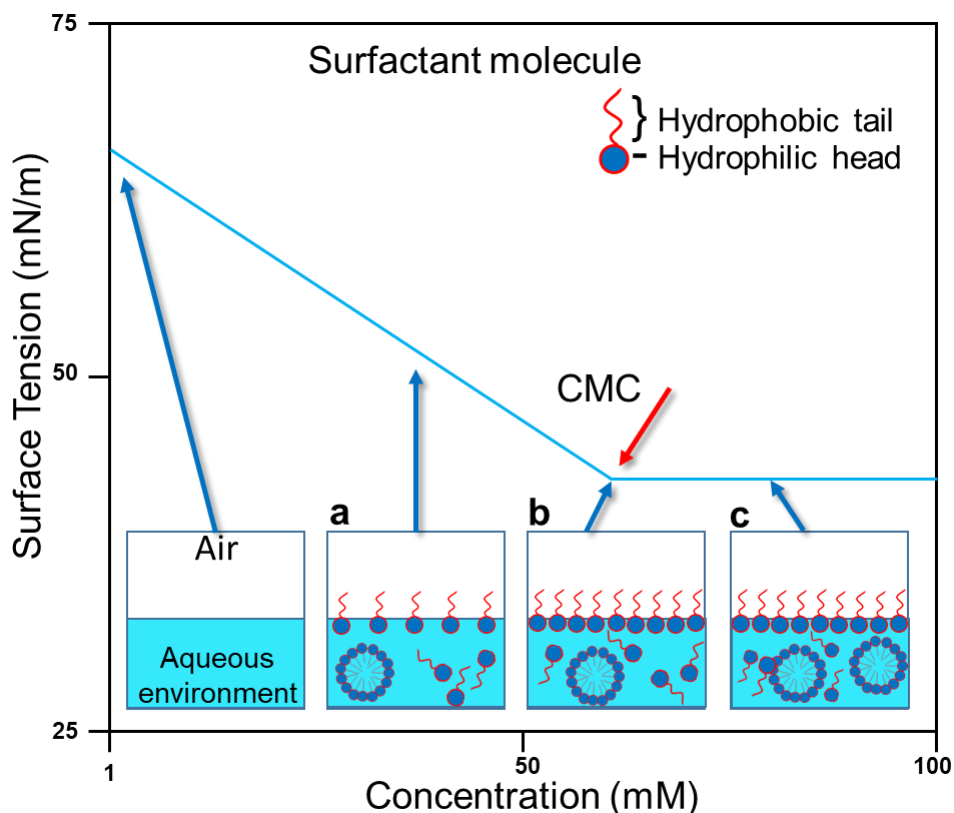
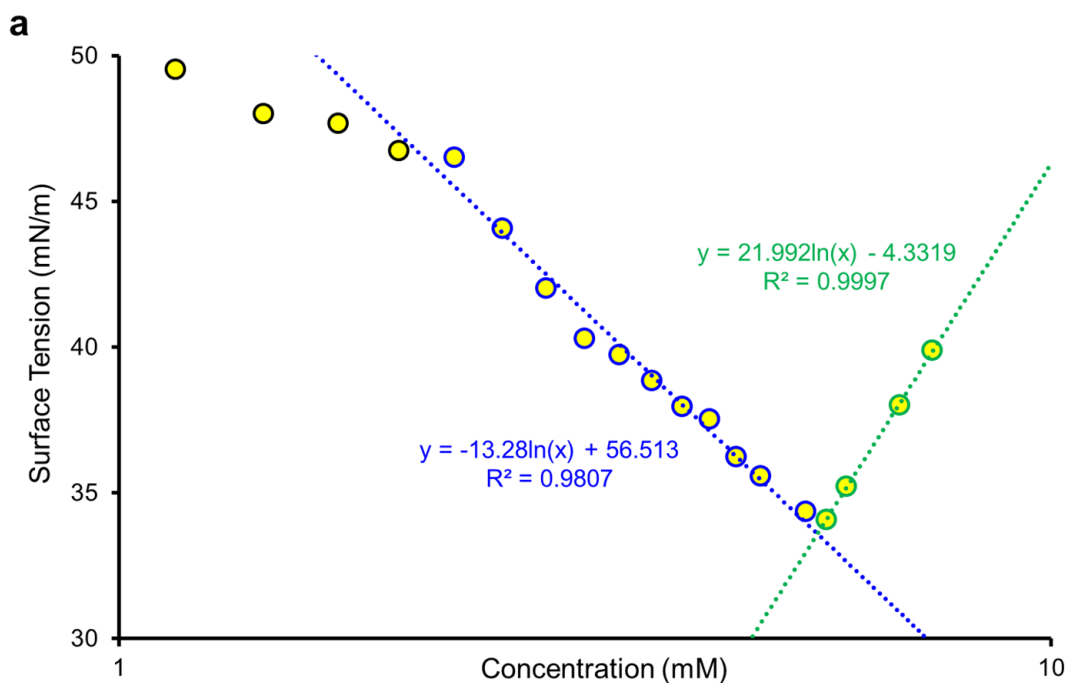


Figure 42 – Cartoon representation of CMC determination. a) Surfactant congregates at the surface, b) surface becomes saturated and c) proposed aggregate formation.¹⁵⁷

In 1955 Williams and co-workers investigated the CMC of pure sodium lauryl sulphate in water and NaCl solutions, using conductivity, light scattering and diffusion mobility. In their study, association colloids were characterised, and it was determined that in dilute solutions only small particles were present but at a higher concentration, both small and large colloidal structures were in equilibrium.¹⁵⁷ However, self-associated aggregates are now known to be present in dilute solutions below the CMC value. It is only with the further addition of solute molecules that we can recognise and detect the aggregation of spherical units by measuring surface tension against concentration.^{136,158} Factors that affect CMC reproducibility include the presence of other surface-active substances,¹⁵⁹ the presence of electrolytes¹⁶⁰ and any variation of temperature¹⁶¹ or pressure.¹⁶²

The CMC and corresponding surfactant properties for **42-52**, **56-58**, **60**, **61**, **65** and **69-72** in an EtOH:H₂O (1:19) solution were observed using the methods analogous with those reported by Costas and co-workers (Chapter 6.1.1).¹⁵⁶

The CMC and surface tension (obtained at CMC) values were calculated using a plot of surface tension against concentration, and taken at the point of which the surface tension is found to no longer decrease with the further addition of compound,^{156,163} as shown in the example tensiometric profiles in Figure 43 (a and b), with the results overviewed in Table 4. With the exception of anthracene substituted **70** and *para*-benzothiazole substituted **72**, all compounds exhibit a CMC above 5.56 mM the concentration used for the DLS studies, and where the presence of larger structures was observed. This confirms the previous statement that self-associated aggregates > 10 nm are present in dilute solutions before the CMC is reached.^{136,158}



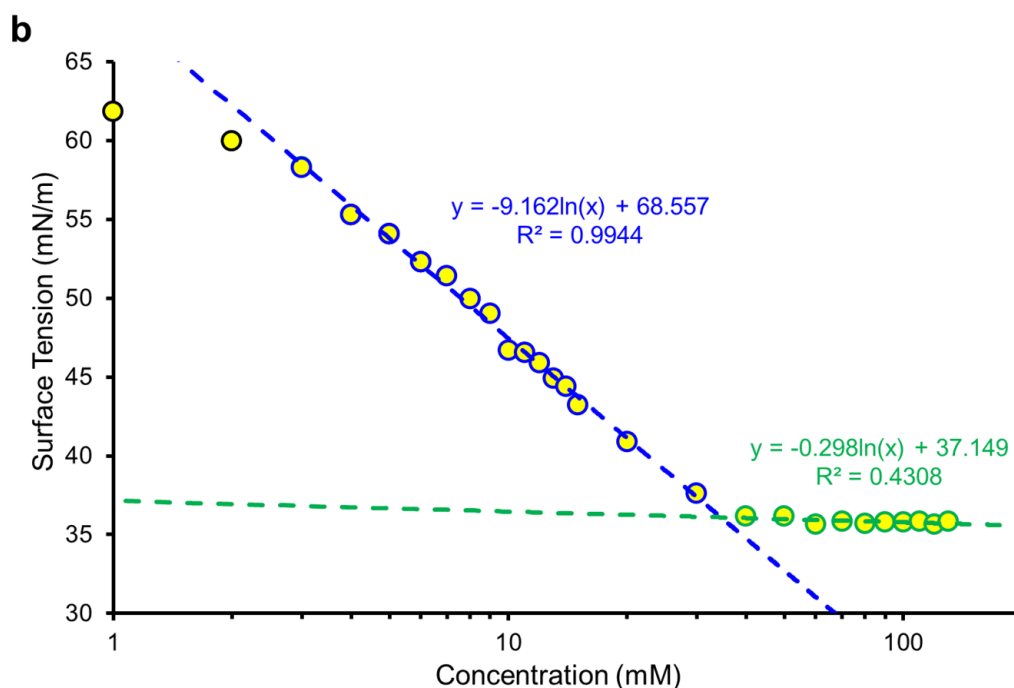


Figure 43 - CMC calculation of 5.61 mM for compound **47** (a) and 34.57 mM for compound **52** (b) in an EtOH:H₂O (1:19) mixture using surface tension measurements. Linear relationship between Log(Conc.) (Green) and surface tension. Surface of droplet saturated, minimum surface tension reached (Blue).

Table 4 – CMC and surface tension (obtained at CMC) measurements for compounds **42-52**, **56-61**, **65** and **69-72** in a solution of EtOH:H₂O (1:19) at 25 °C.

Compound no.	CMC (mM)	Surface tension (mN/m)	Compound no.	CMC (mM)	Surface tension (mN/m)
42	10.39	37.45	57 ^[a]	40.89	47.90
43	10.70	38.49	58	30.29	44.94
44	8.85	36.78	60	65.83	45.05
45	24.14	34.35	61	74.59	42.85
46	6.12	42.24	62	[b]	
47	5.61	33.59	63	[b]	
48	96.35	36.65	64	[b]	
49	198.42	36.16	65	11.21	39.33
50	209.98	41.78	66	[b]	
51	103.13	33.75	67	[b]	
52	34.57	36.09	68	[b]	
53	[b]		69 ^[a]	10.67	46.67
54	[b]		70 ^[a]	2.52	43.15
55	[b]		71 ^[a]	9.54	48.71
56	92.67	46.14	72 ^[a]	0.50	46.50

[a] Previously published results.¹³⁶ [b] not calculated due to sample solubility.

With alkyl chain length extension from $n=1$ to $n=2$, the CF₃ substituted urea-sulfonate amphiphiles **42** and **43**, exhibit a slight increase in CMC, from 10.39 to 10.70 mM respectively. Contrastingly, CF₃ substituted thiourea-sulfonate amphiphiles **45** and **46** ($n=1$ and $n=2$) exhibit a noticeable decrease in CMC from 24.14 to 6.12 mM.

It is hypothesised that the formation of the intramolecular hydrogen bond in **43**, could be attributed to this slight increase (Chapter 2.3, Figure 26). With the additional extension to the alkyl chain length from $n=2$ to $n=3$, a decrease in CMC is observed for both the CF_3 substituted urea-sulfonate and the thiourea-sulfonate amphiphiles from 10.70 to 8.85 mM and 6.12 to 5.61 mM respectively. Substitution of the HBD urea (**43** and **44**) for more acidic thiourea (**46** and **47**) also results in a decrease in CMC (10.70 to 8.85 mM (urea), 6.12 to 5.61 mM (thiourea)). This is expected as it is well known that thiourea receptors establish stronger hydrogen bond interactions and form more stable complexes with anions than their urea containing counterparts.¹²⁵ However, this trend is not observed when comparing urea-sulfonate **42** with thiourea-sulfonate **45**, hypothesised to be due to the formation of a secondary structure that is not involved in the self-association process, as illustrated in Figure 44. This hypothesis is further supported by variable temperature ^1H NMR studies. Where a ^1H NMR performed at 298 K showed the presence of two structures, confirmed through comparative integration of those peaks attributed to the thiourea-sulfonate against counter cation TBA (Figure 45). With an increase of temperature from ≈ 298 K to ≈ 333 K the weak intramolecular hydrogen bond demonstrated in Figure 44 is hypothesised to be disrupted as the peaks present in Figure 45 were shown to coalesce as shown in Figure 46.

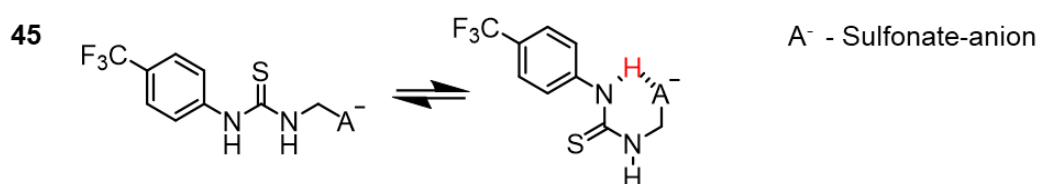


Figure 44 – Proposed formation of the secondary structure of **45**.

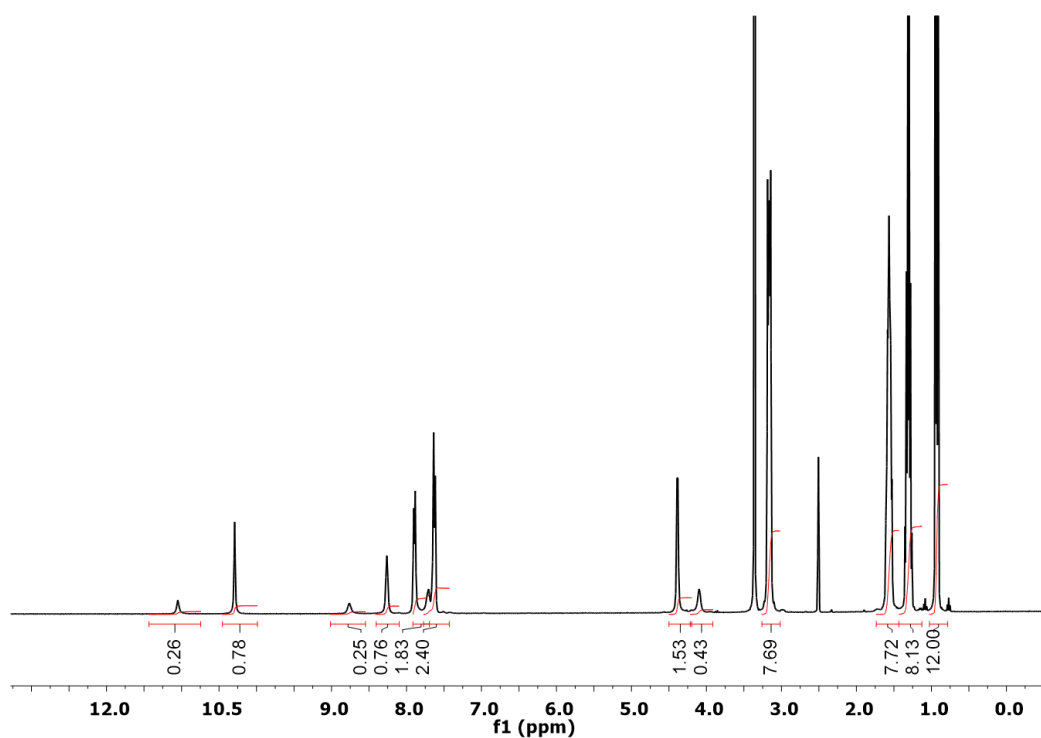


Figure 45 – ^1H NMR of compound **45** in $\text{DMSO-}d_6$ conducted at 298.15 K, comparative integration showing the presence of two structures.

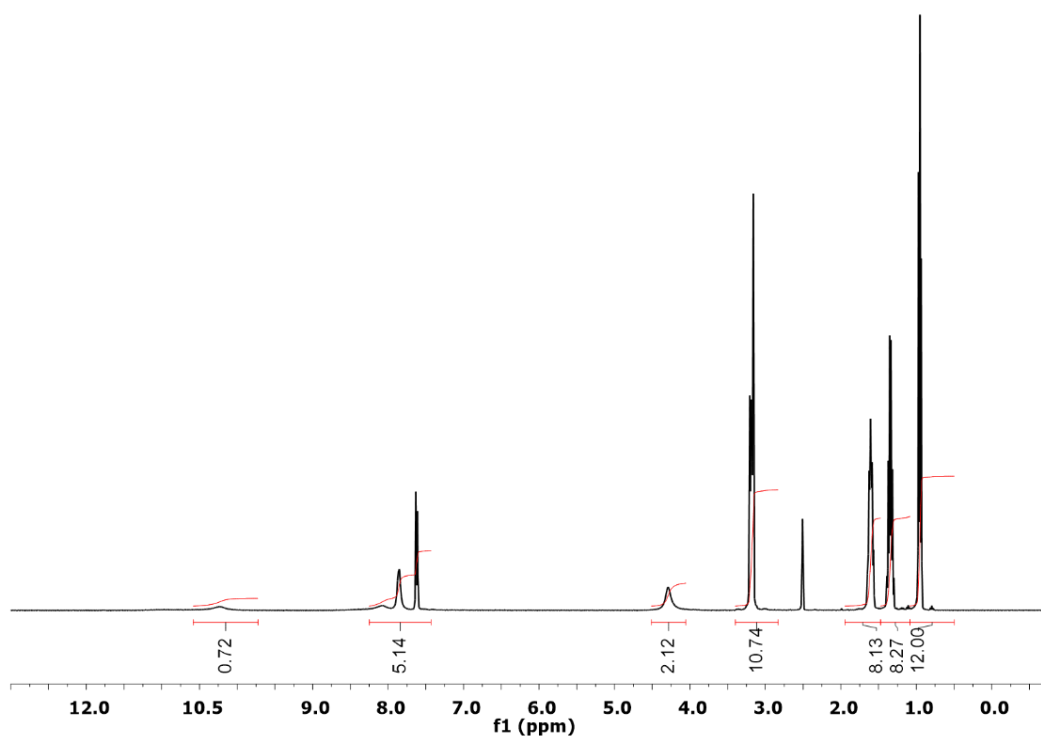


Figure 46 - ^1H NMR of compound **45** in $\text{DMSO-}d_6$ conducted at 333.15 K, showing coalescence of thiourea-sulfonate peaks.

It was hypothesised that the urea-carboxylate analogue (**65**) would exhibit a lower CMC than urea-sulfonate derivative **42**, due to stronger hydrogen bond complexes being formed between carboxylate anions and urea functionalities.

The strengths of these complexes are determined in the ^1H NMR self-association studies (Chapter 2.5.3.4). Whereas, the hydrogen sulfate ion is known to form significantly weaker bonds with the urea group.¹⁶⁴ However, upon comparing the values (**42**, 10.39 mM with **65**, 11.21 mM) the reverse is observed with **42** exhibiting a lower CMC value. An explanation for this could be the difference in hydrogen bonding modes, with **65** adopting the less stable trigonal planer geometry, as illustrated in Chapter 2.3, Figure 37.

A comparative decrease in surface tension recorded at the CMC for solutions containing **42-52**, **56-58**, **60**, **61**, **65** and **69-72**, in general, correlates with the presence of a CF_3 substituted aromatic ring system within the molecular structure. As LogP can be used as a comparative measure of hydrophobicity, theoretically derived LogP¹⁶⁵ (Figure 47) and polarisability values calculated for the R-group on the aromatic ring system, were investigated to determine if there was any correlation with the CMC and surface tension measurements. These theoretically derived values were calculated using optimised geometries of the aromatic ring substituents and counter cations contained within the molecular structures of **42-52**, **56-58**, **60**, **61**, **65** and **69-72** by low-level computational modelling with Spartan '16 software. The results from these calculations demonstrate the CF_3 aromatic ring system to exhibit a LogP value of 2.16, the highest of the substituted functional substituents. It is suggested that this higher affinity for the aqueous phase could be a major contributing factor to the initial observations.

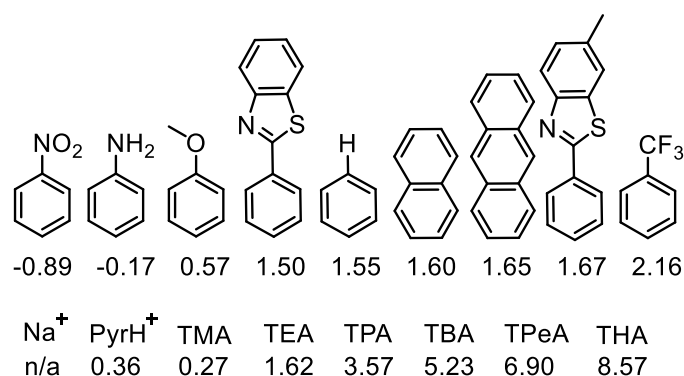


Figure 47 – Calculated LogP values from geometry optimised semi-empirical PM6 methods using Spartan '16. Values for Na^+ were inaccessible by these computational methods.

The effects the counter cation have on the derived CMC values of **42** and **48-52** were then investigated. It was shown that the CMC values adopted the following trend **42** < **52** < **48** < **51** < **49** < **50**. Polarisability acts as a measure of anion-cation coordination and strength, of any ion-pair effects within a system.¹⁶⁶ The theoretical values of polarisability for those counter cations contained within the molecular structure, Na⁺, PyrH⁺, TMA, TEA, TPA and TBA were calculated and are overviewed in Table 5.

Table 5 – Calculated polarisability values for counter cations of **42**, **48-52**.

Compound no.	Cation	Polarisability
42	TBA	65.47
48	Na ⁺	[σ]
49	PyrH ⁺	46.91
50	TMA	46.64
51	TEA	52.85
52	TPA	58.90

[σ] Results could not be calculated, as in an aqueous solution, the sodium ion exists as the hydrated complex [Na(H₂O)₆]⁺.

TBA exhibits a more diffused cationic charge demonstrated by the high polarisability value (65.47), and as a result, weakens any potential for ion-pair interactions between the cation and sulfonate-anion substituent. This subsequently leaves the HBA groups free for hydrogen bonded self-assembly processes, resulting in a CMC value of 10.39 mM. The calculated values for PyrH⁺ and TMA are both relatively low at 46.91 and 46.64 respectively, therefore are more likely to form ion-pair interactions with the anionic component of the amphiphile, resulting in a weaker self-associated structure and consequently higher CMC values (198.42 (**49**) and 209.98 mM (**50**)). This increase of CMC from 10.39 mM (**42**) to 198.42 mM (**49**) and 209.98 mM (**50**) respectively is also be attributed to the decrease lipophilicity of the counter cation from TBA to PyH⁺ and TMA. The polarisability for Na⁺ could not be calculated as it is expected that the Na⁺ exists as the hydrated complex [Na(H₂O)₆]⁺. This hydration process decreases the relative availability for cations to form ion-ion interactions, therefore, instead promotes urea-anion hydrogen bond formation.

Two correlations were observed these are: i) decreasing CMC of **42** and **49-52** with increasing calculated theoretical LogP values of cations, PyrH⁺, TMA, TEA, TPA and TBA (Figure 48, green) and ii) decreasing CMC of **42** and **49-52** with increasing polarisability values of cations, PyrH⁺, TMA, TEA, TPA and TBA (Figure 48, blue). These correlation graphs are shown in Figure 48.

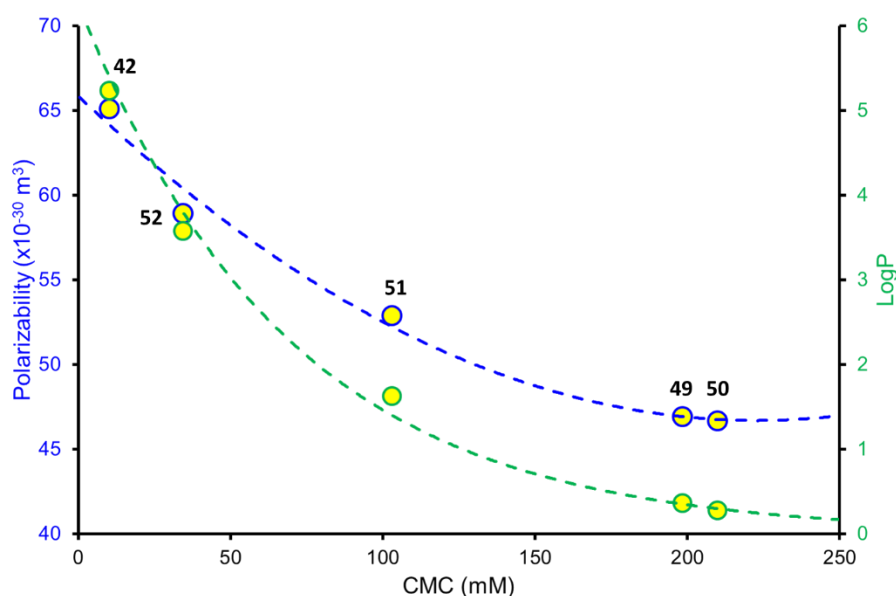


Figure 48 – Comparison of CMC and calculated cation polarisability (blue) and LogP (green) values obtained for **42** and **49-52**.

In summary, it was shown that the substitution of the HBD urea for more acidic thiourea resulted in a CMC value decrease. The urea-sulfonate (**42**) was shown to have a lower CMC (10.39 mM) than analogous urea-carboxylate **65**, this was theorised to be due to the adoption of different hydrogen bonding modes, with **65** adopting the less stable trigonal planer geometry. Comparison of experimentally derived CMC values with theoretically calculated polarisability and LogP values showed a correlation of decreasing CMC of **42** and **49-52** with both increasing calculated theoretical LogP and polarisability values of the counter cations.

2.5.3 ¹H NMR self-association studies

NMR spectroscopy is an important tool that has been routinely used to characterise noncovalent interactions in the solution state. Examples of these interactions include halogen bonding,¹⁶⁷ π- π stacking¹⁶⁸ and hydrogen bonding.^{136,169,170}

To gain an understanding of the self-associated interactions at the molecular level of **42-58** and **60-72**, a series of ^1H NMR studies were employed in a $\text{DMSO-}d_6$ 0.5 % H_2O or an $\text{EtOH:H}_2\text{O}$ (1:19) solution. These solvent conditions allow for the direct observation of the HBD N-H resonances in a competitive solvent environment.

2.5.3.1 DOSY ^1H NMR

As shown in the afore mentioned DLS studies (Chapter 2.5.1), the d_H of compounds **42-52**, **55-58**, **60-62**, **64**, **65**, and **67-72** are all > 100 nm at concentrations of 5.56 mM and 0.56 mM, this was hypothesised to be due to amalgamations of smaller self-associated structures. To further investigate this theory a series of DOSY ^1H NMR studies were carried out at 5.56 mM in a $\text{DMSO-}d_6$ 0.5 % H_2O solution containing **42**, **45**, **65**, **68** and **72**. The obtained translational diffusion constant was applied to the Stokes-Einstein equation (Chapter 2.5.1, Equation 1) to enable the derivation of the d_H . Solutions containing **42**, **45**, **65**, **68** and **72** were chosen to ensure a collective, a comparative data set was obtained due to their molecular structural differences.

The results generated from these studies support the earlier theory (Chapter 2.5.2) of TBA not being a strongly coordinating cation in solution. Figure 49 illustrates the TBA cation diffusing at a different rate to that of the sulfonate-urea anionic moiety of **42**. As **45**, **65**, **68** and **72** all contain TBA as the counter cation within their molecular structure, the same diffusion rate trend is observed for these compounds (Appendix 1.6, Figures S198-S201).

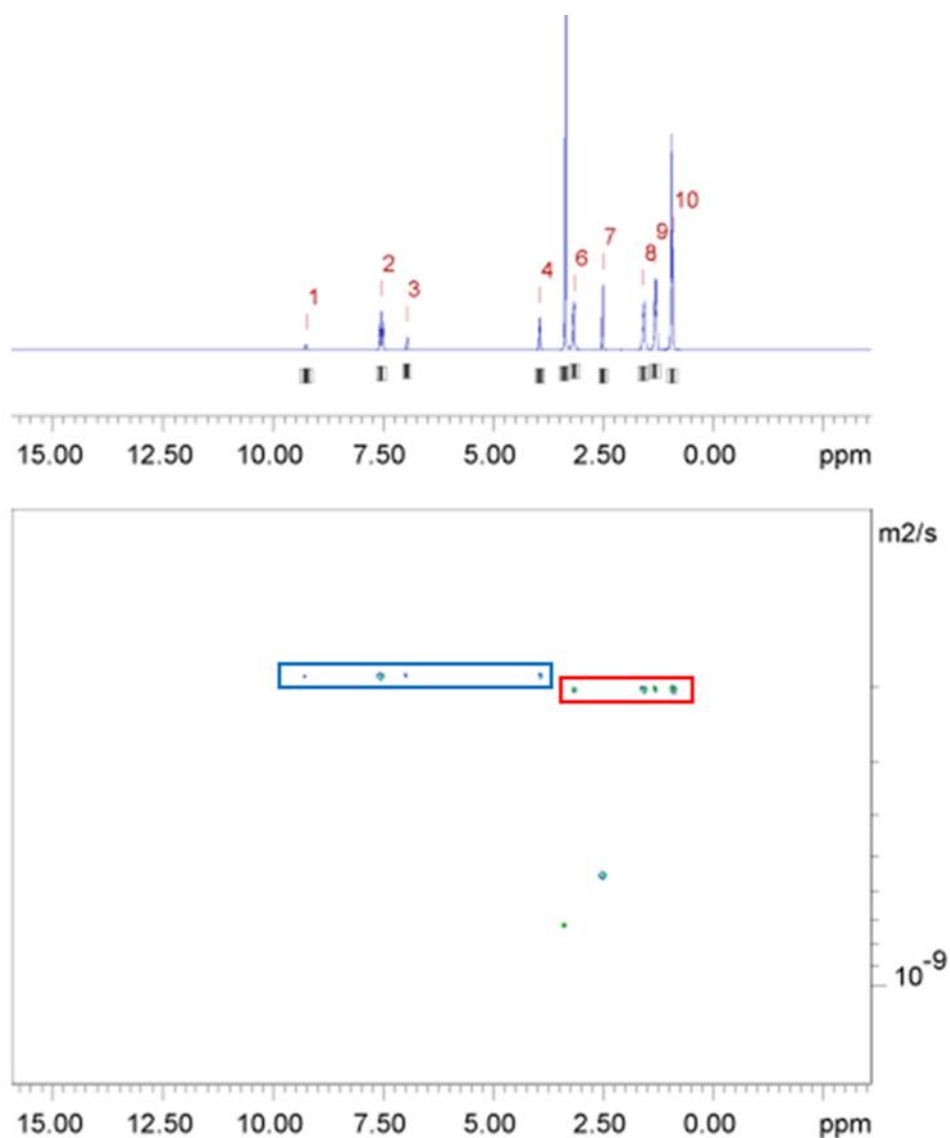


Figure 49 - ^1H NMR DOSY of compound **42** (55.56 mM) in $\text{DMSO-}d_6$ 0.5 % H_2O , conducted at 298.15 K. Anionic component highlighted in blue, TBA counter cation highlighted in red.

The results calculated from this study show no evidence of large aggregates in a solution of $\text{DMSO-}d_6$ 0.5 % H_2O as all anionic species are shown to exhibit a $d_H < 1.7$ nm (Table 6), this size is hypothesised to be indicative of lower-order structures such as dimers.

As with the DLS studies, a limitation of DOSY ^1H NMR studies is the assumption that all species present are spherical (Chapter 2.5.1, Figure 41). A further limitation is the presence of fast exchange processes which may complicate experiments.¹⁷¹ It is hypothesised that the larger species observed in the DLS studies in a solution of $\text{DMSO-}d_6$ 0.5 % H_2O exist in concentrations that are too low to be observed by standard solution state ^1H NMR techniques. This hypothesis is supported by the quantitative ^1H NMR studies shown in Chapter 2.5.3.2.

Table 6 – Calculated d_H for the anionic species of **42**, **45**, **65**, **68** and **72** using the Stokes-Einstein equation.

Compound no.	d_H (nm)
42	1.15
45	1.13
65	1.28
68	1.42
72 ^[a]	1.64

[a] Previously published results.¹³⁶

In summary, DOSY ^1H NMR studies of 55.56 mM solutions containing **42**, **45**, **65**, **68** and **72** at 298 K are hypothesised to be indicative of small low-order dimeric species with a $d_H < 1.7$ nm to be present for all compounds in a solution of DMSO- d_6 0.5 % H_2O .

2.5.3.2 Quantitative ^1H NMR studies

Quantitative ^1H NMR is a commonly used technique to quantify the concentration of low molecular weight (LMW) molecules, providing initial evidence for the presence of lower-order species such as dimers and/or higher-order species such as larger aggregates in solution.¹⁷² These higher-order species are known to adopt solid-like properties, resultantly becoming no longer observable using solution state NMR techniques.

As the magnitude of the peak on an NMR spectrum is proportional to the number of nuclei present¹⁷³ comparative integration of an LMW molecule against a known internal standard allows for the percentage of a molecular component apparently 'lost' from a solution to be quantified. Quantitative ^1H NMR was employed to quantify the concentration of compounds **42**, **45**, **65**, **68** and **72** in a solution of DMSO- d_6 0.5 % H_2O at 111.12 mM, with the exception of **65** which was conducted at 55.56 mM due to solubility.

The internal standard that was used for this study was 5 μL (1 % w/v) of dichloromethane (DCM), chosen due to DCMs miscibility with DMSO and because the peaks for DCM do not overlap with peaks attributed to the compounds being studied. This enables effective spectral signal integration. An analogous series of ^1H NMR studies were performed with **42**, **45**, **65**, **68** and **72** in EtOH: D_2O (1:19) at ≈ 5.56 mM to replicate those conditions within the DLS experiments.

With EtOH (25 μ L) acting as the internal standard, again chosen because of solvent miscibility and the position of the solvent signals. To ensure the entire NMR signal was collected, the relaxation time was increased to 60 seconds as a shortened signal collection time can cause a percentage of the signal to be lost. The limitations of this experimental technique include i) the inability to quantify any absence of self-associated species at a concentration below the limit of detection of the NMR spectrometer; and ii) performing this experiment in D₂O results in the absence of those signals attributed to N-H groups due to proton exchange.

In a solution of DMSO-*d*₆ 0.5 % H₂O, **42**, **45**, **65**, **68** and **72** all showed no discernible loss of signal from solution through comparative integration with the internal standard DCM signal, an example spectrum for CF₃ substituted urea-sulfonate **42** is shown in Figure 50. As no loss of signal was observed, this would suggest that those larger species (> 100 nm) present in the DLS studies (Chapter 2.5.1) exist in concentrations that are too low to be detected by ¹H NMR methods.

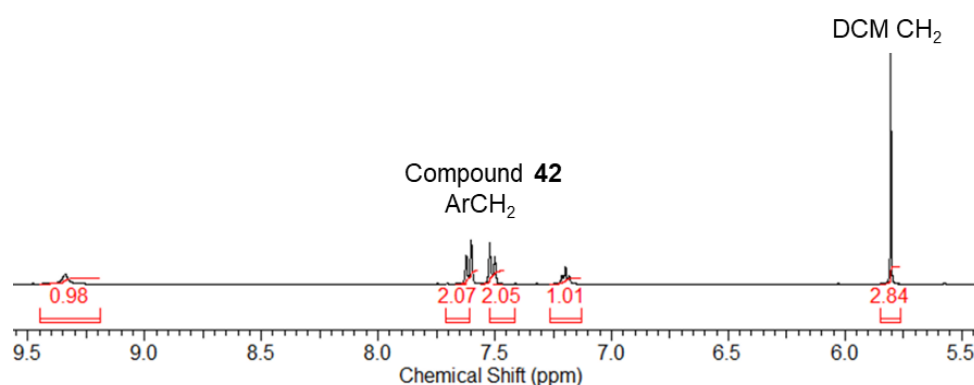


Figure 50 - ¹H NMR spectrum with a delay ($d_1 = 60$ s) of compound **42** (109.8 mM) in DMSO-*d*₆/ 1.0 % DCM. No apparent loss of compound observed upon comparative signal integration.

Moving into a solution of EtOH:D₂O (1:19) at ≈ 5.56 mM, the results from the quantitative ¹H NMR studies performed with **42**, **45**, **65**, **68** and **72** show an apparent ‘loss’ of the compound from the NMR sample through comparative integration with the EtOH signals (Table 7). This apparent ‘loss’ is attributed to the formation of larger higher-order self-associated aggregates, (that are invisible to the NMR (NMR silent)), to be present in a predominantly aqueous environment.

A representative spectrum for CF₃ substituted urea-sulfonate **42** demonstrating the apparent 'loss' of the compound with comparative integration against EtOH is shown in Figure 51. (Quantitative spectra for **45**, **65**, **68** and **72** are available in Appendix 1.7, Figures S202-S209).

Table 7 – Overview of apparent % 'loss' values for **42**, **45**, **65**, **68** and **72** in an EtOH:D₂O (1:19) solution at \approx 5.56 mM derived through quantitative ¹H NMR experiments.

Compound no.	EtOH:D ₂ O (1:19) (%)
42	51
45	50
65	68
68	59
72 ^[a]	10

[a] Previously published results.¹³⁶

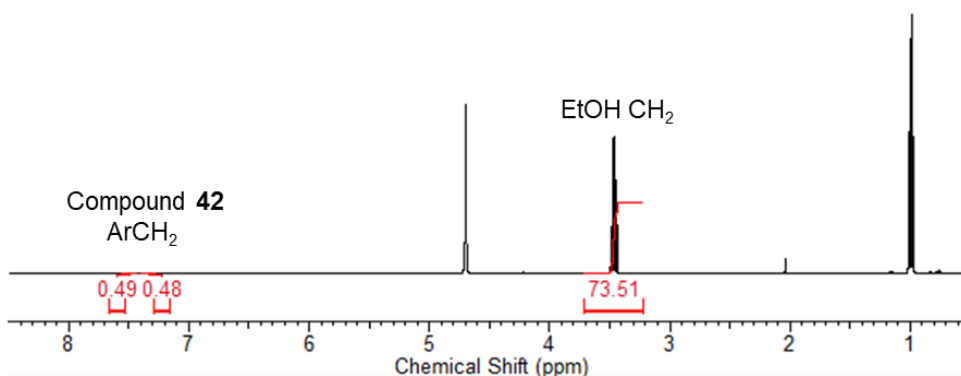


Figure 51 - ¹H NMR spectrum with a delay ($d_1 = 60$ s) of compound **42** (5.80 mM) in D₂O/ 5.0 % EtOH. An apparent 51 % loss of compound was observed upon comparative signal integration.

The results from these ¹H NMR studies indicate that those larger structures observed by the DLS studies (Chapter 2.5.1.) under similar aqueous experimental conditions are significant in number. It is hypothesised that to ensure stabilisation of larger higher-order self-associated aggregates, the solvent environment needs to be hydrophilic as we have observed with EtOH:D₂O (1:19). If the solvent environment is not sufficiently hydrophilic as with DMSO-*d*₆ 0.5 % H₂O, smaller lower-order structures such as (thio)urea-anion dimers are instead stabilised. This was confirmed through the DOSY ¹H NMR studies, where the d_H range of **42**, **45**, **65**, **68** and **72** were shown to be between 1.13 and 1.64 nm in size (Chapter 2.5.3.1).

In summary, quantitative ¹H NMR studies in a solution of DMSO-*d*₆ 0.5 % H₂O with all compounds showed no discernible loss of signal from solution through comparative integration with the internal standard DCM signal.

However, in an aqueous solution of EtOH:D₂O (1:19) at \approx 5.56 mM, **42**, **45**, **65** and **68** all exhibited an apparent 'loss' of the compound of \geq 50 % from the NMR sample through comparative integration with the EtOH signals, with **72** showing a lower 'loss' of 10 %. These apparent 'losses' are attributed to the formation of larger higher-order self-associated aggregates, that are NMR silent.

2.5.3.3 Zeta potential studies

Zeta potential, also termed '*electrokinetic potential*' is a frequently used technique to define the stability of colloid particles or aggregates in solution. Guidelines classifying colloidal dispersion zeta potential values are common in literature, particularly pharmaceutical journals when investigating drug delivery systems.¹⁷⁴ A measurement more positive than +30 mV or more negative than -30 mV is considered stable, a value lower than this suggests aggregate instability and a tendency for the particles to flocculate.¹⁷⁵ However, although zeta potential values provide a good indication of colloid stability, there are occasions, such as liposomes in the cell where a value of between -10 to -40 mV are considered stable,¹⁷⁶ therefore, environmental conditions are an important factor.

To elucidate the stability of the larger higher-order self-associated aggregates observed at 5.56 mM by DLS (2.5.1), present at the CMC (Chapter 2.5.2) and those that became '*NMR silent*' in the quantitative ¹H NMR studies (Chapter 2.5.3.2), zeta potential measurements were obtained for **42-52**, **55-57**, **60**, **61**, **65** and **67-72**. Reproducible measurements could not be produced for solutions **58**, **62** and **64**. It is hypothesised that this is due to the weak HBA nitro groups positioned on the aromatic ring systems of **58** and **62**. Table 8 gives an overview of the results obtained from the zeta potential stability studies for **42-52**, **55-57**, **60**, **61**, **65** and **67-72** in a solution of EtOH:H₂O (1:19) at 5.56 mM.

Table 8 – Zeta potential measurements for compounds **42-52**, **55-57**, **60**, **61**, **65** and **67-72** in a solution of EtOH:H₂O (1:19) at 5.56 mM.

Compound no.	Zeta potential (mV)	Compound no.	Zeta potential (mV)
42	-76	57 ^[a]	-19
43	-78	58	[c]
44	-94	60	-30
45	-92	61	-66
46	-34	62	[c]
47	-38	63	[b]
48	-55	64	[c]
49	-28	65	-37
50	-24	66	[b]
51	-26	67	-23
52	-48	68	-4
53	[b]	69 ^[a]	-96
54	[b]	70 ^[a]	-82
55	-30	71 ^[a]	-79
56	-98	72 ^[a]	-101

[a] Previously published results.¹³⁶ [b] not calculated due to sample insolubility. [c] Could not be accurately determined due to lack of reproducibility.

The zeta potential measurements obtained from solutions containing **49**, **50**, **51**, **57**, **67** and **68** all showed evidence of unstable aggregate formation with zeta potential values < ±30 mV. Compounds **49**, **50** and **51** all contain counter cations within their molecular structure that have been identified by previous polarisability studies, to exhibit low polarisability values (46.91, (PyrH⁺), 46.64 (TMA) and 52.85 (TEA) respectively) (Chapter 2.5.2, Table 5). Therefore, as previously discussed cations PyrH⁺, TMA and TEA are more likely to form ion-pair interactions with the anionic component of the amphiphile, resulting in a weaker self-associated structure. This theory is supported with evidence from these stability experiments where those SSAs that contain PyrH⁺ (**49**), TMA (**50**) and TEA (**51**) were shown to exhibit unstable zeta potential values of -28, -24 and -26 mV respectively.

Upon comparison of the CF₃ substituted urea-sulfonate (**42**) with the urea-carboxylate (**65**) a decrease of stability is observed with zeta potential values going from -76 (**42**) to -37 mV (**65**), these findings correlate with those observations in the CMC experiments (Chapter 2.5.2) and the single crystal data obtained from the solid state studies (Chapter 2.3), where self-associated **65** adopts the less stable trigonal planer geometry (Chapter 2.3, Figure 37).

This same trend is observed for CF₃ substituted thiourea-sulfonate (**45**) which exhibits a stable zeta potential value of -92 mV with analogous thiourea-carboxylate anion (**68**) exhibiting an unstable zeta potential value of -4 mV. A solution of thiourea-sulfonate **57** was shown to contain structures with incipient stability exhibiting a zeta potential value of -19 mV, this instability is hypothesised to be due to the absence of an electron withdrawing functional group on the aromatic ring system. A further example of compound instability is shown with the structural alteration of CF₃ substituted thiourea-sulfonate **45**. The replacement of the sulfonate anion (zeta potential value of -92 mV) with the neutral carboxylic acid functionality as shown in **67**, destabilises the resultant aggregate as evidenced with an unstable zeta potential value of -23 mV.

In summary, elucidation of the stability of those higher-order structures observed at 5.56 mM in the DLS studies; present at the CMC and those that became '*NMR silent*' in the quantitative ¹H NMR studies were conducted through measurement of the zeta potential value under analogous experimental conditions. Aggregate instability (-28, -24 and -26 mV) was observed for solutions containing **49**, **50** and **51**, the destabilisation of these structures is attributed to competitive ion-pair interactions of strongly coordinating cations Na⁺, PyrH⁺ and TMA with the anionic amphiphile, disrupting the self-assembly process this further supports the hypothesis discussed in Chapter 2.5.2. Where the amphiphile is known to adopt a trigonal planer geometry (**65**), a decrease in structure stability is observed of -37 mV, compared to the tetrahedral binding mode adopted by the analogous urea-sulfonate (**42**) which exhibits a zeta potential value of -76 mV.

2.5.3.4 ¹H NMR dilution studies

To quantify the strength of the hydrogen-bonded self-associated complexation events undertaken by the anionic component of **42-58**, **60-62**, **69-72**, the *tert*-butyl ester derivatives of **63**, **66** and carboxylic acids of **64** and **67** a series of ¹H NMR association studies were undertaken. These studies were performed in a DMSO-*d*₆ 0.5 % H₂O solution.

We have previously identified, through the quantitative ^1H NMR experiments, that all the compound is present under these solvent conditions.

Samples of **42-58** and **60-72** were prepared in series, with an aliquot of the most concentrated (≈ 112 mM) undergoing serial dilution. The downfield change in chemical shift with the increasing compound concentration of corresponding HBD N-H resonances of **42-58** and **60-72** was monitored (Figure 52). This process enabled the observation and characterisation of the hydrogen-bonded self-associated complexation events. The data obtained from the ^1H NMR self-association studies performed with **42-44**, **46**, **47**, **50-58** and **64-72** were fitted to a mathematical binding isotherm model using BindFit v0.5.¹⁷⁷ An example of the data obtained for CF_3 substituted **42** is illustrated in Figure 53.

These obtained data were fitted to both the cooperative equal K (CoEK) model, which assumes the first self-association event is different from all subsequent identical self-association events;¹⁷⁸ and the dimerisation/equal K (EK) model where the association constants for all self-associated events are equal,¹⁷⁹ these models allow for elucidation of the corresponding self-association constants. Binding isotherms (CoEK and EK) were first explored by Meijer and co-workers who investigated the effect that temperature and concentration had on the binding strength of self-assembled arrangements, presenting quantitative information about cooperative and isodesmic self-assembly systems.^{180,181}

42

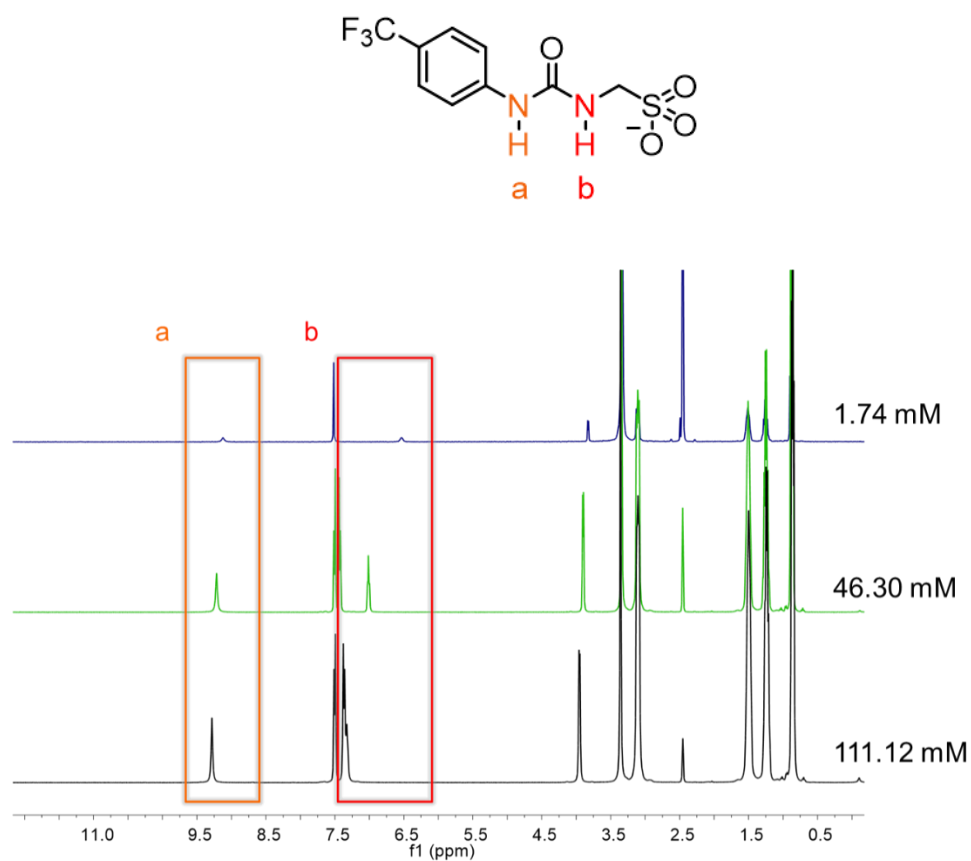


Figure 52 – ^1H NMR stack plot of urea-sulfonate **42** in $\text{DMSO-}d_6$ 0.5 % H_2O , illustrating the change in the chemical shift for the signals corresponding to the N-H residues (a and b) with changing compound concentration.

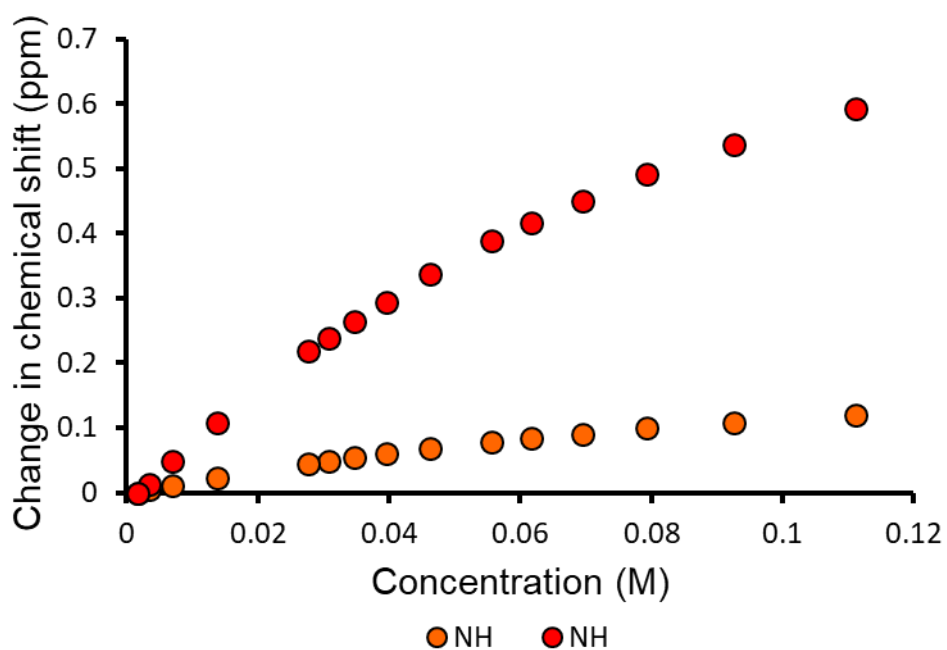


Figure 53 - Graph illustrating the ^1H NMR down-field change in chemical shift of urea N-H resonances with increasing concentration of compound **42** in $\text{DMSO-}d_6$ 0.5 % H_2O (298 K).

The association constants of **42-44**, **46**, **47**, **50-58** and **64-72** calculated by fitting these dilution data to both the CoEK and EK binding isotherms are overviewed in Table 9. The associated errors of these derived values suggest these compounds best fit the (dimerisation) EK binding isotherm (K_{dim}) in preference to the CoEK binding isotherm. This further validates the presence of lower-order anionic dimers in a DMSO- d_6 0.5 % H₂O solution (Chapters 2.5.3.1 and 2.5.3.2).

The association constants of solutions containing **42-44**, **46**, **47**, **50-58**, **64**, **66**, **67** and **69-72** were all calculated to be relatively low with a $K_{\text{dim}} < 15 \text{ M}^{-1}$. When comparing CF₃ substituted urea-sulfonate **42** which has a K_{dim} value of 3 M^{-1} with urea-carboxylate **65** and thiourea-carboxylate **68** ($K_{\text{dim}} 41 \text{ M}^{-1}$ and $K_{\text{dim}} 105 \text{ M}^{-1}$), there is an increase in the association constant of over an order of magnitude, from sulfonate to carboxylate. This increase is hypothesised to be due to the basicity of the anionic species, in addition to the geometry of the self-associated hydrogen bonded complex of (thio)urea-carboxylates **65** and **68**, which form stable dimeric species in a DMSO- d_6 0.5 % H₂O solution. Comparatively, low dimerisation constants were derived for **43** and **46**, $K_{\text{dim}} 0.2 \text{ M}^{-1}$ and $K_{\text{dim}} 0.3 \text{ M}^{-1}$ respectively, these low values are attributed to the potential intramolecular hydrogen bond formation previously identified through the solid state single-crystal XRD studies for **43** (Chapter 2.3, Figure 26). With an extension of the alkyl chain length of the CF₃ substituted urea-sulfonate from $n=1$ (**42**) to $n=3$ (**44**), an increase in dimerisation constant was observed from 5.3 M^{-1} to 6.6 M^{-1} .

Table 9 - Self-association constants (M^{-1}) calculated for **42–44**, **46**, **47**, **50–58** and **63–72** in a DMSO- d_6 0.5 % H_2O solution at 298 K. These constants were obtained from the fitting of 1H NMR dilution data and refined to EK and CoEK models using Bindfit v0.5.¹⁷⁷

No.			42		43		44		46		47	
Model	EK (M^{-1})	K_e	5.3	$\pm 0.6\%$	0.2	$\pm 2.0\%$	6.6	$\pm 2.0\%$	0.3	$\pm 4.2\%$	5.1	$\pm 2.1\%$
		K_{dim}	2.7	$\pm 0.3\%$	0.1	$\pm 1.0\%$	3.3	$\pm 1.0\%$	0.2	$\pm 2.1\%$	2.6	$\pm 1.4\%$
	CoEK (M^{-1})	K_e	13.0	$\pm 0.7\%$	4.0	$\pm 12.0\%$	20.0	$\pm 2.7\%$	1.9	$\pm 51.0\%$	14.1	$\pm 4.4\%$
		K_{dim}	6.5	$\pm 0.4\%$	2.0	$\pm 6.0\%$	10.0	$\pm 1.4\%$	0.9	$\pm 25.5\%$	7.1	$\pm 2.2\%$
		ρ	0.5	$\pm 2.1\%$	0.4	$\pm 20.3\%$	0.3	$\pm 11.6\%$	0.5	$\pm 66.3\%$	0.4	$\pm 14.0\%$
No.			50^[a]		51		52		53		54	
Model	EK (M^{-1})	K_e	13.5	$\pm 0.7\%$	6.3	$\pm 0.9\%$	6.6	$\pm 1.2\%$	4.1	$\pm 0.5\%$	5.0	$\pm 0.9\%$
		K_{dim}	6.7	$\pm 0.3\%$	3.2	$\pm 0.4\%$	3.3	$\pm 0.6\%$	2.1	$\pm 0.3\%$	2.5	$\pm 0.5\%$
	CoEK (M^{-1})	K_e	18.2	$\pm 1.0\%$	12.0	$\pm 2.0\%$	14.9	$\pm 2.1\%$	8.8	$\pm 1.3\%$	9.6	$\pm 2.7\%$
		K_{dim}	9.1	$\pm 0.5\%$	6.0	$\pm 1.0\%$	7.5	$\pm 1.1\%$	4.4	$\pm 0.7\%$	4.8	$\pm 1.3\%$
		ρ	0.8	$\pm 3.4\%$	0.6	$\pm 5.5\%$	0.5	$\pm 6.7\%$	0.6	$\pm 3.0\%$	0.9	$\pm 6.3\%$
No.			55^[a]		56		57^[136]		58^[a]		63	
Model	EK (M^{-1})	K_e	3.6	$\pm 1.5\%$	1.2	$\pm 3.0\%$	0.6	$\pm 3.0\%$	8.9	$\pm 5.1\%$	[c]	
		K_{dim}	1.8	$\pm 0.7\%$	0.6	$\pm 1.5\%$	0.3	$\pm 1.5\%$	4.5	$\pm 2.6\%$		
	CoEK (M^{-1})	K_e	4.6	$\pm 8.3\%$	18.0	$\pm 4.1\%$	13.0	$\pm 5.7\%$	32.2	$\pm 5.1\%$		
		K_{dim}	2.3	$\pm 4.1\%$	9.0	$\pm 2.1\%$	6.5	$\pm 2.9\%$	16.1	$\pm 2.6\%$		
		ρ	0.9	$\pm 13.4\%$	0.1	$\pm 21.5\%$	0.2	$\pm 23.8\%$	0.2	$\pm 37.5\%$		
No.			64		65		66		67		68	
Model	EK (M^{-1})	K_e	< 0.1		82.8	$\pm 2.5\%$	11.9	$\pm 1.5\%$	10.8	$\pm 3.5\%$	209.3	$\pm 1.3\%$
		K_{dim}	< 0.1		41.4	$\pm 1.3\%$	6.0	$\pm 0.8\%$	5.4	$\pm 1.8\%$	104.7	$\pm 0.7\%$
	CoEK (M^{-1})	K_e	7.1	$\pm 18.3\%$	101.8	$\pm 5.1\%$	23.8	$\pm 1.7\%$	4.6	$\pm 20.8\%$	226.1	$\pm 1.4\%$
		K_{dim}	3.6	$\pm 9.2\%$	5.9	$\pm 2.6\%$	11.9	$\pm 0.9\%$	2.3	$\pm 10.4\%$	113.0	$\pm 0.7\%$
		ρ	0.1	$\pm 58.4\%$	2.6	$\pm 37.5\%$	0.5	$\pm 7.5\%$	1.9	$\pm 31.1\%$	1.2	$\pm 3.3\%$
No.			69^{[136]/[b]}		70^[136]		71^[136]		72^[136]			
Model	EK (M^{-1})	K_e	< 0.1		2.9	$\pm 0.5\%$	1.2	$\pm 2.1\%$	5.3	$\pm 0.6\%$		
		K_{dim}	< 0.1		1.5	$\pm 0.2\%$	0.6	$\pm 1.1\%$	2.7	$\pm 0.3\%$		
	CoEK (M^{-1})	K_e	0.5	$\pm 43.1\%$	8.6	$\pm 1.1\%$	6.2	$\pm 8.8\%$	13.0	$\pm 0.7\%$		
		K_{dim}	0.3	$\pm 21.5\%$	4.3	$\pm 0.5\%$	3.1	$\pm 4.4\%$	6.5	$\pm 0.3\%$		
		ρ	0.0	$\pm 47.0\%$	0.5	$\pm 2.5\%$	0.4	$\pm 17.8\%$	0.5	$\pm 2.0\%$		

[a] Possibility of more complex binding events than are being modelled. [b] Data fitted using L-BFGS-B (quasi-Newton) rather than Nelder–Mead (Simplex) methods. [c] Could not be fitted.

A limitation of this 1H NMR association experiment is that both binding isotherms (CoEK and EK) are limited to one component, one-dimensional homogenous aggregation. However, the introduction of the more acidic HBD thiourea functionality to the methyl linked sulfonate amphiphile resulted in the observation of a second slow exchange process for **45** and **60–62**. Figure 54 illustrates both the primary (fast exchange) complex formation (a_1 and b_1) and the secondary (slow exchange) structure formation (a_2 and b_2). The identified secondary structure for **45** was previously hypothesised to be present in the CMC studies (Chapter 2.5.2, Figure 44).

Verification of the presence of this hypothesised hydrogen bond mediated, reversible slow exchange process was verified through variable temperature ^1H NMR studies at 298.15 K and 333.15 K (Appendix 1.1, Figures S5-S6, S23-S24, S26-S27 and S29-S30). To compare the sizes of these fast and slow exchange thiourea-sulfonate species, a further ^1H NMR DOSY experiment was performed with **45**. The results from this study demonstrate that both species were similar in size with a d_{H} of 1.13 nm (Appendix 1.6, Figure S199). For the slow exchange species there is an absence of any comparative downfield chemical shift for the N-H resonances (a_2 and b_2), suggesting that this species is not involved any self-association events, therefore, exists independently. When examining the evidence, it can be concluded that for the slow exchange species to be present in solution the HBD groups are required to be comparatively acidic in nature.

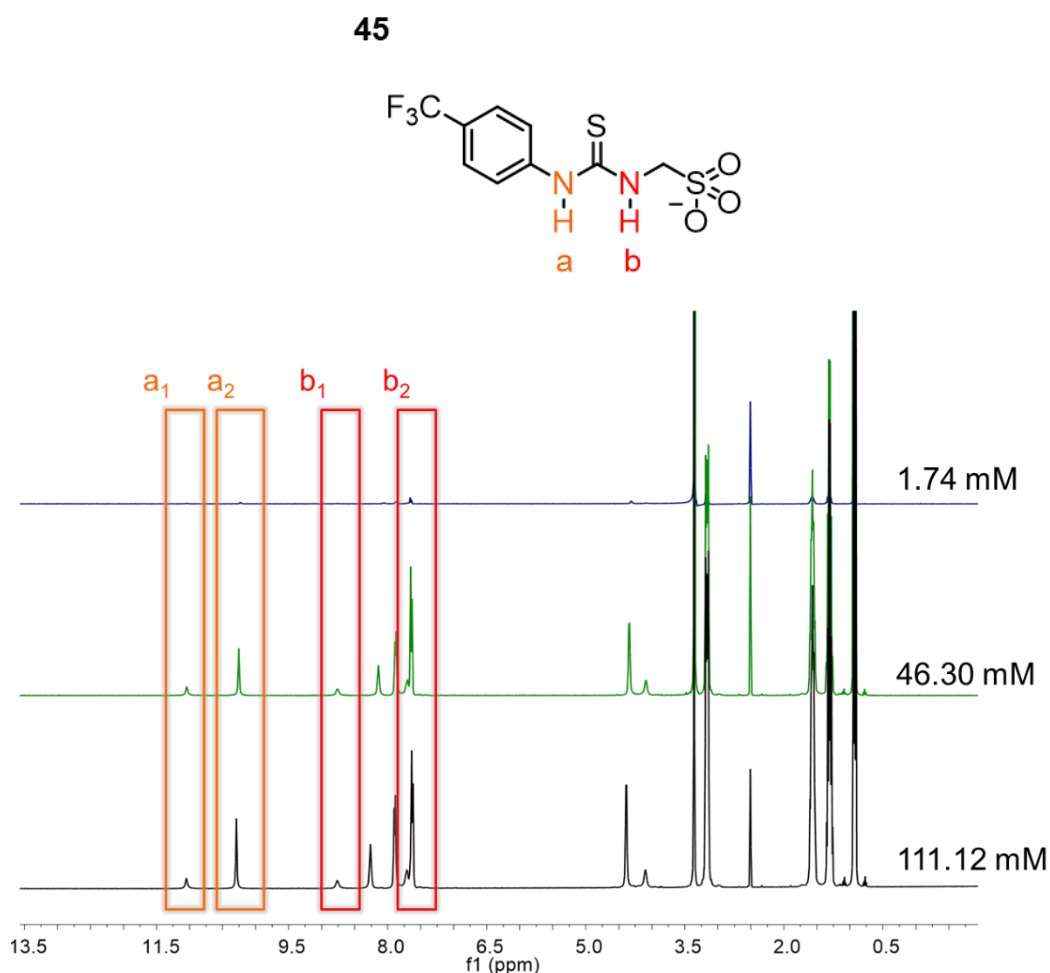


Figure 54 - ^1H NMR stack plot of thiourea-sulfonate **45** in $\text{DMSO-}d_6$ 0.5 % H_2O , illustrating the change in chemical shift for the signals corresponding to the N-H residues (a_1 and b_1) or intramolecular hydrogen bonded/tautomeric species (a_2 and b_2) with changing compound concentration.

Association constants could not be obtained for **48** and **49**, as these compounds contain counter cations Na^+ and PyrH^+ within their molecular structure. It has previously been mentioned in the CMC (Chapter 2.5.2) and zeta potential studies (Chapter 2.5.3.3) that the presence of competitive ion-ion pair effects interferes with any hydrogen-bonded self-association complexation events.

To further explore this theory and in an attempt to establish the extent to which ion-pair effects affect the systems that are discussed within these studies, an additional set of ^1H NMR association experiments were performed with salts **73-80** (Figure 55) in a solution of $\text{DMSO-}d_6$ 0.5 % H_2O .

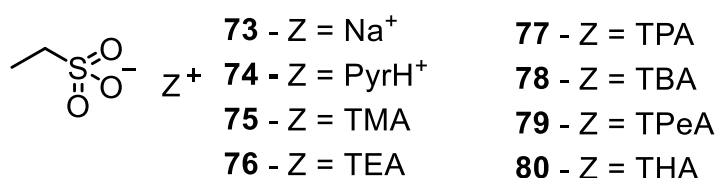


Figure 55 – Chemical structures of those compounds (**73-80**) used to explore ion-pair effects.

As salts **73-80** do not contain an HBD (thio)urea moiety, the downfield change in chemical shift of the ethyl CH_2 resonance was monitored at concentrations of 55.56 mM, 5.56 mM and 0.56 mM, this method allows for any presence of ion-ion interactions to be identified. As shown in Figure 56, counter cations TEA (**76**), TPA (**77**), TBA (**78**), TPeA (**79**) and THA (**80**) show little evidence of sulfonate-cation coordination as there is only a small downfield change in chemical shift of the ethyl CH_2 resonance. However, there is clear evidence of ion-pair effects with counter cations Na^+ and PyrH^+ (**73** and **74**) which at 55.56 mM exhibit chemical shifts of 0.14 and 0.08 ppm respectively. There is also arguable evidence of ion-pair effects for the TMA counter cation (**75**) where a chemical shift of 0.049 ppm was determined.

The strength of these ionic interactions between Na^+ (**73**), PyrH^+ (**74**) and TMA (**75**) with the sulfonate moiety was then investigated through a series of ^1H NMR titration studies with **78** acting as the host and PyrH^+ or TMA hexafluorophosphate salts supplied as guest species. These data were then fitted to a 1:1 binding isotherm where association constants $\approx 10 \text{ m}^{-1}$ were derived.

As a result of this investigation, the binding constant for **50** should be treated with caution due to suspected sulfonate-TMA coordination. The Na⁺ hexafluorophosphate was insoluble in the experiment solvent conditions, therefore, association constants for this salt could not be obtained by this method. The results from these ¹H NMR association studies clarify the reasons as to why ‘weakly coordinating’ TBA is the cation of choice within the field of anion coordination chemistry for establishing HBD receptor:anion complexation strength.

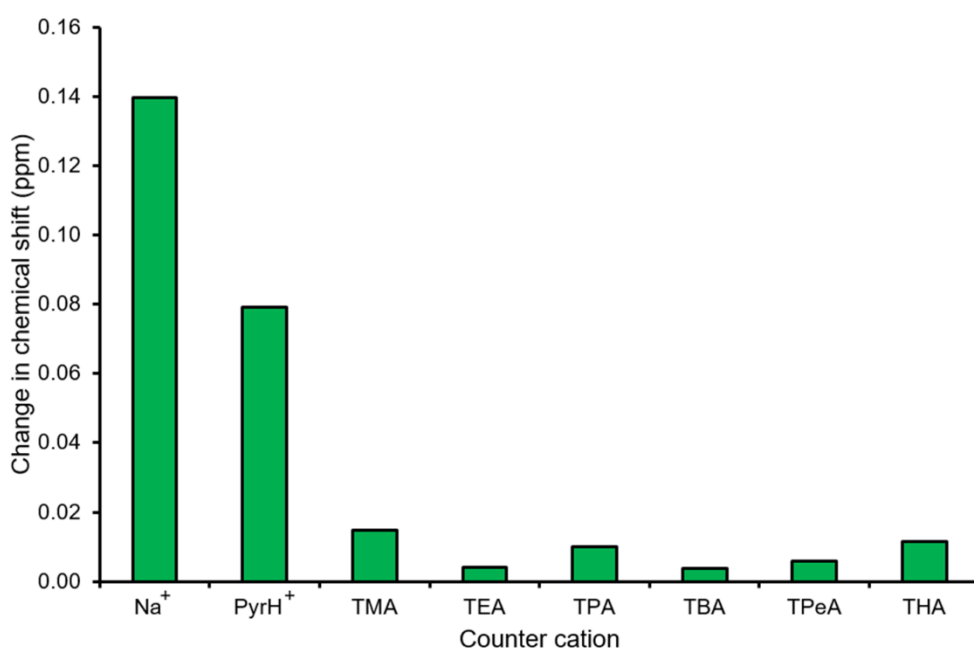


Figure 56 - Change in chemical shift observed for those ¹H NMR signals corresponding to the ethyl sulfonate CH₂ of compounds **73–80** in a DMSO-*d*₆ 0.5 % H₂O mixture at 55.56 mM.

In summary, to quantify the strength of the hydrogen bonded self-associated complexation events undertaken by the anionic component of an SSA, a series of ¹H NMR dilution experiments were performed. Upon evaluation of the errors relating to the derived association constants, it was concluded that all compounds best fit to the EK binding isotherm. The results from this study show **42-44, 46, 47, 50-58, 64, 66, 67** and **69-72** produce a value that is indicative of lower-order anionic dimeric formation ($K_{\text{dim}} < 15 \text{ M}^{-1}$). These observations agree with the observations of the previously discussed ¹H NMR DOSY studies (Chapter 2.5.3.1).

When comparing the CF₃ substituted urea-sulfonate (**42**) with the (thio)urea-carboxylates (**65** and **68**), an increase in dimerisation strength was observed, this was hypothesised to be due to the increase in basicity from sulfonate to carboxylate, in addition to the different binding modes, with the carboxylate preferentially adopting the trigonal planer geometry as observed in Chapter 2.3 Figure 37.

2.6 Low level *in silico* modelling

Electrostatic potential analyses are essential theoretical tools for eliciting non covalent interactions.¹⁸² In 2004, Hunter showed that low level theoretically derived electrostatic potential maps, using energy minimised semi-empirical AM1 modelling methods produced E_{\max} and E_{\min} surface values that correlate well with experimentally derived data.⁵⁸ Where E_{\max} represents the principle HBD group and E_{\min} represents the principle HBA group. Sathyamurthy and co-workers investigated the concept of intramolecular interactions in the form of hydrogen bonding, using the topological properties of electron density.¹⁸³ The results from their studies demonstrated that the electron density at the hydrogen bond critical point increases linearly with increasing stabilisation energy, from weak to strong hydrogen bonds.¹⁸³ These theoretical systems have also been used successfully for predicting the sites and directionality of hydrogen bonds in complexes containing HF, H₂O and NH₃.¹⁸⁴

It has been discussed within this chapter that hydrogen bonded complex strength increases linearly with increased acidity of the HBD groups providing no other factors apply (Chapter 2.5.3.4). Low-level theoretically derived electrostatic potential maps using Spartan '16 software were derived from the geometry optimised anionic/*tert*-butyl and carboxylic acid components of compounds **42-72** to enable elucidation of the more favourable HBD and HBA sites. It is hypothesised that the data retrieved from these computational studies would correlate with experimentally derived dimerisation constants and CMC values, as previously shown in Hiscock and co-workers amphiphile self-association investigations.¹³⁶ For these studies, the AM1 modelling methods were substituted for PM6 modelling methods in line with work conducted by Stewart.¹⁸⁵

The results from these studies demonstrate that the calculated E_{\max} and E_{\min} values from geometry optimised, energy minimised structures of **42-72** correlate with the principle HBD and HBA functionalities within the molecular structure. These values are overviewed in Table 10.

Table 10 - E_{\max} and E_{\min} values (kJ mol⁻¹) calculated for **42-72** using semi-empirical PM6 modelling methods with Spartan '16 software. No. = compound number.

No.	E_{\max} (kJ/mol)	E_{\min} (kJ/mol)	No.	E_{\max} (kJ/mol)	E_{\min} (kJ/mol)	No.	E_{\max} (kJ/mol)	E_{\min} (kJ/mol)
42, 48-54	-34.28	-706.12	57 ^[a]	-69.10	-728.74	65	-41.02	-736.14
43	-71.20	-708.55	58	-16.50	-692.64	66	244.14	-217.03
44	-54.43	-760.64	59	-0.595	-716.56	67	260.70	-202.84
45	-17.83	-687.15	60	-45.05	-716.01	68	-28.66	-716.37
46	-61.68	-680.84	61	-52.82	-710.29	69 ^[a]	-65.85	-720.79
47	-75.64	-757.75	62	2.417	-673.04	70 ^[a]	-60.12	-714.30
55	-12.26	-727.63	63	232.18	-248.94	71 ^[a]	-66.07	-723.07
56	-48.92	-730.37	64	249.96	-232.38	72 ^[a]	-31.97	-703.73

[a] Previously published results.¹³⁶

The computational methods applied within this study, do not only allow for the observation of principle HBD and HBA sites to be identified but the optimised geometries show the preference of intramolecular bond formation. An example is shown in Figure 57 with CF₃ substituted urea-anionic monomeric units of **42-44**. This Figure illustrates linear structures for **42** ($n=1$) and **44** ($n=3$). However for **43**, which contains an ethyl linker ($n=2$), the presence of an intramolecular bond is observed. This trend is also observed for the analogous thiourea-anionic monomers (**45-47**) (Appendix 1.9, Figures S285-S287).

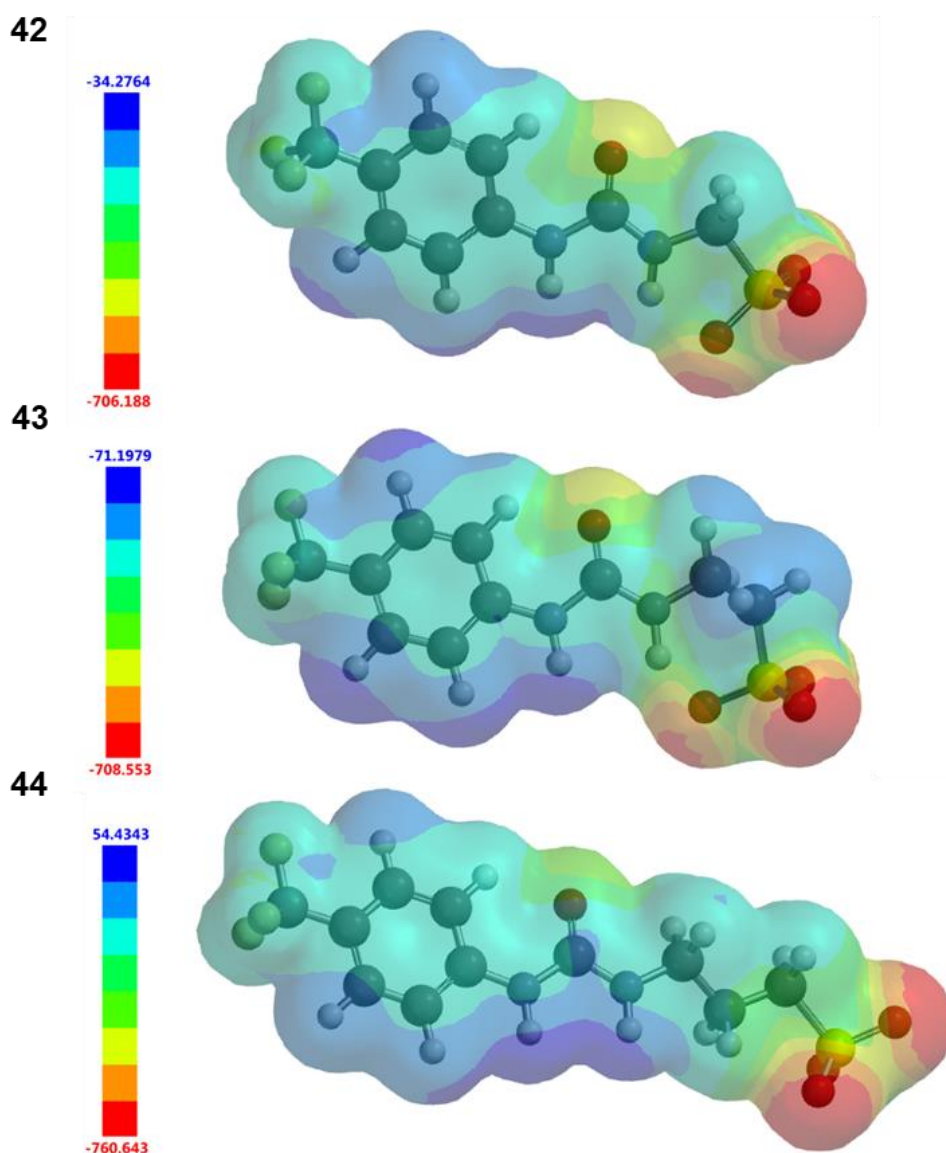


Figure 57 - Electrostatic potential maps calculated for linear, **42-44** using energy minimised semi-empirical PM6 modelling methods. E_{\max} and E_{\min} values depicted in the Figure legend are given in kJ mol^{-1} .

As previously discussed, preliminary investigations by Hiscock and co-workers showed a correlation between theoretically derived E_{\max} and E_{\min} values for **57** and **69-72** and their corresponding dimerisation constants.¹³⁶ This revelation does not come as a surprise because, as discussed within this chapter, the acidity and basicity of the principle HBD and HBA functionalities are a major contributing factor to the strength of self-associated hydrogen bonded complex formation. To further explore this principle, Hiscock and co-workers work was expanded on, to include the additional 26 compounds investigated within this chapter.

The compounds that dimerisation constants could be calculated for (**42-44**, **45**, **46**, **50-58** and **69-72**) (Chapter 2.5.3.4, Table 9), were plotted against the derived E_{\max} and E_{\min} values as shown in Figure 58. Data for **63-68** were not included in this study due to differentiation in potential binding mode. As shown in Figure 58, there is evidence of some correlation between E_{\max} and dimerisation constant. This observation indicates that with increasing HBD acidity (E_{\max}) there is a correlation with increasing values of dimerisation constants. Those data points outlined in black represent compounds with the same anionic substituents with differing counter cations. A relationship between E_{\min} and dimerisation constant, however, was not observed for compounds explored within this study.

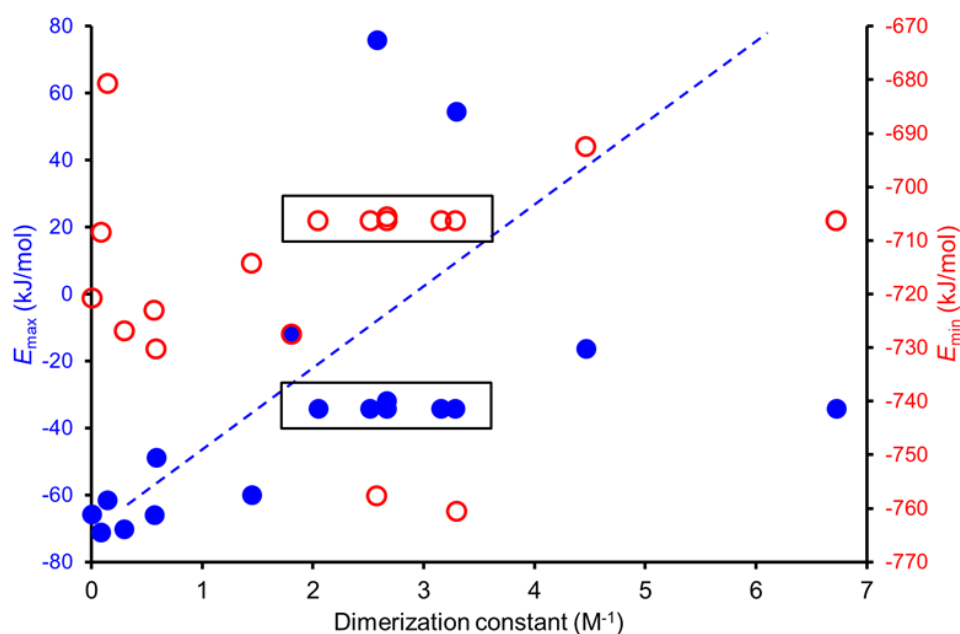


Figure 58 – Comparison of E_{\max} and E_{\min} values obtained for the (thio)urea containing moieties of **42-44**, **45**, **46**, **50-58** and **69-72** with dimerisation constants. The black boxes represent compounds with the same anionic substituent but with different cations.

The comparative effects of both HBD acidity and HBA basicity were then investigated, where the sum of E_{\max} and E_{\min} ($E_{\max}+E_{\min}$) was plotted against dimerisation constant. These data exhibit a linear correlation with the exclusion of five outliers (**43**, **46**, **47**, **50** and **55**) as shown in Figure 59. CF_3 substituted (thio)urea-sulfonate **43** and **46** are outliers, this can be explained by the presence of a secondary anionic monomer, formed through an intramolecular bond.

A limitation of this model is, therefore, the requirement for a one-component, one-dimensional homogeneous solution. The data for CF_3 substituted thiourea-sulfonate **47** were also excluded from the fitting process due to the probable adoption of a slightly twisted geometry due to the thiourea substituent in comparison to the planar urea substituent, Chapter 2.3, Figure 29. TMA containing **50** has extensively been discussed concerning potential competitive ion-pair effects, therefore this may be an explanation for **50** being an outlier. Finally, the additional HBD/HBA amino functionality of **55** results in the structure which has the potential to form two different self-associated binding modes and as a consequence does not fit the trend.

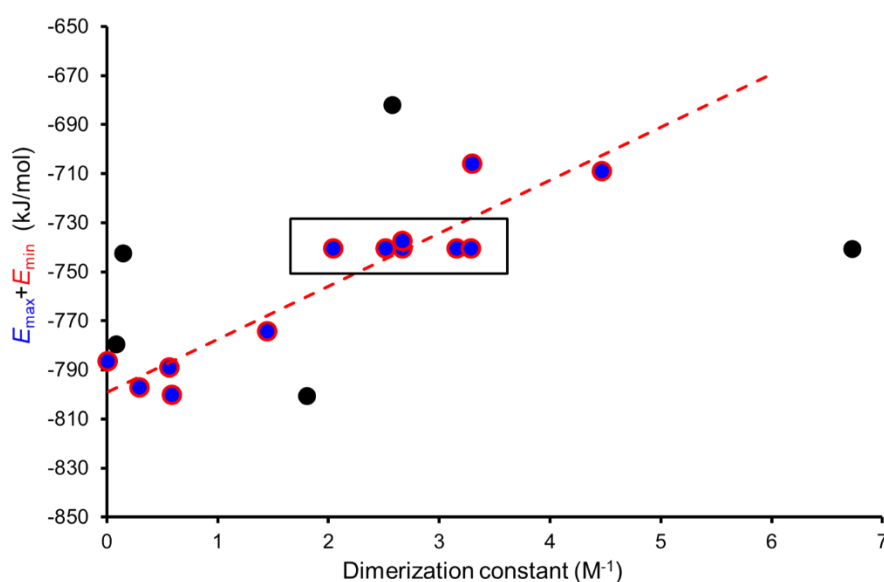


Figure 59 - Comparison of $E_{\text{max}} + E_{\text{min}}$ values obtained for the (thio)urea containing moieties of **42-44**, **45**, **46**, **50-58** and **69-72** with dimerisation constants. Those data points excluded from this fitting process are shown in black. The black box represents compounds with the same anionic substituent but with different cations.

In summary, it was shown that the sum of E_{max} and E_{min} was found to correlate well with the experimentally derived dimerisation constants. The results from the comparative studies illustrated in Figure 59 led to the conclusion that it may be possible to predict the strength of a self-associated complex (considering the equal K model). This can be carried out using simple low-level computation modelling methods, providing the hydrogen bonded mode and competitive ion-pair effects within a system are the same.

2.7 Next-generation prediction models

Hiscock and co-workers previously hypothesised that the CMC is dependent upon the dimerisation process. In their studies, a correlation of comparative increase in strength of the hydrogen bonded dimer formed in a DMSO- d_6 0.5 % H₂O solution with a decrease in CMC value obtained in EtOH:H₂O (1:19) was observed. It was proposed that it may be possible to predict the surfactant properties of their class of amphiphile (**57** and **69-72**), through measuring the dimerisation constant and/or simple computational techniques.¹³⁶ Extending on these preliminary studies, an additional 26 compounds were proposed to be investigated in line with Hiscock and co-workers experimental methods. As with the E_{max} , E_{min} and dimerisation constant model previously discussed in Chapter 2.6, the same limitations apply where the compounds must exhibit the same binding modes, which must not be influenced by ion-pair effects. Additionally, these compounds must not exhibit intramolecular hydrogen bond formation. A further limitation of this model is the requirement of the compounds to contain the same counter cation within their molecular structure this is because, in an aqueous solvent system, the competitive hydrophobicity of a cation will have a substantial effect on the self-assembly process. This limits the number of compounds that can be taken forward for this study, out of the proposed 26 only three meet the criteria (**42**, **56** and **58**), with the initial five from Hiscock and co-workers preliminary studies (**57** and **69-72**) making eight in total as illustrated in Figure 60.

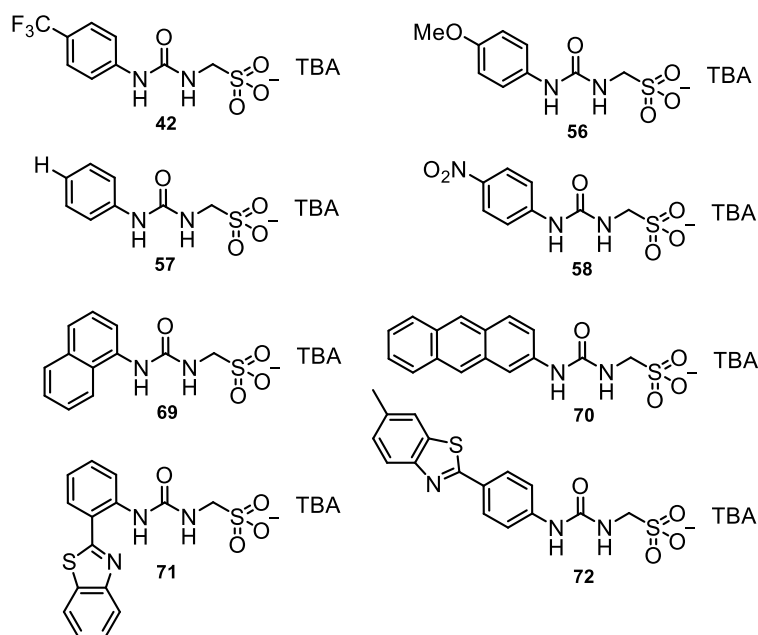


Figure 60 - Chemical structures of the 8 compounds taken forward for the next-generation prediction model study.

Using a variety of complementary techniques the molecular self-association events of **42**, **56-58** and **69-72** have been independently explored in two different solvent systems DMSO- d_6 0.5 % and EtOH:H₂O (1:19). The change in solvent environment, from DMSO to the aqueous solvent system, and the change in molecular arrangement from dimer to extended aggregate, will also be driven by the hydrophobic nature of the self-associated, hydrogen bonded complex. To gain an understanding of these effects, the theoretical LogP values for the aromatic R-groups were calculated as shown in Chapter 2.5.2, Figure 47. The calculated LogP values were then employed to derive the CMC weighting values used within this correlation study, where LogP weighted CMC = CMC (mM) x LogP of the aromatic R-group.

The amphiphiles that qualified for this study (**42**, **56-58** and **69-72**) were then split into two subgroups. Subgroup one consists of those amphiphiles that contain a single aromatic ring (**42**, **56-58**) shown in Figure 61, blue. Subgroup two (Figure 61, yellow) contains amphiphiles with > 1 aromatic ring system (**69-72**). This separation is due to different factors affecting the self-associated hydrogen bonding process, according to the number of aromatic ring systems within their molecular structure.

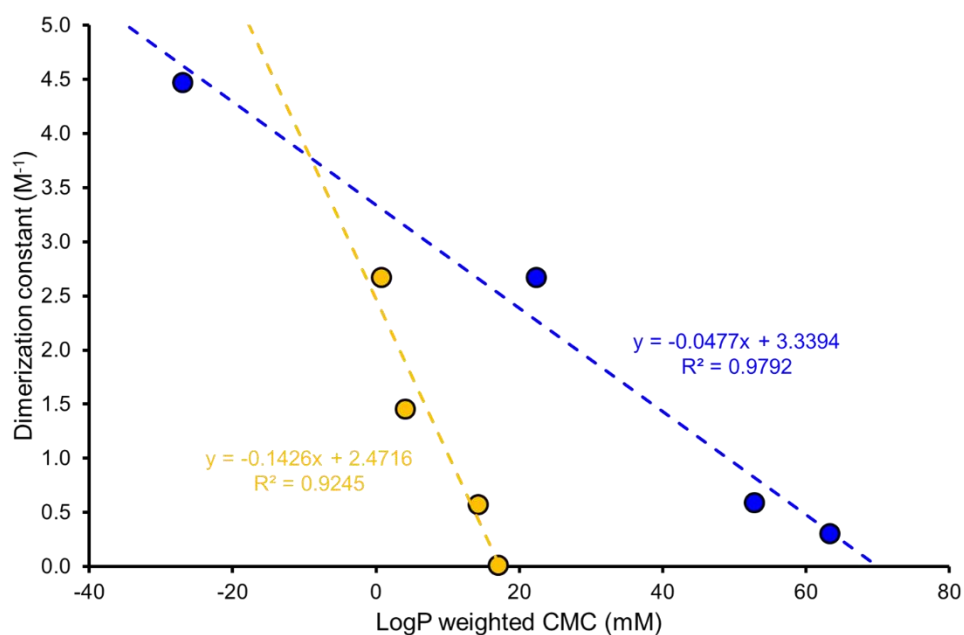


Figure 61 – Comparison of experimentally derived dimerisation constant values for **42, 56-58** (blue) and **69-72** (yellow) with LogP weighted CMC (mM).

The dimerisation constants calculated from a DMSO-*d*₆ 0.5 % H₂O solution containing **42, 56-58** and **69-72** (Chapter 2.5.3.4, Table 9) were plotted against the LogP weighted CMC obtained in an aqueous solution of EtOH:H₂O (1:19) (Chapter 2.5.2, Table 4). This produced two linear correlations, indicating that as hypothesised, both hydrogen bonded dimerisation strength and hydrophobicity of the anionic component are key influences towards CMC. These linear correlations establish that the higher the dimerisation constant and LogP value of the aromatic substituents within the molecular structure of **42, 56-58** and **69-72** the lower the CMC.

As proposed in Chapter 2.6 it may be possible to computationally estimate dimerisation constants using theoretically derived E_{\max} and E_{\min} values. With these data and the computationally calculated LogP values, it is hypothesised that for hydrogen bonded systems, it is potentially possible to predict CMC values using easily accessible, low-level computational methods.

In summary, the results from this study demonstrated two linear correlation graphs, one for each subgroup.

The relationship between the dimerisation constants and LogP weighted CMCs values for **42**, **56-58** and **69-72** supported the earlier hypothesis that hydrogen bonded dimerisation strength and hydrophobicity of the anionic component are both key influences towards CMC (Chapter 2.5.2). This prediction model, when combined with the model in Chapter 2.6, Figure 59 has proven that it is potentially possible to predict CMC using theoretically derived data, from simple, easily accessible low-level computational modelling systems.

2.8 Chapter 2: Summary

This chapter has focussed on understanding and predicting the self-associated properties of 30 structurally related compounds allowing for the elucidation of structure-property relationships governing the self-associated abilities for this class of SSA. It has been established that the physical state and the competitive solvent system in which these compounds are dissolved in plays an integral role in their self-association properties, and with use of low-level computational modelling methods it may be possible to predict dimerisation constants and CMC values.

Building on Hiscock and co-workers preliminary work into the investigation of the self-association events in the solid state,^{135,136} it was identified that compounds containing covalently linked HBD-anionic functionalities and a weakly coordinating counter cation within their molecular structure show a preference towards the formation of HBD:anion complexes.

With an extension of the alkyl chain length, from methyl (**42**) to ethyl (**43**) evidence of cyclisation was observed, this was no longer favourable with a further extension to the propyl linker (**44**). Furthermore, it was observed that the anionic substituent plays an integral role in the geometry of the binding mode with compounds containing the carboxylate moiety (**65**) favouring end-on urea-anion, trigonal planer geometry whilst compounds containing the sulfonate groups favour a tetrahedral geometry forming through the creation of four urea-anion hydrogen bonds.

In the gas phase, dimeric species were observed to be present for all compounds investigated that did not exhibit an intramolecular bond within its molecular structure (Table 11). Moving into the solution state, complimentary DLS and zeta potential experiments have allowed for the presence and stability of both lower-order dimeric species and higher-order hydrogen bonded self-associated aggregates (d_H 100-550 nm) to be investigated in two different solvent environments EtOH:H₂O (1:19) and DMSO-*d*₆ 0.5 % H₂O. The presence of these self-associated structures was verified through quantitative ¹H NMR (Chapter 2.5.3.2) and ¹H DOSY NMR (Chapter 2.5.3.1) experiments, using the latter, it was also possible to determine the d_H of the dimeric species to be < 1.7 nm as overviewed in Table 11.

The CMC and corresponding surfactant properties were investigated, here it was observed that increasing HBD acidity resulted in decreasing CMC values. Furthermore, the presence of strongly coordinating cations Na⁺, PyrH⁺ and TMA was shown to destabilise resultant aggregate formations, resulting in high CMC values. The CMC values for those compounds with a urea functionality, which were shown to form extended aggregates > 100 nm in the DLS studies at 5.56 mM were shown to correlate with the calculated cation polarisability and LogP values. Where CMC decreased with increasing polarisability and LogP.

To quantify the strength of the hydrogen-bonded self-associated complexation events undertaken by the anionic component of a compound, a series of ¹H NMR dilution experiments were performed. The results from this study show that the majority of compounds produced a value that was indicative of lower-order anionic dimeric formation ($K_{dim} < 15 \text{ M}^{-1}$). Further validating the observations in the previously discussed DOSY ¹H NMR studies (Chapter 2.5.3.1).

When comparing the CF₃ substituted urea-sulfonate (**42**) with the (thio)urea-carboxylates (**65** and **68**), an increase in dimerisation strength was observed, this was hypothesised to be due to the increase in basicity from sulfonate to carboxylate, in addition to the different binding modes, with the carboxylate preferentially adopting the trigonal planer geometry as observed in Chapter 2.3, Figure 37.

Association constants could not be obtained for compounds that are hypothesised to be affected by competitive ion pair effects such as **48** and **49**, which contain counter cations Na⁺ and PyrH⁺ within their molecular structure. Evidence of the presence and strength of these ion-pair interactions were confirmed by a second set of ¹H NMR dilution studies performed using **73-80** and, titration studies with **78** acting as the host and PyrH⁺ or TMA hexafluorophosphate salts supplied as guest species.

Simple low-level computational modelling was used to produce electrostatic potential maps, where E_{\max} and E_{\min} values were derived (Table 11). The sum of these derived E_{\max} and E_{\min} values was found to correlate well with the experimentally derived dimerisation constants where the same hydrogen bonding mode was adopted and ion-pair effects were minimal. The results from the comparative studies led to the conclusion that it may be possible to predict the strength of a self-associated complex (considering the equal K model). This can be carried out using simple low-level computation modelling methods.

For those amphiphiles that fitted the criteria of the same counter cation and the adoption of identical binding modes, both the dimerisation constant and CMC values could be compared. In this study, two linear correlations were identified. The relationship between the dimerisation constants and LogP weighted CMCs values for **42**, **56-58** and **69-72** supported the earlier hypothesis that hydrogen bonded dimerisation strength and hydrophobicity of the anionic component are both key influences towards CMC.

The prediction models derived in this chapter have proven that it is potentially possible to predict dimerisation constants and CMC using theoretically derived data, from simple, easily accessible low-level computational modelling systems.

Table 11 – Overall summary of physicochemical data obtained for compounds **42-72** in the solid state, gas phase and solution state in addition to computationally derived E_{\max} and E_{\min} values.

No.	Solid State	Gas Phase	Solution State							Computational			
	XRD	Mass spec	DLS	Zeta potential	¹ H NMR			Tensiometry		Electrostatic potential maps			
	Binding mode	Dimeric species Present/absent	5.56 mM Peak maxima (nm)	(mV)	quantitative D ₂ O (%)	DOSY DMSO- <i>d</i> ₆ (%)	Dilution <i>d</i> _H (nm)	EK model <i>K</i> _{dim} (M ⁻¹)	error	CMC (mM)	Surface tension (mN/m)	<i>E</i> _{max}	<i>E</i> _{min}
42	Dimer ¹³⁵	Present	164	-76	51	0	1.15	2.7	± 0.3 %	10.39	37.45	-34.28	-706.12
43	Dimer	Present	459	-78		[e]		0.1	± 1.0 %	10.70	38.49	-71.20	-708.55
44	Dimer	Present	122	-94		[e]		3.3	± 1.0 %	8.85	36.78	-54.43	-760.64
45	Dimer ¹³⁵	Present	342	-92	50	0	1.13		[f]	24.14	34.35	-17.83	-687.15
46	Tape	Present	142	-34		[e]		0.2	± 2.1 %	6.12	42.24	-61.68	-680.84
47	Dimer	Present	122	-38		[e]		2.6	± 1.4 %	5.61	33.59	-75.64	-757.75
48	Tape ¹³⁵	Present	531	-55		[e]			[f]	96.35	36.65	-34.28	-706.12
49	Tape ¹³⁵	Present	220	-28		[e]			[f]	198.42	36.16	-34.28	-706.12
50	Tape	Present	164	-24		[e]		6.7	± 0.3 %	209.98	41.78	-34.28	-706.12
51	[a]	Present	190	-26		[e]		3.2	± 0.4 %	103.13	33.75	-34.28	-706.12
52	[a]	Present	190	-48		[e]		3.3	± 0.6 %	34.57	36.09	-34.28	-706.12
53	[a]	Present		[c]		[e]		2.1	± 0.3 %		[c]	-34.28	-706.12
54	[a]	Present		[c]		[e]		2.5	± 0.5 %		[c]	-34.28	-706.12
55	Dimer	Present	342	-30		[e]		1.8 ^[f]	± 0.7 %		[c]	-12.26	-727.63
56	Dimer ¹³⁵	Present	190	-98		[e]		0.6	± 1.5 %	92.67	46.14	-48.92	-730.37
57	Tape ¹³⁵	Present ¹³⁶	220 ¹³⁶	-19 ¹³⁶		[e]		0.3 ¹³⁶	± 1.5 %	40.89 ¹³⁶	47.90 ¹³⁶	-69.10 ¹³⁶	-728.74 ¹³⁶
58	Dimer ¹³⁵	Present	91	[d]		[e]		4.5 ^[f]	± 2.6 %	30.29	44.94	-16.50	-692.64
60	[a]	Present	220	-30		[e]			[f]	65.83	45.05	-45.05	-716.01
61	[a]	Present	190	-66		[e]			[f]	74.59	42.85	-52.82	-710.29
62	Dimer	Present	106	[d]		[e]			[f]		[c]	2.417	-673.04
63	[b]	Absent		[c]		[e]			[g]		[c]	232.18	-248.94
64	[a]	Present	396	[d]		[e]		< 0.1			[c]	249.96	-232.38
65	Tape	Present	220	-37	68	0	1.28	41.4	± 1.3 %	11.21	39.33	-41.02	-736.14
66	[a]	Absent		[c]		[e]		6.0	± 0.8 %		[c]	244.14	-217.03
67	[a]	Present	459	-23		[e]		5.4	± 1.8 %		[c]	260.70	-202.84
68	[a]	Present	164	-4	59	0	1.42	104.7	± 0.7 %		[c]	-28.66	-716.37
69	Dimer ¹³⁶	Present ¹³⁶	164 ¹³⁶	-96 ¹³⁶		[e]		< 0.1 ¹³⁶		10.67 ¹³⁶	46.67 ¹³⁶	-65.85 ¹³⁶	-720.79 ¹³⁶
70	[a]	Present ¹³⁶	220 ¹³⁶	-82 ¹³⁶		[e]		1.5 ¹³⁶	± 0.2 %	2.52 ¹³⁶	43.15 ¹³⁶	-60.12 ¹³⁶	-714.30 ¹³⁶
71	Dimer ¹³⁶	Absent ¹³⁶	295 ¹³⁶	-79 ¹³⁶		[e]		0.6 ¹³⁶	± 1.1 %	9.54 ¹³⁶	48.71 ¹³⁶	-66.07 ¹³⁶	-723.07 ¹³⁶
72	Dimer ¹³⁶	Present ¹³⁶	122 ¹³⁶	-101 ¹³⁶	10 ¹³⁶	0	1.64 ¹³⁶	2.7 ¹³⁶	± 0.3 %	0.50 ¹³⁶	46.50 ¹³⁶	-31.97 ¹³⁶	-703.73 ¹³⁶

[a] Crystals not obtained. [b] Form's hydrogen bonded complex with a water molecule. [c] not calculated due to sample solubility. [d] Could not be accurately determined due to lack of reproducibility. [e] Study not conducted.

[f] Possibility of more complex binding events than are being modelled. [g] Could not be fitted.

2.9 Chapter 2: Conclusion

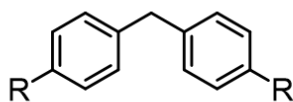
Within this chapter, preliminary results have been expanded on, from the initial five structurally related compounds designed, synthesised and investigated by Hiscock and co-workers.¹³⁶ This chapter introduced a further 39 structurally related compounds. This enabled for the elucidation of structure-property relationships governing the self-associative properties for this class of compound. Allowing for focus to be on understanding and predicting the self-associative properties of amphiphilic (thio)urea-anion monomers. Thus resulting in the extension on the original hypotheses,¹³⁶ the improvement of existing predictive models and the determination of any associated limitations.

2.10 Future work

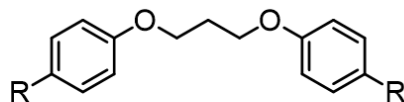
Future work will continue into what factors caused the conversion of the CF₃ functional group to a carboxylic acid group during the crystallisation process of **65** as discussed in Chapter 2.3. Additionally, the preferential binding modes adopted by the trigonal planer carboxylate and the tetrahedral sulfonate moieties will be further explored.

As a further extension to the previous work, the focus will be on the adaption of this class of compounds where **82-85** will be synthesised (Figure 62). As shown through previous experiments, in a solution of DMSO-*d*₆ 0.5 % H₂O the compounds discussed within this chapter show a preference for forming small lower-order structures, hypothesised to be indicative of dimeric species. This proposed new group of symmetrical molecules will be synthesised with the purpose of investigating whether these systems can be pre-organised, the physicochemical properties will then be identified and compared with those compounds already investigated.

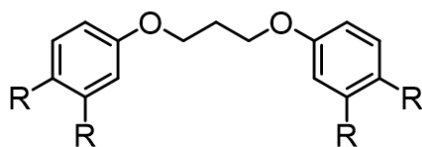
82



83



84



85

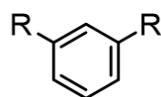


Figure 62 – Proposed structures for a new group of symmetrical amphiphiles

Chapter 3

3.1 Introduction

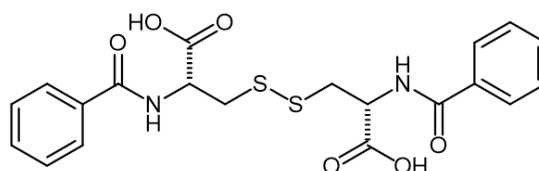
Previous research investigating self-assembly initially centred on bio-macromolecules such as nucleic acids, proteins and their synthetically derived counterparts, due to their significant roles in nature.¹⁸⁶ The self-assembly of small molecules in aqueous or organic solvent conditions has also been found to be influential for many diverse scientific areas. Ranging from fundamental science to practical applications, where accurate and highly programmed self-assembly can produce supramolecular architectures with distinct physical features.¹⁸⁷ This self-assembly process occurs when individual components within a system organise through non-covalent interactions into ordered and/or functional structures or patterns. One type of common self-assembly process is the formation of a supramolecular gel.

Supramolecular gels are a class of soft material, formed through non-covalent interactions (such as hydrogen bonds; π - π stacking; van der Waals forces; dipole-dipole; or charge transfer) between the monomeric units of low molecular weight gelators (LMWG).¹³⁹ These non-covalent interactions enable LMWG to reversibly self-assemble into unidirectional high aspect ratio fibres that constitute a solid-like network. 'Solid-like' in this instance, refers to a soft and resilient material which consists of at least two components, one of which is a liquid.¹⁸⁸ Supramolecular gels can be broadly classified into three categories, based on the immobilised solution components within the three-dimensional gel matrix: i) organogels contain both polar or non-polar organic solvents,^{189,190} ii) ionogels contain ionic liquids¹⁹¹ and iii) hydrogels contain water.^{192–197}

In 1892 Brezinger noted the first LMW hydrogelator as dibenzoyl-L-cystine (Figure 63, **86**).¹⁹⁸ However, the gelation properties were not studied until 1921 by Gortner and Hoffmann, who discovered that **86** was able to form a gelled material at 0.1 % concentration.¹⁹⁹ Prepared by dissolving **86** in 5 mL of hot ethanol and further diluted to 100 mL with water, equating to approximately 12,000:1 (water molecules:gelator molecule).

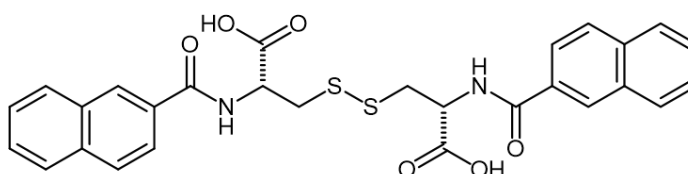
The resultant hydrogel was reported to be rigid enough to retain its shape for > 1 minute when undergoing an inversion test.¹⁹⁹ However, the Hoffmann gel characteristics remained unexplored by modern technology until 1978, when Menger and co-workers applied ¹³C NMR techniques to the system and were able to distinguish two distinct molecular types (monomeric and extended aggregate). This was possible through the observation of the ¹³C NMR spin-lattice relaxation times (T_1). It was shown that in a DMSO-H₂O solvent system the monomeric species self-associated akin to that of surfactants, with minimum effect to the T_1 values and the peak resonances. However, when the dibenzoylcysteine acted as a gelator, in the presence of a greater percentage of H₂O (20 %), the T_1 was dramatically affected, resulting in broad resonances.²⁰⁰ These dibenzoylcysteine gels were further examined in 1995 by X-ray crystallography.²⁰¹

86

Figure 63 – First reported LMWG dibenzoyl-L-cysteine.¹⁹⁸

Menger and co-workers went on to develop a further 14 L-cysteine derivatives through step-wise modifications to **86**. The addition of more electron-withdrawing aromatic ring systems as shown in Figure 64 (**87**), resulted in a hydrogelator capable of self-assembling and rigidifying an aqueous solution at 0.25 mM (0.01 wt %) in < 30 seconds.²⁰² In a report produced in 2010 this naphthalene L-cysteine derivative held the record for lowest gelator concentration and fastest gelation rate.²⁰³

87

Figure 64 – Naphthalene L-cysteine derivative synthesised by Menger and co-workers.²⁰²

The scalability²⁰⁴ and regenerative²⁰⁵ properties of a supramolecular gel make these materials of interest for development towards a number of applications which include chemosensors,^{206,207} biomedicines²⁰⁸ and drug delivery vehicles.²⁰⁹ Hamachi and co-workers developed a hydrogel which could be used as a matrix for immobilising biological and artificial materials without destroying the integrity of the sample. A fluorescent chemosensor (Figure 65, **88b**) which was originally developed to detect phosphate and its derivatives by fluorescence enhancement was embedded into a supramolecular hydrogel, formed through the self-assembly of LMWG **88a**. It was shown that the nanofibers had no deteriorative influences on either the stability of the monomeric gelator units the hydrogel produced or the functions of the embedded chemosensor.²⁰⁶ Subsequently, hydrogel-based delivery devices are habitually used for a number of biological applications, which include: oral;²¹⁰ ocular;²¹¹ transdermal²¹² and subcutaneous.²¹³

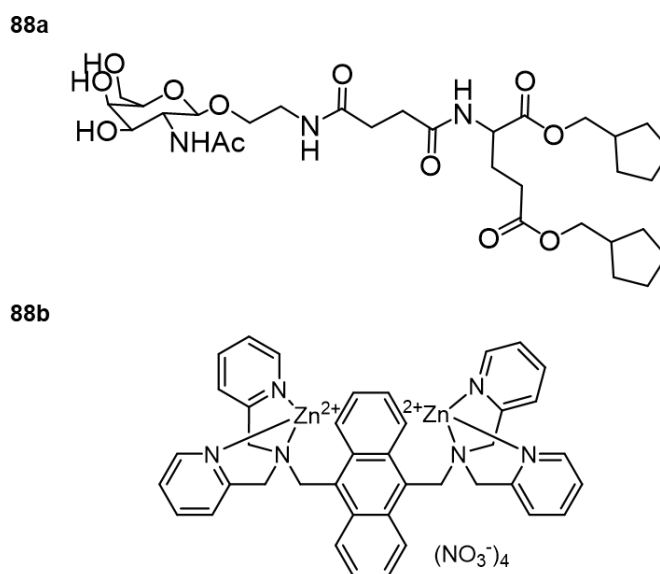


Figure 65 – Chemical structures of LMWG synthesised by Hamachi and co-workers (**88a**) and chemosensor (**88b**) that was embedded into hydrogel of **88a**.²⁰⁶

The supramolecular properties of urea-based gelled materials have been extensively studied by Steed and co-workers.^{123,214,215} A series of four bis(urea) structurally related gelators (Figure 66, **89-92**) of varying solubilities were employed to demonstrate their potential to act as crystallisation media for molecular organic compounds, of both drug and non-drug species.

Preliminary rheological experiments to elucidate whether the presence of the drug molecule within the matrix had any effect on the gelation processes were conducted. From these studies, it was concluded no adverse effect of the material, and conversely, a slight increase in the solid-like behaviour was observed. The results from these studies demonstrated that it was possible to induce crystallisation of molecular organic compounds, in particular anticonvulsant carbamazepine (CBZ) (1 % wt), within the fibrous network of gelled materials **89-91**. In the presence of copper(II) halides, metallo-gelator **92**, was also shown to promote crystal growth. The presence of these crystals was verified using optical microscopy where it was noted that the morphology of the crystal was concentration-dependent, with needles formed at higher concentrations of CBZ and blocks at lower concentrations.²¹⁶

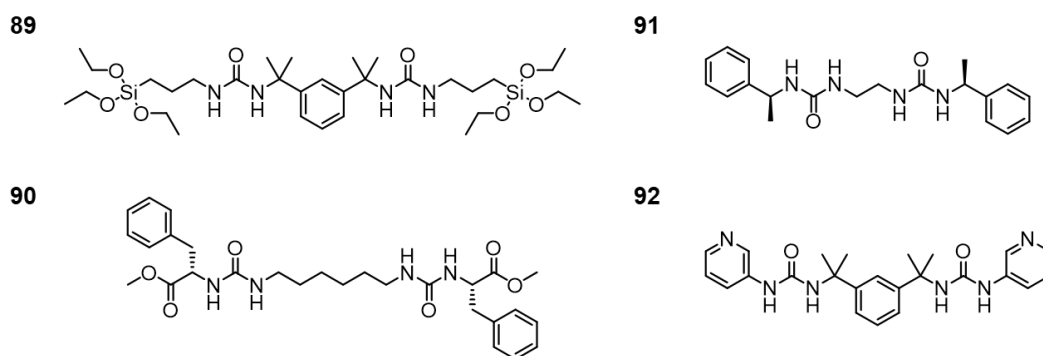


Figure 66 - Bis(urea) structurally related gelators used as crystallisation media for molecular organic compounds.

Hydrogels are extensively used for biomedical applications due to their unique properties which include: absorption of high aqueous content; flexibility; softness and biocompatibility.²¹⁷ Gunnlaugsson and co-workers developed a library of eight novel derivatives (Figure 67), the structures of which were investigated for their ability to function as LMWG, self-associating via urea-pyridyl hydrogen bonds and π - π stacking interactions, forming a robust gelled material. These soft materials were then explored to see if they possessed antibacterial properties. The results from this study demonstrated that all eight gelators prevented bacterial growth for both Gram-positive methicillin-resistant *Staphylococcus aureus* (MRSA) and Gram-negative *Escherichia coli* (*E.coli*).

LMWGs **93-96** were shown to exhibit the least activity against MRSA (zone of inhibition of 7 mm, 6 mm and 10 mm diameter, when concentrations of 4.3 mmol, 3.9 mmol, and 3.6 mmol were applied). Gelators **97** and **99** exhibited moderate activity against *E.coli.*, whilst **98** demonstrated good activity against both bacteria models, gelator **100** was shown to exhibit greater activity towards MRSA with a zone of inhibition of 13 mm (1.8 mmol) and 20 mm (3.6 mmol).²¹⁸

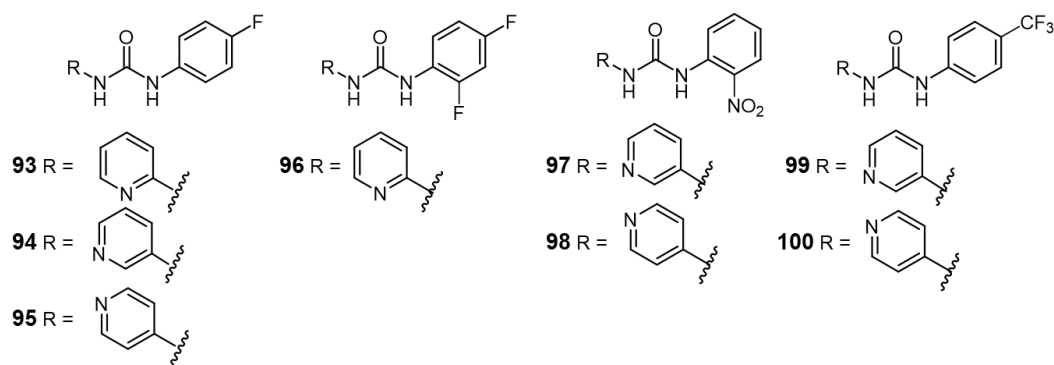


Figure 67 – Chemical structures of pyridyl ureas synthesised by Gunnlaugsson and co-workers.²¹⁸

The development of novel antimicrobials along with the incorporation of novel antimicrobial agents into drug delivery vehicles is becoming increasingly more imperative. Antimicrobial resistance (AMR) within a vast range of infectious agents, which include bacteria, viruses, fungi and parasites, is a growing threat to public health worldwide.²¹⁹ It is predicted that the number of AMR attributed deaths will be greater than those caused by cancer by the year 2050, decreasing the world's GDP by \$100 trillion.²²⁰ Consequently, fighting AMR is of public health priority that requires a collaborative global approach across all sectors.

A diverse range of supramolecular specific approaches are currently being used to combat AMR; for example, the development of four Trp-incorporated pillar[5]arene channels by Zhang and co-workers. These hydrogen bonded channels displayed a high insertion selectivity for the lipid bilayer membrane of Gram-positive bacteria over that of mammalian erythrocytes, demonstrating very low toxicity. All four channels were shown to exhibit antimicrobial activity against multiple Gram-positive bacteria.

The concentrations required to inhibit 50 % bacteria growth (MIC_{50}) ranged from 0.3-7 μM , efforts are continuing to improve the antimicrobial activity of this family of pillar[5]arene channels.²²¹ El-Sheshtawy and co-workers developed their strategy from supramolecular principles for the investigation into extending the shelf-life and efficacy of fluoroquinolone drugs with cucurbit[7]uril (CB7). The results from these studies showed an extended shelf-life and enhanced efficacy of danofloxacin against clinically relevant *Bacillus cereus* (*B. cereus*), with a zone of inhibition increase from ≈ 18 mm (without CB7) to ≈ 20 mm (With CB7), *Salmonella typhi* (*S. typhi*) (≈ 24 mm to ≈ 26 mm), *E. coli* (≈ 22 mm to ≈ 27 mm) and *S. aureus* (≈ 21 mm to ≈ 24 mm) at pH 8.1.²²²

Hiscock and co-workers developed their own supramolecular approach into the investigation of antibacterial design, with an initial focus on increasing antibacterial activity of their first-generation structurally related SSAs, against clinically relevant MRSA.²²³ Within their studies, they explored the self-associative properties and antimicrobial efficacy of electron-rich anthracene and electron-poor anthraquinone derivative SSAs (Figure 68, **101-103**). Compounds **101-103** were individually shown to illicit an antibacterial response against clinically relevant MRSA with MIC_{50} values calculated as (0.71, 0.46 and 0.61 mM respectively). Interestingly, this efficacy was increased when **102** was combined in a 1:1 molar ratio with either **101** (0.33 mM) or **103** (0.31 mM), where large stable aggregated species (d_H 400-500 nm) were observed in an aqueous environment. Demonstrating that the formation of those large self-associated aggregated species is imperative for effective SSA delivery to the bacterial cell wall.²²³

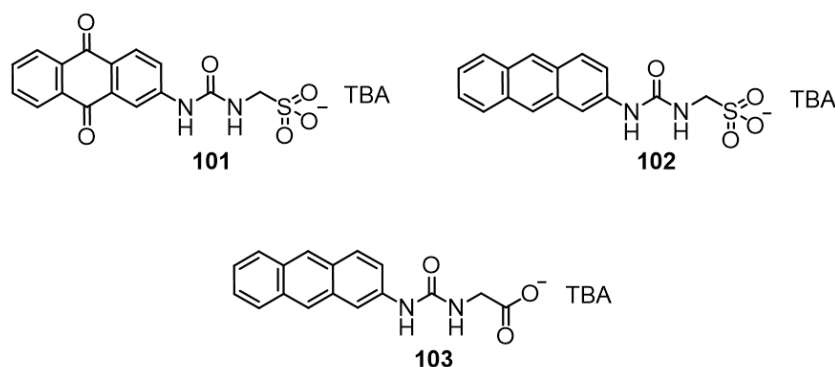


Figure 68 – Chemical structures of electron-poor anthraquinone (**101**) and electron-rich anthracene derivatives (**102** and **103**).

Inspired by previous works conducted by Gunnlaugsson²¹⁸ and Hiscock²²³, this chapter will briefly summarise the self-associative properties of previously discussed CF₃ substituted urea-sulfonate **42**, *ortho*-substituted benzothiazole **71** and *para*-substituted benzothiazole **72**, in addition to introducing novel *bis*-substituted **104** (Figure 69). Furthermore, it will be shown that known antibiotic ampicillin (**105**) can be successfully co-formulated with **72**.

The work detailed in this chapter has been published within the following peer-reviewed journal article:

2. Controllable hydrogen bonded self-association for the formation of multifunctional antimicrobial materials L. J. White, J. E. Boles, N. Allen, L. S. Alesbrook, J. M. Sutton, C. K. Hind, K. L. F. Hilton, L. R. Blackholly, R. J. Ellaby, G. T. Williams, D. P. Mulvihill and J. R. Hiscock, *J. Mater. Chem. B*, 2020, **8**, 4694–4700.²

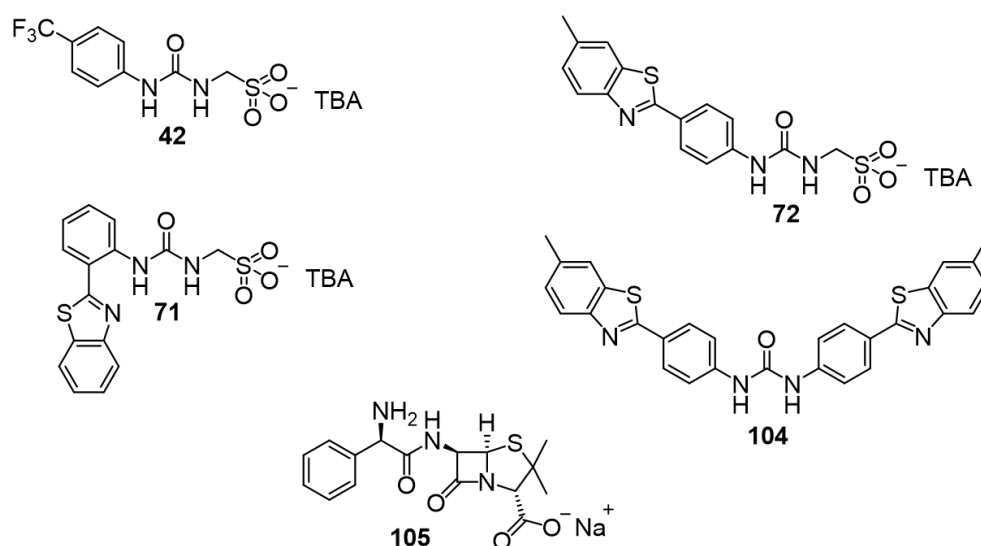


Figure 69 - Chemical structures of the five compounds discussed in this chapter. (**105** = ampicillin sodium salt)

Compound **104** was prepared in a one pot synthesis by firstly forming the isocyanate. To achieve this, triphosgene was added to a stirring solution of 4-(6-methylbenzothiazol)aniline in ethyl acetate and the mixture heated at reflux for 4 hours. Then, one equivalent of 4-(6-methylbenzothiazol)aniline was added to the reaction mixture and heated at reflux overnight, filtered and the solid washed with ethyl acetate. Further purification resulted in production of the pure product (**104**) as a yellow solid with a yield of 84 %.

As discussed in Chapter 2 the presence of dimeric species has been shown to prevail in both the gas phase and in competitive organic (DMSO) solvent systems for **42**, **71** and **72**. However, moving into aqueous solutions of EtOH:H₂O (1:19) those same SSAs were shown to form stable extended self-associated aggregates, with a $\approx d_H$ of 100-550 nm and zeta potential values of -76 mV (**42**), -79 mV (**71**) and -101 mV (**72**).

In preliminary studies by Hiscock and co-workers, the intrinsically fluorescent anionic components of *ortho*-substituted benzothiazole **71** and *para*-substituted benzothiazole **72** were directly visualised through a combination of transmission and fluorescence microscopy, where it was discovered these larger self-associated aggregates are spherical in shape, as shown in Figure 70.¹³⁶

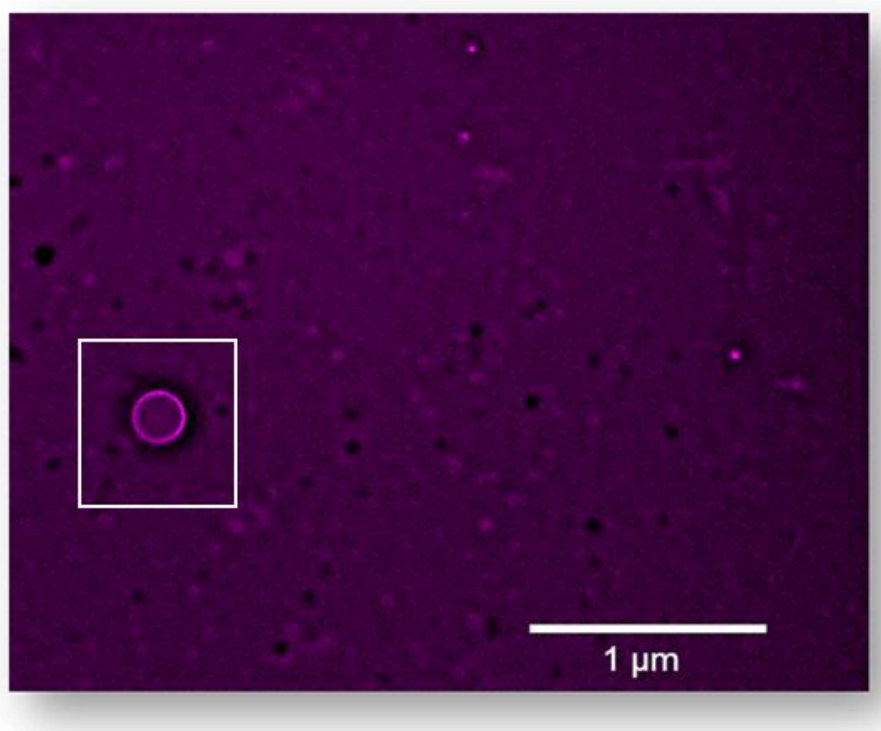


Figure 70 - DAPI filter composite image of **72** in an EtOH:H₂O (1:19) solution showing the presence of a spherical self-associated aggregate.¹³⁶

This chapter explores any structural alterations from spherical aggregate to a fibrous network for structurally related **42**, **71**, **72** and **104** in aqueous salt solutions.

The techniques employed to characterise any subsequent hydrogels include visual inspection (inversion test); scanning electron microscopy (SEM); energy-dispersive X-ray (EDX); fluorescence microscopy; pH detection and rheometry. The propensity for **42**, **71** and **72** to act as antimicrobial agents against Gram-positive MSRA and Gram-negative *E.coli* bacteria will also be explored.

3.2 Hydrogel determination

3.2.1 Inversion test and minimum gelation concentration (MGC) studies

The discovery that this class of compound could gelate was a complete surprise. Whilst preparing a sample of *para*-substituted benzothiazole **72** in phosphate buffer (0.505 M) to determine how this compound interacted with vesicles, it was realised, that after heating and upon cooling, a gel had formed. This discovery then prompted investigations as to why the phosphate buffer induced a change in the self-associated structure formation from the spherical aggregate observed in H₂O to a fibrous network with the addition of salt. Hiscock and co-workers investigated this class of SSA in the solid state where it was discovered, that when strongly coordinating cations Na⁺ or K⁺ were contained within the molecular structure, a change in binding mode was observed.¹³⁵ The presence of a weakly coordinating cation (TBA) resulted in a self-associative urea-anion binding mode (Figure 71a). When stronger coordinating cations (Na⁺ or K⁺) were present, the urea-urea binding mode was then favoured (Figure 71b). This was due to the sulfonate group no longer being free to act as an HBA group, instead, the urea oxygen became the principle HBA in the self-association process.¹³⁵

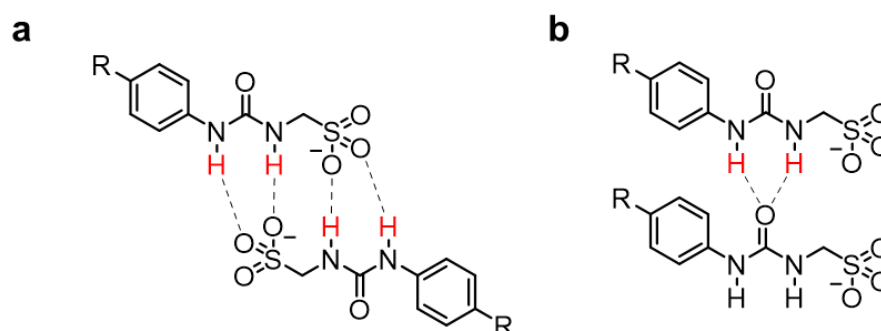


Figure 71 – Examples of binding modes a) urea-anion and b) urea-urea.

This led to the initial hypothesis that the formation of the gel was dependent on the presence of a strongly-coordinating cation that prevents the self-association of the SSA into spherical aggregates formed in H₂O, in favour of fibres. To elucidate as to whether this process was also anion dependent a series of 11 different anionic salts were employed.

The concentration of the aqueous salt solutions (0.505 M) used in this study was determined due to that initial discovery, where it was found **72** gelled in a phosphate buffer with a concentration of 0.505 M. The propensity for **72** (5 mg) to gelate in lower concentrations was then investigated. In the first instance samples of **72** (5 mg) in aqueous salt solutions, at a concentration of 0.0505 M were prepared. This resulted in an incomplete gel as shown in the example in Figure 72a. The aqueous salt solution concentration was then increased to 0.405 M, again resulting in an incomplete gel (Figure 72b). Therefore, it was determined that 0.505 M was the optimal concentration of the aqueous salt solution to enable **72** to act as a gelator. Further investigations into the concentration-dependence of the aqueous salt solution are ongoing.

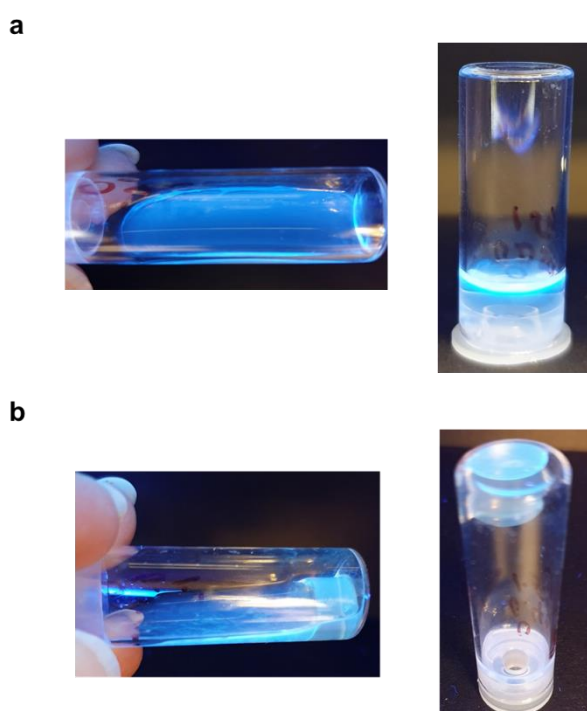


Figure 72 – Incomplete gels formed through the addition of **72** (5 mg) to 1 mL of aqueous NaCl: a) 0.0505 M and b) 0.405 M

The presence of a gelled material in this study was initially verified by an inversion test, in which the gel is characterised by resistance to flow in an inverted vial.¹⁹⁶

Here 1 mL (0.505 M) of the appropriate salt solution (Table 12) was added to 5 mg of either **42**, **71**, **72** or **104** in a glass vial, and heated to approximately 60 °C until the solid matter had dissolved. This solution was then allowed to cool to room temperature and the vial inverted to verify gel formation. Despite its simplicity, the inversion test method is a frequently used successful test to determine the presence of hydrogels.²²⁴

The results from this preliminary experiment showed that of the compounds tested, only *para*-substituted benzothiazole urea-sulfonate **72** was found to form a gelated material. An example of the inversion test performed is illustrated in Figure 73. This example shows the hydrogel formation of **72** (5 mg) in aqueous salt solutions of NaCl (Figure 73a) and NaOAc (Figure 73b) (1 mL, 0.505 M). As observed in H₂O the absence of a gelated material is apparent.

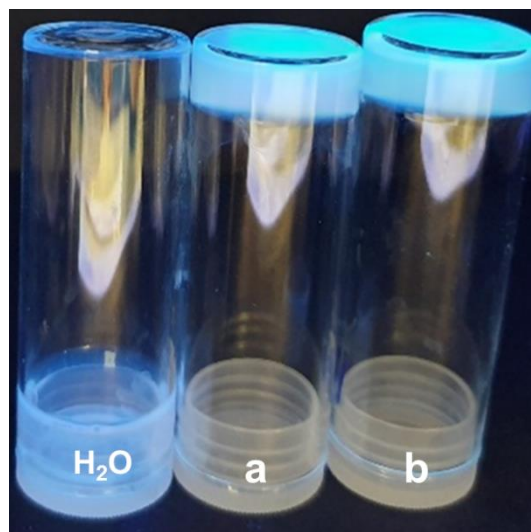


Figure 73 - Inversion test of hydrogels containing **72**: 5 mg in 1 mL of H₂O; a) 5 mg in 1 mL aqueous NaCl (0.505 M); b) 5 mg in 1 mL of aqueous NaOAc (0.505 M).

Compound **42** dissolved, however, it showed no sign of onset gelation. This is hypothesised to be due to the lack of the benzothiazole unit within the molecular structure, causing reduced stabilisation of the self-assembly processes through intermolecular π - π stacking interactions.²²⁵

As extensively discussed in Chapter 2 (Chapter 2.3, 2.5.3.3) the intramolecular bond formed between the urea N-H and nitrogen on the benzothiazole substituent of **71** results in destabilisation of any resultant self-associated structures (Figure 74).

Therefore, as expected this compound did not pass the inversion test as shown in Figure 75, reinforcing the previous hypothesis of the importance of > 2 HBD units free to participate in the self-association process. Finally, **104** does not contain an anionic moiety, removing any anionic HBA sites, this confirms the significance of the salt component for this family of SSAs to self-associate into polymeric gel fibres.

71

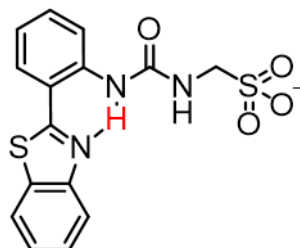


Figure 74 - The proposed structure of monomer of **71**, demonstrating intramolecular bond formation.¹³⁶

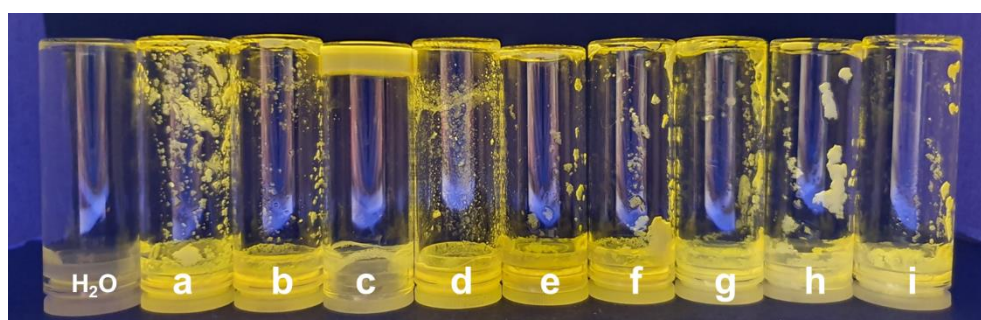


Figure 75 – Failed inversion test for **71** (5 mg) in 1 mL of H₂O and 0.505 M aqueous solutions of: a) NaCl; b) NaHCO₃; c) NaH₂PO₄; d) NaOBz; e) NaNO₃; f) NaOAc; g) Na₂CO₃; h) Na₂SO₄ and i) NaF.

3.3 Characterisation of supramolecular hydrogels

3.3.1 Minimum gelation concentration (MGC)

The MGC is the lowest possible gelator concentration required to form a stable gel. To assess the MGC of *para*-substituted benzothiazole **72** in 14 different aqueous salt solutions, vial inversion experiments were performed. To avoid confounding variables affecting the results of the experiment,¹⁹⁶ all samples were prepared analogously. As temperature is one of the key parameters in the gelation process, the inversion experiments in this study were all performed at 25 °C to allow for comparison of hydrogel characteristics between samples.

Table 12 - Summary of ionic strength of aqueous salt solutions (0.505 M); average ($n = 3$) salt solution (0.505 M) pH values obtained at 25 °C; MGC determined through inversion testing for samples containing **72** and various aqueous salt solutions (0.505 M) at 25 °C.

Salt	Ionic strength (salt soln.)	pH (salt soln.)	MGC (mg/mL)	Salt	Ionic strength (salt soln.)	pH (salt soln.)	MGC (mg/mL)
NaCl	0.505	7.00 ± 0.02	1.5	NaOBz	0.505	7.00 ± 0.04	1.5
KCl	0.505	6.28 ± 0.02	2.5	NaNO ₃	0.505	6.32 ± 0.01	1.5
RbCl	0.505	7.81 ± 0.02	3.5	NaH ₂ PO ₄	0.505	4.01 ± 0.01	1.5
TBACl	0.505	4.22 ± 0.02	[a]	NaHSO ₄	0.505	1.26 ± 0.03	[a]
NaF	0.505	8.82 ± 0.04	2.0	Na ₂ CO ₃	1.515	11.63 ± 0.03	3.0
NaHCO ₃	0.505	8.54 ± 0.04	4.0	Na ₂ HPO ₄	1.515	8.49 ± 0.00	[b]
NaOAc	0.505	7.76 ± 0.02	3.5	Na ₂ SO ₄	1.515	7.00 ± 0.02	3.5

[a] Precipitation at 5 mg/mL, no gel formation. [b] Partial gel formed at 5 mg/mL.

The results from the inversion experiments demonstrate the MGC of **72** needed to gel 1 mL of various aqueous salt solutions was found to be dependent on the salt present. Where the anion remained the same (**72**), the MGC needed to gelate 0.505 M aqueous solutions of NaCl, KCl, RbCl and TBACl was found to increase exponentially with increasing size of the associated counter cation, 1.5, 2.5, 3.5 and > 5 mg/mL respectively (Figure 76).

This is hypothesised to be due to the increasing strength of (SSA) anion-cation (salt solution) coordination where $TBA^+ < Rb^+ < K^+ < Na^+$. As previously discussed in Chapter 2 (2.5.2), strong ion-pair effects within a molecular structure result in instability of any extended hydrogen bonded self-associated aggregate in an EtOH:H₂O (1:19) solution. For **72** to form a stable gel fibre network in an aqueous salt solution, the original packing arrangement and hydrogen bonding network is required to be altered.

Evidence of the stability of those larger aggregated structures present in H₂O was observed when gelation was attempted mechanically. The appropriate salt solution (0.1 mL, 5.05 M) was added to **72** (1.5 mg in 0.9 mL of H₂O) in a glass vial, agitated using a vortex for one minute and left at room temperature for 12 hours.

This mechanical method yielded no formation of gelled material, confirming that, in order to initiate the formation of gel fibres, the addition of heat to the system is required to disrupt the supramolecular structure.

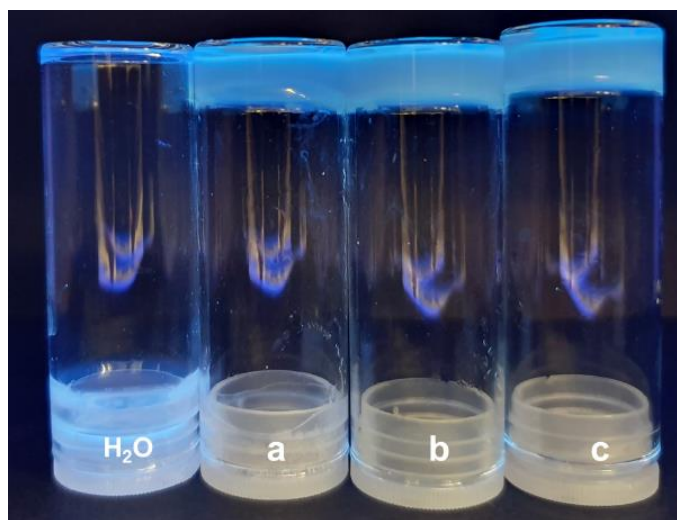


Figure 76 – Inversion test of hydrogels containing **72** (5 mg) in 1 mL of H₂O; a) MGC of **72** (1.5 mg) in 1 mL of aqueous NaCl (0.505 M); b) MGC of **72** (2.5 mg) in 1 mL of aqueous KCl (0.505 M) and c) MGC of **72** (3.5 mg) in 1 mL of aqueous RbCl (0.505 M).

Upon comparison of the effects the different sodium salts have on the resultant hydrogel formation, it was discovered that the ionic concentration and the pH of the aqueous salt solution significantly influenced the stability of the gel fibre network. With a decrease of both the pH and ionic strength of the salt solution (Table 12), a general decrease of MGC was observed.

An example of the effect that the ionic solution has on gel formation is evident with the comparison between **72** in 1 mL aqueous solutions of NaH₂PO₄ and Na₂HPO₄. The NaH₂PO₄ aqueous solution exhibits an ionic strength of 0.505 and pH of 4.01, the MGC is 1.5 mg/mL. Conversely, **72** (5 mg) in 1 mL of aqueous Na₂HPO₄ which has an ionic strength of 1.515 and pH of 8.49 results only in a partial gel, and exhibits an MGC > 5 mg/mL. In this instance, it is hypothesised that the increased number of charged ions may be a contributing factor, where the change in protonation state affects the coordination strength.

In summary, it was shown that changing the solvent environment to an aqueous salt alters the self-associated structure present in H₂O from spherical aggregates into a fibrous 3D network.

In addition to the presence of salt, the benzothiazole group was shown to be essential, thought to be due to the requirement of π - π stacking interactions. The strength of the hydrogels formed was found to be dependent on cation size, ionic strength and pH.

3.3.2 Rheology

Rheology is a commonly used analytical technique to determine the mechanical properties of supramolecular hydrogels.²²⁶ Gelated materials undergo distinctive changes when subjected to tensile and compressive stresses. However, they are more regularly identified based on their deformation and flow behaviour when applied with oscillatory stress, which is quantified by elastic properties such as the storage (G') and loss moduli (G'').¹⁹⁷ Using this technique a range of different measurements are possible, which supply informed information with regard to the 3D viscoelastic network of a gelated material. In this study, the viscoelastic properties of hydrogels formed above the MGC, where **72** (5 mg) in 1 mL of the appropriate aqueous salt solution (0.505 M) were investigated. At this concentration, the fibril formation affords the “*elasticity*” to the gelated materials, which allows for the reliable measurement of mechanical properties of the soft materials. Consequently, those aqueous salt solutions in which 5 mg of **72** did not observe the tube inversion tests were excluded from this study as they cannot be classified as robust gelated materials.

The rheological properties of a viscoelastic material are generally independent of strain up to the yield point. Beyond this yield point, the material's behaviour is no longer linear (where stress and strain are proportional) and resultantly the storage modulus declines and the critical point (commonly known as the gel-sol transition point or flow point) is reached (Figure 77). Between the yield and gel-sol transition points, the material structural strength has decreased, although the sample still largely displays the properties of a gel. Measuring the strain amplitude (γ) dependence of the storage (G') and loss moduli (G'') is the initial step to characterising the viscoelastic behaviour of a hydrogel material.¹²³

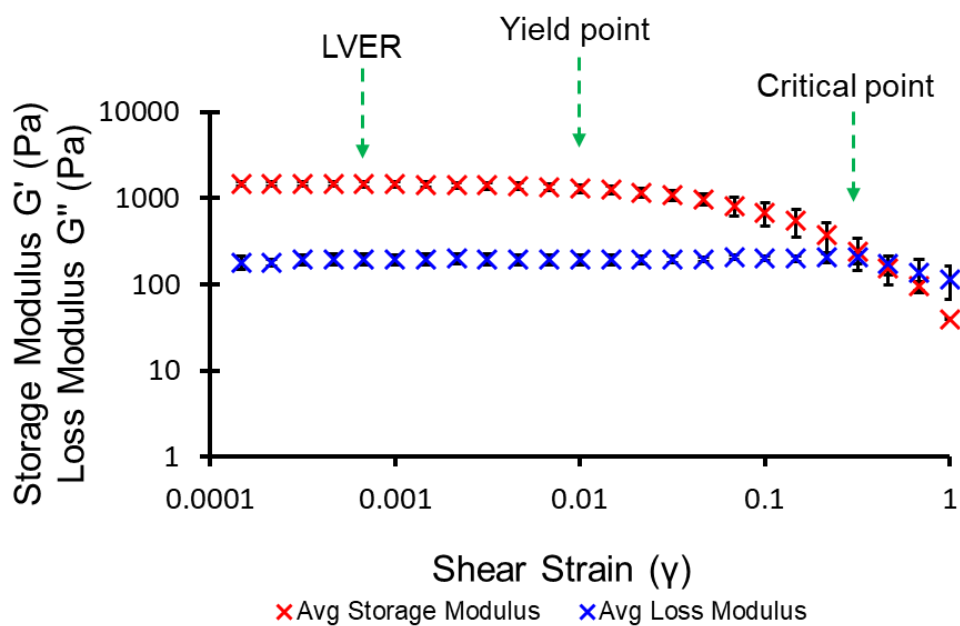


Figure 77 – Average results ($n=3$) from amplitude sweep experiments used to define the linear viscoelastic region, yield point and flow point of **72** (5 mg) in 1 mL of aqueous NaCl (0.505 M) at 25 °C. (1 = 100%).

The results from the amplitude sweeps were used to define the hydrogels linear viscoelastic region (LVER) as overviewed in Table 13. This region is the range in which the material is the most intact, and the point at which any additional experimental methods are applied. The gel-sol transition point was also observed, where **72** (5 mg) in 1 mL of aqueous NaCl (0.505 M) demonstrated a critical strain (γ) of $\approx 46\%$. Below this gel-sol transition point, the gelled material is highly structured and intact, where the material behaves solid (elastic) like where $G' > G''$. Above this critical point the material is more fluid (viscous) like, where $G'' > G'$ (Figure 77). An overview of the gel-sol transition point values (%) obtained from the amplitude sweeps is shown in Table 13.

Table 13 - Summary of rheological data for **72** (5 mg) in 1 mL of the appropriate aqueous salt solution (0.505 M). Characterisation experiments were performed at 25 °C: average ($n=3$) gel-sol transition points obtained from shear strain (γ) amplitude sweeps; average ($n=3$) storage (G') and loss (G'') moduli obtained angular frequency sweeps ($\gamma = 0.1\%$).

Salt	Gel-sol transition point γ (%)	Storage modulus G' (Pa)	Error (Pa)	Loss modulus G'' (Pa)	Error (Pa)
NaCl	46.4	1307	± 11	202	± 12
KCl	6.8	1867	± 74	274	± 12
RbCl	46.4	1308	± 85	176	± 9
NaF	100.0	1448	± 70	216	± 11
NaHCO ₃	4.6	1166	± 54	175	± 14
NaOAc	100.0	1409	± 65	235	± 39
NaOBz	21.5	503	± 23	115	± 7
NaNO ₃	21.5	650	± 21	112	± 8
NaH ₂ PO ₄	3.2	1117	± 37	192	± 10
Na ₂ CO ₃	31.6	1653	± 28	226	± 20
Na ₂ SO ₄	6.8	1503	± 130	228	± 18

Once the LVER was defined by the amplitude sweep, the gelled material structure was further characterised using an angular frequency sweep at a strain below the critical point (γ). This provides more information about the strength of the interactions between the components of the material, thus its overall robustness. In a typical experiment, the G' strain of a gel should vary only weakly with frequency as shown in Figure 78.

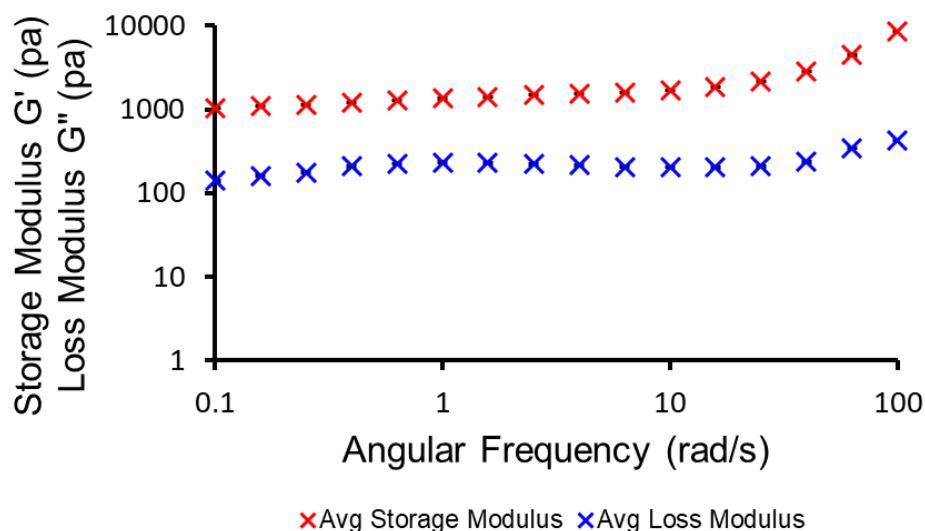


Figure 78 - Average results ($n=3$) from frequency sweep experiments obtained from the LVER, under a constant shear strain (γ) of 0.925 % of a gelled material containing **72** (5 mg) in 1 mL aqueous NaCl (0.505 M) performed at 25 °C.

The results from the angular frequency sweeps applied under a constant strain (γ) of 0.925 % show all materials tested to exhibit a $G' > G''$ over the entire range of frequencies (0.1-100 rad/s), this denotes the elastic character to be always dominant when the frequency is applied. These results from the angular frequency sweeps are summarised in Table 13. Upon comparison of the storage (G') and loss (G'') moduli, it is observed that the values remain fairly constant over the range of gelled materials tested, with the storage modulus ≈ 7.4 times greater than the loss modulus for any comparative hydrogel under these experimental conditions as illustrated in Figure 79.

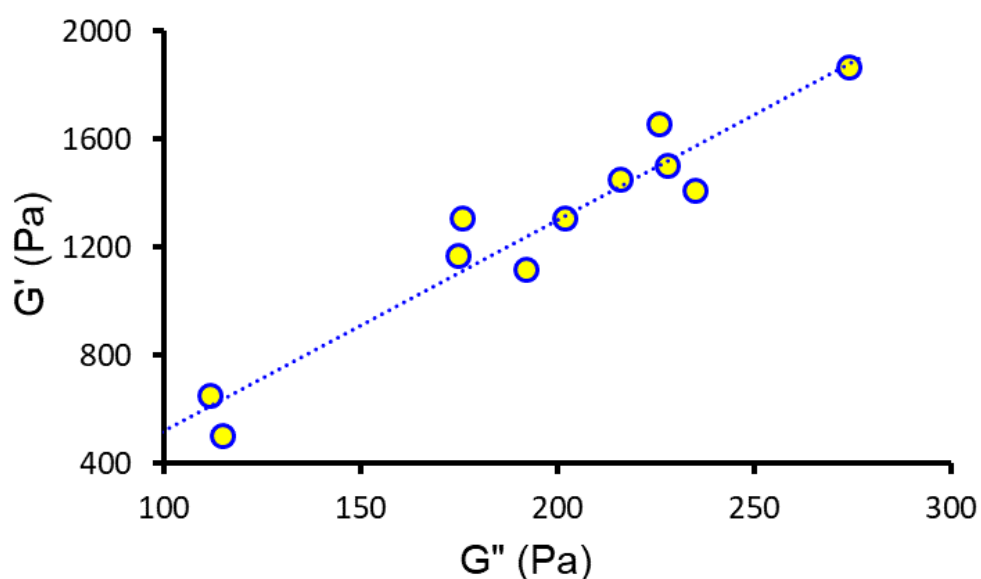


Figure 79 – Comparison of G' and G'' values obtained from the angular frequency rheological experiments summarised in Table 13.

In summary, it was shown that the presence of different salt solutions was found to modulate both the gel-sol transition point and the comparative storage (G') and loss (G'') moduli observed for each gelled material. The solid-like character of the materials was manifested in the fact that the storage modulus (G') was found to be ≈ 7.4 times greater than the viscous modulus G'' up to the yield stress of the gel.

3.3.3 Microscopy studies

Due to having the ability to reveal the structures of LMW compounds with a resolution of up to a nanometre,²²⁷ SEM is routinely employed to characterise the morphology and microstructure of dehydrated hydrogels (xerogels).^{228,229} This technique can generate high-resolution topological images through the utilisation of a focussed beam of high energy electrons as a source of illumination.²³⁰ Consequently, this enables the morphology of the dehydrated hydrogels (xerogels) to be observed. Limitations of this technique include i) high magnification only allows for a small fraction of a sample to be imaged in a realistic timeframe; ii) to be imaged using SEM, a hydrogel must first be dehydrated to form a xerogel, this destructive process may result in artefacts such as line and dark area charging or electron beam damage, resulting in the analysis of artefacts that are not present within the solvent containing hydrogel.²³¹

Due to instrument availability, a selection of the hydrogels/partial gels were taken forward to be observed by SEM. For comparative purposes, this pool of material consisted of hydrogels containing both monovalent and divalent cation salt solutions. Those gels/partial gels with **72** (5 mg) in aqueous i) NaCl; ii) NaH₂PO₄; iii) Na₂CO₃; iv) Na₂HPO₄; NaNO₂; and v) NaHCO₃ (1 mL, 0.505 M) were dehydrated through the use of a shlenk line, to give xerogels. SEM images and corresponding EDX spectra obtained and refined with the assistance of Dr Luke Alesbrook.

Evaporation of the immobilised liquid is known to cause the brittle fibrous structures that form the 3D network to collapse, therefore SEM focuses on general shapes and morphologies of the fibres rather than on the absolute quantities, such as the diameters and lengths. The SEM images of the xerogels prepared from the dehydration of the hydrogels containing NaCl or NaNO₂ showed the presence of platelet like objects (Appendix 2.5, Figure S376 and S390), this was proposed to be due to insufficient magnification of the SEM when observing this samples. Consequently, the magnification of the SEM was increased to allow for elucidation of the gel fibres in future samples.

With an increased magnification of the SEM, the morphology of the xerogels containing Na_2CO_3 (Figure 80) or NaH_2PO_4 (Figure 81) were observed. These images showed the presence of multiple rigid fibres of variable thicknesses emanating from a central point, with the darker patches identified as the end of those rigid fibrillar structures. As the magnification of the SEM is further increased as shown with the xerogel containing NaH_2PO_4 in Figure 81, those ends of the rigid fibres become more apparent.

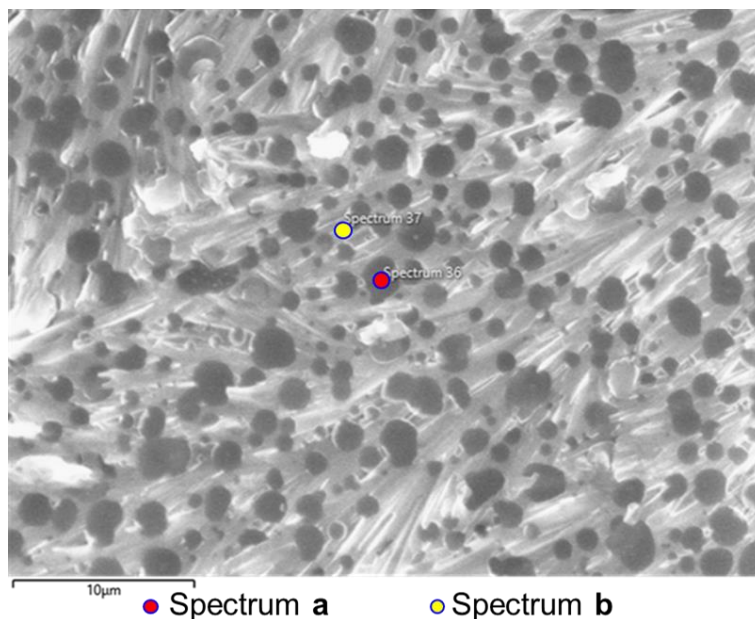


Figure 80 - SEM image of a xerogel prepared from a dehydrated hydrogel containing **72** (5 mg/mL) in aqueous Na_2CO_3 (0.505 M). Locations of analysis by EDX spectra highlighted in pink (Figure 82a) and yellow (Figure 82b). Scale = 10 μm .

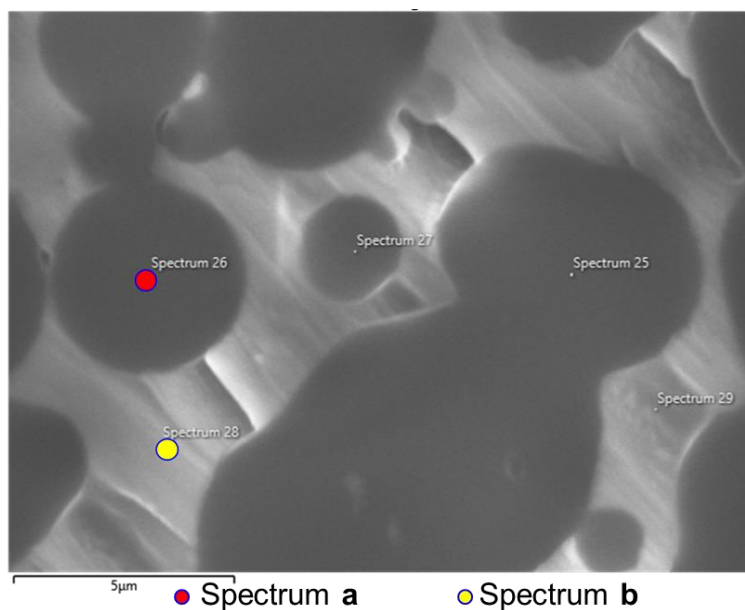


Figure 81 - SEM image of a xerogel prepared from a dehydrated hydrogel containing **72** (5 mg/mL) in aqueous NaH_2PO_4 (0.505 M). Locations of analysis by EDX spectra highlighted in pink (Figure 83a) and yellow (Figure 83b). Scale = 5 μm .

Energy-dispersive X-ray is a complementary analytical technique to SEM, used to determine the elemental analysis or chemical characterisation of a sample.²³² Multiple EDX spectra and corresponding elemental analyses were obtained for each processed SEM image. The spectra shown in Figures 82 and 83 correspond to the SEM images for **72** in aqueous Na₂CO₃ (Figure 80) or NaH₂PO₄ (Figure 81). The spectra shown in Figures 82a and 83a represent the internal core of the fibres, where the sulphur element denotes the presence of **72**. Although the oxygen is present within the molecular structure of **72** it is also present in the molecular structure of the associated aqueous salt solutions (Na₂CO₃ and NaH₂PO₄), therefore, this is not a distinguishable element. The spectra shown in Figures 82b and 83b were taken from the exterior surface of one of the nanofibers, where the elemental analysis once more confirms the presence of **72**.

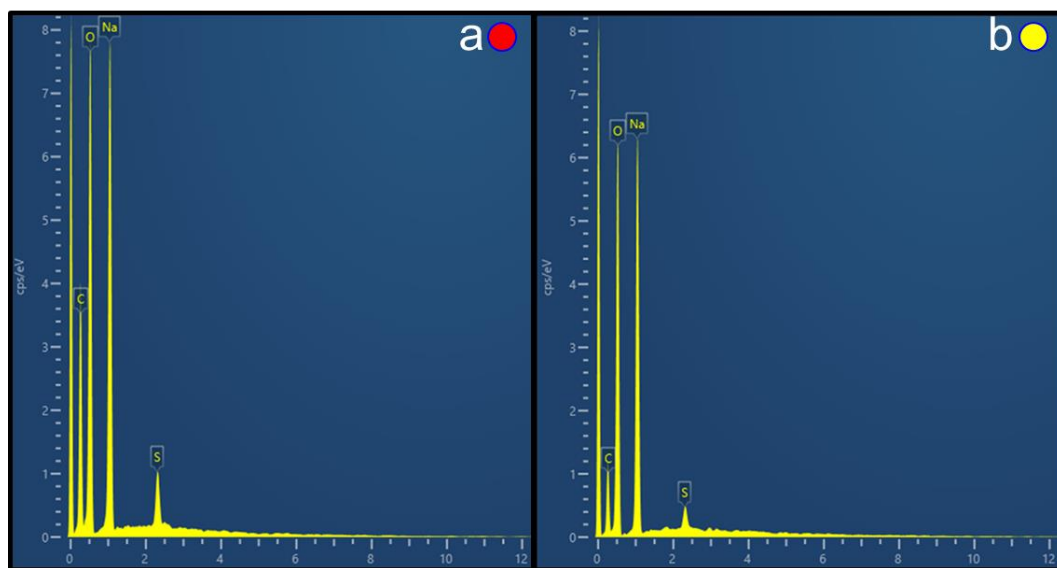


Figure 82 - EDX spectrum showing elemental analysis of the xerogel imaged in Figure 80.

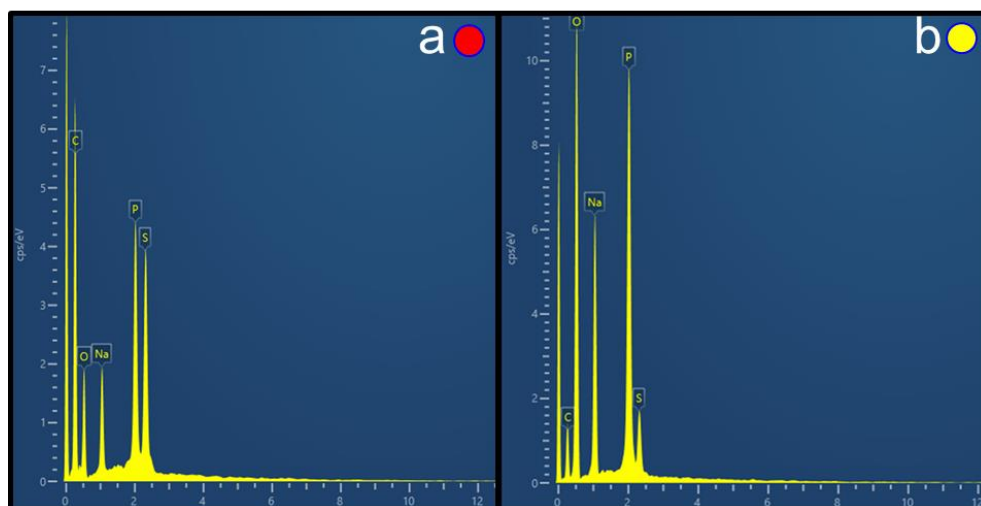


Figure 83 - EDX spectrum showing elemental analysis of the xerogel imaged in Figure 81.

Upon comparison of the SEM image obtained for a xerogel containing NaHCO_3 , with those containing Na_2CO_3 and NaH_2PO_4 a difference in architecture is observed. The xerogel containing NaHCO_3 was shown to exhibit a highly dense porous architecture (Figure 84) compared to the emanating fibrillar structures observed for xerogels containing Na_2CO_3 (Figure 80) and NaH_2PO_4 (Figure 81).

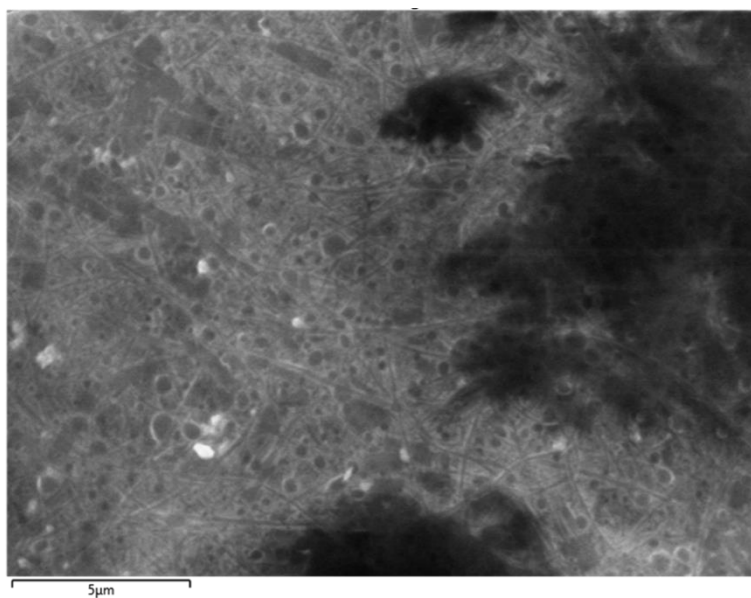


Figure 84 - SEM image of a xerogel prepared from a dehydrated hydrogel containing **72** (5 mg/mL) in aqueous NaHCO_3 (0.505 M). Scale = 5 μm .

Fluorescence microscopy is not as popular as SEM for the visual analysis of hydrogels due to having a relatively low resolution compared to that of SEM.

However, as a non-destructive technique, fluorescence microscopy can provide valuable information on the microstructure and distribution of the fibres in space.²³³ Due to the intrinsically fluorescent nature of the anionic component of **72**, it was possible to utilise this technique within these studies. Due to instrument availability, only a select number of gelled materials were able to be visualised. Herein, four materials were observed, these included three gels with MGCs ranging from 1.5 to 3 mg/mL and one partial gel (> 5 mg/mL) for comparison purposes. These materials were as follows, **72** (5 mg) in aqueous: i) NaCl; ii) NaH₂PO₄; iii) Na₂CO₃; and iv) Na₂HPO₄ (1 mL, 0.505 M). Fluorescence microscopy images obtained and refined with the assistance of Prof. Daniel Mulvihill.

The fluorescence images of the hydrogels comprised of aqueous salt solutions NaCl and NaH₂PO₄ show the presence of continuous multidirectional self-assembled nanofibers, as illustrated in Figures 85a and 85b. Both gels containing NaCl and NaH₂PO₄ within their matrix exhibit an MGC of 1.5 mg/mL (Chapter 3.2.1, Table 12). When these structures are compared with those from a gel with a greater MGC such as NaHCO₃ (4.0 mg/mL) the fibres appear to be shorter with a higher cross-linked density resembling a honeycomb-like structure (Figure 85c). Interestingly, those fluorescence images obtained for hydrogels containing NaH₂PO₄ or NaHCO₃ correlate with the images obtained through SEM where long fibres were shown in the xerogel containing NaH₂PO₄ (Figure 81), and a higher cross-linked density with NaHCO₃ (Figure 84) contained within the structure.

Moving into an aqueous salt solution in which **72** (5 mg) only forms a partial gel (Na₂HPO₄), fewer fibres are observed. Interestingly in this aqueous salt solution, in addition to those fibres, spherical self-associated aggregates are also observed to be present (Figure 85d).

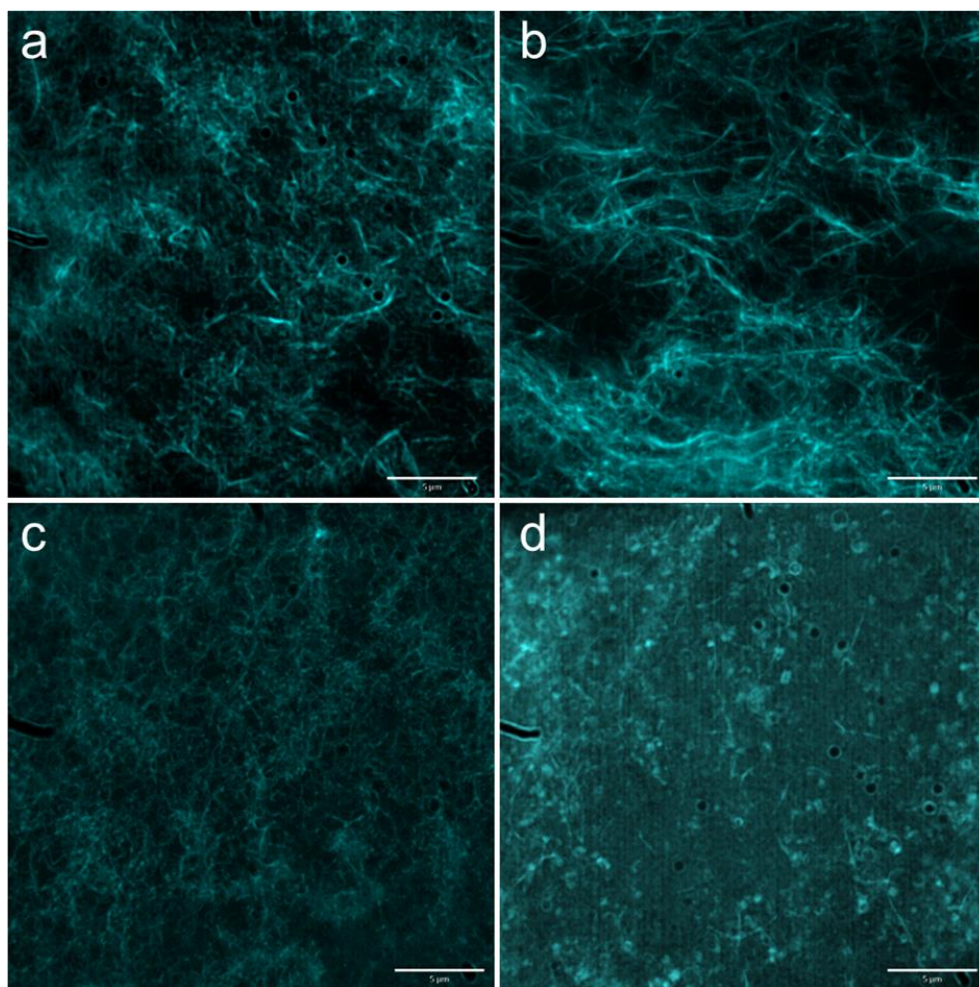


Figure 85 – Fluorescence microscopy images of gels/partial gel containing **72** (5 mg/mL) in 0.505 M aqueous solutions of: a) NaCl; b) NaH₂PO₄; c) NaHCO₃ and d) Na₂HPO₄. Scale = 5 μm.

To aid visualisation and enable a more detailed analysis of those nanofibers formed in aqueous solutions of NaCl and NaHPO₄, the fluorescence images shown in Figures 85a and 85b were refined through deconvolution methods (Chapter 6.1.2). These refined images not only confirmed the presence of long multidirectional fibres (Figures 86ai and 86bi) but with enlargement it was also possible to observe the branching and entanglement of those fibres in more detail (Figures 86aii and 86bii), allowing for a greater understanding of the gelled materials to enable rational design.

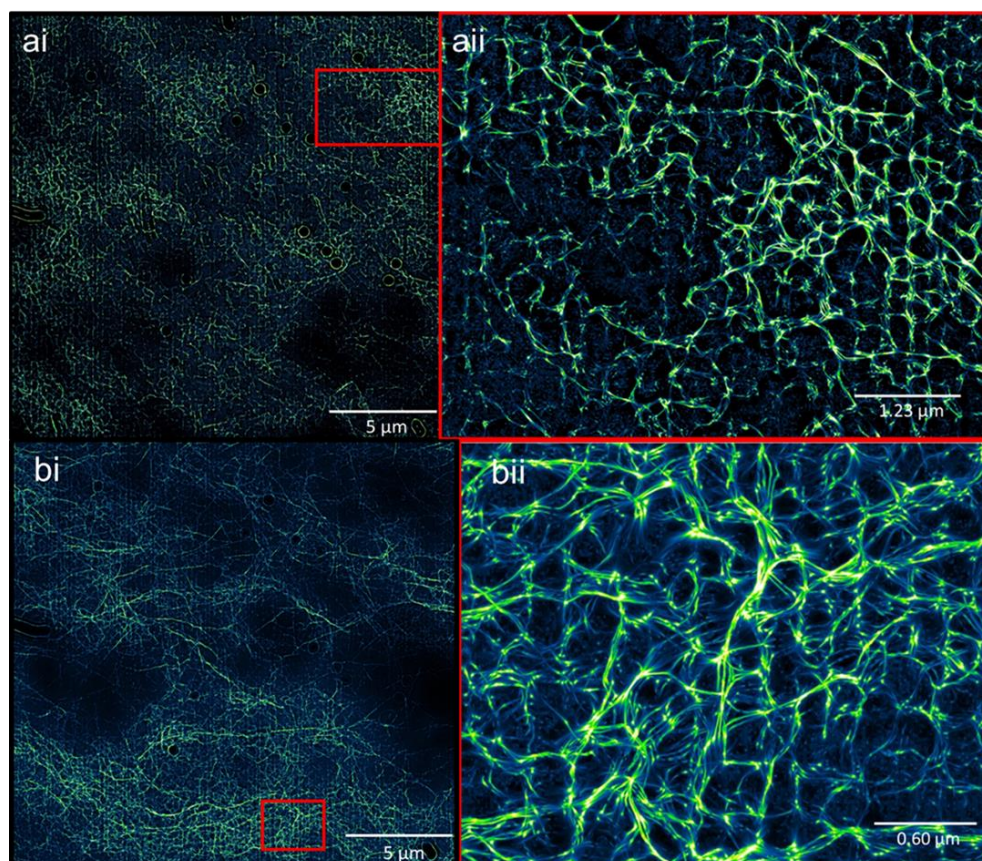


Figure 86 - Refined fluorescence microscopy images of hydrogel containing **72** (5 mg/mL) in 0.505 M aqueous solutions of ai) NaCl and bi) NaH_2PO_4 . Images aii and bii are enlarged areas outlined in red in ai and bi.

As previously discussed, compound **72** has an MGC > 5 mg in a 1 mL 0.505 M aqueous solution of Na_2HPO_4 . In Figure 85d it was observed that both a fibrous network and spherical aggregates were present. In the refined confocal image shown in Figure 87a, these combinations of structures are much more apparent. Interestingly, that same partial gel when visualised as a xerogel using SEM, demonstrated that the spherical shaped aggregates were able to withstand the dehydration process (Figure 87b), possibly supported by the presence of salt within the aqueous solution. Complimentary EDX spectra and corresponding elemental analyses were obtained to confirm the presence of **72** in those spherical aggregates as shown in Figure 87c.

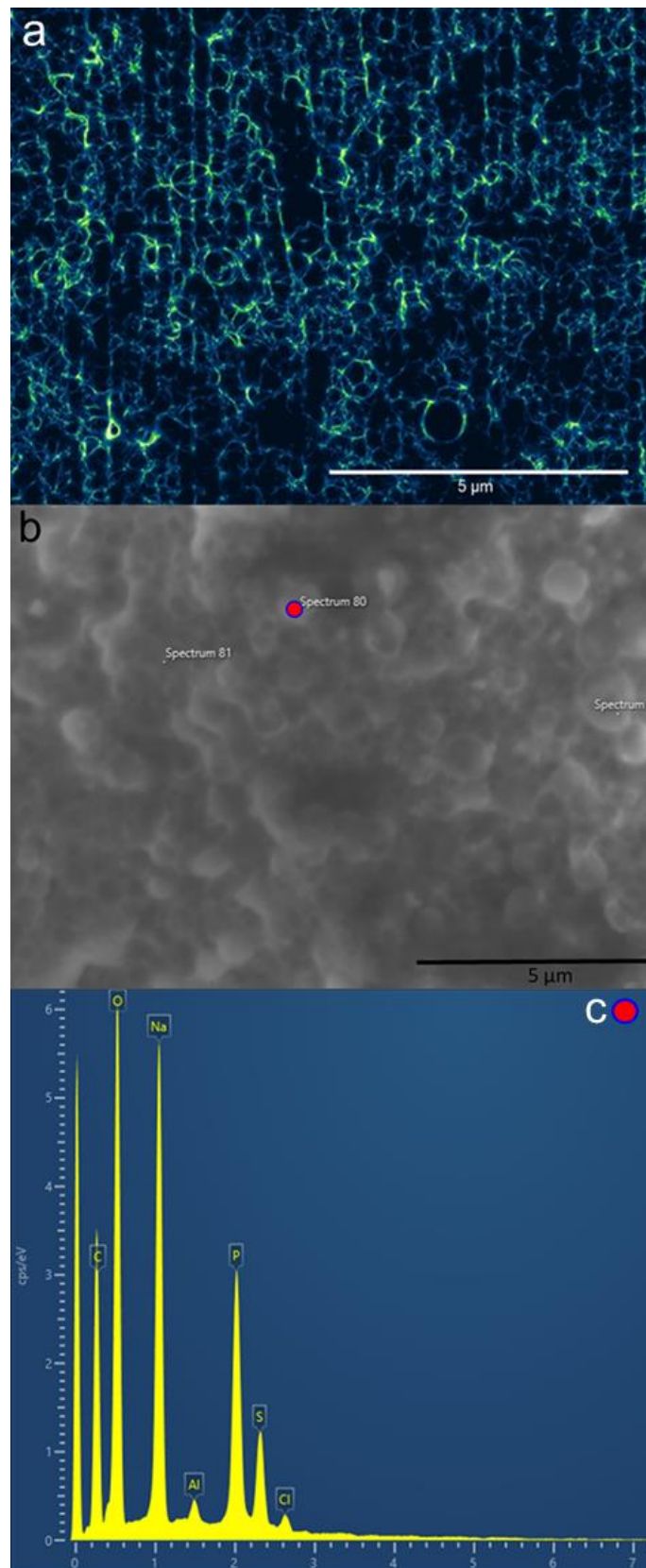


Figure 87 – Images and elemental analysis of a partial gel containing **72** (5 mg/mL) in aqueous Na_2HPO_4 (0.505 M). a) refined fluorescence microscopy image, b) SEM image of a xerogel prepared from a dehydrated hydrogel (a) and c) EDX spectrum showing elemental analysis of b. Scale = 5 μm.

In summary, it was shown that, through the use of fluorescence and SEM techniques, it was possible to observe the morphology of the fibrous networks of gelled materials formed in a variety of aqueous salt solutions. The morphology of the xerogels prepared from the dehydration of hydrogels containing NaH_2PO_4 and Na_2CO_3 show the presence of multiple rigid fibres of variable thickness emanating from a central point.

Using fluorescence microscopy it was shown that for those gelled materials with a low MGC (1.5 mg/mL) such as **72** in aqueous NaCl and NaH_2PO_4 the self-assembled nanofibers were long and multidirectional (Figures 86ai and 86bi), and with further refinement, it was possible to observe the branching and entanglement of those fibres in more detail (Figures 86aii and 86bii). In contrast, for a hydrogel containing aqueous NaHCO_3 which has a higher MGC (4.0 mg/mL) the fibres appeared to be shorter with a high cross-linked density resembling a honeycomb-like structure (Figure 85c).

Through these observations it can be concluded that those nanofiber networks formed through non-covalent interactions are responsible for the gelation process, when spherical aggregates persist the gelled material is unstable with an MGC > 5 mg/mL.

3.4 Antimicrobial efficacy determination

3.4.1 Solution state antimicrobial properties

Previous studies conducted by Hiscock and co-workers have shown members from this class of SSAs to exhibit antimicrobial properties against Gram-positive, clinically relevant MRSA (USA300).²²³ As commonly known, selective antimicrobial activity of many amphiphilic salts are driven by the negative surface charge exhibited by bacterial cell surfaces, compared to those of most healthy eukaryotic cells.^{234,235} Building on Hiscock and co-workers initial proof of principle investigations,^{236,237} the antimicrobial activity of CF_3 substituted **42**; *ortho*-benzothiazole substituted **71**; and *para*-benzothiazole substituted **72** against Gram-positive MRSA and Gram-negative *E. coli* bacteria when supplied to the bacterial cell surface as self-associated spherical aggregates were explored.

The anionic components of this series of SSA (**42**, **71** and **72**) are hypothesised to preferentially interact with phospholipid head groups that are prevalent at the surface of bacteria cells (phosphatidylethanolamine (PE, **106**) and phosphatidylglycerol (PG, **107**)), over those present at the surface of eukaryotic cells (phosphatidylcholine (PC, **108**)).^{236,237}

It is hypothesised that **42**, **71** and **72** will form complexes with both **106** (PE) and **107** (PG) through the formation of a combination of multiple hydrogen bonds and/or favourable electrostatic interactions, using **72** as an example, these binding modes are shown in Figure 88. Also illustrated in Figure 88 are the interactions between the urea of **72** and the phosphate group of **108** (PC), although these interactions may be effective, only comparatively weak, sterically hindered electrostatic interactions are possible between the sulfonate group of **72** and the tertiary ammonium group of **108** (PC).

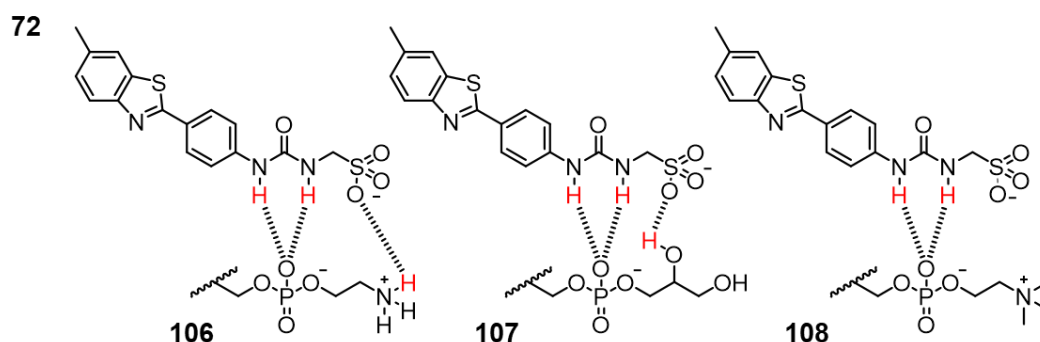


Figure 88 - Potential binding mode of **72** to PE (**106**), PG (**107**) and PC (**108**) phospholipid head groups.

The antimicrobial experiments discussed within this study were conducted and data analysed by Nyasha Allen. Using standard methods (Chapter 6.1.3) the minimum concentration of a compound needed to prevent 50 % of bacterial cell growth (MIC_{50}), of **42**, **71** and **72** against Gram-positive MRSA USA300 and Gram-negative *E. coli* DH10B were determined.²³⁸ As the TBA contained within the molecular structure of **42**, **71** and **72**, has been reported to have antimicrobial activity in itself, the MIC_{50} value of TBACl was also obtained to ensure any antimicrobial activity was due to the SSA and not the TBA cation. An overview of these results is shown in Table 14.

Table 14 - The MIC₅₀ values (mM) as determined for **42**, **71**, **72** and TBACl against clinically relevant Gram-positive MRSA USA300 and Gram-negative *E. coli* DH10B at an initial calibrated cell concentration equal to the 0.5 McFarland standard after 900 minutes (optical density measured at 600 nm).

Compound	MRSA	<i>E. coli</i>	Ratio
42	0.46	3.85	1 : 3.6
71	0.99	3.57	1 : 5.4
72	0.93	5.02	1 : 8.4
TBACl	3.18	6.36	1 : 2.0

The results from the MIC₅₀ experiments show **42**, **71** and **72** to exhibit greater activity against MRSA, with values of 0.46, 0.99 and 0.93 mM respectively, over *E. coli* (3.85 (**42**), 3.57 (**71**) and 5.02 mM (**72**)). It is hypothesised that the increased efficacy against MRSA is due to the phospholipid bilayer composition of the two bacteria. MRSA has a single phospholipid bilayer containing a high proportion of **107** (PG) (57 %), whereas *E. coli* exhibits a double phospholipid bilayer containing a greater proportion of **106** (PE) (85 %).²³⁹ These results suggest that **42**, **71** and **72** show a preference towards **107** (PG), however, other factors need to be taken into consideration such as individual bacteria phospholipid composition, which can alter according to life cycle²⁴⁰ and growth phase.²⁴¹ The MIC₅₀ results for TBACl against both MRSA and *E. coli* provide evidence that the efficacy of **42**, **71** and **72** is due to the anionic component of the molecular structure and not solely due to the presence of the TBA counter cation.

In summary, the preliminary solution state MIC₅₀ antimicrobial studies demonstrate that the anionic components of **42**, **71** and **72** all exhibit antimicrobial properties greater than that of the TBA cation. With all compounds showing greater activity against MRSA over *E. coli*, the composition of the phospholipid bilayer is hypothesised to be a contributing factor. Where **42**, **71** and **72** revealed preferential interactions with **107** (PG) over **106** (PE).

3.4.2 Antimicrobial hydrogel properties

It has been demonstrated in the preliminary studies that the molecular structure of *para*-substituted benzothiazole **72** undergoes structural changes according to the solvent environment in which **72** is in, forming dimers in DMSO-*d*₆ 0.5 % H₂O (Chapter 2.5.3.1),¹³⁶ extended aggregates, spherical in shape in EtOH:H₂O (1:19) (Chapter 2.5.1)¹³⁶ and self-assembled nanofibers in an aqueous salt solution (Chapter 3.2.1). Furthermore, **72** also exhibits antimicrobial properties against both MRSA and *E.coli* in the solution state (Chapter 3.3.1). To determine if **72** maintained the antimicrobial properties against Gram-positive MRSA and Gram-negative *E.coli* in a gelled state, a series of disk diffusion assays were performed. Disk diffusion assays were prepared and analysed with the assistance of Dr George Williams and Jessica Boles.

The physicochemical properties of those hydrogels containing **72** in the appropriate salt solution were initially investigated in order to establish which gelled material(s) were most suitable for potential topical application. For an antimicrobial hydrogel to be considered for use as a topical treatment, it must exhibit a pH within the range of 4-7 when 1 g of a hydrogel is dissolved in 10 mL of water.²⁴² This is the acceptable pH range for skin, any deviance away from these values can result in skin irritation or inflammation at the site of application.²⁴³ As shown in Table 15, **72** in aqueous salt solutions NaCl, KCl, RbCl, NaOBz, NaNO₃, Na₂HPO₄ and NaSO₄ were all shown to have a pH which is within the acceptable pH range (4-7), based on this theory these hydrogels would make good candidates for topical application.

Table 15 - Summary of average ($n = 3$) pH values of aqueous solutions at a concentration of 10% w/v at 25 °C; average ($n = 3$) melting point obtained for 1 mL of a hydrogel containing **72** (5 mg) and the appropriate salt solution (0.505 M); MGC determined through inversion testing for samples containing **72** and various aqueous salt solutions (0.505 M) at 25 °C.

Salt	pH (gel sol.)	T_m (°C)	MGC (mg/mL)
NaCl	6.23 ± 0.02	51.23 ± 0.10	1.5
KCl	6.16 ± 0.02	54.75 ± 0.09	2.5
RbCl	6.63 ± 0.02	50.91 ± 0.18	3.5
TBACl	[a]	[a]	[c]
NaF	7.40 ± 0.03	46.91 ± 0.07	2.0
NaHCO ₃	10.03 ± 0.01	45.39 ± 0.12	4.0
NaOAc	7.07 ± 0.02	46.03 ± 0.13	3.5
NaOBz	5.76 ± 0.03	52.35 ± 0.09	1.5
NaNO ₃	6.74 ± 0.02	54.48 ± 0.15	1.5
NaH ₂ PO ₄	4.75 ± 0.03	43.94 ± 0.10	1.5
NaHSO ₄	[a]	[a]	[c]
Na ₂ CO ₃	11.40 ± 0.00	42.94 ± 0.13	3.0
Na ₂ HPO ₄	8.34 ± 0.00	[b]	[b]
Na ₂ SO ₄	6.92 ± 0.05	43.22 ± 0.12	3.5

[a] Precipitate formation prevented measurement. [b] Partial gel formed at 5 mg/mL. [c] Precipitation at 5 mg/mL, no gel formation.

The melt temperature (T_m) of the hydrogels containing 5 mg of **72** in 1 mL of the appropriate salt solutions were investigated to determine if they were robust enough to not be adversely affected during either the administration process or during storage. The results from these studies show that all of the hydrogels investigated exhibited a T_m above that of average skin temperature (≈ 31 - 32 °C),²⁴⁴ and that the T_m was dependent on the salt solution contained within the gelled material, ranging from ≈ 43 - 55 °C. The hydrogels containing divalent salts Na₂CO₃ or Na₂SO₄ were shown to have the lowest T_m values (≈ 43 °C) this is expected due to the increased ionic strength of the salt solution in addition to high MGCs of 3.0 and 3.5 mg/mL respectively.

The results from the physicochemical analysis of the hydrogels containing **72** (Chapter 3.3.2, Table 13 (storage and loss moduli) and Table 15) identify **72** in aqueous salt solution NaCl to be the lead gelled material for topical antimicrobial development.

This conclusion was made based on a number of factors which include: i) solid-like characteristics as determined through observation of the storage and loss moduli; ii) the pH of the NaCl gel (≈ 6) falls within the normal skin pH range limiting the potential for any adverse skin issues; iii) the T_m is > 50 °C, therefore, is likely to be more robust at temperatures below this; iv) exhibits a low MGC and v) in comparison with the other salt solutions tested the NaCl solution is the least toxic.

In order to establish whether **72** had maintained the antimicrobial activity observed in the solution state as a gelled material, a series of antimicrobial surface gel diffusion assays were performed against MRSA and *E. coli* bacteria using the lead NaCl hydrogel. For this study a ≈ 50 mg aliquot of the hydrogel formed with **72** (5 mg) in 1 mL aqueous NaCl (0.505 M) was transferred to the surface of an agar plate inoculated with either Gram-positive MRSA or Gram-negative *E. coli* bacteria. The agar plate was then incubated at a temperature of 37 °C overnight and the zone of bacterial growth inhibition was used to determine antimicrobial hydrogel activity.

The results from these antimicrobial surface efficacy experiments show that the hydrogel formed with **72** (5 mg) in 1 mL NaCl (0.505 M) acts as an antimicrobial material towards both MRSA and *E. coli* with zones of inhibition averaged ($n=3$) as ≈ 16 mm and ≈ 15 mm in diameter respectively, as illustrated in Figure 89. As anticipated the antimicrobial activity was shown to be localised to the position where the gel was supplied to the surface of the agar plate, this limited diffusion is due to **72** being within the construct of the fibrous 3D network shown in Chapter 3.3.3 as opposed to being immobilised within the mesh of the fibres and therefore able to diffuse out.

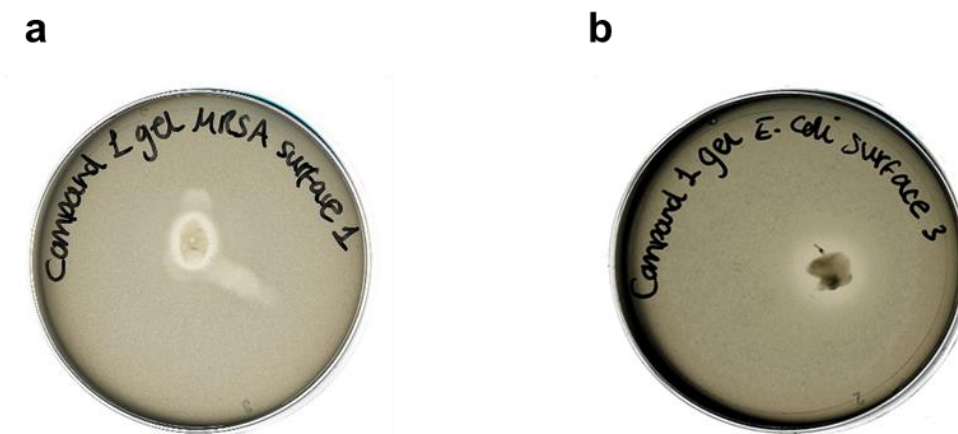


Figure 89 – Surface disk diffusion assays confirming the antimicrobial activity of the hydrogel (≈ 50 mg added to the surface) containing **72** (5 mg/mL) in NaCl (0.505 M) against: a) MRSA USA300; b) *E. coli* DH5B.

3.4.3 Co-formulated hydrogel properties

Hydrogels were first described as potential drug delivery vehicles in the 1950s by Lin and Wichterle.²⁴⁵ Since this first description, a vast amount of hydrogels have been developed for this purpose, utilising a variety of material systems and design principles. Treesuppharat and co-workers successfully combined gelatin with bacterial cellulose to develop a hydrogel composite material which was considered a good candidate for drug delivery systems due to their extensive swelling ratio of ≈ 400 -600 %. The higher the swelling ratio, the greater increase in distance between cross-linked polymer chains, which allow drug molecules to be released and absorbed into the bloodstream.²⁴⁶ In 2002 Xu and co-workers reported the first antibiotic hydrogelator vancomycin-pyrene. Here, a pyrene substituent was attached to the c-terminal of the backbone of clinically relevant vancomycin. Xu and co-workers suggested π - π stacking interactions and intermolecular hydrogen bonding in an aqueous environment provided the driving forces to form a gelled material of ~ 0.36 wt %. However, efficacy studies against 2 *VanA*-positive *Enterococcus faecalis* revealed high potency levels, hypothesised to be due to a high concentration of aggregated polymers at the cell surface. These investigations are still ongoing.²⁴⁷

Hydrogel suitability as drug delivery systems is attributed to their hydrophilic 3D fibrous networks, into which large amounts of water or biological fluids can be imbibed, therefore resembling, to a certain extent biological tissues.²⁴⁸ As the mesh (gel pore) controls the steric interactions between the fibrous network and the drugs, the size of the mesh will determine how drugs diffuse through the hydrogel. If the mesh size is ≥ 1 (where $r_{\text{mesh}}/r_{\text{drug}} \approx 1$) the drug release process will be dominated by Fickian diffusion. However, when the mesh size is < 1 the effect of steric hindrance on drug diffusion becomes prominent. This results in the immobilisation of the drug molecules which can only be released through controlled degradation or deformation via a stimulus (Figure 90).²⁴⁹ Consequently, many hydrogel drug delivery vehicles are synthesised to respond to a number of physiological stimuli present in the body, such as ionic strength, temperature and pH.²⁵⁰

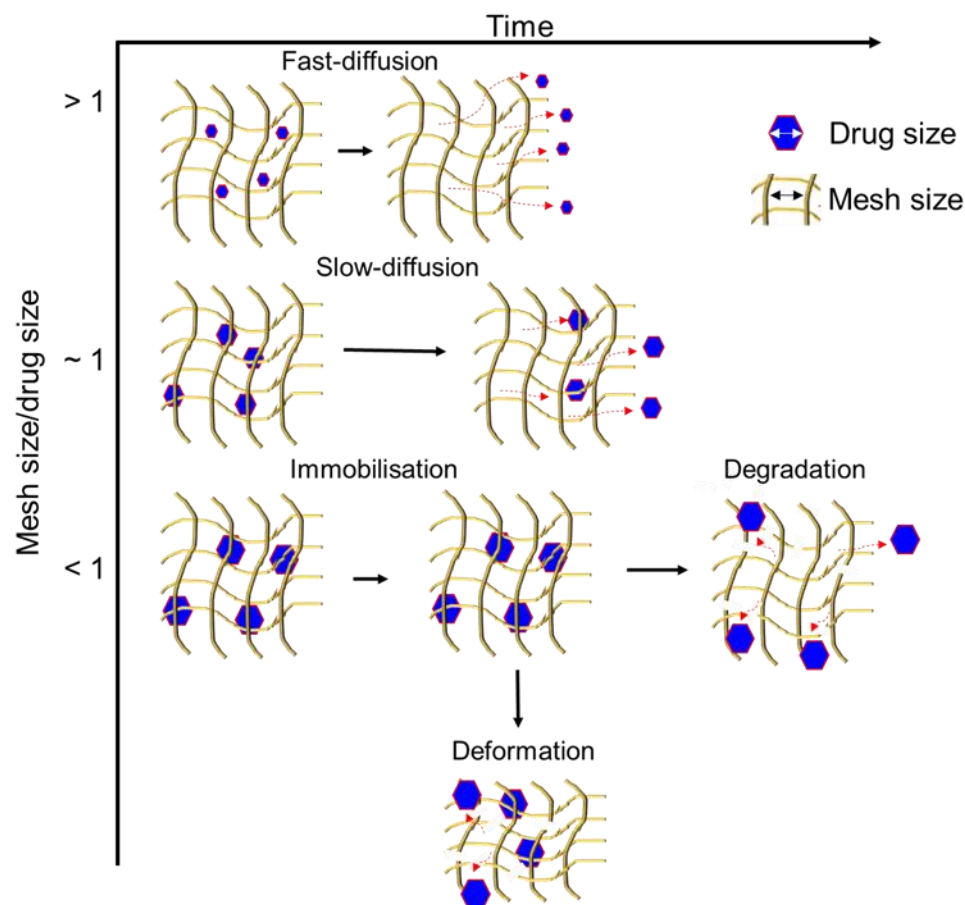


Figure 90 – Cartoon representation illustrating fast and slow diffusion of drug molecules and degradation and deformation of mesh which facilitates immobilised drug release from a hydrogel fibrous network against time.²⁴⁹ The red dashed lines represent the diffusion pathways of the drug molecules.

In an attempt to improve the efficacy of these materials against Gram-positive MRSA and Gram-negative *E.coli*, the SSA hydrogel (**72** in 1 mL of aqueous NaCl (0.505 M)) was co-formulated in a 1:1 molar ratio with the sodium salt of commonly prescribed antibiotic ampicillin (**105**) (Figure 91).

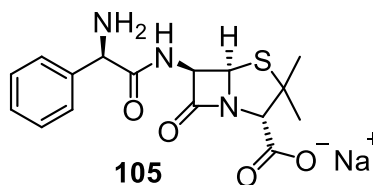


Figure 91 – Chemical structure of the sodium salt of commonly prescribed antibiotic ampicillin (**105**).

Interestingly, here it was observed that the addition of the sodium salt of ampicillin (**105**) resulted in a decrease of MGC from 1.5 mg/mL to < 1.0 mg/mL, this was confirmed through an inversion test, as illustrated in Figure 92. It is hypothesised that the increase in salt concentration stabilised the extended fibrous network resulting in a lower MGC.

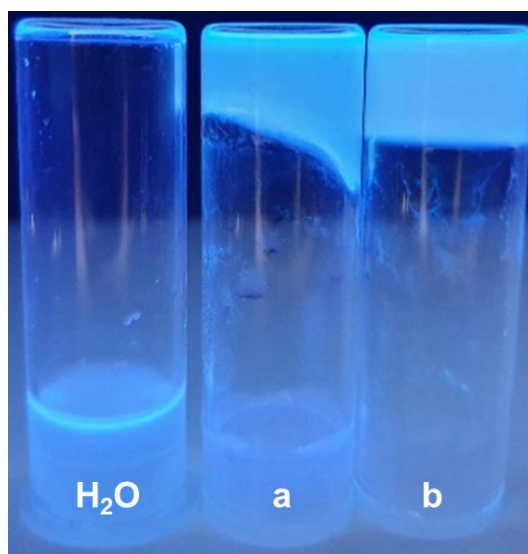


Figure 92 – Inversion tests of **72** (1 mg) in 1 mL of H₂O (left); a) partial hydrogel of compound **72** (1 mg) in 1 mL aqueous NaCl (0.505 M); b) hydrogel of compound **72** (1 mg) on a 1:1 molar ratio with ampicillin (**105**) in 1 mL of aqueous NaCl (0.505 M).

The physicochemical properties of the ampicillin incorporated hydrogel were then investigated to find out whether this hydrogel would be suitable for topical application.

The results from this study demonstrate the ampicillin incorporated hydrogel to exhibit solid-like characteristics similar to those of the other hydrogels investigated in this chapter, where the storage modulus G' was shown to be $\approx 7.4 \times$ greater than the loss modulus (G'') (Chapter 3.3.2). An example is illustrated in Figure 93. Furthermore, an average ($n=3$) pH value of 7.12 ± 0.02 was calculated when 2 g of the ampicillin hydrogel was dissolved in 20 mL of H_2O and the average ($n=3$) T_m was shown to be $> 50 \text{ }^\circ\text{C}$ at $52.26 \text{ }^\circ\text{C} \pm 0.07 \text{ }^\circ\text{C}$.

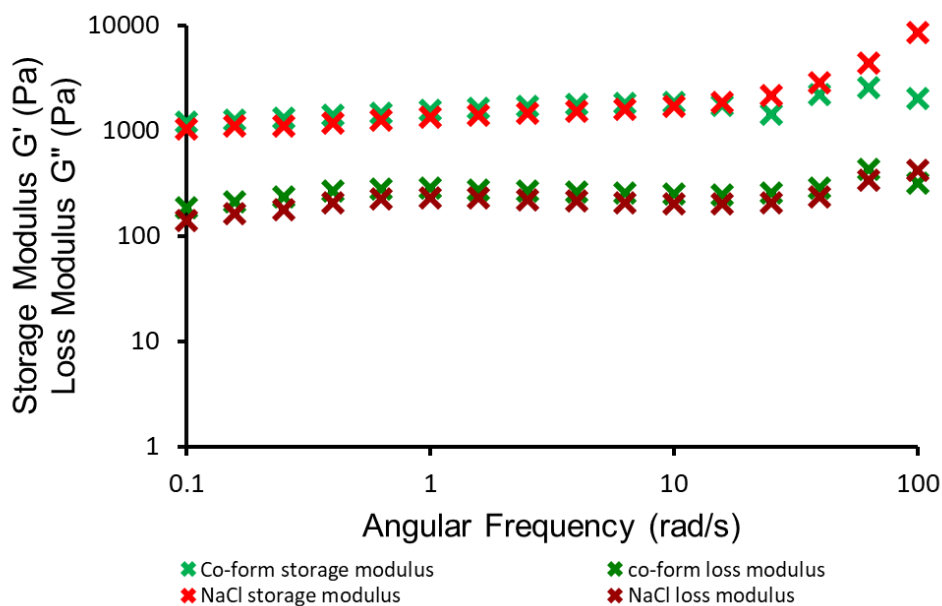


Figure 93 - Graph showing average results ($n=3$) from frequency sweep experiments obtained from the linear viscoelastic region under a constant shear strain (γ) of 0.925 % (298 K). Gelator **72** (5 mg) and ampicillin (**105**) (3 mg) in 1 mL aqueous NaCl (0.505 M) (green), and **72** (5 mg) in 1 mL aqueous NaCl (0.505 M) (red).

In order to establish whether the efficacy of these materials had improved with the incorporation of the sodium salt of antibiotic ampicillin (**105**), a further series of disk diffusion surface assays were performed. These yielded improved zones of inhibition against both MRSA ($\approx 23 \text{ mm}$) and *E. coli* ($\approx 59 \text{ mm}$) as shown in Figure 94.

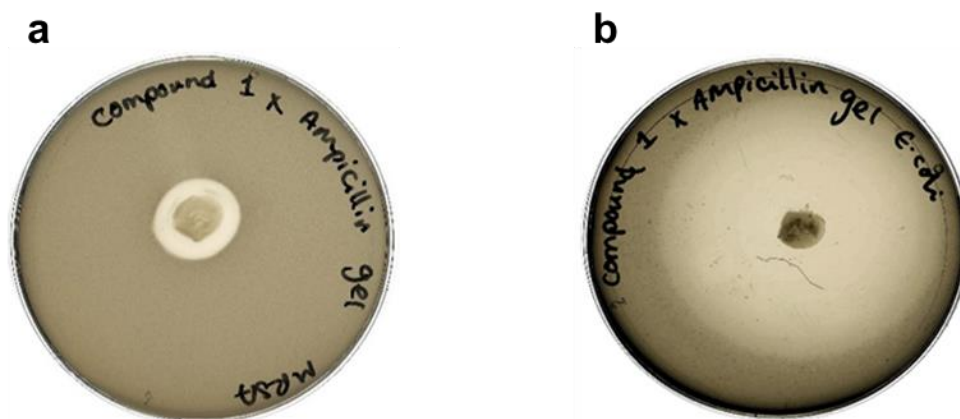


Figure 94 – Surface disk diffusion assays confirming the antimicrobial activity of the hydrogel (≈ 50 mg added to the surface) containing **72** (5 mg/mL) in NaCl (0.505 M) against a) co-formulated in a 1:1 molar ratio with ampicillin (**105**) against MRSA USA300; b) co-formulated in a 1:1 molar ratio with ampicillin against *E. coli* DH5B.

To confirm the increase in zone of inhibition with the addition of ampicillin (**105**) to **72** in aqueous NaCl against MRSA (≈ 16 mm to ≈ 23 mm) and *E. coli* (≈ 15 mm to ≈ 59 mm) (Figures 89a and 89b and 94a and 94b) a series of well diffusion assays were performed in triplicate ($n=3$). For these assays, a well was cut into an agar plate inoculated with either MRSA or *E. coli* bacteria and the antimicrobial hydrogel (≈ 50 mg) added to fill the well. For comparison, two additional series of analogous assays were performed: i) with ampicillin at the same concentration present in the co-formulated hydrogel (8.1 mM) in a 0.505 M aqueous NaCl solution; and ii) with aqueous NaCl (0.505 M). The agar plate was then incubated at a temperature of 37 °C overnight. In this instance, a zone of inhibition is only observed if the antimicrobial hydrogel is able to permeate through the agar gel. The results show that all well diffusion assays exhibit a zone of inhibition (Figure 95).

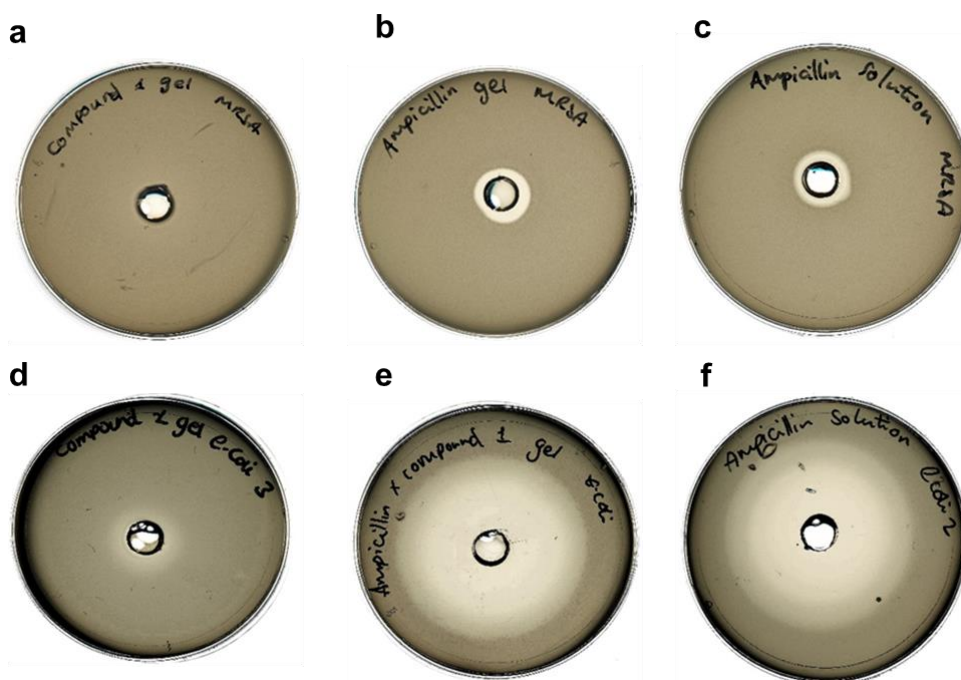


Figure 95 – Well disk diffusion assays confirming the antimicrobial activity of a) the hydrogel containing **72** (5 mg/mL) in NaCl (0.505 M) against MRSA; b) the hydrogel co-formulated in a 1:1 molar ratio with ampicillin (**105**) against MRSA USA300; c) ampicillin (**105**) (8.1 mM) alone in an aqueous solution of NaCl (0.505 M) against MRSA; d) the hydrogel containing **72** (5 mg/mL) in NaCl (0.505 M) against *E. coli*; e) the hydrogel co-formulated in a 1:1 molar ratio with ampicillin (**105**) against *E. coli*; f) ampicillin (**105**) (8.1 mM) alone in an aqueous solution of NaCl (0.505 M) against *E. coli*.

The zone of inhibition observed for the hydrogel containing **72** (5 mg/mL) in aqueous NaCl (0.505 M) against MRSA and *E. coli*, were as expected, relatively small in diameter (≈ 14 mm and ≈ 17 mm respectively) (Figures 95a and 95d). These measurements support the earlier hypothesis that although **72** exhibits antimicrobial activity against both bacteria models, **72** forms the gelled fibrous network so is, therefore, unable to diffuse through the agar gel. However, the hydrogel containing ampicillin (**105**) is shown to have a zone of inhibition greater than that of the hydrogel alone (≈ 17 mm (MRSA) and ≈ 53 mm (*E. coli*)) (Figures 95b and 95e). Those agar plates that were investigated with an 8.1 mM aqueous NaCl solution of ampicillin (**105**) confirmed that the percentage of the released drug (ampicillin, **105**) was not hindered by the gel fibres and could diffuse freely as the zone of inhibition was shown to be similar to that of the co-formulated hydrogel (≈ 15 mm (MRSA) and ≈ 52 mm (*E. coli*)) (Figures 95c and 95f). This supports the hypothesis that the hydrogel formed from **72** (5 mg/mL) in an aqueous NaCl (0.505 M) solution can be used as a drug delivery vehicle.

As expected, the well disk diffusion assays applied with an aqueous solution of NaCl (0.505 M) alone showed no zone of inhibition to be present (Appendix 2.7.1, Figure S418 and Appendix 2.7., Figure S424), therefore confirming that any antimicrobial activity was due to the presence of either **72** and/or ampicillin (**105**).

In summary, it was shown through a series of physicochemical investigations that the NaCl containing hydrogel was the lead material for topical antimicrobial material development. Through a series of surface and well diffusion assays against MRSA and *E.coli* this hydrogel demonstrated apparent minimal antimicrobial activity with small zones of inhibition. This was hypothesised to be due to antimicrobial **72** forming the main construct of the gel fibrous network and, therefore was unable to diffuse through the agar. However, when co-formulated in a 1:1 ratio with ampicillin (**105**) a significantly greater zone of inhibition was observed. This suggests that the ampicillin was free to diffuse through the hydrogel, into the agar, leading to the conclusion that the hydrogel formed from **72** (5 mg/mL) in an aqueous NaCl (0.505 M) solution can be used as a drug delivery vehicle.

3.5 Chapter 3: Summary

It has been shown that in an aqueous salt solution (0.505 M), *para*-substituted benzothiazole **72** was found to form a hydrogel. The stability of the resultant gelled material was found to be dependent on several salt solution-based factors such as cation size; ionic strength and pH (Chapter 3.2).

The intrinsic fluorescent properties of **72** enabled for *in situ* visualisations of the fibrous networks that form the gelled materials. The presence of **72** within the construct of the gelled material was verified using SEM and complimentary EDX analysis (Chapter 3.3.3).

Through these observations, it was concluded that those nanofiber networks formed through non-covalent interactions are responsible for the gelation process, when spherical aggregates persist the gelled material is unstable with an MGC > 5 mg/mL.

The preliminary solution state MIC₅₀ antimicrobial studies demonstrate that the anionic components of **42**, **71** and **72** all exhibit antimicrobial properties. With all compounds showing greater activity against MRSA over *E.coli*, this was attributed to the composition of the phospholipid bilayer. Where it is hypothesised that **42**, **71** and **72** revealed preferential interactions with **107** (PG) over **106** (PE) (Chapter 3.4.1).

Finally, from the physicochemical investigations, the NaCl containing hydrogel was identified as the lead material for topical antimicrobial material development (Chapter 3.4.2). In these studies, it was observed that the hydrogel alone demonstrated minimal antimicrobial activity against MRSA and *E.coli*, thought to be due to **72** being within the construct of the hydrogel preventing it from diffusing through the agar. Consequently, this hydrogel was proven to be more effective as a drug delivery vehicle, as when co-formulated in a 1:1 ratio with ampicillin (**105**) a greater zone of inhibition was observed against both model bacteria (Chapter 3.4.3).

3.6 Chapter 3: Conclusion

To conclude it has been shown that the solvent environment can be used to control self-association events and resultant material formation. In the presence of an aqueous salt solution, *para*-substituted benzothiazole **72** was shown to form a hydrogel, the physicochemical and morphological properties of which were reliant on the salt present. The lead hydrogel (**72** in aqueous NaCl) was shown to maintain its antimicrobial properties against both model Gram-positive and Gram-negative bacteria. Furthermore, the hydrogel formed with **72** in aqueous NaCl was also found to support the incorporation of the antibiotic ampicillin. The activity of the ampicillin was shown to be conserved, and diffusive release was achieved at concentrations great enough to inhibit the growth of both model bacteria.

3.7 Future work

These preliminary studies primarily focussed on four structurally related compounds (**42**, **71**, **72** and **104**), with only one (**72**) shown to gelate in a 0.505 M aqueous salt solution, investigations will continue into the concentration-dependence of these aqueous salt solutions. It was hypothesised that the π - π stacking interactions of the benzothiazole unit within the molecular structure, were essential for stabilising the self-assembly process. Building on Aufderhorst-Roberts and co-workers studies where they investigated the properties of gelled materials formed from amino-acid derivatives Fmoc-tyrosine and Fmoc-phenylalanine.²⁵¹ These materials were found to exhibit two different pore sizes allowing for dyes to diffuse out at different rates.²⁵¹ Future work will include the development and synthesise of second-generation LMWGs, which will incorporate amino acid derivatives within their molecular skeleton. It is hypothesised the additional aromatic ring system will promote gel fibre stabilisation through intermolecular π - π stacking interactions as observed with **72**. Furthermore, there may also be the potential to monitor the rate of diffusion of ampicillin from the hydrogel.

Chapter 4

4.1 Introduction

As discussed in Chapter 3 supramolecular gels can be broadly classified into two categories, based on the immobilised solution components within the 3D gel matrix: organogels contain an organic solvent,^{189,190} whereas hydrogels contain water.^{192–197} Due to the popularity of this material type, a range of characterisation methods have been developed to enable the elucidation of LMWG structure-material property relationships.²⁵²

Within this introduction, the focus will move to detail those techniques commonly used for supramolecular gel characterisation, with appropriate examples and discuss their limitations. Standard experimental methods used to identify the presence of, and effectively compare supramolecular gels include the elucidation of an MGC through inversion testing,²⁵³ (Chapter 3.2) and rheology, to observe bulk materials (Chapter 3.3.2).²⁵⁴ In addition to these standard methods, other more exploratory techniques are often employed. Gunnlaugsson and co-workers have used conventional UV-Vis spectroscopy to identify the formation of europium incorporated organogels. The interaction of the terpyridine-based tripodal ligand (L) with Eu³⁺ ions was investigated in MeOH. The change in absorption was monitored, where it was clear that upon binding to the Eu³⁺ ions, the absorption spectrum of ligand L was bathochromically shifted indicating the formation of a EuCl₃-L complex with a 1:1 stoichiometry.²⁵⁵

As demonstrated in Chapter 3 (3.3.3) microscopy techniques such as SEM and confocal fluorescence microscopy are viable methods for observing the morphology of a 3D fibrous network, either as xerogels or *in situ*, within the solution state.^{2,256} Transmission and SEM techniques have also been utilised by Varghese and co-workers to characterise the gel fibres of the corresponding xerogel to photoresponsive amphiphilic butadiene organogels (Figure 96). The results indicated the initial presence of spherical aggregates for **109-112**, with those spherical aggregates of **112** in MeOH at 1 x 10⁻⁴ M exhibiting diameters of ≈ 2 μm. These aggregates are shown to merge until they finally link together to form organogels.

It is anticipated that these photoresponsive systems, capable of spontaneous hierarchical self-assembly, can be useful in controlled release systems.²⁵⁷

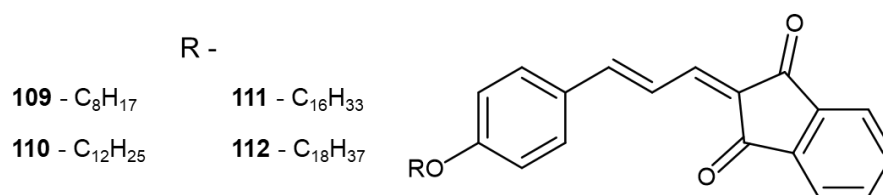


Figure 96 - Novel class of donor–acceptor-substituted amphiphilic LMWG butadienes.²⁵⁷

The architectures of fluorescently labelled biomimetic hydrogels at the subcellular length-scale have been studied by Rocha and co-workers using confocal fluorescence microscopy. The images revealed a fibrillar heterogeneous structure, with an average pore diameter range of 1.8 to 3.7 μm . The size of the pore was shown to decrease with increasing polymer concentration $0.25 > 0.5 > 1 \text{ mg mL}^{-1}$ (Figure 97) or polymer length (145 > 229 nm). As optical imaging techniques can be performed with the sample in their native material state, Rocha and co-workers concluded that the methods employed in this study were shown to be compatible with live-cell imaging.²⁵⁸

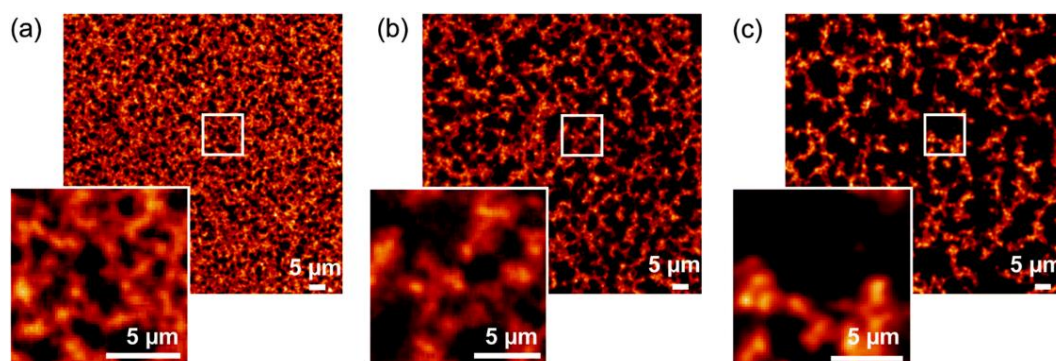


Figure 97 - Influence of polymer (145 nm) concentration on fibre architecture a) 1 mg mL⁻¹; b) 0.5 mg mL⁻¹; and c) 0.25 mg mL⁻¹.²⁵⁸ Reproduced with permission from the Royal Society of Chemistry.

Dynamic light scattering was utilised by Paradossi and co-workers to monitor the dynamic and structural parameters of telechelic poly(vinyl alcohol) hydrogels. Using this technique, they were able to determine the sol-gel transition point, by observing a dramatic change of the normalised correlation function of the scattered electrical field. These results correlated with the data obtained from rheological measurements of the same systems.²⁵⁹

Powder X-ray diffraction is commonly used to obtain information about the molecular packing arrangement of LMWGs in the gelled state.^{260,261} Banerjee and co-workers employed this technique to explore the packing arrangement of xerogels, that were formed through the dehydration of aromatic amino acid-based gels. Using powder XRD the presence of a 1D lamellar structure was identified through the observation of a series of periodic peaks from 6.55 ° to 21.75 °. Additionally, a peak at 23.65 ° corresponded to the π - π stacking distance of the stabilising aromatic phenyl ring of the gelator molecules. These LMWGs were shown to be capable of phase selective gelation of aliphatic hydrocarbons, such as oil from an oil-water mixture, therefore, the development of these LMWGs are suggested to hold future promise for oil spill recovery methods.²⁶²

Solid²⁶³ and solution state high-resolution NMR spectroscopy have frequently been used to characterise polymeric structural features and some physical processes of gelled materials such as mobility and fibre formation.²⁶⁴ The change in chemical shift and peak intensities of spectra enable structural quantities such as polymer composition and sequence distribution to be calculated.^{265,266} Miravet and co-workers employed solution state ¹H NMR to study a supramolecular organogel formed through the self-assembly of LMWG **113** (Figure 98). The intensity of the NMR signal of **113** in CD₃CN at 30 °C was plotted against the concentration of **113** (measured using diphenylmethane as an internal standard). From these NMR analyses, a saturation curve was obtained, when a plateau was observed it was determined the organogel had formed. Consequently, the addition of any new material did not affect signal intensity.²⁶⁷

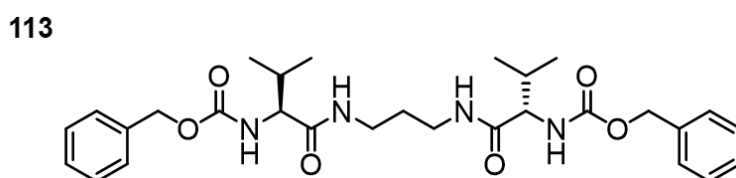


Figure 98 – LMWG synthesised by Miravet and co-workers.²⁶⁷

More recently small-angle neutron diffraction techniques have been developed by Draper and co-workers to derive the packing arrangement for deuterated monomeric units in aggregated (high pH) and gelled (low pH) materials. Here, the gel fibres were considered to have a non-uniformed cross-section, hypothesised to be elliptical cylinders.²⁶⁸

All of these experimental techniques employed to confirm the presence, or further investigate the properties of the gelled material exhibit some limitations. These include the use of expensive often specialised equipment that may not be readily available; the removal of solvent to produce a xerogel which can result in artefacts being present in the produced images; low potential for accurate data interpretation; the requirement of large sample sizes and/or long experimental time frames.

In this chapter, a novel high-throughput gel characterisation method will be introduced using microplate reader technology. A microplate reader is a laboratory instrument commonly used for quantitative biological and chemical assays. This technology allows for multiple biological, chemical or physical reactions of between 5 μL to 200 μL to be measured simultaneously within the well of a microplate. This microplate can consist of between 6 to 384 small wells in which separate reactions take place, the type of microplate should be selected according to the information required from the experimental procedure.

The potential of these methodologies is demonstrated using a compound that has been extensively discussed in Chapter 2 and Chapter 3 of this document. As an overview *para*-substituted benzothiazole **72** (Figure 99) was shown to form anionic, hydrogen bonded dimeric species in DMSO ($d_H \approx 1.4 \text{ nm}$),¹³⁶ spherical aggregates in H_2O and $\text{H}_2\text{O}:\text{EtOH}$ 19:1 mixtures ($d_H \approx 55\text{-}350 \text{ nm}$)¹³⁶ and hydrogels in aqueous salt solutions (Chapter 3.2).

Using this proof of principle method, the absorbance (Abs.), optical density (OD) and excitation/emission measurements of **72** in three different solution dependent material forms were investigated.

72

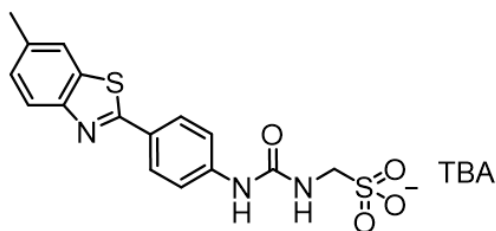


Figure 99 – Chemical structure of the LMWG discussed in this chapter.

For the purpose of this novel characterisation method, supramolecular hydrogels/solutions of **72** were prepared either in black bottom or low UV-transparent 96-well microplates. SSA **72** in the relevant solution was transferred as a 200 μL aliquot to each microplate well, at a temperature higher than the melting point (T_m) of the material (Table 16). Due to the sensitivity of the equipment and to conduct comparative measurements the concentration of **72** was decreased from 5 mg/mL to 1.5 mg/mL. This decrease in concentration means some of the materials are tested below the measured MGC, so are therefore incomplete gels (i). It is hypothesised that these incomplete gels will still exhibit fibre formation which can be observed through the methods applied within this study. Furthermore, the temperature range that the experiments were performed at (25-45 $^{\circ}\text{C}$), were selected for the following reasons: i) 25 $^{\circ}\text{C}$ is the temperature at which the materials studied are known to gelate and ii) 45 $^{\circ}\text{C}$ is the maximum temperature the plate reader can achieve. Standards of all solutions were tested to be certain any observations were due to the presence of **72** in the appropriate solution and not the solution itself. All experiments were repeated in triplicate ($n=3$) to ensure experimental reproducibility. All data were verified by a uniformity experiment which incorporated all 96-wells of the microplate (Appendix 3.5, Figures S538-S547).

The work detailed in this chapter has been published within the following peer-reviewed journal article:

1. High-throughput characterisation of supramolecular gelation processes using a combination of optical density, fluorescence and UV-Vis absorption measurements [L. J. White](#), C. Wark, L. Croucher, E. R. Draper and J. R. Hiscock, *Chem. Commun.*, 2020, **56** (66), 9557-9560.¹

4.2 UV-Vis absorbance measurements

In the first instance, the microplate reader was utilised to determine if it was possible to detect material formation through a comparative change in absorbance readings. For this experimental procedure, a UV-Vis absorbance spectrum was recorded at 25 °C and 45 °C for each 200 μ L sample of **72** (1.5 mg/mL) in the appropriate aqueous salt solution (0.505 M), H₂O or DMSO (Table 16). Upon first observation of the collected spectra, there was shown to be a significant variance in absorbance at \approx 450 nm (Abs.₄₅₀) (Figure 100). The results from these preliminary experiments led to the hypothesis that this increase in Abs.₄₅₀ could be indicative of gel fibre presence, which can absorb at this wavelength and/or cause the observable scattering of the incident light.

Table 16 - Average ($n=3$) T_m (°C) for hydrogels of **72** (5 mg/mL) obtained for a hydrogels/incomplete hydrogels of **72** (1.5 mg/mL) in H₂O, DMSO or a 0.505 M aqueous salt solution. Mat. Prop. = material property of **72** (1.5 mg/mL) in DMSO, H₂O or aqueous salt solutions (0.505 M) at 25 °C (n = no gel, i = incomplete gel, g = gel).

Soln.	T_m °C	MGC mg/mL	Mat. prop.	Soln.	T_m °C	MGC mg/mL	Mat. prop.
H ₂ O	n/a	n/a	n	NaOAc	46	3.5	i
DMSO	n/a	n/a	n	NaF	47	2.0	i
Na ₂ HPO ₄	i	[a]	i	NaCl	51	1.5	g
NaH ₂ PO ₄	44	1.5	g	RbCl	51	3.5	i
Na ₂ CO ₃	43	3.0	i	NaNO ₃	52	1.5	g
Na ₂ SO ₄	43	3.5	i	NaOBz	54	1.5	g
NaHCO ₃	45	4.0	i	KCl	55	2.5	i

[a] Partial gel formed at 5 mg/mL.

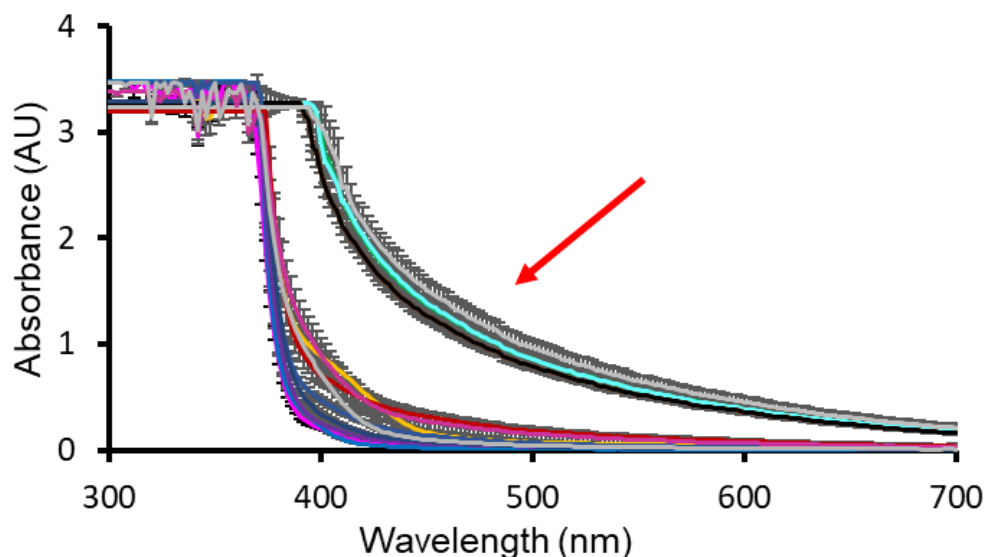


Figure 100 - Average ($n=3$) absorbance graph of **72** (1.5 mg/mL) in all those solutions shown in Table 16 recorded for each 200 μL sample at 45 $^{\circ}\text{C}$. Arrow indicates a change of absorbance at Abs.₄₅₀. Error bars represent the full range of UV-Vis measurements for three repetitions.

As previously identified in Chapter 3.4.2 the T_m of the gelled materials investigated at 5 mg/mL ranged from ≈ 43 $^{\circ}\text{C}$ to 54 $^{\circ}\text{C}$ (Table 15). To further explore the hypothesis that an increased Abs.₄₅₀ value is indicative of gel fibre presence, a series of UV-Vis absorbance spectra were recorded for each 200 μL sample at 5-degree increments from 25-45 $^{\circ}\text{C}$. The reason for the 5-degree increments was to enable comparison with the T_m points of the gelled material, to identify if the Abs.₄₅₀ value decreases as those fibres dissociate with the addition of heat.

In a solution of H_2O , instead of gel fibres, **72** is known to form self-associated spherical aggregates that destabilise at temperatures > 40 $^{\circ}\text{C}$.¹³⁶ Upon observation of the spectra obtained for **72** in H_2O at 25-45 $^{\circ}\text{C}$, as anticipated there was an absence of an increase in Abs.₄₅₀ which would be associated with gel fibre presence, instead Abs.₄₅₀ remained at 0.03 AU for all temperatures (Figure 101). Furthermore, there was also no notable change in spectra for temperatures > 40 $^{\circ}\text{C}$. As a result, this experimental method cannot be used to identify destabilisation of those spherical aggregates in solution at temperatures ≤ 45 $^{\circ}\text{C}$.

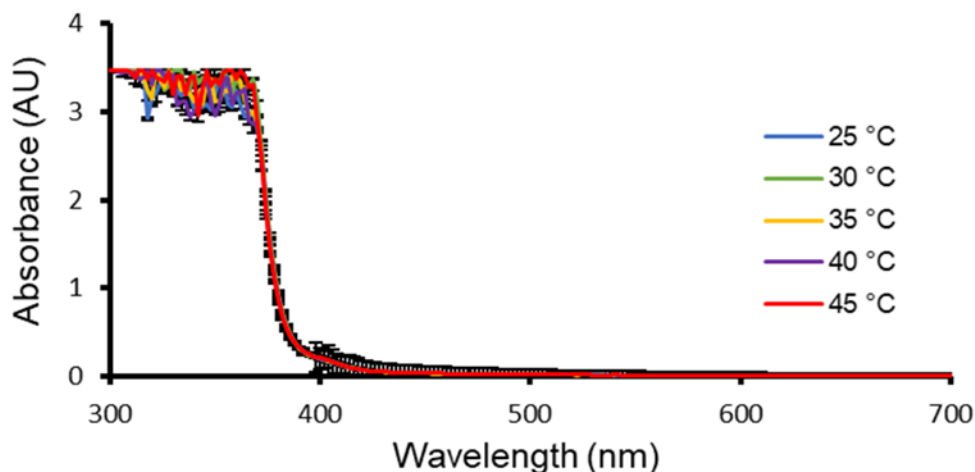


Figure 101 - Average ($n=3$) absorbance graph of **72** (1.5 mg/mL) in H₂O recorded for each 200 μ L sample at 5-degree increments from 25-45 $^{\circ}$ C, showing no notable increase in Abs._{.450}. Error bars represent the full range of UV-Vis measurements for three repetitions.

There was also no discernible difference shown between UV-Vis absorbance spectra obtained for solutions of **72** in DMSO over this same temperature range where instead of gel fibres, dimeric species are known to prevail (Figure 102). The Abs._{.450} remained at 0.02 AU for all temperatures, again supporting the hypothesis that an increase in this region is due to the presence of gel fibres. Mirroring **72** in H₂O, the spectra obtained show no evidence of dimer dissociation with the annealing process. Furthermore, as there was no discernible difference between the spectra obtained for **72** in H₂O and DMSO, it can be concluded that UV-Vis spectroscopy under these experimental conditions is unable to distinguish the difference between spherical aggregates and dimeric species.

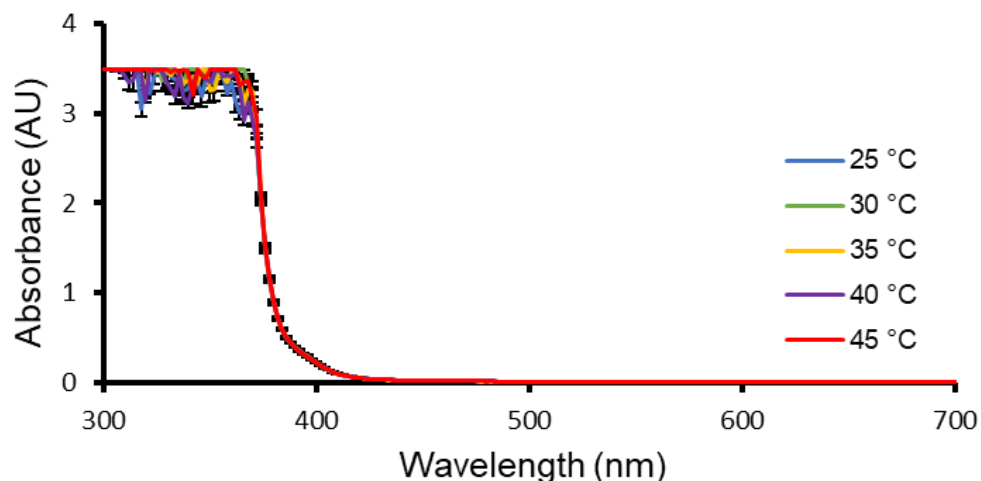


Figure 102 – Average ($n=3$) absorbance graph of **72** (1.5 mg/mL) in DMSO recorded for each 200 μL sample at 5-degree increments from 25-45 $^{\circ}\text{C}$, showing no notable increase in $\text{Abs}_{.450}$. Error bars represent the full range of UV-Vis measurements for three repetitions.

The spectra recorded for when **72** in the presence of a salt solution that forms a hydrogel, show a significant increase in $\text{Abs}_{.450}$. Using **72** in aqueous NaCl as an example, an increase in $\text{Abs}_{.450}$ of between 1.37-1.47 AU (temperature dependant) (Figure 103) was observed. This increase from ≤ 0.03 AU for **72** in $\text{H}_2\text{O}/\text{DMSO}$ (where no fibres are considered to be present) is hypothesised to be due to the presence of a fibrous network constituting a gelled material.

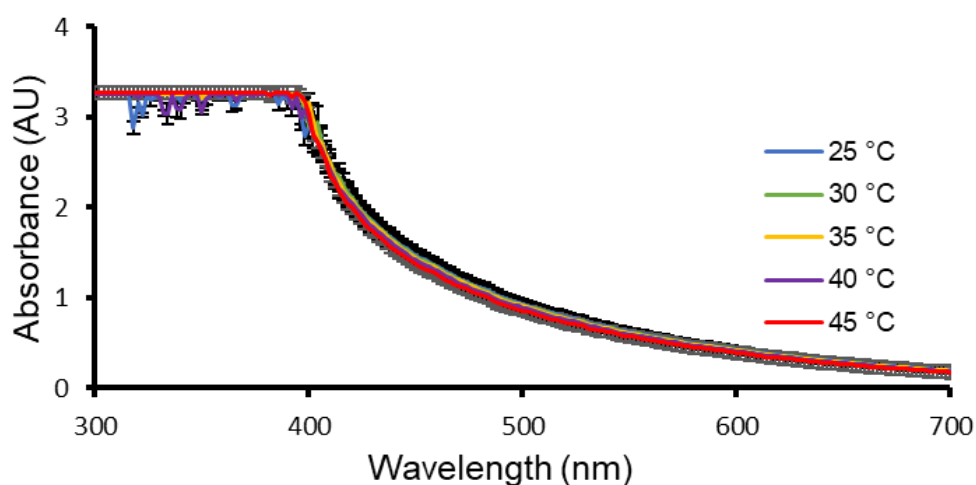


Figure 103 – Average ($n=3$) absorbance graph of **72** (1.5 mg/mL) in aqueous NaCl recorded for each 200 μL sample at 5-degree increments from 25-45 $^{\circ}\text{C}$, showing $\text{Abs}_{.450}$ values of between 1.37-1.47 AU. Error bars represent the full range of UV-Vis measurements for three repetitions.

This hydrogel (**72** in aqueous NaCl) exhibits a T_m of ≈ 51 °C therefore, the fibre disassembly temperature range (T_{fd}) was expected to be greater than the capabilities of the plate reader (> 45 °C). Upon observation of the $Abs_{.450}$ values (Table 17), there is a small decrease of $Abs_{.450}$ with increasing temperature from 25-45 °C. However, this decrease is not significant enough to proclaim the gel fibres have disassembled, therefore the T_{fd} was established to be, as expected > 45 °C, correlating with the T_m value as shown in Table 18 (where T_{fd} refers to the fibre disassembly temperature range).

Table 17 - Average ($n=3$) absorbance values obtained at 450 nm ($Abs_{.450}$) for each 200 μ L sample at 5-degree increments from 25-45 °C. Error = standard error of the mean.

Solution	Temp (°C)					Solution	Temp (°C)				
	25	30	35	40	45		25	30	35	40	45
H ₂ O	0.03 ± 0.00	NaOAc	1.67 ± 0.12	1.67 ± 0.13	1.63 ± 0.12	1.60 ± 0.12	1.51 ± 0.10				
DMSO	0.02 ± 0.00	NaF	1.54 ± 0.11	1.53 ± 0.11	1.50 ± 0.11	1.46 ± 0.10	0.31 ± 0.05				
Na ₂ HPO ₄	0.43 ± 0.03	0.41 ± 0.02	0.39 ± 0.02	0.34 ± 0.01	0.14 ± 0.01	RbCl	1.60 ± 0.00	1.60 ± 0.00	1.55 ± 0.00	1.36 ± 0.00	0.10 ± 0.00
NaH ₂ PO ₄	1.20 ± 0.09	1.17 ± 0.08	1.14 ± 0.08	1.05 ± 0.08	0.17 ± 0.01	NaCl	1.47 ± 0.08	1.46 ± 0.08	1.44 ± 0.08	1.42 ± 0.08	1.37 ± 0.07
Na ₂ CO ₃	1.21 ± 0.04	1.15 ± 0.04	1.07 ± 0.03	0.55 ± 0.04	0.06 ± 0.01	NaNO ₃	1.38 ± 0.07	1.36 ± 0.07	1.34 ± 0.07	1.32 ± 0.07	1.27 ± 0.06
Na ₂ SO ₄	1.52 ± 0.08	1.52 ± 0.09	1.50 ± 0.08	1.46 ± 0.08	0.13 ± 0.01	NaOBz	1.52 ± 0.10	1.54 ± 0.07	1.51 ± 0.06	1.48 ± 0.06	1.39 ± 0.05
NaHCO ₃	1.18 ± 0.04	1.15 ± 0.04	1.12 ± 0.04	1.07 ± 0.04	0.08 ± 0.00	KCl	0.77 ± 0.05	0.75 ± 0.05	0.75 ± 0.05	0.65 ± 0.06	0.27 ± 0.08

Table 18 - Average ($n=3$) T_m (°C) for hydrogels of **72** (5 mg/mL) and T_{fd} (°C) obtained for a hydrogels/incomplete hydrogels of **72** (1.5 mg/mL) in H₂O, DMSO or a 0.505 M aqueous salt solution. T_{fd} refers to the fibre disassembly temperature range.

Soln.	T_m °C	T_{fd} °C	Soln.	T_m °C	T_{fd} °C
H ₂ O	n/a	n/a	NaOAc	46	> 45
DMSO	n/a	n/a	NaF	47	40-45
Na ₂ HPO ₄	[a]	< 25	NaCl	51	> 45
NaH ₂ PO ₄	44	40-45	RbCl	51	40-45
Na ₂ CO ₃	43	40-45	NaNO ₃	52	> 45
Na ₂ SO ₄	43	40-45	NaOBz	54	> 45
NaHCO ₃	45	40-45	KCl	55	25-30

[a] Partial gel formed at 5 mg/mL.

The results observed for **72** in aqueous NaCl were also representative for **72** in aqueous salt solutions NaNO₃, NaOBz and NaOAc, these materials were, like **72** in aqueous NaCl, also shown to have a $T_m > 45$ °C (Table 18) (Appendix 3.1, Figures S436, S437 and S432 respectively). The Abs_{.450} values recorded at 45 °C indicated the presence of what is hypothesised to be gel fibres with values of 1.27, 1.39 and 1.51 AU respectively (Table 17). Interestingly, although **72** in a solution of aqueous NaOAc is an incomplete/partial gel at 1.5 mg/mL, the spectra obtained for this material still correlates with the T_m (≈ 46 °C) value exhibiting a $T_{fd} > 45$ °C. As a result, it can be suggested that as fibres prevail below the MGC the T_m of a gel could be due to fibre disassembly and is therefore concentration-independent.

Compound **72** in an aqueous solution of NaF was also shown to exhibit a $T_m > 45$ °C (≈ 47 °C). However, the UV-Vis spectra recorded for this material at temperatures 25-45 °C, showed a T_{fd} value of between 40 °C to 45 °C, as illustrated in Figure 104. Initial hypotheses led towards the electronegativity of the fluoride ion, destabilising the gel fibres at temperatures > 40 °C, however, there is no evidence currently to support this theory, and therefore investigations are ongoing.

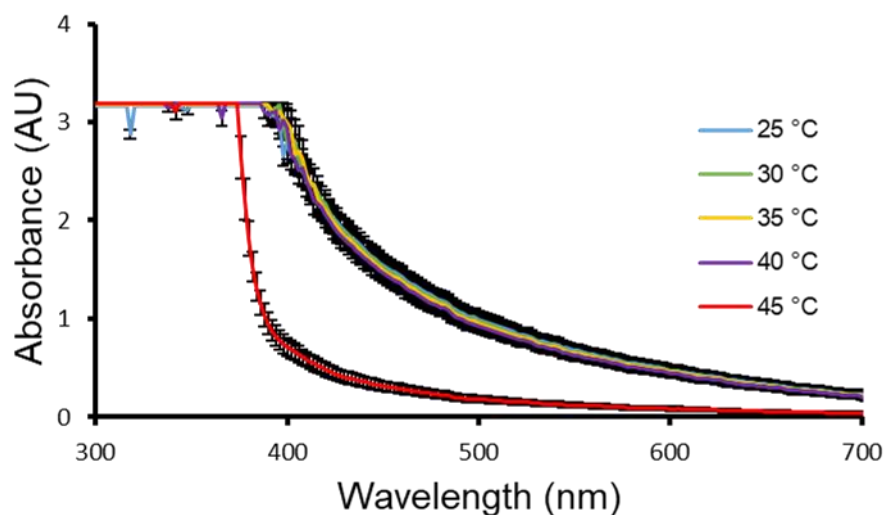


Figure 104 - Average ($n=3$) absorbance graph of **72** (1.5 mg/mL) in aqueous NaF recorded for each 200 μ L sample at 5-degree increments from 25-45 °C, showing Abs_{.450} values of between 0.31-1.54 AU. Error bars represent the full range of UV-Vis measurements for three repetitions.

Comparatively, the spectra recorded for **72** in aqueous solutions of Na_2CO_3 , NaHCO_3 , Na_2SO_4 and NaH_2PO_4 which all form gels/partial gels with a $T_m < 45\text{ }^\circ\text{C}$, were shown to have a decrease in $\text{Abs}_{.450}$ as the T_m point was reached (Appendix 3.1, Figures S429, S431, S430 and S428 respectively). An example of these spectra demonstrating this decrease is shown in Figure 105 where **72** in a solution of Na_2CO_3 exhibits a T_m of $\approx 43\text{ }^\circ\text{C}$. As illustrated, with increasing temperature 25-45 $^\circ\text{C}$ a decrease in $\text{Abs}_{.450}$ is apparent (Table 17).

It is evident that as the T_m is approached the fibres of the gelled material begin to disassemble with a notable decrease observed in $\text{Abs}_{.450}$ from 1.07 AU ($35\text{ }^\circ\text{C}$) to 0.55 AU ($40\text{ }^\circ\text{C}$), this value then decreased further to 0.06 AU ($45\text{ }^\circ\text{C}$) where the T_m was reached and then exceeded. The $\text{Abs}_{.450}$ reading (0.06 AU ($45\text{ }^\circ\text{C}$)) correlated with that of previously discussed **72** in H_2O where a low $\text{Abs}_{.450}$ value ($\leq 0.03\text{ AU}$) was hypothesised to refer to an absence of material fibres. This leads to a further hypothesis that the T_m does not only represent the gel-sol transition temperature but also gelator monomer dissociation thus resulting in fibre solvation.

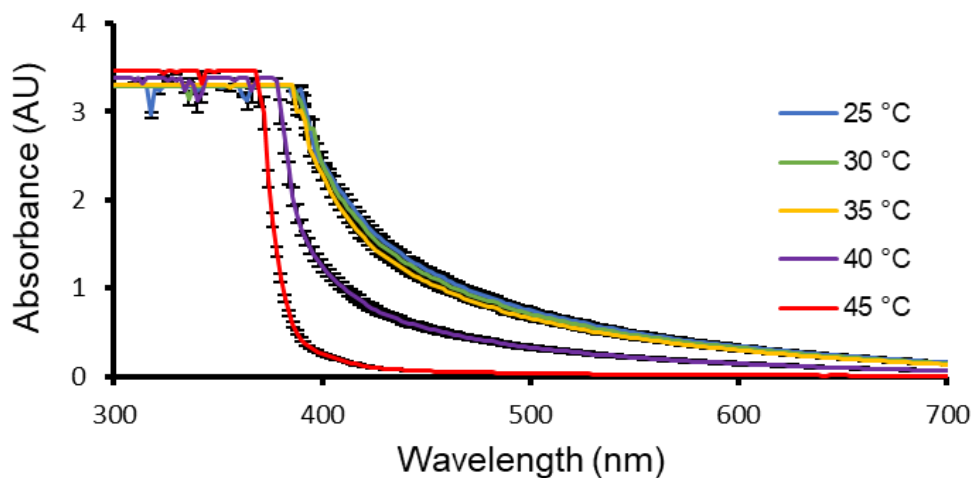


Figure 105 – Average ($n=3$) absorbance graph of **72** (1.5 mg/mL) in aqueous Na_2CO_3 recorded for each 200 μL sample at 5-degree increments from 25-45 $^\circ\text{C}$, showing $\text{Abs}_{.450}$ values of between 0.06-1.21 AU. Error bars represent the full range of UV-Vis measurements for three repetitions.

The experiment to elucidate the T_m was conducted with materials at 5 mg/mL. As **72** in an aqueous solution of Na_2HPO_4 at this concentration is a partial/incomplete gel a T_m was not determined. As expected, the $\text{Abs}_{.450}$ for this partial/incomplete gel was demonstrated to be lower at 25 $^\circ\text{C}$, than those materials where at 5 mg/mL a gel is formed.

As illustrated in Figure 106, this $Abs_{.450}$ value was shown to be 0.43 AU at 25 °C, as the temperature increases to 40 °C this value decreases to 0.34 AU, with a further increase to 45 °C, the $Abs_{.450}$ value significantly drops to 0.04 AU (Table 17). This suggests that any fibres present in this material disassemble between temperatures of 40 °C and 45 °C. It may therefore be possible to predict the T_m of a partial/incomplete gel using this experimental method.

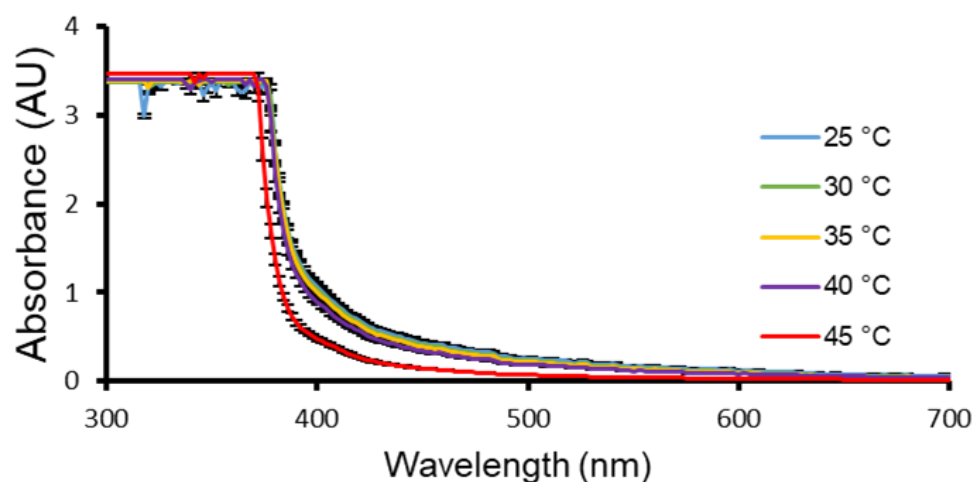


Figure 106 - Average ($n=3$) absorbance graph of **72** (1.5 mg/mL) in aqueous Na_2HPO_4 recorded for each 200 μ L sample at 5-degree increments from 25-45 °C, showing $Abs_{.450}$ values of between 0.04-0.43 AU. Error bars represent the full range of UV-Vis measurements for three repetitions.

This experimental method to elucidate the presence of gel fibres by UV-Vis was shown to be cation dependant. The spectra obtained for **72** in aqueous solutions of KCl or RbCl did not follow the same patterns as those salts which contained a sodium cation. Instead, both partial gels were shown to exhibit a lower $Abs_{.450}$ value at 45 °C (0.27 and 0.10 AU respectively) below that of the relevant T_m points (55 °C and 51 °C respectively) (Appendix 3.1, Figures S438 and S434). It is hypothesised that the increase in ionic conductivity where $Rb^+ > K^+ > Na^+$ could be a contributing factor, however, an exploration into this hypothesis remains the subject of ongoing investigations.

When a salt dissolves in water it is known to have a significant influence on the water structure and dynamics.^{269,270} Hofmeister, classified salts according to their relative ability for stabilising or destabilising materials in aqueous solutions (Figure 107).³⁴

Using this classification, ions are separated into three groups, i) kosmotropes, commonly referred to as structure makers, these well-hydrated ions are known to promote hydrophobic interactions, which in turn stabilises solute aggregate formation;²⁷¹ ii) borderline ions, these ions have a moderate influence on structure stability; iii) chaotropes, commonly referred to as structure breakers due to their ability to destabilise solute aggregates in aqueous conditions.²⁷²

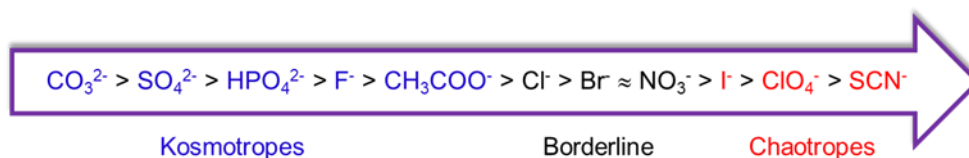


Figure 107 – Conceptual sketch of The Hofmeister series.

Those partial/hydrogels of **72** containing salts with phosphate, carbonate or sulfate anions were all found to exhibit a $T_m < 46$ °C at 5 mg/mL (Table 18). When these partial/hydrogel samples were heated within the microplate wells at 1.5 mg/mL from 25 °C to 45 °C, a decreasing absorbance with increasing temperature was observed (Figure 108). The sequence of decrease in $\text{Abs}_{.450}$ values was found to follow the Hofmeister series. It is hypothesised that those strongly hydrating anions ($\text{CO}_3^{2-} > \text{SO}_4^{2-} > \text{HPO}_4^{2-}$) which promote the hydrophobic effect have an adverse effect on the stability of the gels fibres, resulting in a lower T_m and consequently a lower T_{fd} . However, the moderate hydrating anions ($\text{Cl}^- < \text{NO}_2^-$) promote the formation of gel fibres with higher fibre melting temperatures of ≈ 51 °C and 52 °C respectively and a $T_{fd} > 45$ °C (Table 18).

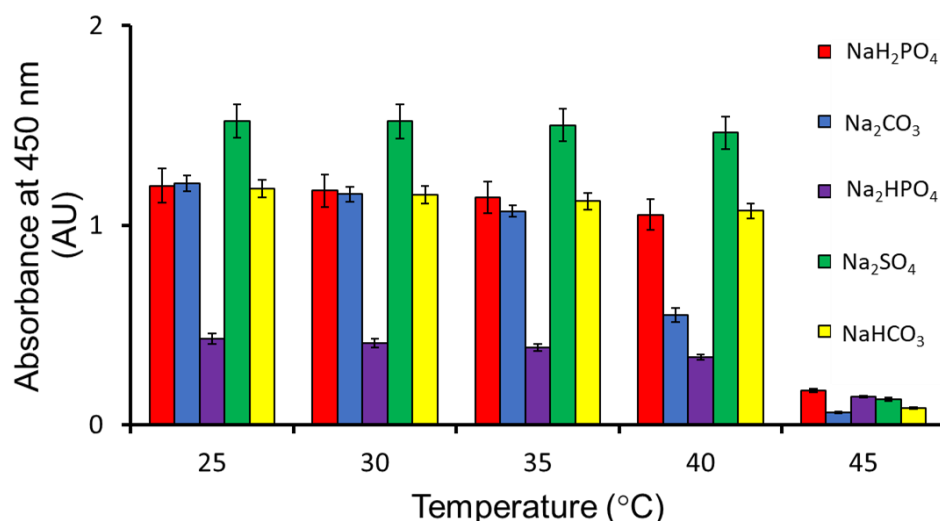


Figure 108 - Average ($n=3$) Abs.₄₅₀ values for gels/partial gels of **72** (1.5 mg/mL) in aqueous salt solutions containing either a phosphate, carbonate or sulfate anion, showing a decrease Abs.₄₅₀ at 45 °C. Error bars represent the full range of Abs.₄₅₀ for three repetitions.

In summary, it was shown that UV-Vis Abs.₄₅₀ measurements can be used to verify the presence of gel fibres within a sample of **72** (1.5 mg/mL) in the appropriate aqueous salt solutions. It was demonstrated that an Abs.₄₅₀ > 0.06 AU was indicative of fibre presence when compared to other self-associated species such as dimers or spherical aggregates where an Abs.₄₅₀ ≤ 0.03 AU, at comparable concentrations. Interestingly the hydrogel fibres were shown to prevail below the MGC, this led to the hypothesis that the T_m of a gel could be due to fibre disassembly and is therefore concentration-independent. To conclude this high-throughput method (up to 384 experiments simultaneously) can be used to detect gelated material formation through observation of change in absorbance.

4.3 Optical density measurements

Optical density (OD) measurements recorded from spectral microplate well scans, were then explored to identify if this method could also be used to further characterise a supramolecular gel. The advantages of spectral microplate well matrix scanning using plate reader technology include i) high-throughput, up to 384 experiments simultaneously; ii) multiple measurements in each well with a resolution of up to 900 points per well.

This an essential requirement when a single reading is inadequate due to uneven sample distribution across the well.

For this study, 3D spectral analysis well scans were conducted analogously to those experimental conditions with the UV-Vis absorbance measurements, where an increase in absorbance at 450 nm was concluded to be indicative of gel fibre presence. Therefore, spectral microplate well scans were conducted for **72** (1.5 mg/mL) in various aqueous salt solutions (0.505 M) (Chapter 4.2, Table 18), H₂O and DMSO at 450 nm (OD₄₅₀) over a 25 °C to 45 °C temperature range. The surface area of each well was divided into 177 sections, with an OD₄₅₀ measurement obtained for the entire depth of the sample. This method allowed for the observation of any self-associated structures of **72** within each microplate well.

The spectral microplate well scan recorded for **72** in an H₂O solution, where spherical aggregates are known to persist, exhibited a greater OD₄₅₀ towards the periphery of the well (Figure 109b). As amphiphilic compounds such as **72**, are known to preferentially self-associate at the interface until the CMC is reached,²⁷³ this greater OD₄₅₀ value towards the periphery of the well is therefore consistent with the surfactant properties of **72**.¹³⁶ However, there is only a negligible increase in OD₄₅₀ values towards the centre of the microplate well, suggesting those large spherical aggregates which exist in the bulk of the solution are not detected by this experimental method. To ensure that the observed increase in OD₄₅₀ was due to the presence of any self-associated structures of **72**, solution standards were tested, as illustrated in Figure 109a. The OD₄₅₀ value of H₂O was shown to be 0.03 AU across the entirety of the well, confirming the increase in OD₄₅₀ in Figure 109b was due to the presence of **72**. As the temperature is increased from 25 °C (Figures 109a and 109b) to 45 °C (Figures 110a and 110b) little notable change is observed between spectral scans, again this suggests that this experimental method cannot be used to evident destabilisation of any self-associated structures at the periphery of the well or in the bulk of the H₂O solution at temperatures ≤ 45 °C.

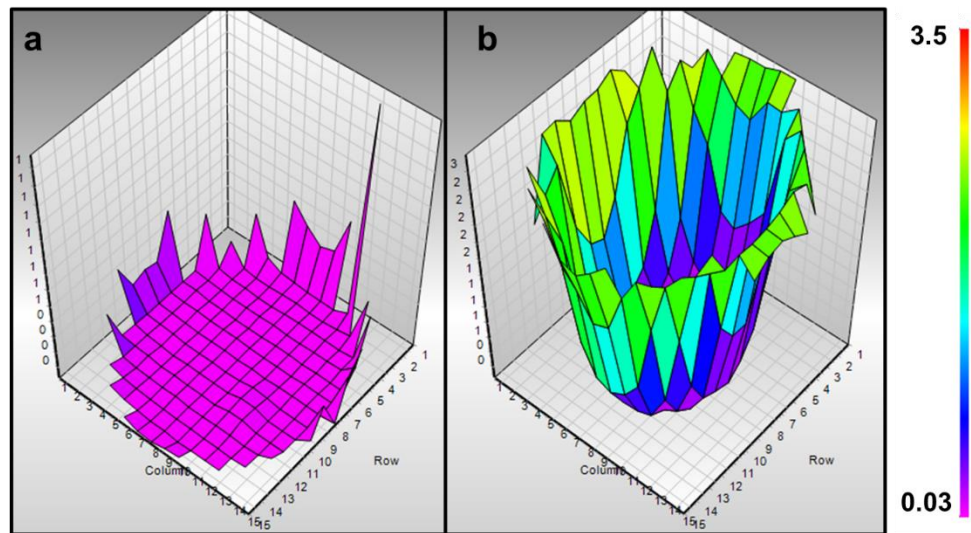


Figure 109 – Spectral analysis microplate well scans conducted at 25 °C at OD₄₅₀ with a) H₂O and b) **72** (1.5 mg/mL) in H₂O.

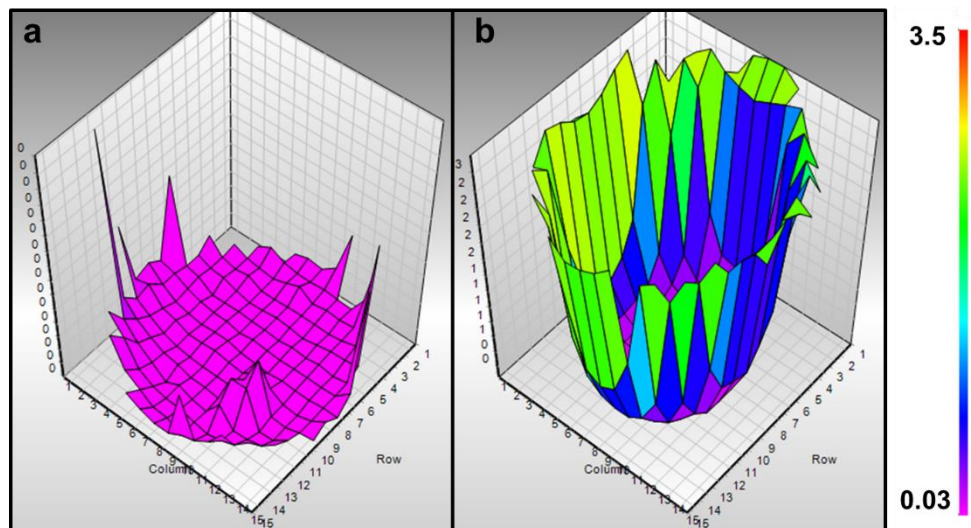


Figure 110 - Spectral analysis microplate well scans conducted at 45 °C at OD₄₅₀ with a) H₂O and b) **72** (1.5 mg/mL) in H₂O.

Within the scope of these experiments, two-dimensional (2D) OD₄₅₀ maps were also produced. These 2D maps are representative of those data shown in Figures 109b and 110b. To analyse these data a colour gradient system was used, such as shown in Figure 111 where each segment (outlined in black) represents a different portion of the microplate well, each individual measurement is recorded for the entire depth of the sample (top to bottom).

These results demonstrate lower OD₄₅₀ values of between 0.00 to 0.99 AU (blue) occurring towards the centre of the microplate well, with higher values of between 2.00 to 3.00 AU (red) occurring towards the periphery of the microplate well. In correlation with previous data shown (Figure 109b and 110b).

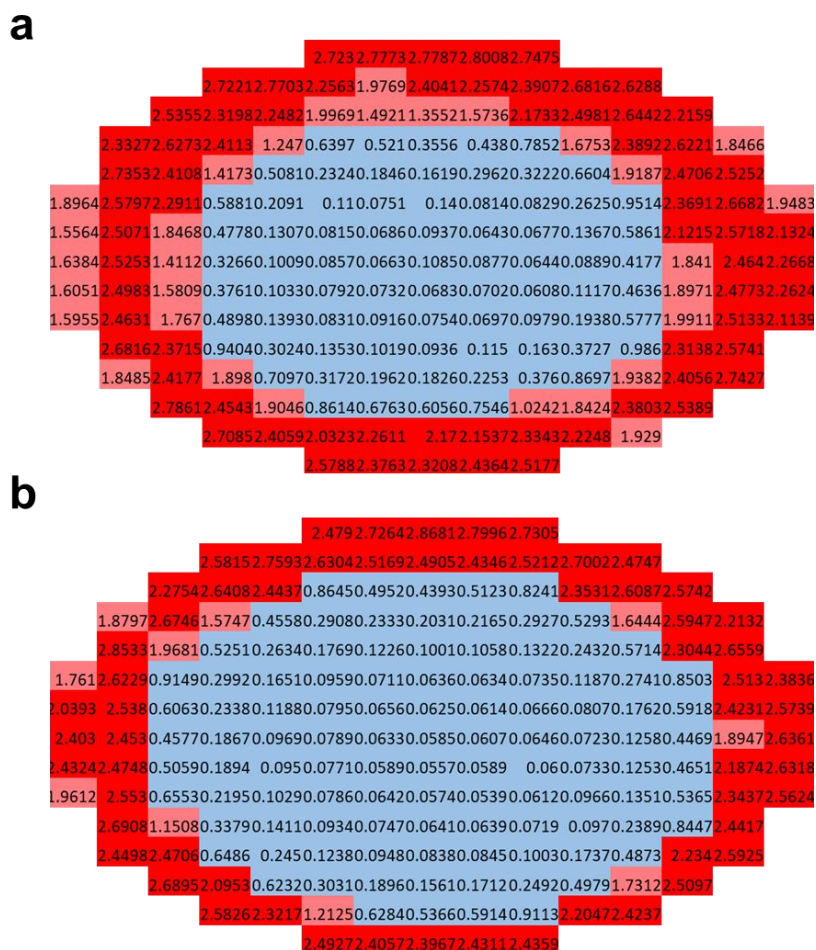


Figure 111 – OD₄₅₀ intensity maps produced for **72** (1.5 mg/mL) in H₂O at a) 25 °C and b) 45 °C. Blue: OD₄₅₀ = 0.00–0.99 AU. Pink: OD₄₅₀ = 1.00–1.99 AU. Red: OD₄₅₀ = 2.00–3.00 AU.

Comparatively, **72** in a solution of DMSO at 25 °C, where only dimeric species are known to exist, a high OD₄₅₀ is again observed at the microplate well periphery (Figure 112a). Conversely when the temperature is increased to 45 °C this OD₄₅₀ value decreases as shown in Figure 112b, where those colours associated with increased OD₄₅₀ values are shown to reduce. It is hypothesised that this observation may be due to the initial disassembly of the self-associated structures.

The 2D OD₄₅₀ maps were shown to correlate with the spectral 3D microplate well scan data illustrated in Figures 113a and 113b, with lower readings towards the centre of the microplate well of 0.00 to 0.99 AU (blue) and a lower percentage of those higher values towards the edge of the microplate well of 2.00 to 3.00 AU (red).

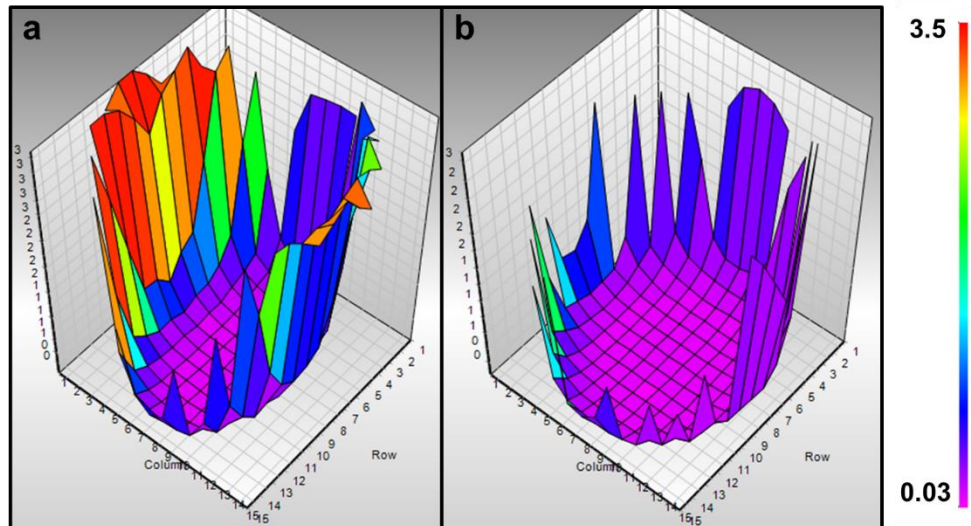


Figure 112 - Spectral analysis microplate well scans conducted with **72** (1.5 mg/mL) in DMSO at temperatures of a) 25 °C and b) 45 °C at OD₄₅₀.

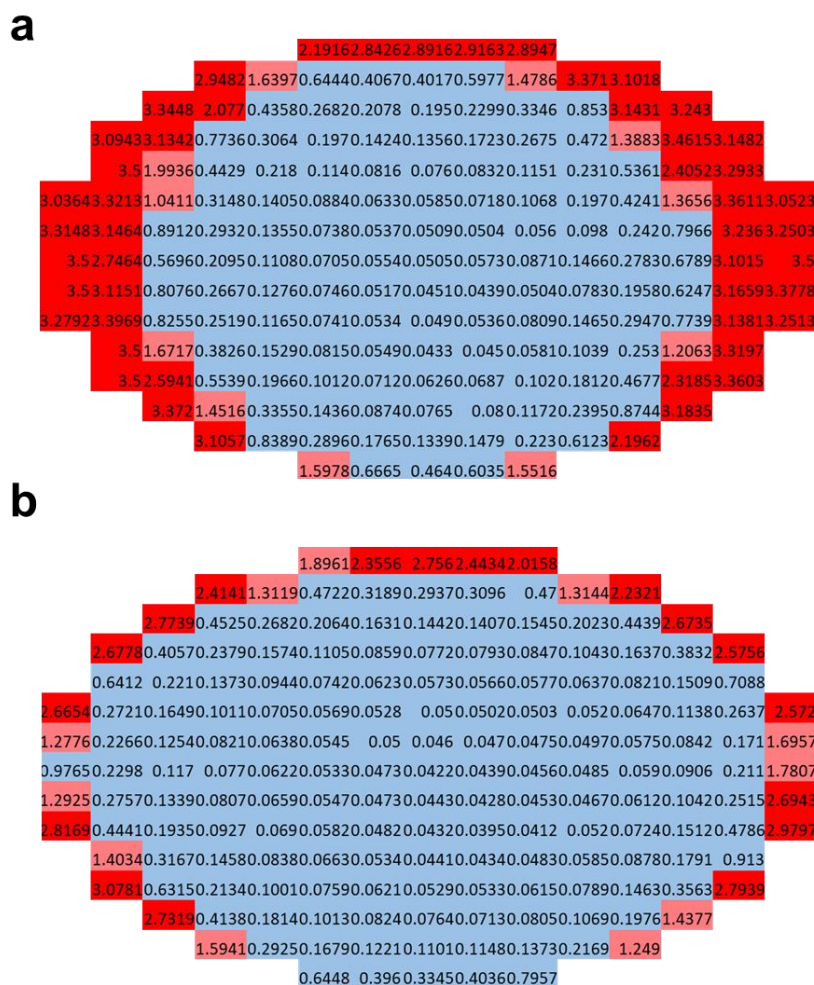


Figure 113 - OD₄₅₀ intensity maps produced for **72** (1.5 mg/mL) in DMSO at a) 25 °C and b) 45 °C. Blue: OD₄₅₀ = 0.00–0.99 AU. Pink: OD₄₅₀ = 1.00–1.99 AU. Red: OD₄₅₀ = 2.00–3.00 AU.

For a solution in which **72** acts as a gelator, where the gelled material exhibits a $T_m > 45$ °C (Chapter 4.2, Table 18), a uniformed intensity across the entirety of the microplate well at 25 °C is observed, in this instance aqueous NaCl which has a T_m of ≈ 51 °C, (Figure 114a). With the increase of temperature to 45 °C, this uniformed intensity continues (Figure 114b). These observations correlated with the previously reported UV-Vis measurements, where there was no observable decrease in Abs.₄₅₀ with an increase in temperature below that of the T_m . The corresponding 2D intensity maps show no discernible difference between the two maps with an increase in temperature from 25 °C (Figure 115a) to 45 °C (Figure 115b) as expected. However, once more, there is a slightly greater OD₄₅₀ value observed towards the periphery of the microplate well (2.00 to 3.00 AU, red).

In this instance, the centre of the microplate wells OD₄₅₀ values, 1.00–1.99 AU (pink) are higher than previously observed for those samples where there is an absence of fibres (0.00 to 0.99 AU, blue). This not only supports the presence of fibres but also shows a greater distribution of amalgamations of fibres towards the microplate well periphery compared to those present in the bulk of the solution.

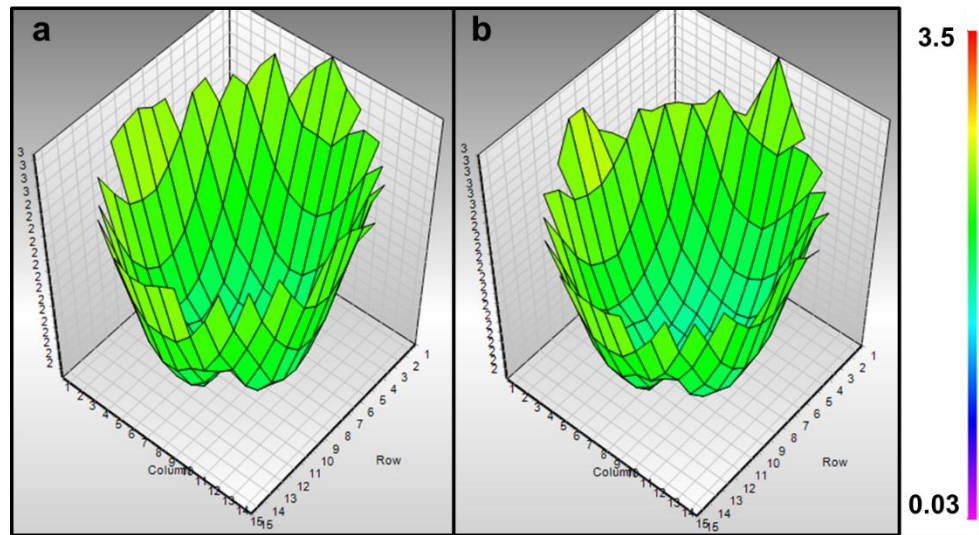


Figure 114 – Spectral analysis microplate well scans conducted with **72** (1.5 mg/mL) in an aqueous NaCl (0.505 M) at temperatures of a) 25 °C and b) 45 °C at OD₄₅₀.

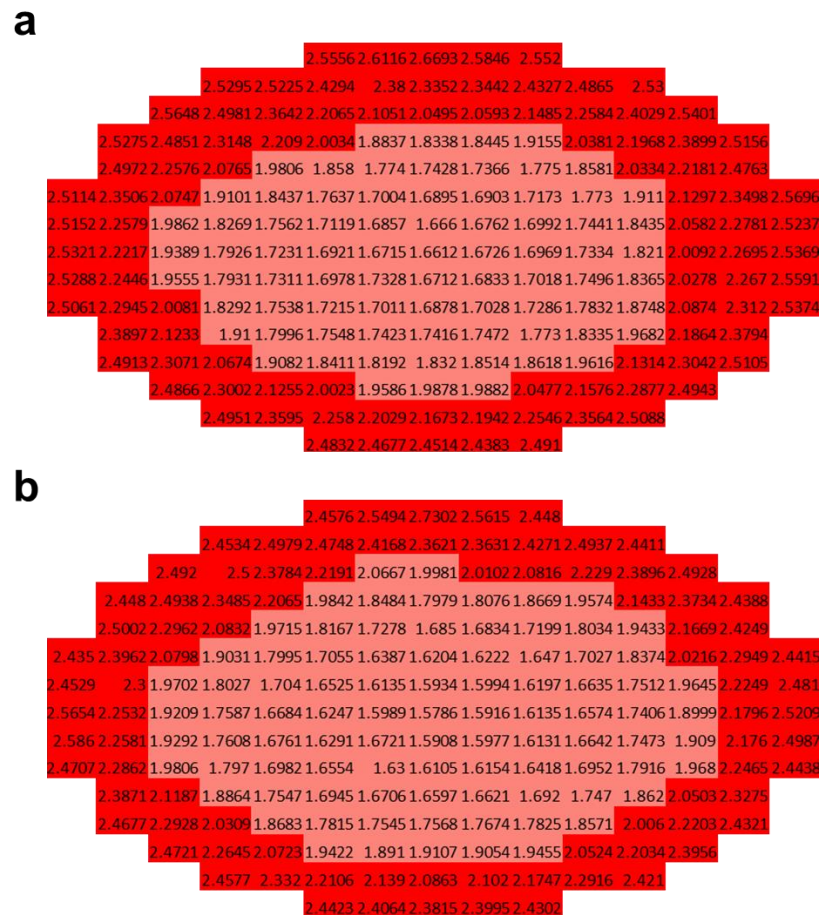


Figure 115 - OD₄₅₀ intensity maps produced for **72** (1.5 mg/mL) in an aqueous solution of aqueous NaCl (0.505 M) at a) 25 °C and b) 45 °C. Blue: OD₄₅₀ = 0.00–0.99 AU. Pink: OD₄₅₀ = 1.00–1.99 AU. Red: OD₄₅₀ = 2.00–3.00 AU.

Aqueous salt solutions of NaOBz, NaNO₃, NaOAc, NaF, RbCl and KCl all when in the presence of **72** forms a gelled material with a $T_m > 45$ °C. Mirroring those results obtained with **72** in aqueous NaCl, where a uniformed intensity across the entirety of the microplate well at temperatures 25–45 °C was observed, again supporting the presence of fibres within the sample (Appendices 3.2 and 3.3). Interestingly, it was previously identified in the UV-Vis experiments that solutions containing different cations to sodium such as rubidium and potassium or strong electronegative anions such as fluoride, all were shown to have a T_{fd} temperature below the T_m of the material (Chapter 4.2). However, this was not observed with the spectral microplate well scans, this would suggest that the UV-Vis measurements are a good preliminary experiment. But, for a more informative investigation, spectral microplate well scans that scan the entire depth of the microplate well at a particular wavelength would be better suited.

For those spectral microplate well scans of **72** in aqueous solutions of Na₂SO₄, NaHCO₃, NaHPO₄ or Na₂CO₃ which all exhibit a $T_m < 45$ °C (Chapter 4.2, Table 18), it was expected that a decrease in OD₄₅₀ would be observed as the T_m is approached. However, when **72** acts as a gelator in the presence of an aqueous solution of Na₂SO₄ or NaHCO₃ the microplate well scans and corresponding intensity maps show a negligible difference between microplate wells with an increase in temperature, as to why these samples are anomalies, is currently under investigation. However, both materials exhibit relatively high MGC values of 3.5 and 4.0 mg/mL respectively, so this could be a contributing factor.

An example of a material where the fibres do disassemble upon approaching the T_m is given for **72** in aqueous Na₂CO₃, which demonstrates no discernible difference between microplate well scans recorded at 25 °C (Figure 116a) and 35 °C (Figure 116b). This was anticipated as the T_m of this material was recorded to be ≈ 43 °C. Upon comparison of the microplate well scan recorded at 35 °C with the microplate well scan recorded at 45 °C (above that of the T_m), a greater increase in OD₄₅₀ was observed at the higher temperature, this is depicted in the significant change in colour towards the centre of the microplate well as shown in Figure 115c.

Upon comparison of the microplate well scans recorded at 25 °C for **72** in aqueous NaCl (MGC, 1.5 mg/mL) with **72** in aqueous Na₂CO₃ (MGC, 3.0 mg/mL) (Chapter 4.2, Table 16), the latter does not exhibit the same uniformed distribution of OD₄₅₀ values across the entire well plate (Figures 114a and 116a). Instead, exhibiting lower values towards the centre of the microplate well. This is hypothesised to be due to, under the experimental conditions performed in this study, **72** in aqueous Na₂CO₃ is an incomplete gel, supporting the theory that fibres for these materials discussed, initially form predominantly at the periphery of the microplate well.

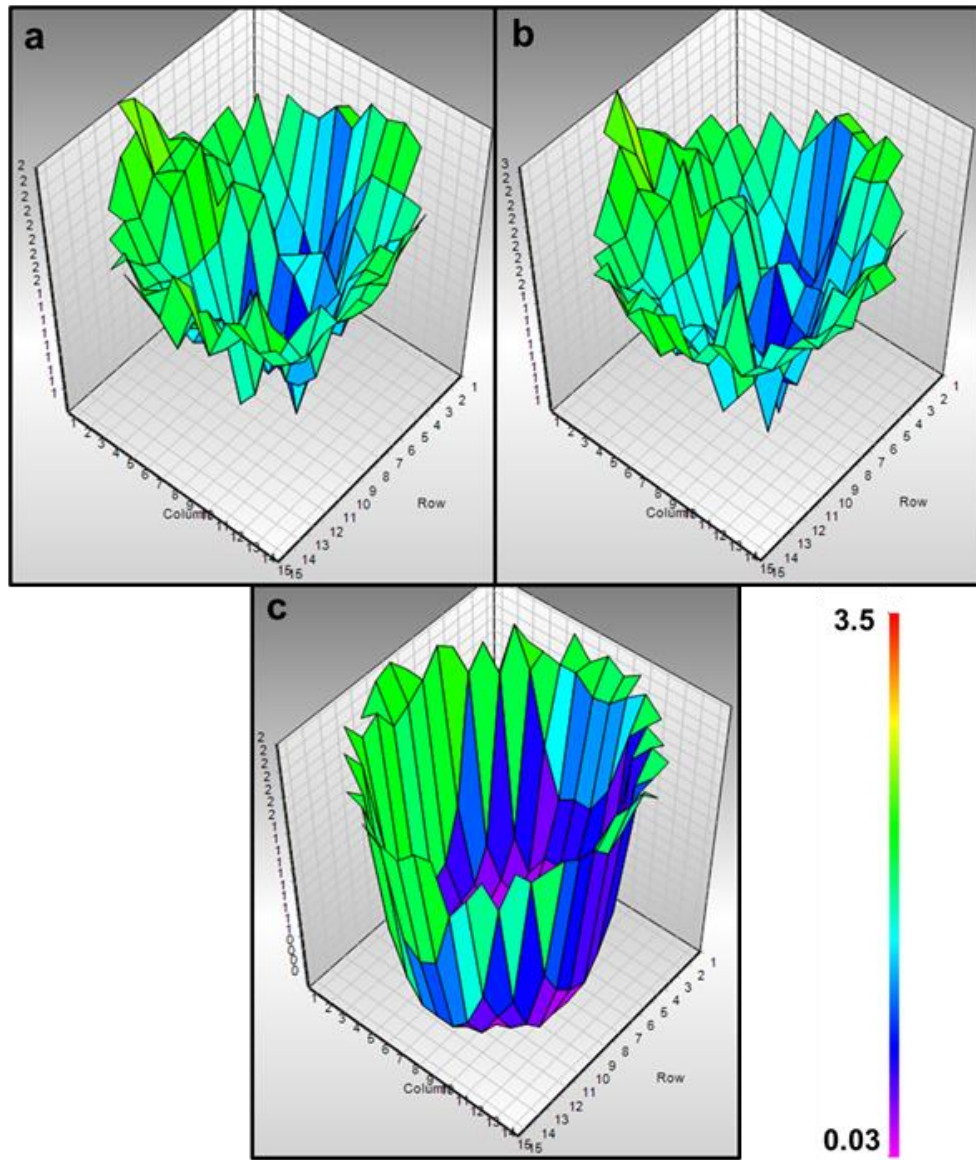


Figure 116 - Spectral analysis microplate well scans conducted with **72** (1.5 mg/mL) in an aqueous solution of Na₂CO₃ (0.505 M) at temperatures of: a) 25 °C; b) 35 °C; c) 45 °C at OD₄₅₀.

The corresponding 2D OD₄₅₀ intensity maps to those microplate well scans of **72** in aqueous Na₂CO₃ show a clear decrease in OD₄₅₀ as the temperature approached the T_m of ≈ 43 °C. Interestingly, the intensity map recorded at 25 °C (Figure 117a) although visually looks similar to that obtained for **72** in aqueous NaCl at the same temperature (Figure 115a), the individual values in the centre are significantly lower supporting the earlier hypothesis that fibres favourably form towards the surface. As the temperature is increased through to 35 °C lower OD₄₅₀ values (0.00–0.99 AU, blue) become more apparent (Figure 117b), again these are located towards the centre of the well.

As the temperature exceeds that of the T_m (≈ 43 °C), the distribution of those lower values become significantly greater as illustrated in Figure 117c, however, a proportion of fibres are shown to prevail towards the edge of the microplate well. This further supports the hypothesis that the T_m (Table 18) is the melting temperature of the material fibres, not simply the melting temperature of the material itself at 5 mg/mL.

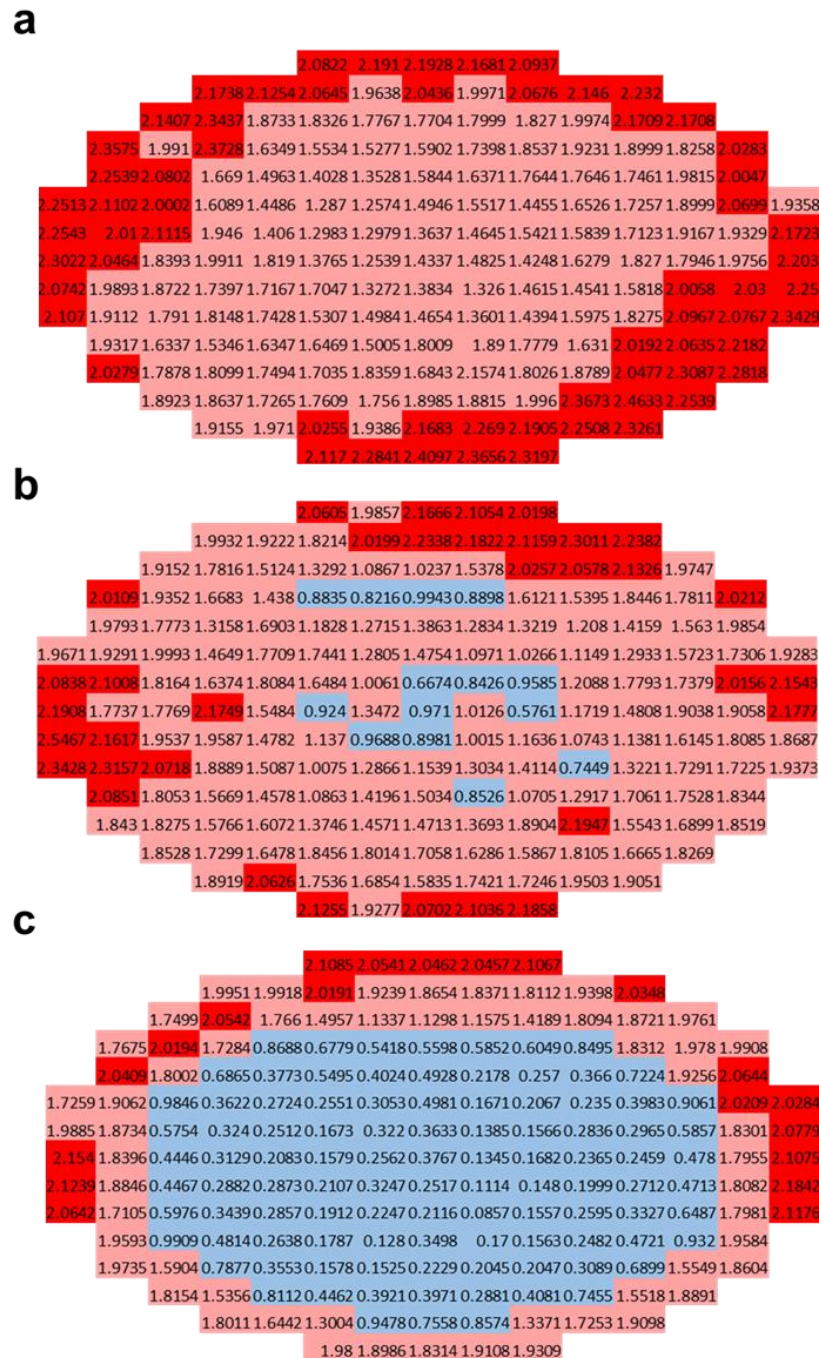


Figure 117 - OD₄₅₀ intensity maps produced for **72** (1.5 mg/mL) in an aqueous solution of Na₂CO₃ (0.505 M) at a) 25 °C, b) 35 °C and c) 45 °C. **Blue**: OD₄₅₀ = 0.00–0.99 AU. **Pink**: OD₄₅₀ = 1.00–1.99 AU. **Red**: OD₄₅₀ = 2.00–3.00 AU.

The spectral microplate well scans and corresponding 2D OD₄₅₀ intensity maps of **72** in an aqueous solution of Na₂HPO₄ which forms a partial/incomplete gel at 5 mg/mL (Chapter 4.2, Table 16), show at a temperature of 25 °C OD₄₅₀ values of 0.00–1.99 AU (pink and blue) across the well (Figures 118a and 119a). Interestingly, with a temperature increase from 25 °C through to 45 °C an increase in OD₄₅₀ is apparent (Figures 118b and 119b), with OD₄₅₀ values of 2.00–3.00 AU present at the periphery of the well. Figures 118b and 119b resemble those of **72** in H₂O at an analogous temperature (Figures 109b and 110b), this would suggest that the addition of heat, in this case, induces self-associated structure formation with **72** demonstrating more surfactant-like properties as opposed to gelator-like properties.

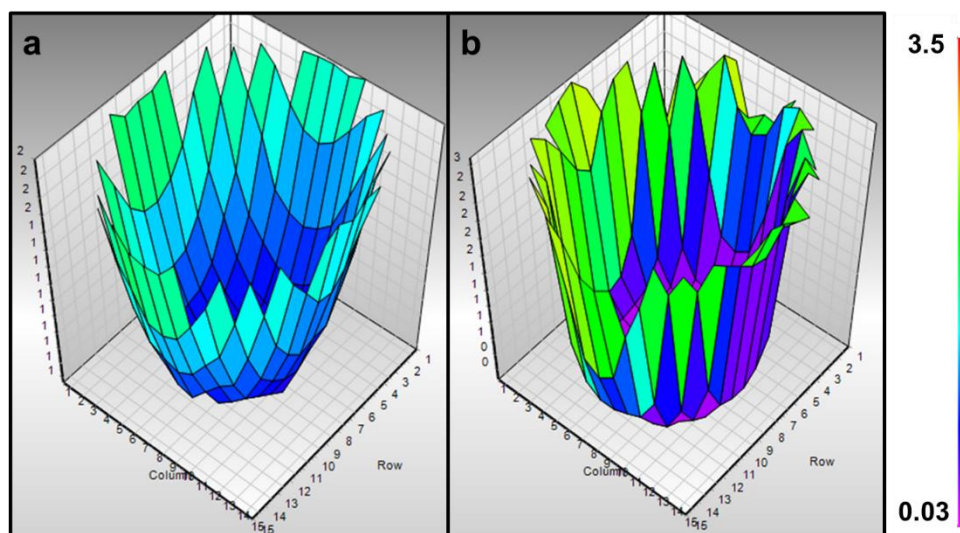


Figure 118 - Spectral analysis microplate well scans conducted with **72** (1.5 mg/mL) in an aqueous solution of Na₂HPO₄ (0.505 M) at temperatures of a) 25 °C and b) 45 °C at OD₄₅₀.

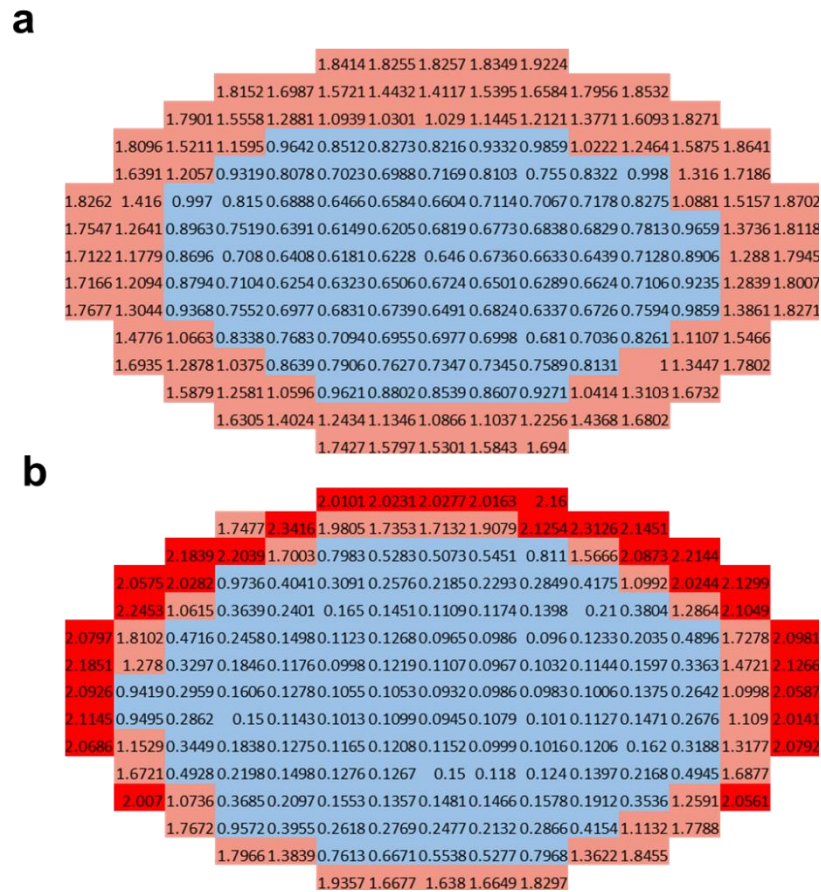


Figure 119 - OD₄₅₀ intensity maps produced for **72** (1.5 mg/mL) in an aqueous solution of Na₂HPO₄ (0.505 M) at a) 25 °C and b) 45 °C. **Blue**: OD₄₅₀ = 0.00–0.99 AU. **Pink**: OD₄₅₀ = 1.00–1.99 AU. **Red**: OD₄₅₀ = 2.00–3.00 AU.

4.3.1 OD₄₅₀ ratio

To identify if it was possible to determine the presence of gel fibres from the data obtained from the 2D OD₄₅₀ intensity maps, the ratio of the highest and lowest (maximum and minimum) OD₄₅₀ values recorded for a single well, of a single sample, at a single temperature were calculated as shown in Table 19. Through ratioing these values it then becomes possible to screen these data for the presence of gel fibres and identify a gel-sol/gel fibre melting temperature (T_m) range. These data can then be validated with comparisons of those values shown in Table 18 (Chapter 4.2).

Table 19 - Average ($n=3$) OD₄₅₀ minimum, maximum and ratio values (minimum/ maximum) taken from the spectral well scan data of **72** (1.5 mg/mL) in H₂O, DMSO and various aqueous salt solutions (0.505 M) at 25 °C - 45 °C. Error = standard error of the mean (\pm).

Soln.	OD ₄₅₀	Temp (°C)					Soln.	OD ₄₅₀	Temp (°C)				
		25	30	35	40	45			25	30	35	40	45
H ₂ O	Min	0.06	0.06	0.06	0.05	0.05	NaOAc	Min	2.05	2.04	2.01	1.97	1.90
	Error (\pm)	0.00	0.00	0.00	0.00	0.00		Error (\pm)	0.01	0.01	0.00	0.01	0.01
	Max	2.80	2.80	2.82	2.85	2.84		Max	2.91	2.96	2.96	2.94	2.92
	Error (\pm)	0.01	0.01	0.03	0.03	0.04		Error (\pm)	0.00	0.02	0.06	0.02	0.05
	Min/Max	0.02	0.02	0.02	0.02	0.02		Min/Max	0.7	0.69	0.68	0.67	0.65
	Error (\pm)	0.00	0.00	0.00	0.00	0.00		Error (\pm)	0.00	0.00	0.01	0.01	0.01
DMSO	Min	0.05	0.05	0.05	0.05	0.05	NaF	Min	1.60	1.44	1.45	1.43	1.40
	Error (\pm)	0.00	0.00	0.00	0.00	0.00		Error (\pm)	0.12	0.34	0.26	0.13	0.03
	Max	3.50	3.50	3.50	3.50	2.95		Max	2.90	2.95	2.92	2.87	2.90
	Error (\pm)	0.00	0.00	0.00	0.00	0.21		Error (\pm)	0.12	0.21	0.31	0.22	0.32
	Min/Max	0.01	0.01	0.01	0.01	0.02		Min/Max	0.55	0.49	0.5	0.5	0.48
	Error (\pm)	0.00	0.00	0.00	0.00	0.00		Error (\pm)	0.01	0.04	0.01	0.00	0.03
Na ₂ HPO ₄	Min	0.60	0.57	0.56	0.53	0.08	RbCl	Min	1.37	1.34	1.24	1.20	1.34
	Error (\pm)	0.02	0.03	0.03	0.02	0.01		Error (\pm)	0.11	0.15	0.17	0.30	0.22
	Max	1.91	1.94	1.92	1.91	2.57		Max	2.77	2.83	2.82	2.74	2.80
	Error (\pm)	0.01	0.02	0.04	0.04	0.20		Error (\pm)	0.11	0.13	0.19	0.04	0.09
	Min/Max	0.31	0.29	0.29	0.28	0.03		Min/Max	0.50	0.48	0.44	0.44	0.48
	Error (\pm)	0.01	0.02	0.01	0.01	0.00		Error (\pm)	0.07	0.08	0.05	0.02	0.10
NaH ₂ PO ₄	Min	1.38	1.33	1.29	1.19	0.14	NaCl	Min	1.69	1.66	1.65	1.63	1.61
	Error (\pm)	0.06	0.06	0.06	0.12	0.00		Error (\pm)	0.03	0.03	0.03	0.03	0.03
	Max	2.51	2.58	2.50	2.45	2.87		Max	2.67	2.66	2.70	2.69	2.73
	Error (\pm)	0.14	0.12	0.14	0.09	0.02		Error (\pm)	0.01	0.02	0.01	0.04	0.04
	Min/Max	0.55	0.51	0.52	0.49	0.05		Min/Max	0.63	0.63	0.61	0.61	0.59
	Error (\pm)	0.01	0.01	0.03	0.00	0.00		Error (\pm)	0.01	0.01	0.01	0.01	0.01
Na ₂ CO ₃	Min	0.86	0.83	0.80	0.68	0.11	NaNO ₃	Min	1.58	1.57	1.54	1.52	1.48
	Error (\pm)	0.34	0.33	0.32	0.31	0.02		Error (\pm)	0.11	0.11	0.10	0.11	0.12
	Max	2.47	2.48	2.47	2.43	2.21		Max	2.54	2.55	2.52	2.50	2.48
	Error (\pm)	0.01	0.07	0.08	0.06	0.02		Error (\pm)	0.04	0.06	0.03	0.05	0.02
	Min/Max	0.35	0.33	0.32	0.28	0.05		Min/Max	0.62	0.61	0.61	0.61	0.60
	Error (\pm)	0.10	0.08	0.10	0.08	0.01		Error (\pm)	0.00	0.00	0.01	0.02	0.05
Na ₂ SO ₄	Min	1.55	1.54	1.51	1.50	1.36	NaOBz	Min	1.74	1.73	1.71	1.69	1.67
	Error (\pm)	0.36	0.37	0.40	0.41	0.33		Error (\pm)	0.01	0.01	0.01	0.01	0.01
	Max	2.49	2.50	2.50	2.55	2.43		Max	2.72	2.80	2.78	2.82	2.85
	Error (\pm)	0.13	0.15	0.19	0.22	0.13		Error (\pm)	0.01	0.03	0.02	0.01	0.03
	Min/Max	0.62	0.61	0.6	0.59	0.56		Min/Max	0.64	0.62	0.62	0.6	0.58
	Error (\pm)	0.14	0.14	0.15	0.14	0.05		Error (\pm)	0.00	0.00	0.00	0.00	0.00
NaHCO ₃	Min	1.25	1.21	1.18	1.15	1.08	KCl	Min	1.79	1.78	1.75	1.73	1.54
	Error (\pm)	0.01	0.02	0.03	0.02	0.02		Error (\pm)	0.19	0.11	0.15	0.13	0.06
	Max	2.21	2.25	2.26	2.24	2.24		Max	3.10	3.20	3.25	3.27	3.29
	Error (\pm)	0.06	0.04	0.04	0.02	0.08		Error (\pm)	0.10	0.03	0.23	0.14	0.24
	Min/Max	0.57	0.54	0.52	0.51	0.48		Min/Max	0.58	0.56	0.54	0.53	0.47
	Error (\pm)	0.02	0.02	0.01	0.00	0.01		Error (\pm)	0.04	0.03	0.01	0.02	0.03

In analysing these data in this manner four distinct observations can be made through ratioing the OD₄₅₀ values, as follows:

1. Identification for the presence of gel fibres. It is known through previous experiments that **72** in aqueous NaCl forms a material that is uniformly gelled. Through the ratioing of OD₄₅₀ values for this gel, a constant value of ≥ 0.59 AU was recorded at temperatures 25-45 °C (Figure 120, **red**), these values are indicative of fibre presence.
2. Identification of the absence of gel fibres. A ratio value < 0.06 AU as depicted for **72** in H₂O (Figure 120, **green**) indicates proportionally very few if any gel fibres present in a sample. This value (< 0.06 AU) is also observed for **72** in aqueous Na₂CO₃ at 45 °C above that of the T_m for this material, where fewer fibres are expected to be present (Figure 120, **blue**).
3. Identification of the gel-sol/gel fibre melting temperature (T_m) range. As shown in Figure 120, **blue** for **72** in aqueous Na₂CO₃, the OD₄₅₀ ratio remains fairly constant at temperatures 25-40 °C, then a decline in OD₄₅₀ was observed from 40 °C (≈ 0.28 AU) to 45 °C (≈ 0.05 AU) this was hypothesised to be due to the disassembly of the gel fibres, from these data it may be possible to predict the T_m value.
4. Identification of the number of fibres present in a material. As illustrated in Figure 120 the data obtained for three different material types show three different levels of absorbance intensity. Those materials with a $T_m > 45$ °C (**red**) exhibit a greater intensity than those with a $T_m < 45$ °C (**blue**), which in turn exhibits a greater intensity than those in which there are little to no fibres known to be present (**green**).

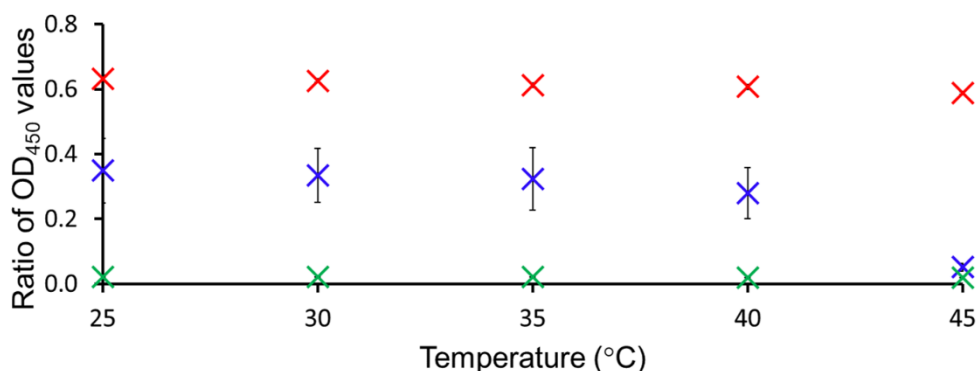


Figure 120 - Average ($n=3$) ratio values (OD_{450} maximum/ OD_{450} minimum) taken from the spectral well scan data of **72** (1.5 mg/mL) in aqueous salt solutions (0.505 M) of NaCl (red), Na_2CO_3 (blue) and in H_2O (green). Error bars represent the full range of OD_{450} ratio values to be calculated from the $n=3$ OD_{450} maxima and minimum data.

Examples of point three from above are illustrated in Figures 121a and 121b where it is shown for those materials which are known to have a $T_m > 40$ °C but < 45 °C (Chapter 4.2, Table 18), a significant decrease in OD_{450} is observed between these two temperatures, signifying the disassembly of gel fibres. Figure 121c interestingly shows the OD_{450} ratio for **72** in aqueous Na_2HPO_4 , which as discussed is a partial/incomplete gel at 5.0 mg/mL, therefore a T_m value was not determined. Upon observation of the graph (Figure 121c) not only was there an indication of the presence of fibres with an OD_{450} value > 0.06 AU recorded for temperatures 25-40 °C, but also a steep decrease in the OD_{450} value from 0.28 (40 °C) to 0.03 AU (45 °C), indicating fibre disassembly between these temperatures. With comparison of the absorbance intensities between **72** in aqueous NaH_2PO_4 with Na_2HPO_4 , which have MGC values of 1.5 mg/mL and > 5.0 mg/mL respectively. A greater intensity is visible for the material which has the lower MGC (Figure 121b) indicating more fibres to be present than the material with a higher MGC (Figure 121c). Additionally, the intensity absorbance for **72** in aqueous NaH_2PO_4 is shown to be similar to that of **72** in aqueous NaCl where both have MGC values of 1.5 mg/mL. This further supports the hypothesis that these methods may be used to predict gel-sol/gel fibre T_m range and fibre quantity.

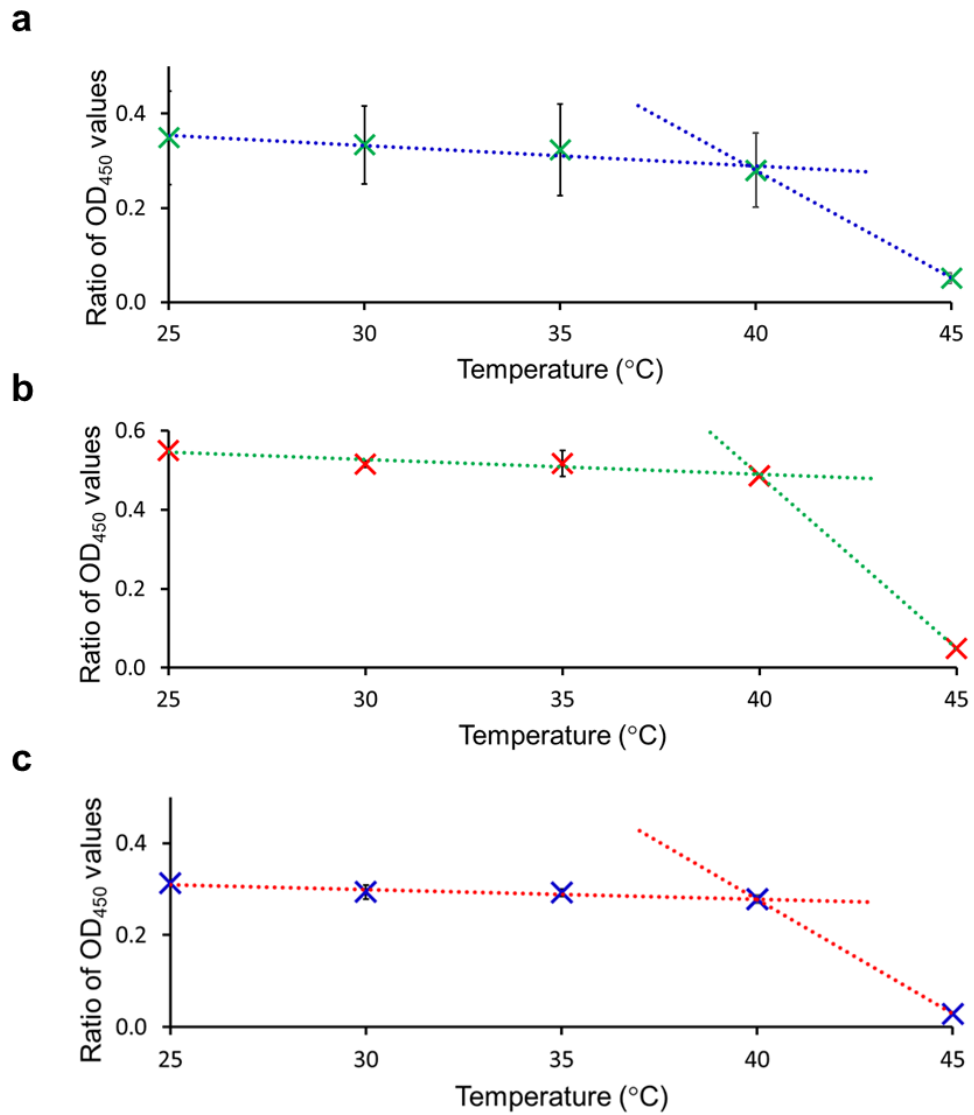


Figure 121 - Average ($n=3$) ratio values (OD_{450} maximum/ OD_{450} minimum) taken from the spectral well scan data of **72** (1.5 mg/mL) in aqueous salt solutions (0.505 M) of: a) Na_2CO_3 ; b) NaH_2PO_4 ; c) Na_2HPO_4 . Error bars represent the full range of OD_{450} ratio values to be calculated from the $n=3$ OD_{450} maxima and minimum data.

In summary, it was shown that 3D OD_{450} spectral microplate well scans and the corresponding 2D intensity maps are a reliable method for determining the presence of gel fibres in a material, this was indicated by the comparatively high OD_{450} measurements uniformly recorded across the entirety of the microplate well. The data recorded for these experiments was shown to correlate with T_m values with a decrease in OD_{450} observed as the T_m was approached. Additionally, through the ratio of the OD_{450} maximum and minimum values, it was possible to determine fibre presence and absence in addition to predicting the T_m range of material.

4.4 Fluorescence spectroscopy

Finally, due to the intrinsic fluorescent nature of **72**, the self-assembly processes of this SSA were investigated using fluorescence spectroscopy combined with microplate reader technology, enabling in this instance 96 experiments to be processed simultaneously. The recorded spectra for **72** in H₂O, where it is known spherical aggregates persist instead of gel fibres, demonstrated an increase in both excitation and emission (when excited at 435 nm) intensity profiles with an increase of temperature from 25 °C to 45 °C (Figure 122). As known temperatures > 40 °C break the monomeric self-associative bonds.¹³⁶ Interestingly, this destabilisation was not observed with the UV-Vis or optical density studies. However, fluorescence spectroscopy is a much more sensitive technique which can detect this transformation when other less sensitive techniques cannot.

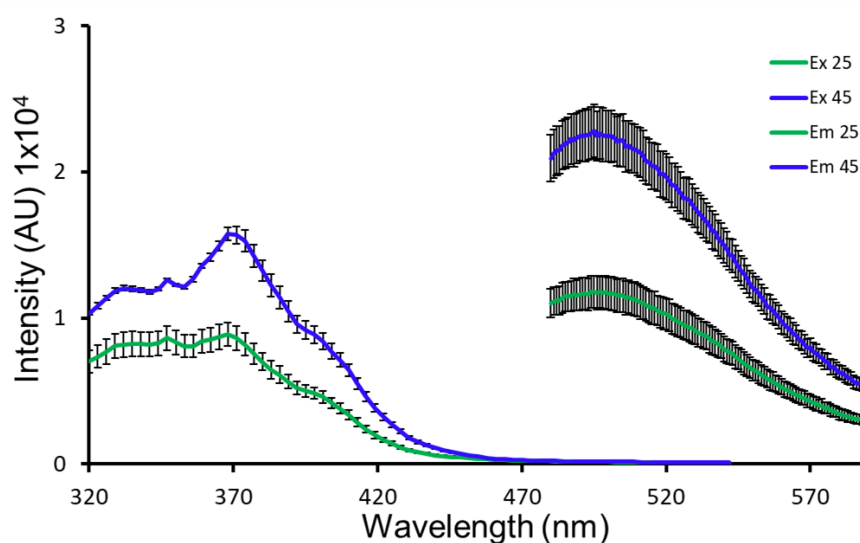


Figure 122 - Average ($n=3$) fluorescence excitation (left) and emission (right) spectra of **72** (1.5 mg/mL) at 25 °C (green) and 45 °C (blue) in H₂O.

Moving into a solution of DMSO, no distinguishable differences between excitation and emission intensity profiles with an increase of temperature was observed (Figure 123). This supports the UV-Vis (Chapter 4.2) and optical density (Chapter 4.3) measurements discussed previously where, with an increase of temperature, a negligible difference was noted.

Comparatively, the excitation and emission maxima are much greater for **72** in DMSO as opposed to H₂O, which in the previous UV-Vis studies of **72** in these solutions were shown to be very similar. This is hypothesised to be due to much smaller dimeric fluorophores, free existence in solution instead of being confined within the spherical aggregate structure or a fibrous network.

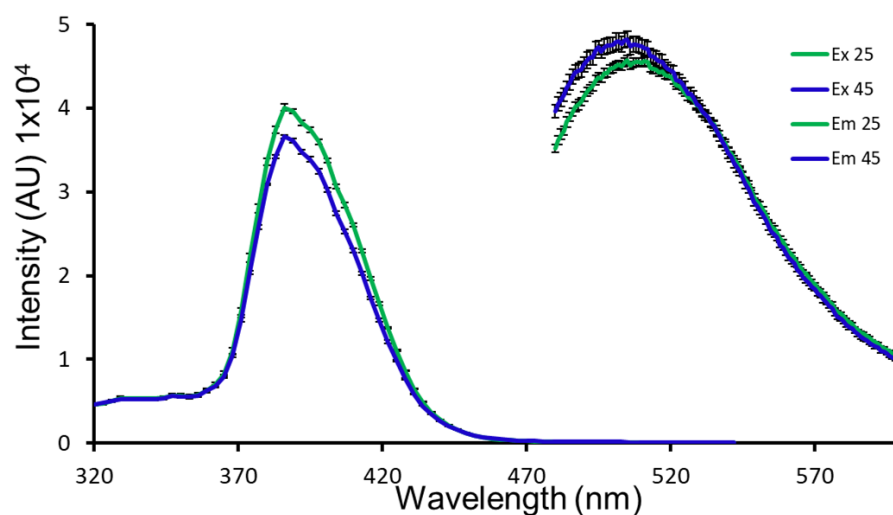


Figure 123 – Average ($n=3$) fluorescence excitation (left) and emission (right) spectra of **72** (1.5 mg/mL) at 25 °C (green) and 45 °C (blue) in DMSO.

Interestingly, when **72** acts as a gelator in the presence of aqueous salt solutions the excitation and emission profiles (Figures 124 and 125) resemble that of **72** in H₂O (Figure 122). Therefore due to the lack of distinguishable spectral features, it was not possible to verify the presence of gel fibres over spherical aggregates using this method. However, with the excitation and emission profiles obtained it was possible to track the disassembly of both the aggregated structure and all those gelled materials which exhibit a $T_m < 45$ °C (**72** in aqueous NaH₂PO₄, Na₂HPO₄, Na₂CO₃, Na₂SO₄ or NaHCO₃) (Appendix 3.4). Here the disassembly process can be identified with increasing emission spectrum, as the destabilisation temperature of the spherical aggregates and T_m of the gelled material is approached (Figures 122 and 125). There is very little change in emission spectra for those materials with a $T_m > 45$ °C such as **72** in aqueous solutions of NaOBz, NaOAc, NaNO₃, KCl, NaF, RbCl and NaCl (Figure 124) (Appendix 3.4) which again supports the presence of gel fibres in these samples at temperatures of 25 °C to 45 °C.

However, no significant difference/pattern was observed between the excitation profiles of the materials tested. It is hypothesised that this may be due to the quantity of fluorophore shielded from the excitation wavelengths supplied through self-associated structure internalisation. This is further supported when comparing these data to those of compound dimerisation observed in DMSO (Figure 123).

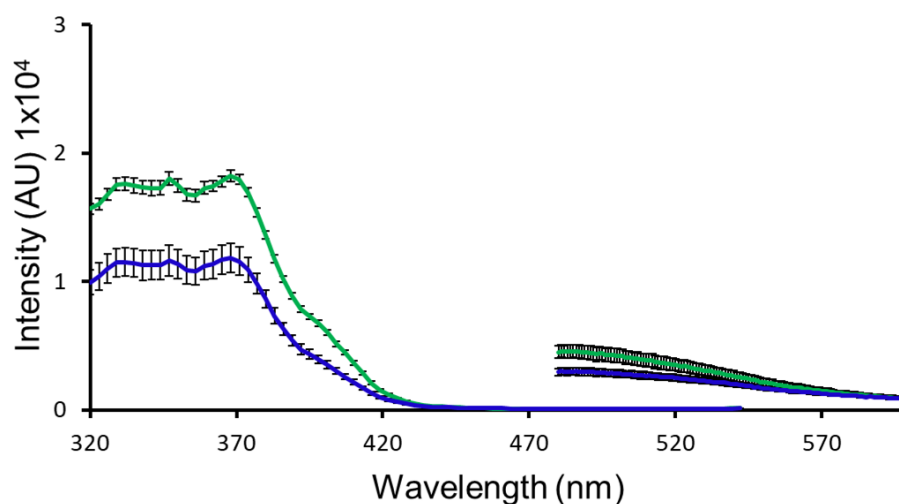


Figure 124 – Average ($n=3$) fluorescence excitation (left) and emission (right) spectra of **72** (1.5 mg/mL) at 25 °C (green) and 45 °C (blue) in aqueous NaCl (0.505 M).

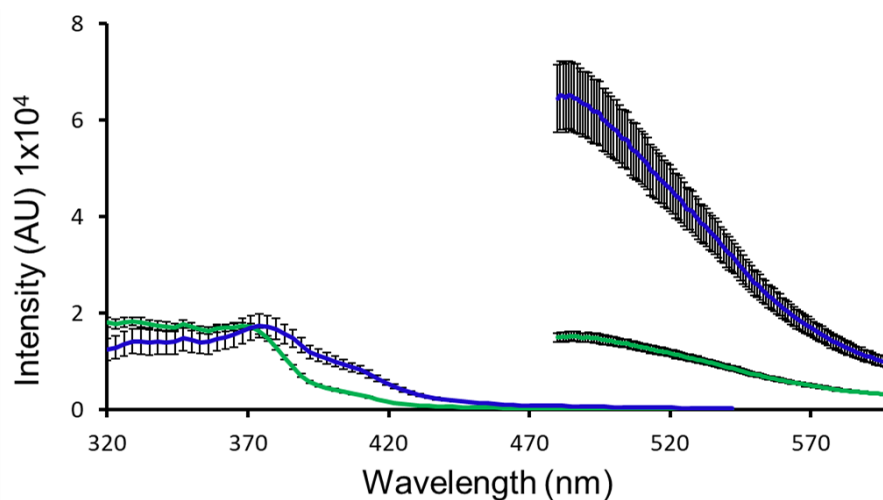


Figure 125 - Average ($n=3$) fluorescence excitation (left) and emission (right) spectra of **72** (1.5 mg/mL) at 25 °C (green) and 45 °C (blue) in aqueous Na₂CO₃ (0.505 M).

In summary, it was shown that this sensitive technique can distinguish the difference between the presence of dimers and larger self-associated aggregates in solution. However, this method could not reliably verify the presence of gel fibres over spherical aggregates.

4.5 Chapter 4: Summary

Using UV-Vis absorbance measurements it has been demonstrated that increased $Abs_{.450}$ values are indicative of gel fibre presence. In aqueous solutions, spectral well-scans confirmed amphiphilic self-assembly processes at the interface of the microplate well in the presence and absence of gel fibre formation. Optical density measurements were used to selectively observe the formation of gel fibres. Furthermore, through the ratio of OD_{450} maximum and minimum values, it was possible to determine fibre presence and absence in addition to predicting the T_m range of material. It was established that although fluorescence spectroscopy is a sensitive technique for molecular characterisation, here this sensitivity means that this method is unable to distinguish between spherical aggregate and gel fibre formation.

Finally, it was also proposed that the T_m of a supramolecular gel may be due to the disassembly temperature of the supramolecular fibre and therefore concentration-independent, however, investigations into this theory are ongoing.

4.6 Chapter 4: Conclusion

In this chapter, a tool-kit of novel high-throughput gel characterisation methods using microplate reader technology for supramolecular LMWG systems has been introduced. The benefits of using this instrumentation for supramolecular gel characterisation affords: i) low sample evaporation; ii) in-situ gel-sol/sol-gel measurement; iii) low sample volume $\approx 200 \mu\text{L}$; iv) multiple experimental measurements per sample; v) retention of sample integrity; vi) up to 384 experiments to be performed simultaneously.

4.7 Future work

Future work will involve further investigations into the hypothesis that those systems investigated within the scope of this chapter are concentration-independent to the point of solution saturation. An additional series of analogous experiments will be performed through serial dilution of the most concentrated sample.

The data from these samples will then be analysed to determine if the proportion of fibres present in a sample, changes exponentially with concentration or whether they remain constant.

Investigations will continue as to whether the destabilisation of the gel fibres observed in the UV-Vis experiments at temperatures $> 40\text{ }^{\circ}\text{C}$ for **72** in aqueous NaF, is due to the electronegativity of the fluoride ion or whether there are other plausible explanations for this. Additionally, the relationship between MGC values when **72** acts as a gelator in the presence of an aqueous solution of Na_2SO_4 or NaHCO_3 and observed negligible difference between microplate wells with an increase in temperature will be further explored.

Furthermore, recent collaboration with Dr Emily Draper (University of Glasgow), has given valuable input with regard to the data interpretation and communication which has resulted in the data from this chapter being published.¹ Dr Drapers recent work investigates the use of neutron diffraction techniques towards the characterisation of selectively deuterated gels.²⁶⁸ We are currently planning to collaborate with Dr Draper to see if this technique will aid us in gaining an understanding of the packing arrangements of those systems discussed within this chapter.

Chapter 5

5.1 Final conclusion

This thesis has focussed on understanding and predicting the self-associated properties of 30 structurally related compounds which have enabled the elucidation of preliminary structure-activity relationships that govern the self-associated abilities for this class of compound. It has been established that the physical state and the competitive solvent system in which these compounds are dissolved in plays an integral role in their self-association properties and that by using low-level computational modelling methods it may be possible to predict dimerisation constants and CMC values.

Additionally, it has been shown that the type of supramolecular materials formed can be controlled through modification of the solvent environment. In the presence of DMSO, dimers with a $d_H < 1.7$ nm were shown to be present, and in H₂O the self-association of spherical aggregates (d_H 100-550 nm) was detected. However, with the addition of salt, the preferential self-association of fibres was observed, resulting in the production of hydrogels. The physicochemical and morphological properties of which were reliant on the salt present. The stability of the resultant gelled material was found to be dependent on several salt solution based factors such as cation size; ionic strength and pH.

Finally, a tool-kit of novel high-throughput gel characterisation methods using microplate reader technology for supramolecular LMWG systems has been produced. These methods allow for the observation of up to 384 samples simultaneously. Using these novel methodologies it became possible to identify the presence or absence of gel fibres. In aqueous solutions, spectral well-scans confirmed amphiphilic self-assembly processes at the interface of the microplate well, in the presence and absence of gel fibre formation. Optical density measurements were used to selectively observe the formation of gel fibres. Furthermore, through the ratio of OD₄₅₀ maximum and minimum values, it was possible to determine fibre presence and absence in addition to predicting the T_m range of these hydrogel materials.

Chapter 6

6.1 General information

6.1.1 General information: Chapter 2

General remarks: A positive pressure of nitrogen and oven dried glassware were used for all reactions. All solvents and starting materials were purchased from known chemical suppliers or available stores and used without any further purification unless specifically stipulated.

The NMR spectra were obtained using a Jeol ECS-400, Burker AV2 400 MHz or AVNEO 400 MHz spectrometer. The data was processed using ACD Labs, MestReNova or Topspin software. NMR Chemical shift values are reported in parts per million (ppm) and calibrated to the centre of the residual solvent peak set (s = singlet, br = broad, d = doublet, t = triplet, q = quartet, m = multiplet). **Self-association constant calculation:** Self-association constants were determined using Bindfit v0.5 (<http://app.supramolecular.org/bindfit/>). All the data can be accessed online using the hyperlinks provided.

The melting point for each compound was measured using Stuart SMP10 melting point apparatus which has a temperature range from ambient to 200 °C, compounds which exhibit a melting point greater than 200 are displayed as > 200 °C. Infrared spectra were obtained using a Shimadzu IR-Affinity-1 model Infrared spectrometer. The data are analysed in wavenumbers (cm^{-1}) using IRsolution software.

DLS and zeta potential studies: DLS and Zeta Potential studies were carried out using Malvern Zetasizer Nano ZS or Anton Paar Litesizer™ 500 and processed using Kalliope™ Professional. **DLS sample preparation:** All vials used for preparing the samples were clean and dry. All solvents used were filtered to remove any particulates that may interfere with the results obtained. Samples of different concentrations were obtained through serial dilution of a concentrated solution. All samples underwent an annealing process, in which they were heated to 40 °C before being allowed to cool to 25 °C. A series of 9 or 10 runs were recorded at 25 °C.

Zeta potential sample preparation: All vials used for preparing the samples were clean and dry. All solvents used were filtered to remove any particulates that may interfere with the results obtained. All samples underwent an annealing process in which the various solutions were heated to approximately 40 °C before cooling to room temperature, allowing each sample to reach a thermodynamic minimum. The final zeta potential value given is an average of the number of experiments conducted at 25 °C.

Single Crystal X-ray Studies: A suitable crystal of each amphiphile was selected and mounted on a Rigaku Oxford Diffraction Supernova diffractometer. Data were collected using Cu K α radiation at 100 K or 293 K as necessary due to crystal instability at lower temperatures. Structures were solved with the ShelXT or ShelXS structure solution programs via Direct Methods and refined with ShelXL by Least Squares minimisation. Olex2 was used as an interface to all ShelX programs (CCDC 1997431-1997433).

Mass Spectrometry: High-resolution mass spectrometry was performed using a Bruker microTOF-Q mass spectrometer and spectra recorded and processed using Bruker's Compass Data Analysis software. **Sample preparation:** Approximately 1 mg of each compound was dissolved in 1 mL of methanol. This solution was further diluted 100-fold before undergoing analysis where 10 μ L of each sample was then injected directly into a flow of 10 mM ammonium acetate in 95 % water (flow rate = 0.02 mL/min).

Tensiometry Studies: Tensiometry measurements were undertaken using the Biolin Scientific Theta Attension optical tensiometer. The data was processed using Biolin OneAttension software. A Hamilton (309) syringe was used for the measurements. **Sample preparation:** All the samples were prepared in an EtOH:H₂O (1:19) solution. All samples underwent an annealing process in which the various solutions were heated to approximately 40 °C before being allowed to cool to room temperature, allowing each sample to reach a thermodynamic minimum.

All samples were prepared through serial dilution of the most concentrated sample. Three surface tension measurements were obtained for each sample at a given concentration, using the pendant drop method. The average values were then used to calculate the critical micelle concentration (CMC).

Low-level computational studies: All calculated parameters relating to logP, polarization or electrostatic potential maps were calculated using spartan'16 from optimised geometries obtained at the PM6 level.^{58,185}

6.1.2 General information: Chapter 3

Hydrogel preparation: The appropriate aqueous salt solution (1 mL, 0.505 M) was added to the specified quantity of the compound in a glass vial and heated to approximately 60 °C until dissolved then left at room temperature to allow gelation to occur. Gel formation was achieved through an annealing process in which the pre-gel mixture was heated until the gelator (**72**) had dissolved. At this point, the samples were sealed and allowed to cool to room temperature, before undergoing an inversion test to confirm the formation of a hydrogel. The formation of a hydrogel was attempted through the addition of the salt solution only, as well as the use of mechanical agitation by a vortexer and sonication. As neither of these conditions yielded hydrogels, this is indicative of the stability of the self-associated aggregates.

Fluorescence microscopy: Samples were visualised using an Olympus IX71 microscope with PlanApo 100x OTIRFM-SP 1.49 NA lens mounted on a PIFOC z-axis focus drive (Physik Instrumente, Karlsruhe, Germany), fitted onto an ASI motorised stage (ASI, Eugene, OR), with the sample holder, objective lens and environmental chamber held at the required temperature. Samples were illuminated using LED light sources (Cairn Research Ltd, Faversham, UK) with DC/ET350/50x excitation and DC/457/50m emission filters (Chroma, Bellows Falls, VT). Samples were visualised using a Zyla 5.5 (Andor) CMOS camera, and the system was controlled with Metamorph software (Molecular Devices). **Sample preparation:** The appropriate salt solution (1 mL, 0.505 M) was added to 5 mg of the compound in a glass vial and heated to 60 °C.

This solution was then transferred to a glass slide where it was then covered by a further glass slide before being mounted onto the microscope stage. Images were analysed using Fiji software with the SRRF plugin.

Rheometer hydrogel preparation and experimental: Rheological measurements were recorded on an Anton Parr modular compact rheometer (MCR302) using cylinder probe ST10-4V-8.8/97.5. **Sample preparation:** Each experiment was run in triplicate. The appropriate salt solution (1 mL, 0.505 M) was added to 5 mg of the compound in a glass vial with an internal diameter of 1 cm and heated to approximately 60 °C until dissolved. The sample was positioned on the rheometer and set with a relaxation time of 60 minutes. Oscillatory amplitude experiments maintained a frequency of 10 rad s⁻¹ and performed with the amplitude of oscillation from 0.01 % up to 100 % at 298 K. Oscillatory frequency sweep experiments maintained a constant shear strain (γ) of 0.0925 % with an increasing frequency from 0.1-100 rad s⁻¹ at 298 K.

Scanning Electron Microscopy (SEM) and xerogel: SEM analysis was performed using a Hitachi S3400 N scanning electron microscope, with a 20 Kv accelerating voltage at a vacuum level of <1 pa. The corresponding images were processed using Oxford Instruments AZtex software. **Sample preparation:** A sample of hydrogel containing the compound (5 mg) in the appropriate aqueous salt solution (1 mL, 0.505 M) was dehydrated to form a xerogel. The sample was then positioned on a carbon tab, which was then mounted on an aluminum stub.

pH determination: The pH was determined using a Fisherbrand hydrous 300 pH detector. The pH meter was calibrated to pH 4, pH 7 and pH 10 using standardized calibration solutions supplied by Oakton. **Salt solution preparation:** All salts were obtained from commercial sources and diluted in 100 mL of distilled H₂O. **Sample preparation:** Samples were prepared for testing by dilution of 2 g of the hydrogel in 20 mL of distilled H₂O and placed in the refrigerator for 2 hours. Before testing the samples were removed from the refrigerator and allowed to acclimatize to room temperature. Measurements were taken in triplicate and the average recorded.

Salt Solution triggered gelation: The appropriate salt solution (0.1 mL, 5.05 M) was added to the compound (1.5 mg in 0.9 mL of H₂O) in a glass vial.

Mechanically triggered gelation: The appropriate salt solution (0.1 mL, 5.05 M) was added to the compound (1.5 mg in 0.9 mL of H₂O) in a glass vial, mixed using a vortex for 1 minute and left at room temperature for 12 hours to allow gelation to occur.

6.1.3 General information: Chapter 4

UV-Vis absorbance, optical density and fluorescence measurements were conducted and analysed using a Clariostar plate reader and MARS data analysis software.

Preparation of 96-well microplates: Standards and supramolecular hydrogels/solutions of **72** ($n=3$) were prepared either in black bottom or low UV-transparent 96-well microplates. Standards or compound **72** in the relevant solutions (1.5 mg/mL) were transferred as 200 μ L aliquots to each microplate well, at a temperature higher than the melting point (T_m) of the material. Recorded at 5 mg/mL of **72**, to reduce the proportion of samples to exist as partial gels.

UV-Vis spectroscopy: After preparation, the low UV-transparent 96-well microplate was then transferred into the plate reader at an equilibrated temperature of 45 °C and absorbance measurements taken at 5-degree decreases from 45 °C to 25 °C. All experiments were repeated in triplicate to ensure experimental reproducibility.

Fluorescence spectroscopy: After preparation, the black bottom 96-well microplate was then transferred into the plate reader at an equilibrated temperature of 45 °C. Fluorescence measurements were taken at 5-degree decreases from 45 °C to 25 °C using an excitation value of 435 nm and an optimised gain of 1200. All experiments were repeated in triplicate to ensure experimental reproducibility.

Optical density (OD) spectral well scans: After preparation, the low UV-transparent 96-well microplate was then transferred into the plate reader at an equilibrated temperature of 45 °C and spectral well scans read through the sample at 5-degree decreases from 45 °C to 25 °C at Abs.₄₅₀. All experiments were repeated in triplicate to ensure experimental reproducibility.

Hydrogel melting point (T_m) determination: Supramolecular hydrogels of **72** (5 mg/mL) in the appropriate aqueous salt solution (1 mL, 0.505 M) was transferred onto the bottom stainless steel plate geometry of an Anton Parr modular compact rheometer (MCR302) at room temperature. The temperature of this bottom rheometry plate geometry was then increased until the hydrogel underwent a gel-sol transition. The temperature at which this phase change occurred was recorded as the hydrogel melting point. Each experiment was run in triplicate.

Microplate reader experimental reproducibility: To test the validity of experimental practices the following studies were undertaken; supramolecular hydrogels/solutions of **72** (1.5 mg/mL) in aqueous NaCl (0.505 M)/ H₂O were transferred as 200 μ L aliquots to each well of a low UV-transparent 96-well microplate at a temperature higher than the melting point (T_m) of the material. These low UV-transparent 96-well microplates were then transferred into the plate reader at an equilibrated temperature of 45 °C where Abs.₄₅₀ measurements were taken at 5-degree decreases from 45 °C to 25 °C. The Abs.₄₅₀ variations between each microplate well were recorded to 2 standard deviations of the mean (2 σ).

The volumes of solution/hydrogel supplied to each microplate well had a significant effect on the reproducibility of data. The addition of 200 μ L afforded reproducible data sets, compared to 100 μ L where the data was not as reliable. It is known that decreased volume, therefore shorter path lengths lead to a significantly greater error than those with increased volume and therefore a longer pathlength.²⁷⁴

6.1.3.1 Biological experimental²³⁸

Cellular growth curve measurements obtained using Thermo Scientific Multiscan Go 1510-0318C plate reader and recorded using the SkanIt Software 4.0.

Preparation of Luria Broth media (LB): Yeast extract (5 g), tryptone (10 g) and sodium chloride (10 g) were dissolved in dH₂O (1 L) then divided into bottles and autoclaved.

Preparation of Luria Broth (LB) agar plates: Agar (6 g) was added to LB (400 mL) and autoclaved. Once cool, the LB agar was poured into sterile petri dishes under sterile conditions and allowed to set. LB plates were stored at 4 °C until use.

Preparation of McFarland standard: Barium chloride (1 %, 50 μ L) was added to sulfuric acid (1 %, 9.95 mL) and mixed together. The optical density was recorded at 600 nm.

Preparation of antimicrobial compounds for MIC₅₀ calculations: Compounds were dissolved into 5 % ethanol to make up solutions on the day of experiment. Eight concentrations ranging were made up using 5 % ethanol.

Preparation of bacterial plates: Sterile LB agar plates were streaked using the desired bacteria (either *Escherichia coli* DH10B or USA300 *Methicillin-Resistant Staphylococcus aureus*) then incubated at 37 °C overnight.

Preparation of Inoculum: An initial culture was made up by inoculating LB media (5 mL) with at least 4 single colonies of the desired bacteria under sterile conditions and incubating at 37 °C overnight. The following day, a subculture was made up using LB (5 mL) and the initial culture (50 μ L), then incubated at 37 °C until the culture had reached an optical density of 0.4 at 600 nm. Density was adjusted using sterile dH₂O to equal 0.5 McFarland standard (10^7 - 10^8 cfu/mL), then a 1:10 dilution was carried out using sterile dH₂O (900 μ L) and the McFarland adjusted suspension (100 μ L). A final dilution (1:100) was carried using the 1:10 suspension (150 μ L) and LB (14.85 mL) before use to achieve a final cell concentration of 10^5 cfu/mL.

Preparation of 96 well microplates for MIC₅₀: The 1:100 cell suspension (150 μ L) was dispensed into individual wells under sterile conditions. Compounds (30 μ L) were added to the wells to equal a total volume of 180 μ L in the wells. Six repeats of each concentration for each compound were created each plate. The plates were sealed using parafilm, then incubated at 37 °C in a microplate reader for 18-25 hours. Absorbance readings were taken at 600 nm every 15 min. Data was used to generate growth curves.

Calculation of MIC₅₀: Growth curves were plotted using OD₆₀₀ absorbance readings in Microsoft[®] Excel[®] 2013. OD₆₀₀ absorbance readings 900 minutes from the start of each of these growth cultures for each concentration of drug were plotted in Origin[®] 2015. The resultant curve was normalised and fitted using the Boltzmann fit to define the MIC₅₀ values for each drug.

Agar well diffusion assay: An initial culture and subsequent subculture was created as previously described. LB Agar was made up by mixing LB (200 mL) and agar (3 g), then autoclaved. Once autoclaved, the molten agar was placed in a 50 °C water bath until it had reached this temperature. The molten agar was then inoculated using the subculture (15 mL), then swirled to mix. The inoculated agar was added to sterile petri dishes (6 mL) then allowed to set under sterile conditions. A sterile cutter was used to remove a disk from the inoculated agar, creating a well in the plate, and the bottom was sealed using fresh agar (5 µL). Once set, the desired solution or gel required was pipetted into the well (50 µL) and then placed into 37 °C incubator for 18 hours then imaged using an ESPON perfection V750 PRO.

Surface diffusion assay: An initial culture and subsequent subculture was created as previously described. LB Agar was made up by mixing LB (200 mL) and agar (3 g), then autoclaved. Once autoclaved, the molten agar was placed in a 50 °C water bath until it had reached this temperature. The molten agar was then inoculated using the subculture (15 mL), then swirled to mix. The inoculated agar was added to sterile petri dishes (6 mL) then allowed to set under sterile conditions. The molten compound gel solutions were pipetted into an empty sterile petri dish (50 µL). Once gel had set, this was carefully placed onto the center of the set agar plates, then placed into 37 °C incubator for 18 hours and imaged using an ESPON perfection V750 PRO.

6.2 Synthetic procedures

Compound 42: This compound was synthesised on a 2 mmol scale in line with our previously published methods,¹³⁴ the pure product was obtained as a white solid with a yield of 97 % (1.02 g, 1.90 mmol) Proton NMR were found to match our previously published values.¹³⁴ ¹H NMR (400 MHz, 298.15 K, DMSO-*d*₆): δ: 9.26 (s, 1H), 7.56 (d, *J* = 8.72 Hz, 2H), 7.49 (d, *J* = 8.72 Hz, 2H), 6.98 (t, *J* = 5.96 Hz, 1H), 3.93 (d, *J* = 5.96 Hz, 2H), 3.18 - 3.14 (m, 8H), 1.60 - 1.52 (m, 8H), 1.35 - 1.25 (m, 8H), 0.92 (t, *J* = 7.36 Hz, 12H).

Compound 43: TBAOH (1N) in methanol (4.0 mL, 4.00 mmol) was added to 2-aminoethanesulfonic acid (0.50 g, 4.00 mmol) and taken to dryness. The TBA salt was added to a stirring solution of 1-isocyanto-4-(trifluoromethyl)benzene (0.58 mL, 4.00 mmol) in chloroform (25 mL), heated at reflux for 3 hrs and taken to dryness, dissolved in chloroform (50 mL) and washed with water (50 mL). The organic phase was then taken to dryness. The pure product was obtained by flash chromatography, 100 % ethyl acetate followed by 100 % methanol. The methanol fraction was taken to dryness with further addition of TBAOH as necessary to give the pure product as a white solid with a yield of 60 % (1.34 g, 2.41 mmol); Melting Point: 180 °C; ¹H NMR (400 MHz, 298.15 K, DMSO-*d*₆): δ: 9.35 (s, 1H), 7.60 (d, *J* = 8.71 Hz, 2H), 7.53 (d, *J* = 8.81 Hz, 2H), 6.53 (t, *J* = 5.33 Hz, 1H), 3.38 (t, *J* = 6.04 Hz, 2H), 3.15 (m, 8H), 2.56 (t, *J* = 5.92 Hz, 2H), 1.55 (m, 8H), 1.40 - 1.20 (m, 8H), 0.92 (t, *J* = 7.33 Hz, 12H); ¹³C{¹H} NMR (100 MHz, 298.15 K, DMSO-*d*₆): δ: 155.2 (CO), 145.1 (ArC), 126.3 (dd, *J* = 3.59 Hz, ArCH), 123.8 (ArC), 121.1 (q, *J* = 31.85 Hz, CF₃), 117.6 (ArCH), 58.0 (CH₂), 51.3 (CH₂), 36.6 (CH₂), 23.5 (CH₂), 19.7 (CH₂), 13.9 (CH₃); IR (film) cm⁻¹: ν = 3273 (NH stretch), 1691, 1180, 1033, 883; HRMS for the sulfonate-urea ion (C₁₀H₁₀F₃N₂O₄S⁻) (ESI⁻): m/z: act: 311.0311 [M]⁻ cal: 311.0319 [M]⁻

Compound 44: TBAOH (1N) in methanol (2.0 mL, 2.00 mmol) was added to 3-amino-1-propane sulfonic acid (0.28 g, 2.00 mmol) and taken to dryness.

The TBA salt was added to a stirring solution of 1-Isocyanto-4-(trifluoromethyl)benzene (0.29 mL, 2.00 mmol) in chloroform (12.5 mL), heated at reflux overnight and taken to dryness, dissolved in chloroform (50 mL) and washed with water (50 mL). The organic phase was then taken to dryness. The pure product was obtained by flash chromatography, 100 % ethyl acetate followed by 100 % methanol. The methanol fraction was taken to dryness with further addition of TBAOH as necessary to give the pure product as a white solid with a yield of 56 % (0.63g, 1.11 mmol); Melting Point: 180 °C; ^1H NMR (400 MHz, 298.15 K, DMSO- d_6): δ : 8.93 (s, 1H), 7.52 (dd, J = 21.49, 8.84 Hz, 4H), 6.41 (t, J = 5.75 Hz, 1H), 3.11 (m, 10H), 2.44 - 2.37 (m, 2H), 1.75 - 1.61 (m, 2H), 1.52 (m, 8H), 1.36 - 1.12 (m, 8H), 0.89 (t, J = 7.34 Hz, 12H); $^{13}\text{C}\{^1\text{H}\}$ NMR (100 MHz, 298.15 K, DMSO- d_6): δ : 155.4 (CO), 145.1 (ArC), 126.3 (dd, J = 7.49 Hz, 3.60 Hz, ArCH), 123.8 (ArC), 121.9 (q, J = 33.95 Hz, CF₃), 117.6 (ArCH), 58.0 (CH₂), 49.5 (CH₂), 38.7 (CH₂), 26.5 (CH₂), 23.5 (CH₂), 19.7 (CH₂), 13.9 (CH₃); IR (film) cm^{-1} : ν = 3116 (NH stretch), 1697, 1176, 1031, 879; HRMS for the sulfonate-urea ion (C₁₁H₁₂F₃N₂O₄S⁻) (ESI⁻): m/z : act: 325.9465 [M]⁻ cal: 325.04575 [M]⁻.

Compound 45: This compound was synthesised on a 2 mmol scale in line with our previously published methods,¹³⁵ the pure product was obtained as a white solid with a yield of 94 % (1.04 g, 1.88 mmol). Proton NMR were found to match our previously published values.¹³⁵ ^1H NMR (400 MHz, 333.15 K, DMSO- d_6): δ : 10.28 (s, 1H), 8.19 (br s, 1H), 7.87 (br s, 2H), 7.60 (d, J = 8.24 Hz, 2H), 4.34 (br s, 2H), 3.20 - 3.16 (m, 8H), 1.63 - 1.55 (m, 8H), 1.33 (m, 8H), 0.94 (t, J = 7.33 Hz, 12H).

Compound 46: TBAOH (1N) in methanol (4.0 mL, 4.00 mmol) was added to 2-aminoethanesulfonic acid (0.50 g, 4.00 mmol) and taken to dryness. The TBA salt was added to a stirring solution of 4-(trifluoromethyl) phenyl isothiocyanate (0.82 mL, 4.00 mmol) in chloroform (25 mL), heated at reflux for 3 hrs and taken to dryness, dissolved in chloroform (50 mL) and washed with water (50 mL). The organic phase was then taken to dryness. The pure product was obtained by flash chromatography, 100 % ethyl acetate followed by 100 % methanol.

The methanol fraction was taken to dryness with further addition of TBAOH as necessary to give the pure product as a white solid with a yield of 60 % (2.0 g, 3.30 mmol); Melting Point: 138 °C; ^1H NMR (400 MHz, 298.15 K, DMSO- d_6): δ : 10.23 (s, 1H), 8.23 (s, 1H), 7.68 (dd, J = 49.51 Hz, 8.62 Hz, 4H), 3.76 (d, J = 5.33 Hz, 2H), 3.16 (m, 8H), 2.69 (t, J = 12.32 Hz, 2H), 1.66 - 1.42 (m, 8H), 1.42 - 1.12 (m, 8H), 0.93 (t, J = 7.34 Hz, 12H); $^{13}\text{C}\{^1\text{H}\}$ NMR (100 MHz, 298.15 K, DMSO- d_6): δ : 180.2 (CS), 143.9 (ArC), 126.2 (d, J = 1.85 Hz, ArCH), 126.0 (ArC), 123.6 (q, J = 63.69, 31.90 Hz, CF_3), 122.1 (ArCH), 58.0 (CH_2), 49.9 (CH_2), 41.5 (CH_2), 23.5 (CH_2), 19.7 (CH_2), 13.9 (CH_3); IR (film) cm^{-1} : ν = 3327 (NH stretch), 1610, 1168, 1037, 883; HRMS for the sulfonate-thiourea ion ($\text{C}_{10}\text{H}_{10}\text{F}_3\text{N}_2\text{O}_3\text{S}_2^-$) (ESI $^-$): m/z: act: 327.0090 [M] $^-$ cal: 327.3168 [M] $^-$

Compound 47: TBAOH (1N) in methanol (2.0 mL, 2.00 mmol) was added to 3-amino-1-propane sulfonic acid (0.28 g, 2.00 mmol) and taken to dryness. The TBA salt was added to a stirring solution of 4-(trifluoromethyl) phenyl isothiocyanate (0.41 g, 2.00 mmol) in chloroform (12.5 mL), heated at reflux overnight and taken to dryness, dissolved in chloroform (50 mL) and washed with water (50 mL). The organic phase was then taken to dryness. The pure product was obtained by flash chromatography, 100 % ethyl acetate followed by 100 % methanol. The methanol fraction was taken to dryness with further addition of TBAOH as necessary to give the pure product as a white solid with a yield of 76 % (0.89 g, 1.11 mmol); Melting Point: 149 °C; ^1H NMR (400 MHz, 333.15 K, DMSO- d_6): δ : 9.95 (s, 1H), 8.25 (s, 1H), 7.77 (d, J = 8.10 Hz, 2H), 7.62 (d, J = 8.66 Hz, 2H), 3.56 (d, J = 5.29 Hz, 2H), 3.21 - 3.10 (m, 8H), 1.94 - 1.75 (m, 2H), 1.56 (m, 8H), 1.39 - 1.20 (m, 8H), 0.93 (t, J = 7.33 Hz, 12H); $^{13}\text{C}\{^1\text{H}\}$ NMR (100 MHz, 298.15 K, DMSO- d_6): δ : 180.7 (CS), 144.4 (ArC), 126.3 (ArC), 125.8 (d, J = 2.89 Hz, ArCH), 123.5 (q, J = 65.49 Hz, CF_3), 121.9 (ArCH), 58.0 (CH_2), 49.6 (CH_2), 43.3 (CH_2), 25.2 (CH_2), 23.5 (CH_2), 19.7 (CH_2), 14.0 (CH_3); IR (film) cm^{-1} : ν = 3323 (NH stretch), 1614, 1170, 1033, 883; HRMS for the sulfonate-thiourea ion ($\text{C}_{11}\text{H}_{12}\text{F}_3\text{N}_2\text{O}_3\text{S}_2^-$) (ESI $^-$): m/z: act: 341.3438 [M] $^-$ cal: 341.0247 [M] $^-$.

Compound 48: This compound was synthesised on a 2 mmol scale in line with our previously published methods,¹³⁵ the pure product was obtained as a white solid with a yield of 100 % (0.64 g, 2.00 mmol). Proton NMR were found to match our previously published values.¹³⁵

^1H NMR (400 MHz, 298.15 K, $\text{DMSO-}d_6$): δ : 3.93 (d, J = 5.95 Hz, 2H), 6.87 (t, J = 4.58 Hz, 1H), 7.51 (d, J = 9.16 Hz 2H), 7.56 (d, J = 8.70 Hz, 2H), 9.22 (s, 1H).

Compound 49: This compound was synthesised on a 4 mmol scale in line with our previously published methods,¹³⁵ the pure product was obtained as a white solid with a yield of 96 % (1.44 g, 3.84 mmol). Proton NMR were found to match our previously published values.¹³⁵ ^1H NMR (400 MHz, 298.15 K, $\text{DMSO-}d_6$): δ : 9.17 (s, 1H), 8.87 (d, J = 4.58 Hz, 2H), 8.45 (t, J = 6.41 Hz, 1H), 7.95 (t, J = 7.33 Hz, 2H), 7.56 (s, 4H), 6.60 (s, 1H), 3.88 (d, J = 5.48 Hz, 2H).

Compound 50: Aminomethanesulfonic acid (0.44 g, 4.00 mmol) was added to a stirring solution of 1-Isocyanato-4-(trifluoromethyl) benzene (0.58 mL, 4.00 mmol) in anhydrous pyridine (20 mL) under an inert atmosphere. The mixture was heated to 60 °C overnight. The pyridinium salt was then removed by filtration. Yield: 82 % (0.56 g, 1.49 mmol). The pyridinium salt (0.38 g, 1.00 mmol) was dissolved in a solution of TMAOH pentahydrate (0.095 g) and H_2O (0.45 g) to give the pure product as a white solid with a yield of 97 % (0.36 g, 0.97 mmol); Melting Point: > 200 °C; ^1H NMR (400 MHz, 298.15 K, $\text{DMSO-}d_6$): δ : 9.18 (s, 1H), 7.55 (s, 4H), 6.68 (s, 1H), 3.89 (d, J = 5.89 Hz, 2H), 3.09 (s, 12H); $^{13}\text{C}\{^1\text{H}\}$ NMR (100 MHz, 298.15 K, $\text{DMSO-}d_6$): δ : 154.7 (CO), 144.7 (ArC), 126.1 (dd, J = 7.31 Hz, 3.55 Hz, ArCH), 123.8 (ArC), 121.3 (q, J = 31.86 Hz, CF_3), 117.7 (ArCH), 56.4 (CH_2), 54.9 (CH_3); IR (film) cm^{-1} : ν = 3113 (NH stretch), 1697, 1182, 1033, 839; HRMS for the sulfonate-urea ion ($\text{C}_9\text{H}_8\text{F}_3\text{N}_2\text{O}_4\text{S}^-$) (ESI $^-$): m/z: act: 297.0164 [M] $^-$ cal: 297.0162 [M] $^-$.

Compound 51: This compound was produced with an analogous method to that described with the synthesis of compound 50. The pyridinium salt (0.38 g, 1.00 mmol) was dissolved in a solution of TEAOH in H_2O (0.26 g, 1.00 mmol) to give the pure product as a white solid with a yield of 97 % (0.41 g, 0.97 mmol); Melting Point: 165 °C; ^1H NMR (400 MHz, 298.15 K, $\text{DMSO-}d_6$): δ : 9.33 (s, 1H), 7.78 - 7.18 (m, 5H), 4.01 (s, 2H), 3.18 (d, J = 3.71 Hz, 8H), 1.13 (s, 12H); $^{13}\text{C}\{^1\text{H}\}$ NMR (100 MHz, 298.15 K, $\text{DMSO-}d_6$): δ : 154.7 (CO), 144.9 (ArC), 126.1 (d, J = 3.01 Hz, ArCH), 123.8 (ArC), 121.2 (q, J = 32.05 Hz, CF_3), 117.7 (ArCH), 56.4 (CH_2), 51.9 (CH_2), 7.5 (CH_3); IR (film) cm^{-1} : ν = 3120 (NH stretch), 1697, 1182, 1037, 842; HRMS for the sulfonate-urea ion ($\text{C}_9\text{H}_8\text{F}_3\text{N}_2\text{O}_4\text{S}^-$) (ESI $^-$): m/z: act: 297.0174 [M] $^-$ cal: 297.0162 [M] $^-$.

Compound 52: This compound was produced with an analogous method to that described with the synthesis of compound **50**. The pyridinium salt (0.38 g, 1.00 mmol) was dissolved in a solution of TPAOH in H₂O (0.36 g, 1.00 mmol) to give the pure product as a white solid with a yield of 97 % (0.47 g, 0.97 mmol); Melting Point: 145 °C; ¹H NMR (400 MHz, 298.15 K, DMSO-*d*₆): δ: 9.19 (s, 1H), 7.56 (s, 4H), 6.69 (s, 1H), 3.89 (d, *J* = 5.87 Hz, 2H), 3.23 - 2.95 (m, 8H), 1.61 (q, *J* = 14.96 Hz, 7.31 Hz, 8H), 0.89 (t, *J* = 7.27 Hz, 12H); ¹³C{¹H} NMR (100 MHz, 298.15 K, DMSO-*d*₆): δ: 154.7 (CO), 144.8 (ArC), 126.2 (dd, *J* = 7.50 Hz, 3.73 Hz, ArCH), 123.8 (ArC), 121.3 (q, *J* = 31.85 Hz, CF₃), 117.6 (ArCH), 59.8 (CH₂), 56.4 (CH₂), 15.3 (CH₂), 11.0 (CH₃); IR (film) cm⁻¹: ν = 3118 (NH stretch), 1697, 1182, 1039, 856; HRMS for the sulfonate-urea ion (C₉H₈F₃N₂O₄S⁻) (ESI⁻): m/z: act: 297.0156 [M]⁻ cal: 297.0162 [M]⁻.

Compound 53: This compound was produced with an analogous method to that described with the synthesis of compound **50**. The pyridinium salt (0.38 g, 1.00 mmol) was dissolved in a solution of 20 % TPeAOH in H₂O (1.58 g, 1.00 mmol) to give the pure product as a white solid with a yield of 99 % (0.58 g, 0.99 mmol); Melting Point: 90 °C; ¹H NMR (400 MHz, 298.15 K, DMSO-*d*₆): δ: 9.20 (s, 1H), 7.48 (dd, *J* = 23.57 Hz, 8.5 Hz, 4H), 6.89 (s, 1H), 3.88 (d, *J* = 5.65 Hz, 2H), 3.31 (d, *J* = 1.11 Hz, 4H), 3.21 - 3.01 (m, 8H), 2.45 (d, *J* = 1.23 Hz, 2H), 1.52 (s, 1H), 1.39 - 1.02 (m, 17H), 0.83 (t, *J* = 6.82 Hz, 12H); ¹³C{¹H} NMR (100 MHz, 298.15 K, DMSO-*d*₆): δ: 154.7 (CO), 144.8 (ArC), 126.4 (d, *J* = 24.22 Hz, ArCH), 123.8 (ArC), 121.3 (q, *J* = 32.80 Hz, CF₃), 117.6 (ArCH), 58.1 (CH₂), 56.4 (CH₂), 28.4 (CH₂), 22.1 (CH₂), 21.2 (CH₂), 14.3 (CH₃); IR (film) cm⁻¹: ν = 2956 (NH stretch), 1695, 1182, 1031, 841; HRMS for the sulfonate-urea ion (C₉H₈F₃N₂O₄S⁻) (ESI⁻): m/z: act: 297.0155 [M]⁻ cal: 297.0162 [M]⁻.

Compound 54: This compound was produced with an analogous method to that described with the synthesis of compound **50**. The pyridinium salt (0.38 g, 1.00 mmol) was dissolved in a solution of 40 % THAOH in H₂O (0.93 g, 1.00 mmol) to give the pure product as an oil with a yield of 98 % (0.64 g, 0.98 mmol); ¹H NMR (400 MHz, 298.15 K, DMSO-*d*₆): δ: 9.42 (s, 1H), 7.51 (dd, *J* = 44.67 Hz, 8.27 Hz, 4H), 7.23 (s, 1H), 3.96 (d, *J* = 5.54 Hz, 2H), 3.15 (d, *J* = 12.42 Hz, 8H), 1.55 (s, 8H), 1.27 (s, 24H), 0.86 (s, 12H); ¹³C{¹H} NMR (100 MHz, 298.15 K, DMSO-*d*₆): δ: 154.8 (CO), 144.7 (ArC), 126.3 (d, *J* = 13.13 Hz, ArCH), 123.8 (ArCH), 121.2 (q, *J* = 108.04 Hz, ArC), 117.6 (ArCH), 58.1 (CH₂), 56.4 (CH₂), 31.1 (CH₂), 25.9 (CH₂), 22.4 (CH₂), 21.5 (CH₂), 14.3 (CH₃); IR (film) cm⁻¹: ν = 3288 (NH stretch), 1695, 1182, 1035, 840; HRMS for the sulfonate-urea ion (C₉H₈F₃N₂O₄S⁻) (ESI⁻): m/z: act: 297.0141 [M]⁻ cal: 297.0162 [M]⁻.

Compound 55: Hydrazine hydrate (2.15 mL, 4.29 mmol) and 10 % palladium on carbon (2 g) were added to a stirring solution of compound **58** (2.21 g, 4.29 mmol) in ethanol (25 mL) and heated at reflux overnight under an inert atmosphere. Filtered, and the organic layer taken to dryness to give a brown solid with a yield of 96 % (2.00 g, 4.11 mmol); Melting Point: 189 °C; ¹H NMR (400 MHz, 298.15 K, DMSO-*d*₆): δ: 8.42 (s, 1H), 7.04 (d, *J* = 8.64 Hz, 2H), 6.51 (d, *J* = 8.64 Hz, 2H), 6.41 (t, *J* = 5.92 Hz, 1H), 3.88 (d, *J* = 5.93 Hz, 2H), 3.28 - 3.01 (m, 8H), 1.73 - 1.40 (m, 8H), 1.29 (m, 8H), 0.92 (t, *J* = 7.33 Hz, 12H); ¹³C{¹H} NMR (100 MHz, 298.15 K, DMSO-*d*₆): δ: 155.4 (CO), 142.4 (ArC), 131.0 (ArC), 120.1 (ArCH), 115.3 (ArCH), 58.0 (CH₂), 56.7 (CH₂), 23.5 (CH₂), 19.7 (CH₂), 14.0 (CH₃); IR (film) cm⁻¹: ν = 3227 (NH stretch), 1685, 1213, 1168, 883; HRMS for the sulfonate-urea ion (C₈H₁₀N₃O₄S⁻) (ESI⁻): m/z: act: 244.0394 [M]⁻ cal: 244.0398 [M]⁻.

Compound 56: This compound was synthesised on a 2 mmol scale in line with our previously published methods,¹³⁵ the pure product was obtained as a white waxy solid with a yield of 72 % (0.72 g, 1.44 mmol). Proton NMR were found to match our previously published values.¹³⁵ ¹H NMR (400 MHz, 298.15 K, DMSO-*d*₆): δ: 8.62 (s, 1H), 8.70 (d, *J* = 7.27 Hz, 2H), 6.79 (d, *J* = 9.16 Hz, 2H), 6.50 (t, *J* = 5.95 Hz, 1H), 3.87 (d, *J* = 5.95 Hz, 2H), 3.68 (s, 3H), 3.18 - 3.13 (m, 8H), 1.60 - 1.52 (m, 8H), 1.30 (m, 8H), 0.93 (t, *J* = 7.33 Hz, 12H).

Compound 57: This compound was synthesised on a 3 mmol scale in line with our previously published methods,¹³⁵ the pure product was obtained as a white solid with a yield of 64 % (0.91 g, 1.92 mmol). Proton NMR were found to match our previously published values.¹³⁵ ¹H NMR (400 MHz, 298.15 K, DMSO-*d*₆): δ: 8.76 (s, 1H), 7.36 (d, *J* = 8.28 Hz, 2H), 7.21 (t, *J* = 7.32 Hz, 2H), 6.87 (t, *J* = 7.32 Hz, 1H), 6.47 (t, *J* = 5.52 Hz, 1H), 3.86 (d, *J* = 5.92 Hz, 2H), 3.18 - 3.14 (m, 8H), 1.60 - 1.52 (m, 8H), 1.32 (m, 8H), 0.93 (t, *J* = 7.32 Hz, 12H).

Compound 58: This compound was synthesised on a 4 mmol scale in line with our previously published methods,¹³⁵ the pure product was obtained as a pale yellow solid with a yield of 86 % (1.77 g, 3.44 mmol). Proton NMR were found to match our previously published values.¹³⁴ ¹H NMR (400 MHz, 298.15 K, DMSO-*d*₆): δ: 9.63 (s, 1H), 8.04 (d, *J* = 9.16 Hz, 2H), 7.58 (d, *J* = 9.16 Hz, 2H), 7.30 (t, *J* = 5.96 Hz, 1H), 3.96 (d, *J* = 5.96 Hz, 2H), 3.18 - 3.14 (m, 8H), 1.60 - 1.52 (m, 8H), 1.35 - 1.25 (m, 8H), 0.92 (t, *J* = 7.36 Hz, 12H).

Compound 59: Tin shavings (0.65 g) were added to a stirring solution of compound **62** (0.50 g, 0.94 mmol) in ethanol (10 mL) and concentrated HCl (1 mL) and left to stir for 24 hours at room temperature. Crude product precipitates out to give a white solid with a yield of 70 % (0.33 g, 0.66 mmol). IR (film) cm⁻¹: ν = 3219 (NH stretch), 1685, 1203, 1177, 846; HRMS for the sulfonate-thiourea ion (C₈H₁₀N₃O₃S₂⁻) (ESI⁻): *m/z*: act: 260.0271 [M]⁻ cal: 260.3100 [M]⁻.

Compound 60: TBAOH (1N) in methanol (1.73 mL, 1.73 mmol) was added to 2-aminomethanesulfonic acid (0.19 g, 1.73 mmol) and taken to dryness overnight. The TBA salt was added to a stirring solution of 4-methoxyphenyl isothiocyanate (0.24 mL, 1.73 mmol) in ethyl acetate (10 mL), heated at reflux overnight under an inert atmosphere, forming an oil. The oil was decanted, dissolved in chloroform (20 mL) and washed with water (20 mL).

The organic phase was then taken to dryness to give the pure product as a white solid with a yield of 50 % (0.45 g, 0.86 mmol); Melting Point: 145 °C; ^1H NMR (400 MHz, 333.15 K, $\text{DMSO-}d_6$): δ : 9.79 (s, 1H), 7.56 (s, 1H), 7.36 (d, J = 7.94 Hz, 2H), 6.87 (d, J = 7.89 Hz, 2H), 4.23 (s, 8H), 3.75 (s, 1H), 3.34 - 3.03 (m, 1H), 1.76 - 1.46 (m, 8H), 1.47 - 1.20 (m, 8H), 0.95 (t, J = 7.25 Hz, 12H); $^{13}\text{C}\{^1\text{H}\}$ NMR (100 MHz, 298.15 K, $\text{DMSO-}d_6$): δ : 181.1 (CS), 156.6 (ArC), 132.8 (ArC), 125.5 (ArCH), 114.1 (ArCH), 60.9 (CH_2), 58.0 (CH_2), 55.7 (CH_3), 23.5 (CH_2), 19.7 (CH_2), 14.0 (CH_3); IR (film): ν = 3234 (NH stretch), 1550, 1220, 1155, 877; HRMS for the sulfonate-thiourea ion ($\text{C}_9\text{H}_{11}\text{N}_2\text{O}_4\text{S}_2^-$) (ESI $^-$): m/z : act: 275.0238 [M] $^-$ cal: 275.0166 [M] $^-$.

Compound 61: TBAOH (1N) in methanol (1.73 mL, 1.73 mmol) was added to 2-aminomethanesulfonic acid (0.19 g, 1.73 mmol) and taken to dryness overnight. Phenyl isothiocyanate (0.21 mL, 1.73 mmol) was added to a stirring solution of the TBA salt in ethyl acetate (10 mL), heated at reflux overnight under an inert atmosphere, forming an oil. The oil was decanted, dissolved in chloroform (20 mL) and washed with water (20 mL). The organic phase was then taken to dryness to give the pure product as a white solid with a yield of 61 % (0.51 g, 1.05 mmol); Melting Point: 146 °C; ^1H NMR (400 MHz, 333.15 K, $\text{DMSO-}d_6$): δ : 9.93 (s, 1H), 7.77 (s, 1H), 7.54 (d, J = 7.84 Hz, 2H), 7.29 (t, J = 7.29 Hz, 2H), 7.07 (t, J = 7.46 Hz, 1H), 4.24 (s, 2H), 3.30 - 2.95 (m, 8H), 1.60 (m, 8H), 1.48 - 1.14 (m, 8H), 0.95 (t, J = 7.27 Hz, 12H); $^{13}\text{C}\{^1\text{H}\}$ NMR (100 MHz, 298.15 K, $\text{DMSO-}d_6$): δ : 180.7 (CO), 140.1 (ArC), 128.7 (d, J = 24.30 Hz, ArCH), 124.3 (ArCH), 123.0 (ArCH), 60.8 (CH_2), 58.0 (CH_2), 23.5 (CH_2), 19.7 (CH_2), 14.0 (CH_3); IR (film): ν = 3317 (NH stretch), 1651, 1232, 1159, 883; HRMS for the sulfonate-thiourea ion ($\text{C}_8\text{H}_9\text{N}_2\text{O}_3\text{S}_2^-$) (ESI $^-$): m/z : act: 245.0116 [M] $^-$ cal: 245.0060 [M] $^-$.

Compound 62: TBAOH (1N) in methanol (4.0 mL, 4.0 mmol) was added to 2-aminomethanesulfonic acid (0.44 g, 4.0 mmol) and taken to dryness overnight. To a stirring solution of the TBA salt in acetonitrile (15 mL), 4-nitrophenyl isothiocyanate (0.73 g, 4.0 mmol) was added, heated at reflux overnight and taken to dryness, dissolved in ethyl acetate (20 mL) and left-over night at 2 °C.

The pure product crystallised out with a yield of 89 % (1.32 g, 3.6 mmol); Melting Point: 145 °C; ^1H NMR (400 MHz, 333.15 K, DMSO- d_6): δ : 10.50 (bs, 1H), 8.33 (bs, 1H), 8.14 (d, J = 7.68 Hz, 2H), 7.96 (s, 2H), 4.33 (s, 2H), 3.25 - 3.14 (m, 1H), 1.61 (d, J = 6.69 Hz, 8H), 1.34 (m, 8H), 0.94 (t, J = 6.54 Hz, 12H); $^{13}\text{C}\{^1\text{H}\}$ NMR (100 MHz, 298.15 K, DMSO- d_6): δ : 180.2 (CS), 147.0 (CO), 142.3 (ArC), 124.5 (d, J = 15.02 Hz, ArCH), 121.7 (ArC), 120.7 (ArCH), 60.6 (CH₂), 58.0 (CH₂), 23.5 (CH₂), 19.7 (CH₂), 14.0 (CH₃); IR (film): ν = 3224 (NH stretch), 1550, 1228, 1165, 852; HRMS for the sulfonate-thiourea ion (C₈H₈N₃O₅S₂⁻) (ESI⁻): m/z : act: 290.0001 [M]⁻ cal: 289.9911 [M]⁻.

Compound 63: *Tert*-butyl 2-aminoacetate (0.27 mL, 2.00 mmol) was added to a stirring solution of 1-Isocyanato-4-(trifluoromethyl) benzene (0.29 mL, 2.00 mmol) in chloroform (10 mL) and left at RT overnight. The mixture was placed on the rotary-evaporator until 5 mL remained. Hexane was added dropwise and the precipitate removed by filtration to give the pure product as a white solid with a yield of 45 % (0.29 g, 0.91 mmol); Melting Point: 110 °C; ^1H NMR (400 MHz, 298.15 K, DMSO- d_6): δ : 9.23 (s, 1H), 7.73 - 7.41 (m, 4H), 6.53 (t, J = 5.90 Hz, 1H), 3.77 (d, J = 5.91 Hz, 2H), 1.42 (s, 9H); $^{13}\text{C}\{^1\text{H}\}$ NMR (100 MHz, 298.15 K, DMSO- d_6): δ : 170.2 (CO), 155.3 (CO), 144.5 (ArC), 126.5 (d, J = 3.79 Hz, ArCH), 123.7 (ArCH), 121.7 (q, J = 31.81 Hz, CF₃), 117.8 (ArC), 81.1 (C), 42.4 (CH₂), 28.2 (CH₃); IR (film): ν = 2993 (NH stretch), 1730, 1442, 1319, 1219; HRMS for the *tert*-butyl carboxylate-urea (C₁₄H₁₇F₃N₂O₃) (ESI⁻): m/z : act: 317.1097 [M]⁻ cal: 318.1191 [M]⁻.

Compound 64: Trifluoroacetic acid (5 mL) was added to a stirring solution of compound **63** (0.15 g, 0.47 mmol) in dichloromethane (10 mL). Additional dichloromethane (10 mL) was added and washed with sodium hydroxide (20 mL, 6 M). The aqueous phase was then taken to dryness, dissolved in H₂O (20 mL) and hydrochloric acid (2 M) added dropwise until pH neutral, with the precipitate removed by filtration to give the pure product as a white solid with a yield of 65 % (0.08 g, 0.31 mmol);

Melting Point: > 200 °C; ^1H NMR (400 MHz, 298.15 K, DMSO- d_6): δ : 9.22 (s, 1H), 7.58 (s, 4H), 6.51 (t, J = 5.64 Hz, 1H), 3.79 (d, J = 5.71 Hz, 2H); $^{13}\text{C}\{^1\text{H}\}$ NMR (100 MHz, 298.15 K, DMSO- d_6): δ : 172.5 (CO), 155.4 (CO), 144.5 (ArC), 144.4 (ArC), 126.5 (d, J = 3.65 Hz, ArCH), 121.4 (q, J = 43.30 Hz, CF_3), 117.8 (ArCH), 41.8 (CH_2); IR (film): ν = 2962 (NH stretch), 1685, 1448, 1319, 882; HRMS for the carboxylic acid-urea ($\text{C}_{10}\text{H}_9\text{F}_3\text{N}_2\text{O}_3$) (ESI^-): m/z : act: 261.0501 [M] $^-$ cal: 262.0565 [M] $^-$.

Compound 65: Compound **64** (0.05 g, 0.17 mmol) was dissolved in a solution of TBAOH (1N) in methanol (0.17 mL) and taken to dryness to give the pure product as a white solid with a yield of 83 % (0.07 g, 0.14 mmol); Melting Point: > 200 °C; ^1H NMR (400 MHz, 298.15 K, DMSO- d_6): δ : 9.51 (s, 1H), 7.73 (d, J = 8.74 Hz, 2H), 7.42 (d, J = 8.74 Hz, 2H), 6.49 (s, 1H), 3.38 (d, J = 4.00 Hz, 8H), 3.20 - 3.07 (m, 14H), 1.67 - 1.44 (m, 8H), 1.40 - 1.18 (m, 8H), 0.92 (t, J = 7.34 Hz, 12H); $^{13}\text{C}\{^1\text{H}\}$ NMR (100 MHz, 298.15 K, DMSO- d_6): δ : 172.2 (CO), 168.6 (CO), 155.2 (d, J = 8.89 Hz, ArCH), 145.0 (ArC), 130.6 (ArC), 119.5 (q, J = 24.27 Hz, 13.69 Hz, CF_3), 116.6 (ArCH), 58.0 (CH_2), 44.8 (CH_2), 23.5 (CH_2), 19.7 (CH_2), 14.0 (CH_3); IR (film): ν = 2958 (NH stretch), 1734, 1436, 1321, 948; HRMS for the carboxylate-urea ion ($\text{C}_{10}\text{H}_8\text{F}_3\text{N}_2\text{O}_3^-$) (ESI^-): m/z : act: 261.0501 [M] $^-$ cal: 261.0493 [M] $^-$.

Compound 66: *Tert*-butyl 2-aminoacetate (0.27 mL, 2.00 mmol) was added to a stirring solution of 4-(trifluoromethyl)phenyl isothiocyanate (0.41 g, 2.00 mmol) in chloroform (10 mL) and left at RT overnight. The mixture was placed on the rotary-evaporator until 5 mL remained. Hexane was added dropwise and the precipitate removed by filtration to give the pure product as a white solid with a yield of 77 % (0.52 g, 1.54 mmol); Melting Point: 135 °C; ^1H NMR (400 MHz, 298.15 K, DMSO- d_6): δ : 10.27 (bs, 1H), 8.23 (t, J = 5.53 Hz, 1H), 7.71 (dd, J = 26.91 Hz, 8.68 Hz, 4H), 4.18 (d, J = 5.50 Hz, 2H), 1.43 (s, 9H); $^{13}\text{C}\{^1\text{H}\}$ NMR (100 MHz, 298.15 K, DMSO- d_6): δ : 181.6 (CO), 169.0 (CO), 143.5 (ArC), 128.9 (ArC), 126.3 (d, J = 3.47 Hz, ArCH), 123.9 (q, J = 32.02 Hz, 31.89 Hz, CF_3), 122.5 (ArCH), 81.4 (C), 46.6 (CH_2), 28.2 (CH_3); IR (film): ν = 3035 (NH stretch), 1734, 1508, 1323, 1224; HRMS for the *tert*-butyl carboxylate-thiourea ($\text{C}_{14}\text{H}_{17}\text{F}_3\text{N}_2\text{O}_2\text{S}$) (ESI^-): m/z : act: 333.0874 [M] $^-$ cal: 334.0963 [M] $^-$.

Compound 67: Trifluoroacetic acid (5 mL) was added to a stirring solution of Compound **66** (0.30 g, 0.90 mmol) in dichloromethane (10 mL). Additional dichloromethane (10 mL) was added and washed with sodium hydroxide (20 mL, 6 M). The aqueous phase was then taken to dryness, dissolved in H₂O (20 mL) and hydrochloric acid (2 M) added dropwise until pH neutral. The precipitate was removed by filtration to give the pure product as a brown solid with a yield of 83 % (0.21 g, 0.75 mmol); Melting Point: 154 °C; ¹H NMR (400 MHz, 298.15 K, DMSO-*d*₆): δ: 12.78 (s, 1H), 10.26 (s, 1H), 8.20 (t, *J* = 5.38 Hz, 1H), 7.73 (dd, *J* = 38.27 Hz, 8.60 Hz, 4H), 4.23 (d, *J* = 5.32 Hz, 2H); ¹³C{¹H} NMR (100 MHz, 298.15 K, DMSO-*d*₆): δ: 181.3 (CS), 171.3 (CO), 143.6 (ArC), 126.2 (d, *J* = 4.14 Hz, ArCH), 124.3 (ArC), 124.2 (q, *J* = 54.66 Hz, 23.28 Hz, CF₃), 46.0 (CH₂); IR (film): ν = 2964 (NH stretch), 1691, 1487, 1319, 883; HRMS for the carboxylic acid-thiourea (C₁₀H₉F₃N₂O₂S) (ESI⁻): *m/z*: act: 277.0265 [M]⁻ cal: 278.0337 [M]⁻.

Compound 68: Compound **67** (0.10 g, 0.35 mmol) was dissolved in a solution of TBAOH (1N) in methanol (0.35 mL) and taken to dryness to give the pure product as a white solid with a yield of 62 % (0.11 g, 0.21 mmol); Melting Point: > 200 °C; ¹H NMR (400 MHz, 298.15 K, DMSO-*d*₆): δ: 12.30 (s, 1H), 8.77 (s, 1H), 8.38 (d, *J* = 8.09 Hz, 2H), 7.55 (d, *J* = 8.28 Hz, 2H), 3.73 (s, 2H), 3.22 - 3.01 (m, 8H), 1.66 - 1.43 (m, 8H), 1.43 - 1.15 (m, 8H), 0.92 (t, *J* = 7.33 Hz, 12H); ¹³C{¹H} NMR (100 MHz, 298.15 K, DMSO-*d*₆): δ: 178.7 (CS), 170.3 (CO), 145.7 (ArC), 125.5 (d, *J* = 3.29 Hz, ArCH), 123.8 (ArC), 122.2 (q, *J* = 31.70 Hz, CF₃), 120.3 (ArCH), 58.0 (CH₂), 50.0 (CH₂), 23.5 (CH₂), 19.7 (CH₂), 13.9 (CH₃); IR (film): ν = 2970 (NH stretch), 1734, 1435, 1323, 983; HRMS for the carboxylate-thiourea ion (C₁₀H₈F₃N₂O₂S⁻) (ESI⁻): *m/z*: act: 277.0261 [M]⁻ cal: 277.0264 [M]⁻.

Compound 69: This compound was synthesised on a 2 mmol scale in line with our previously published methods,¹³⁶ the pure product was obtained as a pale brown solid with a yield of 44 % (0.46 g, 0.88 mmol). Proton NMR were found to match our previously published values.¹³⁶ ¹H NMR (400 MHz, 298.15 K, DMSO-*d*₆): δ: 8.80 (s, 1H), 8.17 (d, *J* = 7.99 Hz, 1H), 8.09 (d, *J* = 5.44 Hz, 1H), 7.88 (d, *J* = 8.18 Hz, 1H), 7.60 – 7.46 (m, 3H), 7.41 (t, *J* = 7.89 Hz, 1H), 7.11 (t, *J* = 5.68 Hz, 1H), 3.94 (d, *J* = 5.72 Hz, 2H), 3.21 – 3.05 (m, 8H), 1.64 – 1.40 (m, 8H), 1.41 – 1.21 (m, 8H), 0.92 (t, *J* = 7.31 Hz, 12H).

Compound 70: This compound was synthesised on a 2 mmol scale in line with our previously published methods,¹³⁶ the pure product was obtained as a yellow solid with a yield of 49 % (0.56 g, 0.98 mmol). Proton NMR were found to match our previously published values.¹³⁶ ¹H NMR (400 MHz, 298.15 K, DMSO-*d*₆): δ: 9.11 (br s, 1H), 8.41 (s, 1H), 8.30 (s, 1H), 8.21 (s, 1H), 7.97 (dd, *J* = 12.97, 8.00 Hz, 3H), 7.50 – 7.29 (m, 3H), 6.80 (t, *J* = 5.67 Hz, 1H), 3.98 (t, *J* = 8.12 Hz, 2H), 3.23 – 3.00 (m, 8H), 1.64 – 1.43 (m, 8H), 1.38 – 1.20 (m, 8H), 0.91 (t, *J* = 7.32 Hz, 12H).

Compound 71: This compound was synthesised on a 3 mmol scale in line with our previously published methods,¹³⁶ the pure product was obtained as a pale yellow solid with a yield of 61 % (1.11 g, 1.83 mmol). Proton NMR were found to match our previously published values.¹³⁶ ¹H NMR (400 MHz, 298.15 K, DMSO-*d*₆): δ: 10.67 (s, 1H) 8.45 (d, *J* = 7.77 Hz, 1H), 8.30 (d, *J* = 7.79 Hz, 1H), 8.15 (d, *J* = 7.92 Hz, 1H), 7.85 (d, *J* = 7.72 Hz, 2H), 7.58 (t, *J* = 7.58 Hz, 1H), 7.47 (tt, *J* = 11.69, 7.49 Hz, 2H), 7.10 (t, *J* = 7.52 Hz, 1H), 3.96 (s, 2H), 3.23 – 2.99 (m, 8H), 1.62 – 1.44 (m, 8H), 1.41 – 1.19 (m, 8H), 0.92 (t, *J* = 7.32 Hz, 12H).

Compound 72: This compound was synthesised on a 4 mmol scale in line with our previously published methods,¹³⁶ the pure product was obtained as a pale yellow solid with a yield of 81 % (2.01 g, 3.24 mmol). Proton NMR were found to match our previously published values.¹³⁶ ¹H NMR (400 MHz, 298.15 K, DMSO-*d*₆): δ: 9.25 (s, 1H), 7.95 – 7.75 (m, 4H), 7.58 (d, *J* = 8.74 Hz, 2H), 7.37 – 7.20 (m, 1H), 6.98 (t, *J* = 5.88 Hz, 1H), 3.96 (d, *J* = 5.88 Hz, 2H), 3.20 – 3.01 (m, 9H), 2.43 (s, 3H), 1.63 – 1.43 (m, 9H), 1.40 – 1.17 (m, 9H), 0.91 (t, *J* = 7.32 Hz, 12H).

Compounds 73 and 75-80: One equivalent of hydroxide salt was added to ethane sulfonic acid (0.22 g, 2.0 mmol) and taken to dryness to give the pure product as a white solid/clear oil with a yield of 100 %.

Compound 74: One equivalent of pyridine was added to ethane sulfonic acid (0.22 g, 2.0 mmol) and taken to dryness to give the pure product as a white solid with a yield of 100 %.

Compound 104: Triphosgene (0.31 g, 1.0 mmol) was added to a stirring solution of 4-(6-methylbenzothiazol)aniline (0.50 g, 2.0 mmol) in ethyl acetate (30 mL) and the mixture heated at reflux for 4 hours. 4-(6-methylbenzothiazol)aniline (0.50 g, 2.0 mmol) was then added to the reaction mixture and heated at reflux overnight, filtered and the solid washed with ethyl acetate (10 mL). The impurities were removed through recrystallization, followed by filtration of the solid from methanol. The filtration was then taken to dryness to give the pure product as a yellow solid with a yield of 84 % (0.85 g, 1.68 mmol); Melting Point: > 200 °C; ¹H NMR (400 MHz, DMSO-*d*₆): δ: 9.19 (s, 2H), 8.02 (d, *J* = 8.72 Hz, 4H), 7.91 (ds, 4H), 7.69 (d, *J* = 8.52 Hz, 4H), 7.35 (d, *J* = 8.44 Hz, 2H), 2.47 (s, 6H); ¹³C{¹H} NMR (100 MHz, DMSO-*d*₆): δ: 166.4 (CO), 152.5 (ArC), 152.3 (ArC), 142.8 (ArC), 135.4 (ArC), 134.8 (ArC), 128.3 (ArCH), 127.1 (ArC), 122.5 (ArCH), 122.2 (ArCH), 118.1 (ArCH), 21.5 (CH₃); IR (film): ν = 3270 (NH stretch), 1687, 1100, 995; HRMS (C₂₉H₂₂N₄OS₂) (ESI⁺): m/z: act: 507.8847 [M + H]⁺ cal: 506.1235 [M].

6.3 References

- 1 L. J. White, C. Wark, L. Croucher, E. R. Draper and J. R. Hiscock, *Chem. Commun.*, 2020, **56**, 9557–9560.
- 2 L. J. White, J. E. Boles, N. Allen, L. S. Alesbrook, J. M. Sutton, C. K. Hind, K. L. F. Hilton, L. R. Blackholly, R. J. Ellaby, G. T. Williams, D. P. Mulvihill and J. R. Hiscock, *J. Mater. Chem. B*, 2020, **8**, 4694–4700.
- 3 L. J. White, S. N. Tyuleva, B. Wilson, H. J. Shepherd, K. K. L. Ng, S. J. Holder, E. R. Clark and J. R. Hiscock, *Chem. - Eur. J.*, 2018, **24**, 7761–7773.
- 4 C. J. Pedersen, *Angew. Chemie Int. Ed.*, 1988, **27**, 1021–1027.
- 5 D. J. Cram, *Angew. Chemie Int. Ed.*, 1988, **27**, 1009–1020.
- 6 J. M. Lehn, *Acc. Chem. Res.*, 1978, **11**, 49–57.
- 7 J.-M. Lehn, *Angew. Chemie Int. Ed.*, 1988, **27**, 89–112.

- 8 G. M. Whitesides, *Science*, 2002, **295**, 2418–2421.
- 9 D. Philp and J. F. Stoddart, *Angew. Chemie Int. Ed.*, 1996, **35**, 1154–1196.
- 10 J. F. Stoddart, *Acc. Chem. Res.*, 2001, **34**, 410–411.
- 11 B. Olenyuk, A. Fechtenkötter and P. J. Stang, *J. Chem. Soc. Dalt. Trans.*, 1998, **11**, 1707–1728.
- 12 E. Kinne-Saffran and R. K. H. Kinne, *Am. J. Nephrol.*, 1999, **19**, 290–294.
- 13 P. S. Cohen and S. M. Cohen, *J. Chem. Educ.*, 1996, **73**, 883–886.
- 14 G. N. Lewis, *J. Am. Chem. Soc.*, 1916, **38**, 762–785.
- 15 G. N. Lewis, *J. Am. Chem. Soc.*, 1913, **35**, 1448–1455.
- 16 I. Langmuir, *J. Am. Chem. Soc.*, 1919, **41**, 868–934.
- 17 H. Margenau, *Rev. Mod. Phys.*, 1939, **11**, 1–35.
- 18 D. E. Koshland, *Angew. Chemie Int. Ed.*, 1995, **33**, 2375–2378.
- 19 D. J. Cram and J. M. Cram, *Science*, 1974, **183**, 803–809.
- 20 U. Boas and P. M. H. Heegaard, *Chem. Soc. Rev.*, 2004, **33**, 43–63.
- 21 T. S. Moore and T. F. Winmill, *J. Chem. Soc. Trans.*, 1912, **101**, 1635–1676.
- 22 W. M. Latimer and W. H. Rodebush, *J. Am. Chem. Soc.*, 1920, **42**, 1419–1433.
- 23 R. M. Izatt, *Chem. Soc. Rev.*, 2017, **46**, 2380–2384.
- 24 G. M. Lein and D. J. Cram, *J. Chem. Soc. Chem. Commun.*, 1982, **5**, 301–304.
- 25 V. Richards, *Nat. Chem.*, 2016, **8**, 1090–1090.
- 26 J.-P. Sauvage, *Angew. Chemie Int. Ed.*, 2017, **56**, 11080–11093.
- 27 C. J. Bruns and J. F. Stoddart, *Acc. Chem. Res.*, 2014, **47**, 2186–2199.

- 28 B. L. Feringa, *Angew. Chemie Int. Ed.*, 2017, **56**, 11060–11078.
- 29 Y. Liu, A. H. Flood, P. A. Bonvallet, S. A. Vignon, B. H. Northrop, H.-R. Tseng, J. O. Jeppesen, T. J. Huang, B. Brough, M. Baller, S. Magonov, S. D. Solares, W. A. Goddard, C.-M. Ho and J. F. Stoddart, *J. Am. Chem. Soc.*, 2005, **127**, 9745–9759.
- 30 D. H. Williams and M. S. Westwell, *Chem. Soc. Rev.*, 1998, **27**, 57–63.
- 31 I. E. Dzyaloshinskii, E. M. Lifshitz and L. P. Pitaevskii, *Adv. Phys.*, 1961, **10**, 165–209.
- 32 J. W. Steed and J. L. Atwood, *Supramolecular chemistry*, John Wiley & Sons, Ltd, Chichester, UK, 2013.
- 33 K. H. Sippel and F. A. Quioco, *Protein Sci.*, 2015, **24**, 1040–1046.
- 34 R. L. Baldwin, *Biophys. J.*, 1996, **71**, 2056–2063.
- 35 C. A. Hunter and J. K. M. Sanders, *J. Am. Chem. Soc.*, 1990, **112**, 5525–5534.
- 36 C. R. Martinez and B. L. Iverson, *Chem. Sci.*, 2012, **3**, 2191–2201.
- 37 S. L. Cockroft, C. A. Hunter, K. R. Lawson, J. Perkins and C. J. Urch, *J. Am. Chem. Soc.*, 2005, **127**, 8594–8595.
- 38 M. O. Sinnokrot, E. F. Valeev and C. D. Sherrill, *J. Am. Chem. Soc.*, 2002, **124**, 10887–10893.
- 39 E. C. Lee, B. H. Hong, J. Y. Lee, J. C. Kim, D. Kim, Y. Kim, P. Tarakeshwar and K. S. Kim, *J. Am. Chem. Soc.*, 2005, **127**, 4530–4537.
- 40 I. I. Cisse, H. Kim and T. Ha, *Nat. Struct. Mol. Biol.*, 2012, **19**, 623–627.
- 41 H. D. B. Jenkins and K. F. Pratt, *J. Chem. Soc. Faraday Trans. 2*, 1977, **73**, 812–821.
- 42 *Choice Rev. Online*, 2013, **51**, 51-0034-51-0034.
- 43 J. D. Smith, C. D. Cappa, K. R. Wilson, R. C. Cohen, P. L. Geissler and R. J. Saykally, *Proc.*

- Natl. Acad. Sci.*, 2005, **102**, 14171–14174.
- 44 A. Gavezzotti, *New J. Chem.*, 2016, **40**, 6848–6853.
- 45 M. J. Mayoral, N. Bilbao and D. González-Rodríguez, *ChemistryOpen*, 2016, **5**, 10–32.
- 46 R. C. Dougherty, *J. Chem. Phys.*, 1998, **109**, 7372–7378.
- 47 J. W. Steed, D. R. Turner and K. Wallace, *Core Concepts in Supramolecular Chemistry and Nanochemistry: From Supramolecules to Nanotechnology*, John Wiley & Sons, Ltd, West Sussex, UK, 2007.
- 48 W. G. Schneider, *J. Chem. Phys.*, 1955, **23**, 26–30.
- 49 M. L. Huggins, *J. Chem. Educ.*, 1960, **37**, A754–A756.
- 50 E. N. Baker and R. E. Hubbard, *Prog. Biophys. Mol. Biol.*, 1984, **44**, 97–179.
- 51 G. Alagona, C. Ghio and P. Kollman, *J. Am. Chem. Soc.*, 1983, **105**, 5226–5230.
- 52 R. D. Bach and O. Dmitrenko, *J. Am. Chem. Soc.*, 2004, **126**, 4444–4452.
- 53 F. Biedermann and H.-J. Schneider, *Chem. Rev.*, 2016, **116**, 5216–5300.
- 54 J. Černý and P. Hobza, *Phys. Chem. Chem. Phys.*, 2007, **9**, 5291–5303.
- 55 Y. Yokoyama and S. Yusa, *Polym. J.*, 2013, **45**, 985–992.
- 56 K. E. Riley and P. Hobza, *WIREs Comput. Mol. Sci.*, 2011, **1**, 3–17.
- 57 P. Jurečka and P. Hobza, *J. Am. Chem. Soc.*, 2003, **125**, 15608–15613.
- 58 C. A. Hunter, *Angew. Chemie Int. Ed.*, 2004, **43**, 5310–5324.
- 59 Y. Liu and D. W. Bolen, *Biochemistry*, 1995, **34**, 12884–12891.
- 60 M. A. Roseman, *J. Mol. Biol.*, 1988, **200**, 513–522.
- 61 R. E. Hubbard and M. Kamran Haider, in *Encyclopedia of Life Sciences*, John Wiley & Sons, Ltd, Chichester, UK, 2010.

- 62 C. O. Mackenzie, J. Zhou and G. Grigoryan, *Proc. Natl. Acad. Sci.*, 2016, **113**, E7438–E7447.
- 63 S. Hauri, H. Khakzad, L. Happonen, J. Teleman, J. Malmström and L. Malmström, *Nat. Commun.*, 2019, **10**, 192–202.
- 64 A. Klug, *Nature*, 1968, **219**, 808–810.
- 65 J. D. Watson and F. H. C. Crick, *Nature*, 1953, **171**, 737–738.
- 66 J.-M. Lehn, *Eur. Rev.*, 2009, **17**, 263–280.
- 67 G. M. Whitesides and M. Boncheva, *Proc. Natl. Acad. Sci.*, 2002, **99**, 4769–4774.
- 68 J.-M. Lehn, *Chem. Soc. Rev.*, 2007, **36**, 151–160.
- 69 G. M. Whitesides and M. Boncheva, *Proc. Natl. Acad. Sci.*, 2002, **99**, 4769 LP – 4774.
- 70 C. H. Park and H. E. Simmons, *J. Am. Chem. Soc.*, 1968, **90**, 2431–2432.
- 71 B. Dietrich, J. Guilhem, J.-M. Lehn, C. Pascard and E. Sonveaux, *Helv. Chim. Acta*, 1984, **67**, 91–104.
- 72 M. C. T. Fyfe, P. T. Glink, S. Menzer, J. F. Stoddart, A. J. P. White and D. J. Williams, *Angew. Chemie Int. Ed.*, 1997, **36**, 2068–2070.
- 73 D. Yang, J. Zhao, X.-J. Yang and B. Wu, *Org. Chem. Front.*, 2018, **5**, 662–690.
- 74 J.-M. Lehn, *Science*, 2002, **295**, 2400–2403.
- 75 B. Hasenknopf, J. M. Lehn, G. Baum and D. Fenske, *Proc. Natl. Acad. Sci.*, 1996, **93**, 1397–1400.
- 76 I. Alfonso, M. Bolte, M. Bru, M. I. Burguete, S. V. Luis and J. Rubio, *J. Am. Chem. Soc.*, 2008, **130**, 6137–6144.
- 77 J. K. Clegg, J. Cremers, A. J. Hogben, B. Breiner, M. M. J. Smulders, J. D. Thoburn and J.

- R. Nitschke, *Chem. Sci.*, 2013, **4**, 68–76.
- 78 J. C. Biffinger, H. W. Kim and S. G. DiMugno, *ChemBioChem*, 2004, **5**, 622–627.
- 79 Y. Kang, K. Liu and X. Zhang, *Langmuir*, 2014, **30**, 5989–6001.
- 80 C. Wang, Z. Wang and X. Zhang, *Acc. Chem. Res.*, 2012, **45**, 608–618.
- 81 V. A. Karetsi, C. N. Banti, N. Kourkoumelis, C. Papachristodoulou, C. D. Stalikas, C. P. Raptopoulou, V. Psycharis, P. Zoumpoulakis, T. Mavromoustakos, I. Sainis and S. K. Hadjikakou, *Antibiotics*, 2019, **8**, 213–228.
- 82 G. Viscardi, P. Quagliotto, C. Barolo, P. Savarino, E. Barni and E. Fiscaro, *J. Org. Chem.*, 2000, **65**, 8197–8203.
- 83 N. Alwadani and P. Fatehi, *Carbon Resour. Convers.*, 2018, **1**, 126–138.
- 84 G. P. Kumar and P. Rajeshwarrao, *Acta Pharm. Sin. B*, 2011, **1**, 208–219.
- 85 A. Wu, Y. Gao and L. Zheng, *Green Chem.*, 2019, **21**, 4290–4312.
- 86 P. Fischer, H. Rehage and B. Grüning, *J. Phys. Chem. B*, 2002, **106**, 11041–11046.
- 87 W. Kim, J. Thévenot, E. Ibarboure, S. Lecommandoux and E. L. Chaikof, *Angew. Chemie Int. Ed.*, 2010, **49**, 4257–4260.
- 88 D. Lombardo, M. A. Kiselev, S. Magazù and P. Calandra, *Adv. Condens. Matter Phys.*, 2015, **2015**, 1–22.
- 89 T. J. Moyer, J. A. Finbloom, F. Chen, D. J. Toft, V. L. Cryns and S. I. Stupp, *J. Am. Chem. Soc.*, 2014, **136**, 14746–14752.
- 90 J. N. Israelachvili, *Intermolecular and Surface Forces*, Academic Press, London, UK, 3rd editio., 2011.
- 91 Y. Lu and K. Park, *Int. J. Pharm.*, 2013, **453**, 198–214.

- 92 W. Qiu, Z. Fu, G. G. Xu, R. A. Grassucci, Y. Zhang, J. Frank, W. A. Hendrickson and Y. Guo, *Proc. Natl. Acad. Sci.*, 2018, **115**, 12985–12990.
- 93 M. Doktorova, F. A. Heberle, B. Eicher, R. F. Standaert, J. Katsaras, E. London, G. Pabst and D. Marquardt, *Nat. Protoc.*, 2018, **13**, 2086–2101.
- 94 J. Berg, J. Tymoczko and L. Stryer, *Biochemistry fifth edition*, W.H. Freeman, 5th edn., 2002.
- 95 P. Alexandridis and K. Andersson, *J. Phys. Chem. B*, 1997, **101**, 8103–8111.
- 96 X. Zhang and C. Wang, *Chem. Soc. Rev.*, 2011, **40**, 94–101.
- 97 Y. Kang, X. Tang, Z. Cai and X. Zhang, *Adv. Funct. Mater.*, 2016, **26**, 8920–8931.
- 98 C. Shan, X. Huang, H. Wei, W. Wei, H. Sun and X. Tang, *RSC Adv.*, 2014, **4**, 11216–11218.
- 99 C. Wang, Q. Chen, Z. Wang and X. Zhang, *Angew. Chemie Int. Ed.*, 2010, **49**, 8612–8615.
- 100 K. Liu, Y. Yao, Y. Liu, C. Wang, Z. Li and X. Zhang, *Langmuir*, 2012, **28**, 10697–10702.
- 101 C. B. Minkenberg, B. Homan, J. Boekhoven, B. Norder, G. J. M. Koper, R. Eelkema and J. H. van Esch, *Langmuir*, 2012, **28**, 13570–13576.
- 102 X. Wu, X.-X. Chen, M. Zhang, Z. Li, P. A. Gale and Y.-B. Jiang, *Chem. Commun.*, 2016, **52**, 6981–6984.
- 103 G. Yu, K. Jie and F. Huang, *Chem. Rev.*, 2015, **115**, 7240–7303.
- 104 F. Huang and X. Zhang, *Mater. Chem. Front.*, 2020, **4**, 11–11.
- 105 X. Zhang, Z. Chen and F. Würthner, *J. Am. Chem. Soc.*, 2007, **129**, 4886–4887.
- 106 A. V Kabanov, T. K. Bronich, V. A. Kabanov, K. Yu and A. Eisenberg, *J. Am. Chem. Soc.*, 1998, **120**, 9941–9942.
- 107 A. Wilson, G. Gasparini and S. Matile, *Chem. Soc. Rev.*, 2014, **43**, 1948–1962.

- 108 J. Zou, F. Tao and M. Jiang, *Langmuir*, 2007, **23**, 12791–12794.
- 109 Y. Chang, Y. Jiao, H. E. Symons, J.-F. Xu, C. F. J. Faul and X. Zhang, *Chem. Soc. Rev.*, 2019, **48**, 989–1003.
- 110 K. P. Nartowski, S. M. Ramalhete, P. C. Martin, J. S. Foster, M. Heinrich, M. D. Eddleston, H. R. Green, G. M. Day, Y. Z. Khimyak and G. O. Lloyd, *Cryst. Growth Des.*, 2017, **17**, 4100–4109.
- 111 X. Lin, M. Suzuki, M. Gushiken, M. Yamauchi, T. Karatsu, T. Kizaki, Y. Tani, K. Nakayama, M. Suzuki, H. Yamada, T. Kajitani, T. Fukushima, Y. Kikkawa and S. Yagai, *Sci. Rep.*, 2017, **7**, 43098–43110.
- 112 Nonappa, J. S. Haataja, J. V. I. Timonen, S. Malola, P. Engelhardt, N. Houbenov, M. Lahtinen, H. Häkkinen and O. Ikkala, *Angew. Chemie Int. Ed.*, 2017, **56**, 6473–6477.
- 113 X. Zhou, G. Liu, K. Yamato, Y. Shen, R. Cheng, X. Wei, W. Bai, Y. Gao, H. Li, Y. Liu, F. Liu, D. M. Czajkowsky, J. Wang, M. J. Dabney, Z. Cai, J. Hu, F. V. Bright, L. He, X. C. Zeng, Z. Shao and B. Gong, *Nat. Commun.*, 2012, **3**, 949–957.
- 114 N. Busschaert, C. Caltagirone, W. Van Rossom and P. A. Gale, *Chem. Rev.*, 2015, **115**, 8038–8155.
- 115 P. A. Gale and C. Caltagirone, *Chem. Soc. Rev.*, 2015, **44**, 4212–4227.
- 116 T. Gunnlaugsson, A. P. Davis, G. M. Hussey, J. Tierney and M. Glynn, *Org. Biomol. Chem.*, 2004, **2**, 1856–1863.
- 117 V. Blažek Bregović, N. Basarić and K. Mlinarić-Majerski, *Coord. Chem. Rev.*, 2015, **295**, 80–124.
- 118 M. C. Etter, Z. Urbanczyk-Lipkowska, M. Zia-Ebrahimi and T. W. Panunto, *J. Am. Chem. Soc.*, 1990, **112**, 8415–8426.
- 119 P. J. Smith, M. V. Reddington and C. S. Wilcox, *Tetrahedron Lett.*, 1992, **33**, 6085–6088.

- 120 P. J. Smith, E. Kim and C. S. Wilcox, *Angew. Chemie Int. Ed.*, 1993, **32**, 1648–1650.
- 121 P. A. Gale, R. Pérez-Tomás and R. Quesada, *Acc. Chem. Res.*, 2013, **46**, 2801–2813.
- 122 L. E. Santos-Figueroa, M. E. Moragues, E. Climent, A. Agostini, R. Martínez-Mañez and F. Sancenón, *Chem. Soc. Rev.*, 2013, **42**, 3489–3613.
- 123 J. W. Steed, *Chem. Soc. Rev.*, 2010, **39**, 3686–3699.
- 124 V. Štrukil, *Beilstein J. Org. Chem.*, 2017, **13**, 1828–1849.
- 125 D. E. Gómez, L. Fabbrizzi, M. Licchelli and E. Monzani, *Org. Biomol. Chem.*, 2005, **3**, 1495–1500.
- 126 A. Scozzafava, A. Mastrolorenzo and C. T. Supuran, *J. Enzyme Inhib.*, 2001, **16**, 425–432.
- 127 J. R. Hiscock, N. J. Wells, J. A. Ede, P. A. Gale and M. R. Sambrook, *Org. Biomol. Chem.*, 2016, **14**, 9560–9567.
- 128 A. E. Hooper, S. R. Kennedy, C. D. Jones and J. W. Steed, *Chem. Commun.*, 2016, **52**, 198–201.
- 129 C. M. C. Faustino, A. R. T. Calado and L. Garcia-Rio, *J. Phys. Chem. B*, 2009, **113**, 977–982.
- 130 C. M. C. Faustino, A. R. T. Calado and L. Garcia-Rio, *Biomacromolecules*, 2009, **10**, 2508–2514.
- 131 C. M. C. Faustino, A. R. T. Calado and L. Garcia-Rio, *J. Colloid Interface Sci.*, 2011, **359**, 493–498.
- 132 C. M. C. Faustino, A. R. T. Calado and L. Garcia-Rio, *J. Colloid Interface Sci.*, 2012, **367**, 286–292.
- 133 C. M. C. Faustino, A. R. T. Calado and L. Garcia-Rio, *J. Colloid Interface Sci.*, 2010, **351**, 472–477.

- 134 J. R. Hiscock, G. P. Bustone, B. Wilson, K. E. Belsey and L. R. Blackholly, *Soft Matter*, 2016, **12**, 4221–4228.
- 135 L. R. Blackholly, H. J. Shepherd and J. R. Hiscock, *CrystEngComm*, 2016, **18**, 7021–7028.
- 136 L. J. White, N. J. Wells, L. R. Blackholly, H. J. Shepherd, B. Wilson, G. P. Bustone, T. J. Runacres and J. R. Hiscock, *Chem. Sci.*, 2017, **8**, 7620–7630.
- 137 S. Kumar, K. Ludwig, B. Schade, H. von Berlepsch, I. Papp, R. Tyagi, M. Gulia, R. Haag and C. Böttcher, *Chem. – Eur. J.*, 2016, **22**, 5629–5636.
- 138 D. Yan, *Chem. - Eur. J.*, 2015, **21**, 4880–4896.
- 139 J. W. Steed, *Chem. Commun.*, 2011, **47**, 1379–1383.
- 140 B. Domon, *Science*, 2006, **312**, 212–217.
- 141 E. Nordhoff, F. Kirpekar and P. Roepstorff, *Mass Spectrom. Rev.*, 1996, **15**, 67–138.
- 142 C. E. C. A. Hop and R. Bakhtiar, *J. Chem. Educ.*, 1996, **73**, A162–A169.
- 143 S. R. Wilson and Y. Wu, *J. Am. Soc. Mass Spectrom.*, 1993, **4**, 596–603.
- 144 M. J. Keith-Roach, *Anal. Chim. Acta*, 2010, **678**, 140–148.
- 145 S. Banerjee and S. Mazumdar, *Int. J. Anal. Chem.*, 2012, **2012**, 1–40.
- 146 M. Przybylski and M. O. Glocker, *Angew. Chemie Int. Ed.*, 1996, **35**, 806–826.
- 147 C. A. Bunton, *Medium effects of micelles as microreactors and the scope of the Hughes-Ingold solvent theory*, Santa Barbara, 1996.
- 148 J. L. Anderson, V. Pino, E. C. Hagberg, V. V. Sheares and D. W. Armstrong, *Chem. Commun.*, 2003, 2444–2445.
- 149 V. M. Wallace, N. R. Dhumal, F. M. Zehentbauer, H. J. Kim and J. Kiefer, *J. Phys. Chem. B*, 2015, **119**, 14780–14789.

- 150 B. Lorber, F. Fischer, M. Bailly, H. Roy and D. Kern, *Biochem. Mol. Biol. Educ.*, 2012, **40**, 372–382.
- 151 W. I. Goldberg, *Am. J. Phys.*, 1999, **67**, 1152–1160.
- 152 J. T. Edward, *J. Chem. Educ.*, 1970, **47**, 261.
- 153 P. M. Carvalho, M. R. Felício, N. C. Santos, S. Gonçalves and M. M. Domingues, *Front. Chem.*, 2018, **6**, 1–17.
- 154 S. Bhattacharjee, *J. Control. Release*, 2016, **235**, 337–351.
- 155 L. Maibaum, A. R. Dinner and D. Chandler, *J. Phys. Chem. B*, 2004, **108**, 6778–6781.
- 156 Á. Piñeiro, X. Banquy, S. Pérez-Casas, E. Tovar, A. García, A. Villa, A. Amigo, A. E. Mark and M. Costas, *J. Phys. Chem. B*, 2007, **111**, 4383–4392.
- 157 R. J. Williams, J. N. Phillips and K. J. Mysels, *Trans. Faraday Soc.*, 1955, **51**, 728–737.
- 158 R. Nagarajan and E. Ruckenstein, *Langmuir*, 1991, **7**, 2934–2969.
- 159 K. Shinoda, *J. Phys. Chem.*, 1954, **58**, 541–544.
- 160 D. Attwood, *Kolloid-Zeitschrift und Zeitschrift für Polym.*, 1969, **232**, 788–792.
- 161 S. K. Hait and S. P. Moulik, *J. Surfactants Deterg.*, 2001, **4**, 303–309.
- 162 M. Lesemann, K. Thirumoorthy, Y. J. Kim, J. Jonas and M. E. Paulaitis, *Langmuir*, 1998, **14**, 5339–5341.
- 163 A. Fluksman and O. Benny, *Anal. Methods*, 2019, **11**, 3810–3818.
- 164 M. Boiocchi, L. Del Boca, D. E. Gómez, L. Fabbrizzi, M. Licchelli and E. Monzani, *J. Am. Chem. Soc.*, 2004, **126**, 16507–16514.
- 165 A. K. Ghose, A. Pritchett and G. M. Crippen, *J. Comput. Chem.*, 1988, **9**, 80–90.
- 166 T. Niemann, D. H. Zaitsau, A. Strate, P. Stange and R. Ludwig, *Phys. Chem. Chem. Phys.*,

- 2020, **22**, 2763–2774.
- 167 J. E. Del Bene, I. Alkorta and J. Elguero, *J. Phys. Chem. A*, 2008, **112**, 7925–7929.
- 168 Y. Xu, J. Yao, P. Yao, H. Li and S. Han, *Chinese J. Chem. Eng.*, 2010, **18**, 455–461.
- 169 G. A. Kumar and M. A. McAllister, *J. Org. Chem.*, 1998, **63**, 6968–6972.
- 170 J. E. Del Bene, S. A. Perera and R. J. Bartlett, *J. Phys. Chem. A*, 1999, **103**, 8121–8124.
- 171 J. A. Aguilar, R. W. Adams, M. Nilsson and G. A. Morris, *J. Magn. Reson.*, 2014, **238**, 16–19.
- 172 S. K. Bharti and R. Roy, *TrAC Trends Anal. Chem.*, 2012, **35**, 5–26.
- 173 R. F. Evilia, *Anal. Lett.*, 2001, **34**, 2227–2236.
- 174 V. R. Patel and Y. K. Agrawal, *J. Adv. Pharm. Technol. Res.*, 2011, **2**, 81–87.
- 175 J. D. Clogston and A. K. Patri, in *Characterization of nanoparticles intended for drug delivery*, Humana Press, Totowa, NJ, 2011, pp. 63–70.
- 176 R. Vogel, A. K. Pal, S. Jambhrunkar, P. Patel, S. S. Thakur, E. Reátegui, H. S. Parekh, P. Saá, A. Stassinopoulos and M. F. Broom, *Sci. Rep.*, 2017, **7**, 17479–17492.
- 177 Supramolecular.org - Binding Constant Calculators | Supramolecular, <http://app.supramolecular.org/bindfit/>, (accessed 1 July 2020).
- 178 R. B. Martin, *Chem. Rev.*, 1996, **96**, 3043–3064.
- 179 P. R. Stoesser and S. J. Gill, *J. Phys. Chem.*, 1967, **71**, 564–567.
- 180 M. M. J. Smulders, M. M. L. Nieuwenhuizen, T. F. A. De Greef, P. van der Schoot, A. P. H. J. Schenning and E. W. Meijer, *Chem. - Eur. J.*, 2010, **16**, 362–367.
- 181 T. F. A. De Greef, M. M. J. Smulders, M. Wolffs, A. P. H. J. Schenning, R. P. Sijbesma and E. W. Meijer, *Chem. Rev.*, 2009, **109**, 5687–5754.

- 182 N. Mohan and C. H. Suresh, *J. Phys. Chem. A*, 2014, **118**, 1697–1705.
- 183 R. Parthasarathi, V. Subramanian and N. Sathyamurthy, *J. Phys. Chem. A*, 2006, **110**, 3349–3351.
- 184 P. Kollman, J. McKelvey, A. Johansson and S. Rothenberg, *J. Am. Chem. Soc.*, 1975, **97**, 955–965.
- 185 J. J. P. Stewart, *J. Mol. Model.*, 2007, **13**, 1173–1213.
- 186 R. N. Perham, *Philos. Trans. R. Soc. London. B, Biol. Sci.*, 1975, **272**, 123–136.
- 187 Q. Zhang, Y.-X. Deng, H.-X. Luo, C.-Y. Shi, G. M. Geise, B. L. Feringa, H. Tian and D.-H. Qu, *J. Am. Chem. Soc.*, 2019, **141**, 12804–12814.
- 188 K. Almdal, J. Dyre, S. Hvidt and O. Kramer, *Polym. Gels Networks*, 1993, **1**, 5–17.
- 189 A. Vintiloiu and J.-C. Leroux, *J. Control. Release*, 2008, **125**, 179–192.
- 190 N. M. Sangeetha and U. Maitra, *Chem. Soc. Rev.*, 2005, **34**, 821–836.
- 191 P. C. Marr and A. C. Marr, *Green Chem.*, 2016, **18**, 105–128.
- 192 E. M. Ahmed, *J. Adv. Res.*, 2015, **6**, 105–121.
- 193 L. A. Estroff and A. D. Hamilton, *Chem. Rev.*, 2004, **104**, 1201–1218.
- 194 L. E. Buerkle and S. J. Rowan, *Chem. Soc. Rev.*, 2012, **41**, 6089–6102.
- 195 P. R. A. Chivers and D. K. Smith, *Nat. Rev. Mater.*, 2019, **4**, 463–478.
- 196 C. D. Jones and J. W. Steed, *Chem. Soc. Rev.*, 2016, **45**, 6546–6596.
- 197 X. Du, J. Zhou, J. Shi and B. Xu, *Chem. Rev.*, 2015, **115**, 13165–13307.
- 198 Z. Brezinger, *Physiol. Chem.*, 1892, **16**, 537–538.
- 199 R. . Gortner and W. F. Hoffman, *J. Am. Chem. Soc.*, 1921, **43**, 2199–2201.
- 200 F. M. Menger and K. S. Venkatasubban, *J. Org. Chem.*, 1978, **43**, 3413–3414.

- 201 F. M. Menger, Y. Yamasaki, K. K. Catlin and T. Nishimi, *Angew. Chemie Int. Ed.*, 1995, **34**, 585–586.
- 202 F. M. Menger and K. L. Caran, *J. Am. Chem. Soc.*, 2000, **122**, 11679–11691.
- 203 J. Shi, Y. Gao, Z. Yang and B. Xu, *Beilstein J. Org. Chem.*, 2011, **7**, 167–172.
- 204 B. O. Okesola and D. K. Smith, *Chem. Soc. Rev.*, 2016, **45**, 4226–4251.
- 205 Z. Yang, G. Liang, Z. Guo, Z. Guo and B. Xu, *Angew. Chemie Int. Ed.*, 2007, **46**, 8216–8219.
- 206 M. Ikeda, R. Ochi and I. Hamachi, *Lab Chip*, 2010, **10**, 3325–3334.
- 207 S. Xu, A. C. Sedgwick, S. A. Elfeky, W. Chen, A. S. Jones, G. T. Williams, A. T. A. Jenkins, S. D. Bull, J. S. Fossey and T. D. James, *Front. Chem. Sci. Eng.*, 2020, **14**, 112–116.
- 208 L. Yu and J. Ding, *Chem. Soc. Rev.*, 2008, **37**, 1473–1481.
- 209 C. Liu, C. Ruan, R. Shi, B.-P. Jiang, S. Ji and X.-C. Shen, *Biomater. Sci.*, 2019, **7**, 1705–1715.
- 210 K. Knuth, M. Amiji and J. R. Robinson, *Adv. Drug Deliv. Rev.*, 1993, **11**, 137–167.
- 211 R. Gaudana, H. K. Ananthula, A. Parenky and A. K. Mitra, *AAPS J.*, 2010, **12**, 348–360.
- 212 R. Donnelly, R. Shaikh, T. Raj Singh, M. Garland and Ad. Woolfson, *J. Pharm. Bioallied Sci.*, 2011, **3**, 89–100.
- 213 Y. Liu, W.-L. Lu, J.-C. Wang, X. Zhang, H. Zhang, X.-Q. Wang, T.-Y. Zhou and Q. Zhang, *J. Control. Release*, 2007, **117**, 387–395.
- 214 G. O. Lloyd and J. W. Steed, *Nat. Chem.*, 2009, **1**, 437–442.
- 215 L. Meazza, J. A. Foster, K. Fucke, P. Metrangolo, G. Resnati and J. W. Steed, *Nat. Chem.*, 2013, **5**, 42–47.

- 216 J. A. Foster, M.-O. M. Piepenbrock, G. O. Lloyd, N. Clarke, J. A. K. Howard and J. W. Steed, *Nat. Chem.*, 2010, **2**, 1037–1043.
- 217 E. Caló and V. V. Khutoryanskiy, *Eur. Polym. J.*, 2015, **65**, 252–267.
- 218 K. Pandurangan, J. A. Kitchen, S. Blasco, F. Paradisi and T. Gunnlaugsson, *Chem. Commun.*, 2014, **50**, 10819–10822.
- 219 B. Aslam, W. Wang, M. I. Arshad, M. Khurshid, S. Muzammil, M. H. Rasool, M. A. Nisar, R. F. Alvi, M. A. Aslam, M. U. Qamar, M. K. F. Salamat and Z. Baloch, *Infect. Drug Resist.*, 2018, **Volume 11**, 1645–1658.
- 220 S. Davies, J. Farrar, J. Rex, L. White, R. Murry and J. O’Neill, *Antimicrobial Resistance: Tackling a crisis for the health and wealth of nations*, 2014.
- 221 M. Zhang, P.-P. Zhu, P. Xin, W. Si, Z.-T. Li and J.-L. Hou, *Angew. Chemie Int. Ed.*, 2017, **56**, 2999–3003.
- 222 H. S. El-Sheshtawy, S. Chatterjee, K. I. Assaf, M. N. Shinde, W. M. Nau and J. Mohanty, *Sci. Rep.*, 2018, **8**, 13925–13935.
- 223 S. N. Tyuleva, N. Allen, L. J. White, A. Pépés, H. J. Shepherd, P. J. Saines, R. J. Ellaby, D. P. Mulvihill and J. R. Hiscock, *Chem. Commun.*, 2019, **55**, 95–98.
- 224 E. R. Draper and D. J. Adams, *Chem*, 2017, **3**, 390–410.
- 225 A. L. García-Ortiz, R. Domínguez-González, M. Romero-Ávila, B. Flores-Pérez, L. Guillén, M. Castro and N. Barba-Behrens, *Inorganica Chim. Acta*, 2018, **471**, 550–560.
- 226 L. S. Birchall, S. Roy, V. Jayawarna, M. Hughes, E. Irvine, G. T. Okorogheye, N. Saudi, E. De Santis, T. Tuttle, A. A. Edwards and R. V. Ulijn, *Chem. Sci.*, 2011, **2**, 1349–1355.
- 227 J. Chen, H. Park and K. Park, *J. Biomed. Mater. Res.*, 1999, **44**, 53–62.
- 228 S. Lü, C. Gao, X. Xu, X. Bai, H. Duan, N. Gao, C. Feng, Y. Xiong and M. Liu, *ACS Appl.*

- Mater. Interfaces*, 2015, **7**, 13029–13037.
- 229 P. K. Sukul and S. Malik, *Soft Matter*, 2011, **7**, 4234.
- 230 K. D. Vernon-Parry, *III-Vs Rev.*, 2000, **13**, 40–44.
- 231 M. T. Postek and A. E. Vladár, *Scanning Microsc.*, 2015, **9636**, 963605–963616.
- 232 A. J. D’Alfonso, B. Freitag, D. Klenov and L. J. Allen, *Phys. Rev. B*, 2010, **81**, 100101–100105.
- 233 A. R. Clarke, G. Archenhold and N. C. Davidson, *Compos. Sci. Technol.*, 1995, **55**, 75–91.
- 234 B. Findlay, G. G. Zhanel and F. Schweizer, *Antimicrob. Agents Chemother.*, 2010, **54**, 4049–4058.
- 235 B. Gottenbos, *J. Antimicrob. Chemother.*, 2001, **48**, 7–13.
- 236 G. van Meer and A. I. P. M. de Kroon, *J. Cell Sci.*, 2011, **124**, 5–8.
- 237 R. F. Epand, P. B. Savage and R. M. Epand, *Biochim. Biophys. Acta - Biomembr.*, 2007, **1768**, 2500–2509.
- 238 J. M. Andrews, *J. Antimicrob. Chemother.*, 2001, **48**, 5–16.
- 239 R. F. Epand, J. E. Pollard, J. O. Wright, P. B. Savage and R. M. Epand, *Antimicrob. Agents Chemother.*, 2010, **54**, 3708–3713.
- 240 S. Furse, H. Wienk, R. Boelens, A. I. P. M. de Kroon and J. A. Killian, *FEBS Lett.*, 2015, **589**, 2726–2730.
- 241 J. Gidden, J. Denson, R. Liyanage, D. M. Ivey and J. O. Lay, *Int. J. Mass Spectrom.*, 2009, **283**, 178–184.
- 242 A. M. Samy, M. M. Ghorab, S. G. Shadeed and E. A. Mazyed, *Int. J. Pharm. Pharm. Sci.*, 2013, **5**, 600–601.

- 243 H. Lambers, S. Piessens, A. Bloem, H. Pronk and P. Finkel, *Int. J. Cosmet. Sci.*, 2006, **28**, 359–370.
- 244 M. J. Price and M. Trbovich, in *Thermoregulation: From Basic Neuroscience to Clinical Neurology, Part II*, ed. A. A. B. T.-H. of C. N. Romanovsky, Elsevier, 2018, vol. 157, pp. 799–820.
- 245 O. Wichterle and D. Lim, *Nature*, 1960, **185**, 117–118.
- 246 W. Treesuppharat, P. Rojanapanthu, C. Siangsanoh, H. Manuspiya and S. Ummartyotin, *Biotechnol. Reports*, 2017, **15**, 84–91.
- 247 B. Xing, C.-W. Yu, K.-H. Chow, P.-L. Ho, D. Fu and B. Xu, *J. Am. Chem. Soc.*, 2002, **124**, 14846–14847.
- 248 Q. Chai, Y. Jiao and X. Yu, *Gels*, 2017, **3**, 6–21.
- 249 J. Li and D. J. Mooney, *Nat. Rev. Mater.*, 2016, **1**, 16071–16076.
- 250 N. Peppas, *Eur. J. Pharm. Biopharm.*, 2000, **50**, 27–46.
- 251 W. J. Frith, A. M. Donald, D. J. Adams and A. Aufderhorst-Roberts, *J. Nonnewton. Fluid Mech.*, 2015, **222**, 104–111.
- 252 A. Karoyo and L. Wilson, *Gels*, 2017, **3**, 1–18.
- 253 G. Yu, X. Yan, C. Han and F. Huang, *Chem. Soc. Rev.*, 2013, **42**, 6697–6722.
- 254 C. Yan and D. J. Pochan, *Chem. Soc. Rev.*, 2010, **39**, 3528–3540.
- 255 O. Kotova, R. Daly, C. M. G. dos Santos, M. Boese, P. E. Kruger, J. J. Boland and T. Gunnlaugsson, *Angew. Chemie Int. Ed.*, 2012, **51**, 7208–7212.
- 256 M. Ahearne, Y. Yang, A. J. El Haj, K. Y. Then and K.-K. Liu, *J. R. Soc. Interface*, 2005, **2**, 455–463.
- 257 N. S. S. Kumar, S. Varghese, G. Narayan and S. Das, *Angew. Chemie Int. Ed.*, 2006, **45**,

- 6317–6321.
- 258 J. Vandaele, B. Louis, K. Liu, R. Camacho, P. H. J. Kouwer and S. Rocha, *Soft Matter*, 2020, **16**, 4210–4219.
- 259 P. Barretta, F. Bordi, C. Rinaldi and G. Paradossi, *J. Phys. Chem. B*, 2000, **104**, 11019–11026.
- 260 D. Adams, *Gels*, 2018, **4**, 32–37.
- 261 P. Sahoo, R. Sankolli, H.-Y. Lee, S. R. Raghavan and P. Dastidar, *Chem. - Eur. J.*, 2012, **18**, 8057–8063.
- 262 S. Basak, J. Nanda and A. Banerjee, *J. Mater. Chem.*, 2012, **22**, 11658–11664.
- 263 N. Nonappa and E. Kolehmainen, *Soft Matter*, 2016, **12**, 6015–6026.
- 264 A. M. Mathur and A. B. Scranton, *Biomaterials*, 1996, **17**, 547–557.
- 265 R. C. Ferguson and D. W. Ovenall, *Macromolecules*, 1987, **20**, 1245–1248.
- 266 J. Baselga, M. A. Llorente, J. L. Nieto, I. Hernández-Fuentes and I. F. Piérola, *Eur. Polym. J.*, 1988, **24**, 161–165.
- 267 B. Escuder, M. LLusar and J. F. Miravet, *J. Org. Chem.*, 2006, **71**, 7747–7752.
- 268 E. R. Draper, B. Dietrich, K. McAulay, C. Brasnett, H. Abdizadeh, I. Patmanidis, S. J. Marrink, H. Su, H. Cui, R. Schweins, A. Seddon and D. J. Adams, *Matter*, 2020, **2**, 764–778.
- 269 P. Terpstra, D. Combes and A. Zwick, *J. Chem. Phys.*, 1990, **92**, 65–70.
- 270 W. Wachter, W. Kunz, R. Buchner and G. Hefter, *J. Phys. Chem. A*, 2005, **109**, 8675–8683.
- 271 P. A. Gale, E. N. W. Howe and X. Wu, *Chem*, 2016, **1**, 351–422.

- 272 J. Zhang, B. Zhang, Q. Chen, B. Zhang and J. Song, *Nanoscale Res. Lett.*, 2019, **14**, 5–14.
- 273 D. Chandler, *Nature*, 2005, **437**, 640–647.
- 274 R. O. Harrison and B. D. Hammock, *J. Assoc. Off. Anal. Chem.*, 1988, **71**, 981–987.

